Theoretical, Numerical and Experimental Investigation of the Flow in Rotor-Stator Cavities with Application to a Centrifugal Pump

Von der Fakultät für Ingenieurwissenschaften, Abteilung Maschinenbau der

Universität Duisburg-Essen

zur Erlangung des akademischen Grades

DOKTOR-INGENIEURIN/
DOKTOR-INGENIEUR

genehmigte Dissertation

von

Björn-Christian Will
aus
Essen / Ruhr

Referent: Prof. Dr.-Ing. F.K. Benra
Korreferent: Prof. Dr. G. Bois
Tag der mündlichen Prüfung: 17.11.2011

Vorwort

Die vorliegende Arbeit entstand während meiner Zeit als wissenschaftlicher Mitarbeiter am Lehrstuhl für Strömungsmaschinen der Universität Duisburg-Essen und am Fachgebiet für Kolben- und Strömungsmaschinen im Fachbereich Maschinenbau der Fachhochschule Trier. Während dieses Zeitraums haben zahlreiche Personen zum Gelingen dieser Arbeit beigetragen, wovon zumindest einige nicht unerwähnt bleiben sollen.

An erster Stelle möchte ich mich bei Herrn Prof. Dr.-Ing. F.K. Benra, dem Leiter des Lehrstuhls für Strömungsmaschinen, dafür bedanken, dass er mir die Erstellung dieser Arbeit ermöglicht und mich während der vergangenen Jahre fortlaufend unterstützt hat.

Des Weiteren danke ich Herrn Prof. Dr. G. Bois für die Übernahme des Korreferats und das Interesse an der vorliegenden Arbeit.

Herrn Dr.-Ing. H.J. Dohmen, dem akademischen Oberrat des Lehrstuhls für Strömungsmaschinen, danke ich für die fachliche Unterstützung und die stets konstruktive Zusammenarbeit.

Weiterhin möchte ich an dieser Stelle Herrn Prof. Dr.-Ing. Ch. Simon, dem Leiter des Fachgebiets für Kolben- und Strömungsmaschinen an der Fachhochschule Trier, danken, der mich bereits während meines Studiums gefördert und meinen weiteren Weg geebnet hat. Auch die weitere Unterstützung während der Promotionsphase war stets zielführend und hilfreich.

Meine Dankbarkeit gilt weiterhin allen Mitarbeitern des Lehrstuhls für Strömungsmaschinen für die Vielzahl an fruchtbaren Diskussionen und Gesprächen, sowie die menschlich stets gute Zusammenarbeit.

Auch allen Studierenden, die im Rahmen von Studien- und Abschlussarbeiten wertvolle Beiträge zu dieser Arbeit geliefert haben, sei an dieser Stelle vielmals gedankt.

Letztendlich danke ich auch meiner ganzen Familie und allen mir nahestehenden Personen, die mich während der gesamten Promotionszeit stets unterstützt haben.

Björn-Christian Will
Duisburg im November 2011

Content

Nomenclature

Variables

a	Hub radius
a^+	Term in boundary layer formula
a_R, a_S	Velocity factors for the rotor and stator in case of separated boundary layers
$a^\#$	Velocity factor in case of merged boundary layers
A	Area
A_{Shaft}	Shaft area
A_1	Peripheral area of a small cylindrical volume element
A_2	Cross sectional area of a small cylindrical volume element
A^*	Constant in the logarithmic law of the wall
A^+	Constant in the expression for the boundary layer thickness
b	Outer impeller radius
B^+	Constant in the expression for the boundary layer thickness
B^*	Constant in the logarithmic law of the wall
c	Constant in the flow model
$c_m = \frac{M}{\frac{\rho}{2}\Omega^2 b^5}$	Moment coefficient
c_{m1deg}	Moment coefficient for a 1 deg segment
$c_D' = \frac{\dot{m}}{b\mu}$	Through-flow coefficient used in the FVV report
$c_p = \frac{p(b) - p(r)}{\rho\Omega^2 b^2}$	Pressure coefficient used in the FVV report
C	Sutherland constant
C_{fmean}	Friction coefficient
C^+	Constant in the equation for the boundary layer thickness on the stator
C_1	Constant depending on the velocity profile
C_1, C_2, C_3, C_4	Coefficients in a third-order polynomial function
$C_R = \frac{0.18}{\gamma_R^{\frac{1}{4}}}$	Factor in the flow model formulation
$C_S = \frac{0.18}{\gamma_S^{\frac{1}{4}}}$	Factor in the flow model formulation
d_{gap}	Gap diameter
D	Pipe diameter
$\dot{D}_e$	Entering angular momentum flux
$\dot{D}_{out}$	Exiting angular momentum flux
$Ek = \frac{1}{G^2 Re_\varphi}$	Ekman number
f	Body force
f'	Function in the flow model
f^*	Correction function
$F = \frac{v_r}{\Omega r}$	Dimensionless radial velocity on the free disk

F	Force
F_{ax}	Axial force
F_{BS}	Pressure force on the backside of the impeller
F_{FS}	Pressure force on the front side of the impeller
F_g	Other axial forces on the impeller like the mass force for non horizontal pumps
F_I	Momentum force on the impeller
F_{mech}	Mechanical force on the impeller
F_{SP}	Pressure force on the shaft
$G = \frac{v_\varphi}{\Omega r}$	Dimensionless tangential velocity on the free disk
$G = {}^{s}/_{b}$	Dimensionless gap width
$H = \frac{v_z}{\sqrt{\Omega \nu}}$	Dimensionless axial velocity on the free disk
H	Delivery head
H_∞	Dimensionless axial velocity at infinity for the free disk
$H_{\infty R}$	Dimensionless axial velocity component for a rotating disk in a rotating fluid
$H_{\infty S}$	Dimensionless axial velocity component for a stationary disk in a rotating fluid
i, j, l	Counting indices for sums
I	Momentum
k_S	Sand roughness
$K = \frac{v_{mean}}{v_{max}}$	Velocity ratio
l	Length of a flat plate
l_1	Radial gap height between outer rotor shroud and casing
l_2	Radial gap height between shaft and casing
m	Mass
m	Exponent for velocity profiles
m	Exponent in the formulation for the boundary layer thickness
$\dot{m}$	Mass flow rate
$\dot{m}_R$	Mass flow rate in the rotor boundary layer
$\dot{m}_S$	Mass flow rate in the stator boundary layer
M	Torque
M_I	Radial angular momentum
M_{Rotor}	Torque on the rotating disk
M_{Stator}	Torque on the stationary disk
M_{secR}	Torque due to the secondary flow in the rotor boundary layer
M_{secS}	Torque due to the secondary flow in the stator boundary layer
n	Exponent for velocity profiles
n	Exponent in the Sutherland law
$n_q = n\frac{\sqrt{Q}}{H^{\frac{3}{4}}}$	Specific speed (old definition)
p_{tot}	Total pressure
p	Pressure
p_e	Entrance pressure

$p^* = \frac{2 \cdot p}{\rho \Omega^2 b^2}$	Dimensionless pressure
Δp	Pressure difference
$\Delta \bar{p}(r) = \frac{p(r) - p(b)}{\frac{\rho}{2} \Omega^2 b^2}$	Dimensionless pressure based on the pressure difference $p(r) - p(b)$
p_1, p_2	Pressure at the positions 1 and 2
Δp_{gap}	Pressure difference across the sealing gap
Q	Volume flow rate
Q_{gap}	Leakage flow rate across the sealing gap
r	Radial coordinate
r_{gap}	Inner radius of the sealing gap
$\bar{r} = {}^{r}/_{b}$	Dimensionless radius
R	Pipe radius
Re	Reynolds number
Re_{crit}	Critical Reynolds number
Re_{mean}	Mean Reynolds number based on the mean velocity at the cross-section
$Re_{gap} = \sqrt{\left(\frac{2tv_{axgap}}{\nu}\right)^2 + 0.25\left(\frac{2tv_{gap}}{\nu}\right)^2}$	Gap Reynolds number
$Re_P = \frac{2t \cdot v_{gap}}{\nu}$	Perimeter Reynolds number for the sealing gap
$Re_{Pipe} = \frac{v_{mean} \cdot D}{\nu}$	Pipe Reynolds number
$Re_{Plate} = \frac{v_\infty \cdot l}{\nu}$	Reynolds number for a flat plate
$Re_l = \frac{\Omega \cdot r^2}{\nu}$	Local Reynolds number
$Re_s = \frac{\Omega \cdot s^2}{\nu}$	Gap Reynolds number
$Re_\varphi = \frac{\Omega \cdot b^2}{\nu}$	Circumferential Reynolds number
s	Axial gap width
t	Time
t	Sealing gap height
T	Temperature
T_0	Reference temperature
$Ta = \frac{v_{gap} t}{\nu} \sqrt{\frac{t}{r_{gap}}}$	Taylor number
v_{axgap}	Mean axial gap velocity
$v_{gap} = \frac{2\pi \cdot r_{gap} \cdot n}{60}$	Sealing gap circumferential velocity
v_i	General velocity vector
v_{max}	Centerline velocity in pipe flow
v_{mean}	Mean velocity
v_{meanR}	Characteristic velocity in the rotor boundary layer
v_{meanS}	Characteristic velocity in the stator boundary layer
v_r	Radial velocity
v_{re}	Radial velocity at cavity entrance
v_{res}	Resulting velocity
v_{rR}, v_{rS}	Radial velocity in the rotor and stator boundary layer

$v_r^* = \frac{v_r}{\Omega r}$	Dimensionless radial velocity
v_{r1}, v_{r2}	Radial velocity at position 1 and 2
v_z	Axial velocity
v_φ	Tangential velocity
$v_{\varphi R}, v_{\varphi S}$	Tangential velocity in the rotor and the stator boundary layer
$v_{\varphi e}$	Circumferential velocity at cavity entrance
$v_{\varphi 1}, v_{\varphi 2}$	Tangential velocity at position 1 and 2
$v_\tau = \sqrt{\frac{\tau}{\rho}}$	Friction velocity
v_∞	Free stream velocity
v_1	Radial velocity profile from through-flow
v_2	Radial velocity profile for merged boundary layers
v_1, v_2	Velocity at position 1 and 2
x_i	Position vector
X	General variable
$y = R - r$	Wall distance in pipe flow
$y+= \frac{y\sqrt{\frac{\tau}{\rho}}}{\nu}$	Dimensionless wall distance
$y+_{max}$	Maximum y+ value
z	Axial coordinate
z_R, z_S	Axial coordinates (positive from the rotor respectively stator wall)

Greek symbols

α	Angle between the resulting and the tangential wall shear stress
α	Flow angle beyond guide vane
$\beta = {}^{\omega}/_{\Omega}$	Core rotation coefficient
$\beta_e = \frac{v_{\varphi e}}{\Omega b}$	Dimensionless entrance rotation at the cavity inlet depending on the through-flow direction
β_{out}	Core rotation factor at the domain exit
β_{I0}	Fluid rotation at the impeller outlet
β_0	Constant core rotation factor
γ_R, γ_S	Proportionality factor for the boundary layer thickness on the rotor
	Proportionality factor for the boundary layer thickness on the stator
δ	Kronecker delta
δ	Boundary layer thickness
δ_R, δ_S	Thickness of rotor and stator boundary layer
ε	Transition vortex angle on the free disk
$\zeta = z\sqrt{\frac{\Omega}{\nu}}$	Dimensionless wall distance on the free disk
η	Pump efficiency
η_{hydr}	Hydraulic efficiency
η_{mech}	Mechanical efficiency
$\eta_{sidecha}$	Side chamber efficiency
η_{vol}	Volumetric efficiency
κ	Van Kármán constant
λ	Friction factor

λ_R, λ_S	Friction factors for the rotor and stator wall
$\lambda_{RNew}, \lambda_{SNew}$	Temporary memory variables for the friction factors on rotor and stator wall
μ	Dynamic viscosity
μ	Loss coefficient
μ_0	Reference dynamic viscosity
ν	Kinematic viscosity
π	Pi
π	Pressure ratio
ρ	Fluid density
τ	Shear stress
τ_{res}	Total wall shear stress
τ_r	Radial wall shear stress
τ_{rzR}	Radial wall shear stress on the rotor
τ_{rzS}	Radial wall shear stress on the stator
$\tau_{\varphi zR}$	Tangential wall shear stress on the rotor
$\tau_{\varphi zS}$	Tangential wall shear stress on the stator
τ_φ	Total wall shear stress in azimuthal direction
τ'	Turbulent wall shear stress
φ	Azimuthal coordinate
$\varphi_G = \frac{Q}{\pi \cdot \Omega \cdot b^3}$	Dimensionless through-flow rate
Ω	Angular speed of the rotor
ω	Angular speed of the fluid

1 Abstract

In the present work, the complex flow in rotor-stator cavities is investigated by means of analytical, numerical and experimental approaches. This kind of flow can be found in nearly all kinds of turbomachinery in the side chambers located between the rotating impeller and the stationary casing. The flow conditions in these small side gaps have a strong impact on the overall losses (disk friction and leakage) and thus the efficiency of the machine. Many more effects are related to the side chamber flow such as the resulting axial force on the impeller, rotordynamic issues or acoustic resonances.
The present manuscript is structured into three parts. In the first part, a new one-dimensional flow model is derived on the basis of a simplified model of the side chamber flow which allows the determination of the radial tangential velocity distribution as the major flow parameter. Related parameters such as the radial pressure distribution or the frictional resistance can then be calculated thereafter. The underlying, fundamental differential equation is derived from two different approaches. First, the derivation is shown emerging from the Navier-Stokes equations in cylindrical coordinates by applying several simplifications. Secondly, the principal of conservation of angula momentum is applied to a small cylindrical volume element located between a rotating and a stationary disk. Based on a substantial literature review, it is assumed in the derivation that a boundary layer flow structure with two boundary layers on the rotating and the stationary wall, separated by an inviscid core region, establishes. The flow model accounts for the influence of the outer cylindrical wall by means of an additional correction function. Moreover, a new approach for the determination of the friction factors is introduced based on the logarithmic law of the wall whereas usually the empirical resistance law according to Blasius is employed by most researchers. Comparisons with available experimental data from the literature as well as two other well-known flow models demonstrate an improvement of the achievable results. Furthermore, the flow model is successfully applied for two practical cases namely a centrifugal pump of low specific speed with volute casing (hydraulic turbomachine) and a radial compressor (thermal turbomachine).
In the second part, numerical flow solutions obtained with commercial CFD solvers are compared to experimental data from the literature. The investigations focuse on the prediction of the mean flow quantities and confirm the previous assumptions concerning the flow fields encountered in rotor-stator cavities. The numerical results clearly highlight the complexity of the encountered flow patterns. Even the prediction of the flow created by an enclosed rotating disk can become severly difficult with respect to turbulence modeling due to transition from laminar to turbulent flow. Furthermore, the results confirm the superior impact of an external through-flow on the flow field.
Based on the previous experiences, the flow in a complete centrifugal pump including both side chambers and the volute casing is simulated with CFD. The numerical results are supported by measurements of the radial static pressure distributions in the side chambers and the delivery head at three different operating conditions (partload, design flow rate and overload). On this occasion, an impeller either with or without balancing holes to reduce the resulting axil thrust is used. Balancing holes lead to a radial inward directed leakage flow in the rearside chamber which strongly influences the flow conditions. A very good agreement between measured and computed delivery heads for all three operating points is found which confirms an (overall) accurate modeling of the flow with CFD. In the front side chamber, the predicted radial static pressure distributions consistently compare well to the measured ones while somewhat greater discrepancies are present in the rearside chamber. Due to different axial gap widths in the side chambers, the encountered flow structures are inherently different. In the front side chamber, the axial spacing is wide enough to allow the formation of two boundary layers with core region. In the rearside chamber, the boundary layers are merged due to the significantly smaller axial spacing. Generally, a strong coupling in terms of mass and momentum exchange between the side chambers and the flow in the adjacent components such as the volute or the impeller outlet can be observed. A characteristic feature of the present pump is the inhomogenous tangential pressure built up in the volute which is found in all investigated configurations but with different markedness. Due to the close coupling, this strongly influences the flow in the side chambers. If an impeller without balancing holes is used, the secondary flow field at the impeller outlet drifts towards the suction side of the pump and increases the entering angular momentum flux in the frontside chamber. Furthermore, the omission of the balancing holes leads to the creation of a three-dimensional, counter rotating wake region in the narrow rearside chamber. This effect can also be recognized from the measurements as well as the difference in the flow regimes. The application of the

previously derived flow model yields good results in the front side chamber while the dissimilar shear flow in the rearside chamber requires the implementation of a modified approach from the literature.

2 Introduction and Scope of Work

Due to design constraints, rotor-stator cavity flows are present in nearly all kinds of turbomachinery. They are closely related to many practical problems such as axial force calculation, friction losses, leakage flows, shaft vibrations, hot gas ingress in gas turbines or the occurrence of acoustic resonances in centrifugal compressors to name but a few.

The rotation of the impeller induces a tangential fluid motion and secondary flows in the side cavities, leading to very complex flow structures. In general, a leakage flow further complicates the situation for example by introducing additional angular momentum. This can lead to high rotation rates, conceivably the fluid rotates even faster than the impeller. The rotation of the flow is responsible for disturbances concerning rotor dynamics. A swirling velocity component in the labyrinth seal reduces damping and acts as a source for rotor-excitation. Therefore, the determination of the pre-swirl in front of the labyrinth seal is crucial for the rotor dynamics.

In Fig. 1, a centrifugal pump impeller is sketched. The side chambers are typical examples for rotor-stator cavities in actual turbomachinery applications. Additionally, the various forces determining the axial thrust of the impeller are displayed. In general, the axial thrust is directed towards the suction side of the pump (**Sigloch [87]**).

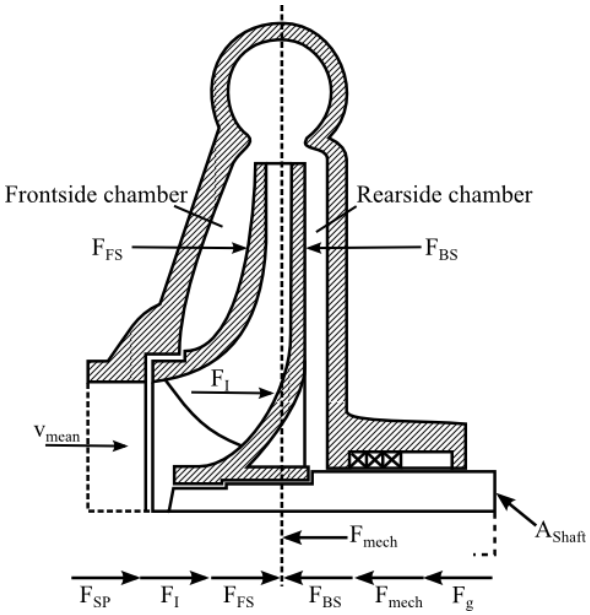

Fig. 1: Sketch of a centrifugal pump impeller with different forces responsible for the resulting axial thrust

The efficiency of a centrifugal pump, with regard to disk friction and volumetric losses, is essentially influenced by the flow in the side chambers. Especially for low specific speed pumps, disk friction and volumetric losses are dominant. The efficiency can be subdivided into several individual efficiencies:

$$\eta = \eta_{hydr} \cdot \eta_{vol} \cdot \eta_{sidecha} \cdot \eta_{mech} \qquad \textbf{Eq. 1}$$

In this equation the volumetric and the side chamber efficiency are directly related to flow in the side cavities which highlights the importance of these flow components on the overall performance. Moreover, the pressure increase in the impeller leads to hydraulic forces on the rotor. The radial load depends on the pressure distribution on the rotor in the circumferential direction, while the axial thrust is mainly determined by the radial pressure distribution in the side cavities. The knowledge of both force components (F_{FS} and F_{BS}) is necessary for an appropriate design of the bearings.

Despite their frequently encountered simple geometrical configurations, the flow situations in rotor-stator cavities are rich in diverse physical phenomena such as strong streamline curvature, truly three dimensional boundary layers or different kinds of instabilities. For example, the flows in rotor-stator cavities are a severe test for turbulence modelling in CFD which can still be one of the major sources

of error in the computation of rotating flows. Furthermore, such flows are very well suited to study the influence of rotation on turbulence.
In many cases, the fluid mechanics in rotor-stator cavities are essential for the correct prediction of related effects like heat transfer. This field is of special importance in the secondary flow path of modern gas turbine engines where ingress in the wheel spaces from the hot gas path can lead to severe damages.
The problems discussed beforehand require accurate and reliable calculation methods for the flow in rotor-stator cavities. Especially during the design process, one-dimensional models are necessary for pre-estimation or, at least, for interpretive purposes.
The goal of the present work is to evaluate, how the flow in the side chambers can be calculated both analytically and numerically to determine the main magnitudes of engineering interest such as the radial pressure distribution or the frictional resistance. With reference to the analytical calculation, the main focus is on the prediction capabilities of relatively simple correlations that are suitable for estimation purposes. On that basis, a flow model is developed that comprises a new approach for the determination of the friction coefficients and the boundary layer thickness on the rotor. Additionally, a new correction function is employed that accounts for some deficiencies in the derivation of the underlying differential equation. Comparisons with available experimental data and two other common flow models confirm the proposed concept of the model. Furthermore, comparisons with measured pressure data in the front side chamber of a centrifugal compressor and a centrifugal pump demonstrate the model's practicality.
In the second part of the work, numerical calculations using the commercial CFD codes Ansys Fluent and Ansys CFX are employed to evaluate the capability of the RANS approach to capture the mean flow structure in rotor-stator cavities.
Based on these experiences, the flow in a centrifugal pump under real operating conditions is investigated. In contrast to the majority of investigations in the literature, which are basically devoted to isolated studies of rotor-stator models, the cavity flow in an actual machine application is strongly coupled with other adjacent parts such as the volute or the impeller. The flow in the side chambers is therefore explored in terms of the complex interaction with the other machine components as the third goal of the study. Two different impellers are tested: In the first configuration, the impeller is equipped with balancing holes to reduce the resulting axial force. In the second configuration, the balancing holes are closed which leads to completely different flow conditions in the whole pump. Moreover, three different operating points, namely at design flow rate, part load and overload conditions are explored. The investigation of the cavity flow in an actual pump application is an important step to check for the transferability of the theoretical results for rotor-stator cavities on practical applications. Besides, not much is yet known about the present pump configuration with a very narrow axial gap width in the rearside chamber combined with balancing holes.

3 Theoretical Background

In the following, a general survey about the main physical aspects of the flow in rotor-stator cavities is presented. Due to the numerous number of publications related to the topic, only a brief survey can be given here. A more complete review up to the year 1989 can be found in **Owen and Rogers [64]**.

3.1 The Free Disk

The flow created by a rotating disk is three dimensional from inception and was first theoretically investigated by **Theodore Van Kármán [42]** in 1921. Van Kármán derives an exact solution of the Navier-Stokes equations assuming steady, axisymmetric, incompressible, isothermal, and laminar flow. His basic step towards a further simplification of the underlying equations is the introduction of dimensionless variables for the radial and tangential velocities that scale linearly with the radius and a new axial coordinate made dimensionless with viscosity and angular speed (see also chapter 5.2). With these modifications, the simplified equations of motion reduce to ordinary differential equations which enable a similarity solution. The ordinary differential equations are nowadays known as "Van Kármán equations" and provide the basis for many later analyses. It is worth mentioning, that the differential equations for the free disk are derived without the usual assumptions from boundary layer theory, but in fact confirm them. This can be regarded as a confirmation of the boundary layer theory itself. **Cochran [19]** gives a more exact solution of the ordinary differential equations derived by **Van Kármán [42]**. He solves the equations using a power series expansion in the near wall vicinity which

is combined with an asymptotic approach in the outer region. The general flow structure of the free disk problem is shown schematically in Fig. 2.

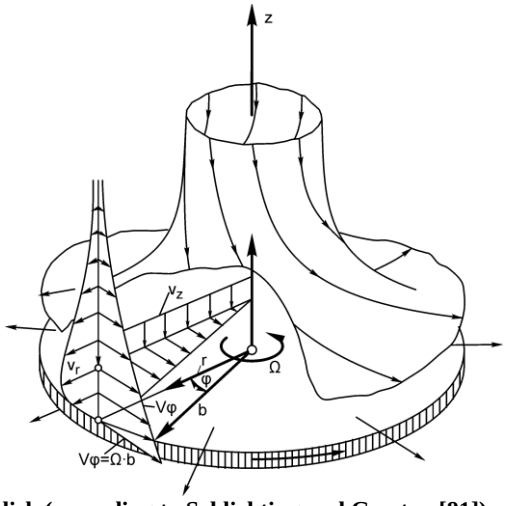

Fig. 2: Flow structure on the free disk (according to Schlichting and Gersten [81])

Due to viscosity, the flow close to the disk is centrifuged radially outwards. The radial flow component is often called secondary flow because its direction is perpendicular to the main tangential velocity component. Due to the no-slip condition, the fluid at the surface has the same circumferential velocity as the disk. The influence of viscosity is restricted to the near wall region where the velocity is reduced from the maximum on the disk surface to zero outside the boundary layer. The free stream flow is directed axially towards the disk to ensure mass conservation. The pressure remains constant across the boundary layer which is in agreement with the general boundary layer theory. The results of **Van Kármán [42]** and **Cochran [19]** are principally valid for the case of a disk with infinite radius, but an expression for the frictional moment can be derived by integration of the shear stress across the radius. The moment coefficient for the free disk for one wetted side can be expressed as:

$$c_m = \frac{M}{\frac{\rho}{2}\Omega^2 b^5} = 1.935 Re_\varphi^{-\frac{1}{2}} \qquad \textbf{Eq. 2}$$

The circumferential Reynolds number is defined as $Re_\varphi=(\Omega b^2)/\nu$. **Eq. 2** is in good agreement with the measurements of **Theodorsen and Regier [96]** and other experimentalists as can be seen in Fig. 3.

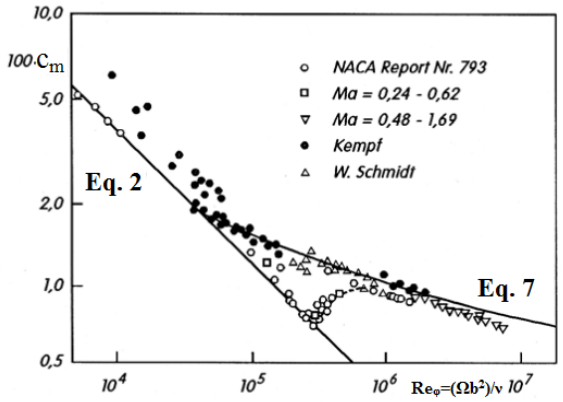

Fig. 3: Moment coefficients for a both side wetted rotating disk (Schlichting and Gersten [81])

In the radial direction, the viscous force resulting from the radial wall shear stress is in equilibrium with the centrifugal force. In the tangential direction, the viscous force resulting from the tangential wall shear stress is in equilibrium with the angular momentum of the flow. The proportionality of the boundary layer thickness can be derived from the force balance in the radial direction:

$$\delta \sim \sqrt{\frac{\nu}{\Omega}} \qquad \textbf{Eq. 3}$$

It is interesting to note from this relation, that for laminar flow over a single disk, the boundary layer thickness is constant with respect to the radius. This result implies that the viscosity affected thickness of the rotating fluid region above the disk becomes smaller as the viscosity decreases. The mass flow rate pumped out by the centrifugal effect can be determined from integration of the radial velocity in axial direction:

$$Q = 2\pi b \int_{z=0}^{z=\infty} v_r dz = \frac{0.886\pi b^3 \Omega}{\sqrt{Re_\varphi}} \qquad \textbf{Eq. 4}$$

The pumping efficiency can be derived by integrating the product of mass flow rate and total pressure of the fluid in axial direction between zero and infinity. According to **Schlichting and Gersten [81]** the free disk has a pumping efficiency of 29%. If the boundary conditions for the free disk are changed, the case of a rotating fluid above a rotating surface can also be computed using the ordinary differential equations according to Van Kármán. More precisely, the tangential velocity of the fluid approaches a finite value as the wall distance tends towards infinity. This particular case is treated in detail by **Lance and Rogers [48]** who solve the Van Kármán equations numerically for the fluid being in solid body rotation.

As can be seen in Fig. 3, **Eq. 2** underestimates the frictional resistance in case of higher Reynolds numbers. This can be explained by the flow being turbulent at this state. For $Re_l < 1.85 \cdot 10^5$, the flow is laminar. Transition takes place at $1.85 \cdot 10^5 \leq Re_l \leq 2.85 \cdot 10^5$ and the fully turbulent state establishes for $Re_l > 3 \cdot 10^5$. These regimes are valid for hydraulic smooth surfaces. The onset of transition is moved to smaller Reynolds numbers by increasing the surface roughness as shown by **Theodorsen and Regier [96]**. **Gregory et al. [32]** thoroughly study the effect of boundary layer transition on the free disk as an example of real three-dimensional boundary layers as they occur on swept wings. A china clay evaporation technique is used to visualize standing vortices in the transition zone and the critical Reynolds number for instability and transition is determined. Moreover, velocity measurements of the radial and tangential velocity component are performed using "exploring tubes". The theoretical stability analysis carried out by the authors assumes linear and inviscid conditions. The prediction of the vortex axis direction corresponds very well to the measured data, but the predicted number of vortices occurring in circumferential direction is too large. The discrepancy is attributed to disregarding the viscosity in the analysis. For increasing Reynolds numbers, transition appears first at the outer disk radius where the maximum circumferential velocity is present and moves further inwards, respectively downstream for increasing Reynolds numbers. From the comparison of measured and theoretical profiles used by **Van Kármán [42]** and **Goldstein [31],** the authors note that neither profile satisfactorily matches the experimental one in all features.

For turbulent flow, the general flow structure remains the same. **Van Kármán [42]** uses an approximate integral boundary layer method to solve the simplified equations of motion. Most of the many successive (theoretical) analyses differ only in small detail from this treatment. One main result is that the boundary layer thickness increases now with the radius:

$$\delta \sim r^{\frac{3}{5}} \left(\frac{\nu}{\Omega}\right)^{\frac{1}{5}} \qquad \textbf{Eq. 5}$$

In the approximate method, the simplified equations of motion are integrated across the boundary layer thickness and assumptions about the velocity distributions and the shear stresses are made. Usually, the 1/7 power law is applied for the velocity distribution within the turbulent boundary layer. This law was originally determined to be a good approximation for the flow along a flat plate and in pipes. The shear stresses are expressed using the empirical law by Blasius which will be described in greater detail in chapter 4.4. The moment coefficient for turbulent flow results to:

$$c_m = 0.07288 Re_\varphi^{-\frac{1}{5}}$$ **Eq. 6**

In contrast to Van Kármán's treatment **Goldstein [31]** uses the logarithmic law of the wall, which is continuously differentiable at the point where transition to the outer flow takes place. His aim is to find a more accurate solution for higher Reynolds numbers. However, the results are based on experimental data which are now considered as non-reliable (**Owen and Rogers [64]**). **Schlichting and Gersten [81]** give the following implicit relation based on the results of **Goldstein [31]** for the moment coefficient under turbulent flow conditions:

$$\frac{1}{\sqrt{c_m}} = \frac{1}{\kappa\sqrt{8}} ln\left(Re_\varphi \sqrt{c_m}\right) + 0.03$$ **Eq. 7**

Dorfman [29] applies the same concept and derives an equation for the moment coefficient that gives good results in the range of $10^6 < Re_\varphi < 10^7$. **Owen [61]** performs experiments on the free disk and correlates his measurements to obtain an empirical equation for the case of a free disk under fully turbulent conditions. Other studies, for example **Dorfman [28],** focus on the influence of surface roughness.

Outgoing from the free disk, other similar configurations can be investigated. **Bödewald [12]** finds a similarity solution for the case of a rotating fluid above a stationary surface (Fig. 4). Outside the boundary layer, centrifugal and pressure forces are in equilibrium. Inside the boundary layer, the velocity is reduced and an inward directed flow develops due to the dominant pressure forces. Because of continuity, the inward directed flow must leave the disk surface axially outwards. These conditions principally apply for the flow close to the stationary casing wall in a rotor-stator cavity. Besides, this flow structure is responsible for the accumulation of tea leaves in the middle of a cup of water.

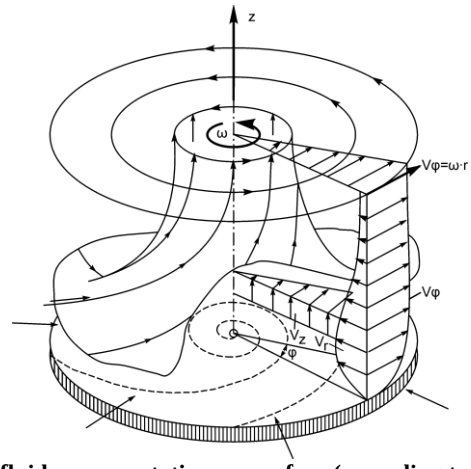

Fig. 4: Flow structure of a rotating fluid across a stationary surface (according to Schlichting and Gersten [81])

Truckenbrodt [97] analyzes a rotating disk that is subjected to an axial flow towards the surface. A major conclusion is that the boundary layer thickness decreases for increasing axial flow which results in a stronger velocity gradient and thus a higher frictional resistance. **Stuart [92]** solves the theoretical case of uniform suction along a rotating disk. Further solutions for the case of a suddenly accelerated, respectively decelerated, disk can be found in **Dorfman [29]**. **Cebeci and Abbott [16]** present numerical simulations of the flow along the free disk. Their method uses an improved eddy viscosity formulation and is principally similar to the one described later in this text by **Cooper and Reshotko [20]**. **Wu and Squires [106]** numerically resolve the large scale turbulent structures with the LES approach to investigate the flow in the three dimensional boundary layer over a rotating disk. The results show a good agreement with the experimental data of **Littell and Eaton [53]** and support the hypothesis that vortices with the same sign in vorticity in streamwise direction are predominantly responsible for strong sweep events. These are considered to produce turbulence in boundary layers.

3.2 Enclosed Rotating Disk

Apart from the fundamental free disk case, a disk rotating in a casing more closely resembles the configurations commonly encountered in actual turbomachinery applications. A common practice is to define a gap Reynolds number to distinguish between the various cases. The number is defined as (**Owen and Rogers [64]**):

$$Re_s = \frac{\Omega \cdot s^2}{\nu} = G^2 Re_\varphi \qquad \textbf{Eq. 8}$$

G is the gap ratio and defined as the quotient of the axial gap width to the outer disk radius. Re_φ is the circumferential Reynolds number as already introduced for the free disk. For small gap widths, a strongly viscous affected shear flow develops while for higher axial distances, a flow with two boundary layers and a core region establishes.

Schultz-Grunow [84] is one of the first to analyze the flow caused by a rotating disk in a stationary housing. For small gap sizes and circumferential Reynolds numbers, the tangential velocity varies linearly with the axial coordinate. Neglecting radial and axial velocities in the gap, a simple relationship for the moment coefficient is found analytically (laminar flow, one wetted side):

$$c_m = \frac{\pi}{G Re_\varphi} \qquad \textbf{Eq. 9}$$

This relation is in good agreement with his measurements and corresponds to a simple, laminar shear flow (Couette-flow). For higher Reynolds numbers, based on his combined analytical and experimental investigation, **Schultz-Grunow [84]** proposes a division of the flow pattern into three distinct layers: a boundary layer with radial outflow on the rotor, a boundary layer with radial inflow on the stator and a core region in solid body rotation in the middle of the cavity. A calculated value of 0.512 for the core rotation factor β, defined as the ratio of the angular velocity of the fluid to the angular velocity of the disk, is given neglecting the influence of the outer radial shroud. However, the experimentally determined value amounts 0.357 and the discrepancy is attributed to a shear stress in the outer radial gap between the shroud of the rotating disk and the fixed housing. The boundary layer thickness on the rotating disk is assumed to evolve similarly to the free disk but with a different proportionality factor γ_R:

$$\delta_R = \gamma_R r^{\frac{3}{5}} \left(\frac{\nu}{\Omega}\right)^{\frac{1}{5}} \qquad \textbf{Eq. 10}$$

This equation has been used by many other authors who developed flow models that require expressions for the boundary layer thickness (see e.g**. Zilling [109]**, **Möhring [59]**). For a free disk, the factor γ_R has a constant value of 0.526. According to **Schultz-Grunow [84]**, γ_R depends on the core rotation for the enclosed rotating disk:

$$\gamma_R = \left(\frac{\Omega}{\omega}\right)^{\frac{1}{5}} \left(\frac{\Omega}{\omega} - 1\right) \left[\frac{0.0225}{\left(0.313\frac{\Omega}{\omega} + 0.504\right) a^+}\right]^{\frac{4}{5}} \qquad \textbf{Eq. 11}$$

The term a^+ is defined as:

$$a^+ = \sqrt{\frac{0.0278 + 0.1944\frac{\omega}{\Omega} - 0.222\left(\frac{\omega}{\Omega}\right)^2}{\left(1 - \frac{\omega}{\Omega}\right)\left(1.058 - 0.241\frac{\omega}{\Omega}\right)}} \qquad \textbf{Eq. 12}$$

The evolution of the boundary layer thickness is valid for the enclosed rotating disk without through-flow. However, this formulation has later also been used by other authors in case of a superposed through-flow.

Soo [88] theoretically investigates the laminar flow of a rotor-stator system for small through-flow and gap widths in order to resolve some inconsistencies from older reports. The basic solution is similar to the one obtained by **Schultz-Grunow [84]** (e.g. Eq. 9). Furthermore, plots of the variation of the velocity components across the axial gap width and a theoretical equation for frictional resistance in case of a small gap and turbulent flow (one wetted side) is given:

$$c_m = 0.0308 \cdot G^{-\frac{1}{4}} Re_{\varphi}^{-\frac{1}{4}} \qquad \textbf{Eq. 13}$$

This equation is derived by adapting the empirical Blasius law of resistance to the cavity flow which has been originally correlated for the flow in hydraulically smooth pipes.

Batchelor [9] uses a similarity approach to solve the steady, rotationally periodic equations of motion qualitatively for the flow between a rotating and a stationary disk with infinite radial extent. He predicts the occurrence of an inviscid core region in solid body rotation with zero radial velocity between two boundary layers on rotor and stator. **Stewartson [93]** in contrast states that the circumferential velocity is confined to a small region close to the rotating disk. The velocity is zero everywhere else in the cavity. In fact, this means that a boundary layer forms only close to the rotating surface while the rest of the fluid is essentially at rest, similar to the free disk. This discrepancy led to a historic controversy (see **Owen and Rogers [64]**) which is founded in the solution multiplicity that can occur in rotor-stator cavity problems depending on the boundary conditions. In fact, self-similar solutions do not necessarily match the boundary conditions found in case of finite disks. In conclusion, the solutions of **Batchelor [9]** and **Stewartson [93]** can occur in practice dependent on the present boundary conditions as shown by **Brady and Durlofsky [13]**. These authors present numerical solutions of the Navier-Stokes equations in the meridional plane by applying various boundary conditions at the outer disk radius. The results turn out to depend strongly on the chosen boundary conditions. Practical evidence of this behavior can be found for example in the experimental work by **Radtke and Ziemann [78]**. Their strongly experimental oriented study shows that even a small external through-flow without swirl can completely suppress the core rotation of the fluid. This considerably changes the pressure distribution and consequently the axial force exerted on the rotating disk. **Debuchy et al. [26]** investigate the effect of geometrical changes at the outer periphery of a rotor-stator cavity opened towards the atmosphere in a combined approach using CFD, velocity and pressure measurements. Especially the influence of a radius difference between the rotating and the stationary disk turns out to have a strong effect on the flow structure inside the cavity. The authors find that the fluid, which is expelled radially by the rotating disk, is replaced both by reinjection of the expelled and ambient fluid. The latter is essentially characterized by a zero tangential velocity while the fluid pumped out on the rotating surface contains a considerable amount of angular momentum. Exactly this amount of re-entering angular momentum is controlled by the radius difference of the disks. The sensitiveness of the cavity flow on the outer boundary condition becomes also clear in terms of the creation of the computational domain for a numerical simulation. The domain boundaries need to extend far away from the cavity itself in order to achieve a solution independent of the finite domain size. Further research on this topic can be found for example in the publication of **Abdel Nour et al. [1]**.

A flow structure similar to the one proposed by **Batchelor [9]** is likely to occur in closed cavities for large axial gap widths, high Reynolds numbers and small through-flow rates. Especially the flow conditions in turbomachinery applications favor the occurrence of this kind of flow. Stewartson kind of flow is likely to be encountered in case of non-shrouded cavities opened towards the atmosphere or in case of strong through-flow (**Poncet et al. [71]**). A review about the multiple classes of solutions in rotor-stator cavities is given by **Zandbergen and Dijkstra [108]**.

Pantell [66] measures the housing torque of an enclosed rotating disk varying the Reynolds number, the gap width and the surface roughness. Outgoing from a very small axial gap width, the frictional resistance of the disk first decreases for increasing the axial gap width. For higher distances, the frictional resistance starts to increase again. These results indicate a change in the flow regime if the gap distance is increased which leads to a reduction of the moment coefficient. The fact that the

frictional resistance starts to increase again is clear evidence for the braking effect of a stationary outer shroud.

Daily and Nece [24] examine the flow of an enclosed rotating disk both analytically and experimentally. The experiments consist of pressure, velocity and torque measurements by varying the disk speed and the axial gap width. From the analysis, they are able to distinguish between four different flow regimes that can occur in dependance on the circumferential Reynolds number Re_φ and the dimensionless gap width G:

- Regime I: Small clearance, laminar flow
- Regime II: Large clearance, laminar flow
- Regime III: Small clearance, turbulent flow
- Regime IV: Large clearance, turbulent flow

A map of the different flow regimes including the respective mean velocity profiles for the tangential and radial velocity component is given in Fig. 5 (see also **Owen and Rogers [64]**). The diagram shows that in case of increasing Reynolds numbers, the boundary layers become thinner. For this reason, a flow structure similar to regime IV is likely to be expected for high Reynolds number applications as they occur in modern centrifugal compressors for example. To the knowledge of the author, the flow structures investigated in the literature until now are limited to a range of $Re_\varphi<10^7$.

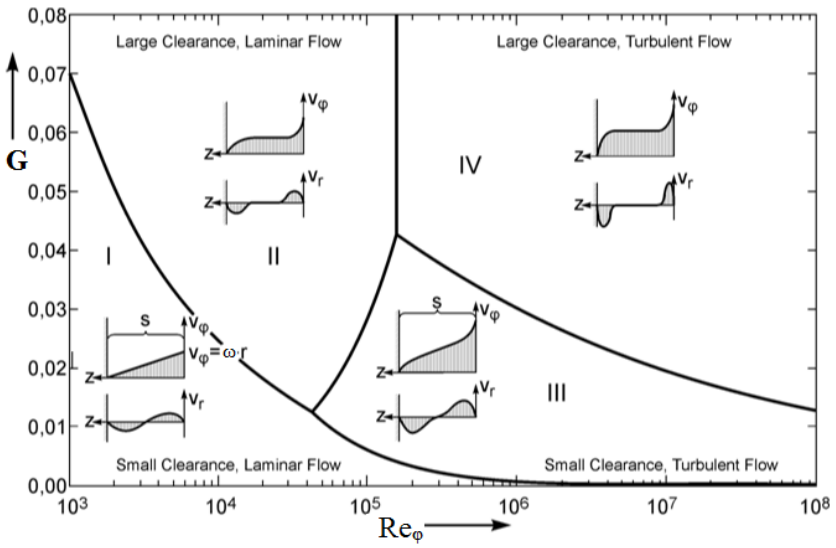

Fig. 5: Flow regimes according to Daily & Nece [24]

The correlated moment coefficient for the different flow regimes write:

Regime I $$c_m = \frac{\pi}{G \cdot Re_\varphi}$$ **Eq. 14**

Regime II $$c_m = 1.85 \cdot G^{\frac{1}{10}} Re_\varphi^{-\frac{1}{2}}$$ **Eq. 15**

Regime III $$c_m = 0.04 \cdot G^{-\frac{1}{6}} Re_\varphi^{-\frac{1}{4}}$$ **Eq. 16**

Regime IV $$c_m = 0.0501 \cdot G^{\frac{1}{10}} Re_\varphi^{-\frac{1}{5}}$$ **Eq. 17**

The turbulent flow regimes III and IV are the most likely to occur in practice. The small gap cases (I and III) essentially represent a viscous Couette-type of flow while the other two regimes correspond to the Batchelor-flow solution characterized by an inviscid core region. A contrary dependance of the disk friction torque in dependance on the axial gap width is noticed for the different flow regimes. For merged boundary layers (Regime I and III), the frictional resistance decreases with increasing gap width as a consequence of the reduced velocity gradient. In contrast, the frictional resistance increases with raising gap width in case of separated boundary layers (Regime II and IV) due to the braking

influence of the outer cylindrical shroud. By the way, the empirical **Eq. 14** is identical to the analytical one given by **Schultz-Grunow [84]** in **Eq. 9**. By equating the formulas for regimes I, II and III, IV, expressions for the optimum gap width with a minimum frictional resistance can be deduced. The theoretical model of the authors belongs to the integral boundary layer method and assumes three layers: A boundary layer with radial flow attached to rotor and stator separated by a core region without radial flow. In the analysis, the axial convection terms in the equations are ignored in order to find a solution. But exactly these terms carry the major amount of angular momentum in the cavity as noted by **Hamkins [36]**. As a consequence, the obtained solutions do not fulfill the momentum equations. In contrast to **Schultz-Grunow [84]**, the model accounts for the stationary outer shroud. A solution is obtained using the integral method similar to the one used by **Van Kármán [42]**. In order to apply the method, assumptions about the velocity profiles, the boundary layer thickness and the shear stresses are required.

Based on previous results (e.g. **Schultz-Grunow [84]**), **Broecker [14]** discusses the influence of the outer radial boundary condition on the flow between a rotating and a stationary wall. The core rotation varies strongly whether the cavity is closed by a cylindrical wall or opened towards the atmosphere.

The frictional resistance of the enclosed rotating disk is smaller compared to the free disk. The reason is that the fluid entering the rotor boundary layer contains a considerable amount of angular momentum, while in case of the free disk, the rotation of the fluid is confined to the wall adjacent fluid layer and the axial flow is essentially swirl-free. The resulting torque follows from the angular momentum difference between the radially expelled fluid and the axially entering fluid in the boundary layer of the rotating disk.

Lance and Rogers [48] numerically solve the Van Kármán equations for the flow between two infinite rotating disks. The authors investigate the effect of the Reynolds number on the velocity profiles in radial and tangential direction for laminar flow. The tangential velocity profile changes from Couette-type of flow with a linear profile to Batchelor-type of flow. The core rotates approximately with 30% of the rotor angular velocity for a gap Reynolds number of Re_s=441.

Additional insight into the influence of surface roughness can be obtained by the works of **Pantell [66]**, **Daily and Nece [24]** and **Kurokawa and Toyokura [46]**. The frictional resistance strongly increases if the roughness of the rotor, as well as of the casing walls, is raised. According to **Daily and Nece [24]**, the frictional resistance is not dependent on the Reynolds number any more as soon as the turbulent and rough regime covers the whole disk and the casing. In case of a rough disk and a smooth casing, a dependency on the Reynolds number is present. **Kurokawa et al. [46]** investigate the influence of surface roughness on the rotor and/or the stator wall on the flow field. The core rotation increases in case of a rough rotor surface and a smooth casing, while a reduction is observed in the opposite case. For equal roughness on the rotating and the stationary wall, the core rotation does not change at all.

Cooper and Reshotko [20] perform numerical calculations of the flow between a rotating and a stationary disk of infinite radius using a shooting technique. They use a scalar effective viscosity method to model the influence of turbulence and involve stream functions for the radial and tangential velocity components. Instead of solving the full Navier-Stokes equations, the radial and tangential momentum equations are treated as ordinary differential equations in the axial direction by estimating the derivatives in the radial direction. Initial values for the stream functions and their derivatives have to be assumed. The equations are then integrated in axial direction until all boundary conditions are fulfilled. Then, the calculation proceeds to the next radial location. An intermittency factor is applied in the eddy viscosity relation to account for transition from laminar to turbulent flow. In this method, the velocity profiles are found as a part of the solution and not assumed a priori as in the integral boundary layer method. Two configurations for Re_s=296 and Re_s=2852 are examined. Turbulent flow according to regime III is present in the narrow gap case while a mixed state applies for the wider gap. For $Re_l<2.56\cdot10^6$ the flow belongs to Regime IV while the layers are merged at greater Re_l. The laminar flow in both gaps belongs to regime II. A comparison of the wide gap velocity profiles for $Re_l=2.56\cdot10^6$ with the experimental data of **Daily and Nece [24]** shows a good agreement. For high local Reynolds numbers and a narrow gap, the radial velocity is nearly suppressed and the flow resembles a two-dimensional, turbulent Couette-flow. The core rotation factor approaches 0.5 for turbulent flow, while for laminar flow a value of 0.3135 is obtained.

Another study is performed by **Szeri et al. [94]** for a cavity with a large radial gap width. The authors perform LDA measurements in water and show that a value of 0.313 for the core rotation is a good

estimation for the mid radius ($0.3<r/b<0.5$), where the flow is relatively independent of the outer radial boundary conditions. For greater radii, the core rotation increases with the radial position.
Further evidence for the radial dependance of the core rotation is given in the works of **Pearson [69]** and **Dijkstra and Van Heijst [27]** who show that a rotating radial shroud leads to an acceleration of the fluid in circumferential direction. Although the assumption of a solid body rotation is only strictly correct in case of infinite disks, some authors obtained satisfactory results using this model. For example, **Altmann [3]** proposes a calculation method to determine the pressure distribution in the rearside chamber of a centrifugal pump equipped with "back vanes" based on the solid body model. His results are in reasonable agreement with the experimental data of **Möhring [59]**. However, the experiments of **Möhring [59]** are limited to a non-swirling leakage flow only.
Radtke and Ziemann [78] show that for increasing radial gap width (that is when the outer casing extents significantly further than the outer disk radius) the core rotation becomes a function of the radius, too. With increasing radial location, the core rotation decreases because of the higher ratio of decelerating to accelerating surfaces.
Itoh et al. [40] measure radial and tangential velocity distributions in a closed rotor-stator cavity ($G=0.08$) with a stationary shroud at $Re_\varphi=1\cdot10^6$ using hot-wire anemometry. Additionally, they provide detailed measurements of the turbulent quantities. Their results confirm that the velocity profiles in the boundary layers scale with the local Reynolds number ($Re_l=\Omega r^2/\nu$). The core rotation changes sharply between a value of 0.31 at $Re_l=1.6\cdot10^5$ and 0.4 at $Re_l=3.6\cdot10^5$ because of transition from laminar to turbulent flow. This means that the flow in the Ekman boundary layer is partly laminar and partly turbulent while the Bödewald layer turns out to be entirely turbulent. The authors ascribe this behavior to the fact that the flow on the rotor is basically an accelerated one in contrast to the decelerated flow on the stator. The measurements prove further that the velocity gradient and the shear stress direction vector differ as it is typical for three dimensional boundary layers. This means that a skewed velocity vector is present whose direction changes with the wall distance.
Subsequently, **Cheah et al. [17]** present LDA, hot-film velocimetry and yaw-tube measurements in a similar configuration for a somewhat wider cavity ($G=0.127$) and Re_φ varying between $Re_\varphi=0.3\cdot10^6$ and $Re_\varphi=1.6\cdot10^6$. In contrast to the results of **Itoh et al. [40]**, they argue that the turning at the outer radial shroud is mainly responsible for the entirely turbulent flow in the stator boundary layer by causing upstream disturbances which destabilize the flow. Although the local Reynolds number is confirmed to be the major parameter for the local velocity profiles, the authors suggest that the global Reynolds number and probably the gap aspect ratio have to be taken into account too. At the lowest Reynolds number investigated, the flow along the rotor is almost completely laminar while the Bödewald layer remains turbulent. As a consequence, the fluid which flows in axial direction from the stator to the rotor must relaminarize.
Itoh [41] extends his experiments to the case of a narrow gap with merged boundary layers for two different aspect ratios ($G=0.016$, $G=0.008$). The radial velocity component exhibits the typical S-shaped profile in the axial direction and the influence of viscosity extends across the whole gap width. The conclusions are basically the same as for the wider gap, namely that fully turbulent conditions establish on the stator for smaller local Reynolds numbers than on the rotor. If the gap width is reduced, the turbulence characteristics become more similar. For fully turbulent flow, the profiles of the Reynolds stresses are similar to each other in both near wall regions.
Watanabe et al. [100] study the influence of fine spiral grooves on the frictional resistance of an enclosed rotating disk in case of merged and separated boundary layers. A maximum drag reduction of up to 15% can be obtained for the small axial gap width, while for the large distance, a maximum reduction of 11% is achieved. The reason for the drag reduction is the damping of local disturbances caused by the velocity fluctuations.
In practical cases, the bounding walls of rotor-stator cavities are frequently inclined. The inclination angle influences the effective area in the formulation of the torques on the rotating and the stationary wall. **Zilling [109]** notices that this effect can be neglected for inclination angles smaller than 15 degree.
Due to the central role of the core rotation factor in the flow structure in rotor-stator cavities (flow regime IV), some of the typical values found in the literature are summarized in Table 1.

Author	Year	Core Rotation Factor β	Gap Width G	Flow State	How Derived?
Schultz-Grunow [84]	1935	0.512	Infinite Disks	Turbulent	Theoretical
Schultz-Grunow [84]	1935	0.357	0.3	Turbulent	Experimental
Daily & Nece [24]	1960	0.46	0.0637	Turbulent	Experimental (r/b=0.765)
Daily & Nece [24]	1960	0.454	0.0637	Turbulent	Theoretical
Daily & Nece [24]	1960	0.444	0.102	Turbulent	Experimental (r/b=0.765)
Daily & Nece [24]	1960	0.432	0.102	Turbulent	Theoretical
Daily & Nece [24]	1960	0.412	0.217	Turbulent	Experimental (r/b=0.765)
Daily & Nece [24]	1960	0.388	0.217	Turbulent	Theoretical
Daily & Nece [24]	1960	0.46	0.051	Laminar	Experimental (r/b=0.765)
Daily & Nece [24]	1960	0.504	0.051	Laminar	Theoretical
Daily & Nece [24]	1960	0.44	0.102	Laminar	Experimental (r/b=0.765)
Daily & Nece [24]	1960	0.46	0.102	Laminar	Theoretical
Daily & Nece [24]	1960	0.36	0.217	Laminar	Experimental (r/b=0.765)
Daily & Nece [24]	1960	0.386	0.217	Laminar	Theoretical
Lance & Rogers [48]	1962	0.3	Infinite Disks	Laminar	Numerical
Cooper & Reshotko [20]	1975	0.3135	Infinite Disks	Laminar	Numerical
Cooper & Reshotko [20]	1975	0.5	Infinite Disks	Turbulent	Numerical
Zilling [109], Möhring [59]	1973, 1979	0.5	Infinite Disks	Turbulent	Theoretical
Kurokawa [46]	1978	0.43	0.078	Turbulent	Experimental (r/b=0.79)
Dijkstra & Van Heijst [27]	1983	0.313	Infinite Disks	Laminar	Numerical
Radtke & Ziemann [78]	1983	0.41	0.125	Turbulent	Experimental (r/b=0.691)
Owen [63]	1989	0.382	0.069	Laminar	Theoretical
Owen [63]	1989	0.426	0.069	Turbulent	Theoretical
Itoh et al. [40]	1992	0.42	0.08	Turbulent	Experimental (r/b=0.94)
Itoh et al. [40]	1992	0.31	0.08	Laminar	Experimental (r/b=0.4)
Cheah et al. [17]	1994	0.4	0.127	Turbulent	Experimental (r/b=0.8)
Cheah et al. [17]	1994	0.35	0.127	Turbulent	Experimental (r/b=0.4)
Andersson &Lygren [5]	2006	0.4	0.1	Turbulent	Numerical (LES)
Andersson & Lygren [5]	2006	0.47	0.0632	Turbulent	Numerical (LES)

Table 1: Core rotation factors in the literature

3.3 Rotor-Stator Cavities with Superposed Through-Flow

Fewer results are available for the flow in rotor-stator systems subjected to a superposed leakage flow. In general, a leakage flow is present in the majority of turbomachinery applications. In centrifugal pumps, the so called wear ring leakage is driven by the pressure difference across the impeller. It is now clear that the leakage flow, respectively the angular momentum flux, has by far the most significant effect on the flow structure. The through-flow can also affect the boundaries between the different flow regimes defined by **Daily and Nece [24]** because of its influence on the boundary layer thickness. For example, in case of flow regime IV, the through-flow takes place in either the rotor or the stator boundary layer depending on the flow direction. **Kurokawa and Sakuma [47]** mention that a radially outward through-flow favors the merging of the boundary layers. More on, transition from laminar to turbulent flow is additionally influenced by the through-flow because in general, the externally applied leakage is in a turbulent state. Consequently, in this case the whole flow in the cavity is likely to be entirely turbulent.

Daily et al. [25] measure mean velocity profiles for the case of an outward directed (centrifugal) leakage flow. Based on their experiments, an empirical relation for the radial evolution of the boundary layer thickness on the rotor is proposed:

$$\delta_R = B^+ \frac{r}{Re_l^{0.2}} (1-\beta)^m \qquad \textbf{Eq. 18}$$

In this equation, B^+ and m are empirical constants that are chosen to fit to the measurements. This correlation is used with slight modifications in all the flow models proposed by **Kurokawa et al. [44] [45] [46] [47]**.

Altmann [2] measures the radial static pressure distribution and determines the corresponding core rotation distribution from the assumption of radial equilibrium between pressure and centrifugal forces in the core region. In the case of a centripetal through-flow, a strong magnification of the core rotation towards the center is observed. In the opposite flow direction, the contrary situation prevails. The core rotation decreases as the radius increases. This behavior in founded in the principle of conservation of angular momentum which is additionally introduced by the through-flow. For an inviscid flow, a situation similar to a forced vortex ($v_\varphi \cdot r$=const.) prevails. Friction reduces the magnification in real flows but the general characteristics remain the same.

For increased core rotation values, the frictional resistance of the rotating disk is considerably lowered. Measurements to check for the influence of the axial gap width (G=0.15, G=0.056) are also performed by **Altmann [2]** and indicate a comparatively small impact on the core rotation. The general tendency is that for a given radial position, the magnitude of the core rotation in case of a small axial gap width is somewhat higher for centripetal respectively lower for centrifugal flow compared to a wider gap. However, the largest deviations in case of centripetal flow are present at the outer disk radius. In the case of zero leakage, a slightly smaller core rotation is present in the wider gap case. An influence of the impeller outflow on the outer boundary condition is also given.

Poncet et al. [71] perform a comprehensive study on the radial evolution of the core rotation factor in a rotor-stator system subjected to an inward (centripetal) through-flow with swirl. In the experiments, the gap width is large enough so that a turbulent flow with two boundary layers and a central core region (regime IV) establishes. LDA (Laser Doppler Anemometry) is used to measure the core rotation for three different gap widths (G=0.048, G=0.036, G=0.024). For this parameter range, the gap width has a very small effect on the core rotation as long as the flow regime IV is maintained but the general tendency is clear, namely that for larger gap widths the core rotation is consistently lowered. An influence of the Reynolds number on the core rotation is also noticed. Higher Reynolds numbers lead to a reduction of the fluid rotation caused by the increased inertia to viscosity ratio. The most dominant effect comes from the external momentum flux which leads to a strong magnification of the core rotation at smaller radii. As soon as the core rotation coefficient becomes equal to one, a stagnation line establishes and the common boundary layer structure breaks down. Both boundary layers become centripetal in this case because the pressure now drives the fluid inwards even in the rotor boundary layer.

Similar relationships have been observed in the experimental study of **Radtke and Ziemann [78]**. Based on their velocity measurements, they give a qualitative picture of the flow for rotation faster

than the disk which will be shown later in this text (Fig. 94). According to this figure, two counter rotating eddies develop close to the walls at the radial position of β=1 while a radial outward directed flow establishes in the middle of the axial gap.

Bayley and Owen [10] investigate the influence of a centrifugal through-flow on the flow structure between a rotating and a stationary disk (G=0.008, G=0.03). The system is open towards the atmosphere at the outer radius. The boundary layer equations are solved numerically using a finite difference method and the flow is treated as turbulent for $Re_\varphi > 3 \cdot 10^5$. The externally applied flow has no swirl. Consequently the measured torque of the disk increases with increasing flow rate because the core rotation is lowered. This agrees with the principal relations found by **Truckenbrodt [97]** in case of a free disk subjected to an impinging external flow.

The assumption of radial equilibrium in the core region can yield information about the fluid rotation in case of flow regime IV. If the static pressure is measured, a polynomial fit can be used to gain a function for the radial pressure distribution in dependance on the radius. This function can then be integrated in order to determine the core rotation. **Poncet et al. [71]** find a good agreement between the directly measured values from the LDV and the pressure based ones. **Lauer [50]** verifies the validity of the radial equilibrium relation in order to determine the core rotation. He notices larger discrepancies at the outer cavity radius where the leakage flow enters the side gap and momentum exchange takes place.

Schubert [83] performs substantial measurements in a pump-like test rig where the pre-swirl of the fluid can be adjusted. He notes that even if no through-flow is present, a momentum exchange across the cavity anteroom can be present that extends throughout the whole cavity until the lower radii.

Lauer [50] studies the influence of the cavity anteroom and the geometrical shape of a rotor-stator cavity on the flow with application to centrifugal pumps. His analysis consists of an analytical model for the radial core rotations distribution, CFD calculations, LDA and pressure measurements of the flow in the cavity and the anteroom. The influence of different parameters concerning the anteroom is investigated using CFD and experimental data. A strong dependance on the inflow conditions is observed which supports the statement that the flow in rotor-stator cavities is very sensitive to the boundary condition even when a through-flow is applied.

Most of the flow models in the literature used to determine the major magnitudes of engineering interest emerge from the integral boundary layer analysis. The method in principle equals the treatment of the free disk as first proposed by **Van Kármán [42]**. Velocity profiles and expressions for the wall shear stresses have to be applied a priori and are not found as a part of the solution. Logically, the quality of the solution depends strongly on the chosen profiles and assumptions for the shear stresses. The different methods can be generally classified according to the number of layers which the equations are applied to.

Stepanoff [91] investigates the resulting axial force in centrifugal pumps. For his theoretical analysis, he assumes that the fluid rotates as a solid body with a fixed value for the core rotation factor (β=0.5). The assumption of a constant core rotation has nowadays proven as inefficient by various reasons although it is the simplest model for the flow that can be assumed and considerably eases the calculation since no information about the leakage flow or the core rotation at the outer cavity radius are necessary.

Daily et al. [25] give an empirical correlation for the radial evolution of the core rotation in case of centrifugal through-flow with zero entrance rotation. The equation is obtained in agreement with the measurements:

$$\beta(r) = \frac{\beta_0}{12.74 \frac{Q}{\Omega b^3} Re_\varphi^{\frac{1}{5}} \left(\frac{b}{r}\right)^{\frac{13}{5}} + 1} \qquad \textbf{Eq. 19}$$

It is said that β_0 can be assumed to be 0.5 since **Daily et al. [25]** cannot find a unique dependance on the axial gap width. In fact, β_0 depends on the gap ratio and decreases with increasing axial spacing (β_0=0.475 for G=0.0276; β_0=0.45 for G=0.069; β_0=0.42 for G=0.124). If the through-flow is zero the core rotation is equal to β_0. Otherwise, the core rotation is lowered in the presence of leakage. With increasing radii the entering flow is entrained in the rotor boundary layer and the influence on the core rotation decreases. The relationship has been obtained for the following ranges of test variables:

$$0.55 < G < 0.069$$
$$0.01 < \frac{Q}{\Omega b^3} Re_\varphi^{\frac{1}{5}} < 0.14 \qquad \textbf{Eq. 20}$$
$$Re_\varphi = 6.9 \cdot 10^5$$

Senoo and Hayami [85] propose a detailed flow model for the case of separated boundary layers by applying the momentum equations for each layer individually. They take into account the convection terms and extend the usual three layer model with an outward flow layer located between stator boundary layer and core region. The inward flowing angular momentum in the wall layer leads to a spin up (rotation faster than in the core) in the outward flow layer. The introduction of additional free parameters solves the problem of imaginary solutions for the stator boundary layer that many researchers encountered when using a three-layer model. This issue is discussed in greater detail by **Hamkins [36]**. The fluid is convected in axial direction from the stator boundary layer to the rotor boundary layer across the core. The usual velocity profiles for the wall boundary layer implicitly assume that the exiting angular momentum leaving the wall layer is the same as in the core. The core region is expected to exert only a static pressure on the boundary layers and no shear force. For this reason, the usual velocity profiles presume implicitly that there is somehow a mechanism which adjusts the axial convected momentum flux to fit the core. However, from a global point of view, both boundary layers are virtually independent of each other.
This can be shown by considering the laminar flow between a rotating and a stationary disk split into two separate systems. The first case is a rotating disk in a rotating fluid and the second one is a rotating fluid above a stationary surface. These two cases can be coupled using the continuity equation stating that the sum of the mass fluxes in the rotor and the stator boundary layer is zero. From the Bödewald layer, the analytical value for the dimensionless axial velocity is known. Since the axial outflow from the stationary disk is equal to the inflow on the rotating disk, the value of the core rotation is fixed. It can be interpolated from the numerically calculated values for the rotating fluid above the rotating disk given in **Owen and Rogers [64]** using linear interpolation.

Core Rotation β	$H_{\infty R}(H = \frac{v_z}{\sqrt{\Omega\nu}})$	$\frac{H_{\infty R}}{\sqrt{\beta}}$
0	-0.8845	Not defined
0.1	-0.9177	-2,90202221
0.2	-0.8618	-1,92704338
0.4	-0.6600	-1,04355163
0.6	-0.4308	-0,55616041
0.8	-0.2080	-0,23255107
0.9	-0.1020	-0,10751744
1	0	0

Table 2: Asymptotic values from the numerical solution of the flow of a rotating fluid over a rotating disk (Owen and Rogers [64])

The mass flow rate for the rotor, idealized as a rotating fluid over a rotating disk, can be expressed as (see **Owen and Rogers [64]**):

$$\dot{m}_R = -\rho\pi r^2\sqrt{\Omega\nu}H_{\infty R} \qquad \textbf{Eq. 21}$$

For the stator:

$$\dot{m}_S = -\underbrace{1.3494}_{H_{\infty S}}\rho\pi r^2\sqrt{\beta\Omega\nu} \qquad \textbf{Eq. 22}$$

If these two expressions are inserted in the continuity equation ($\dot{m}_R + \dot{m}_S = 0$), the parameter $H_{\infty R}$ and the core rotation β must fulfill the following constraint:

$$\frac{H_{\infty R}}{\sqrt{\beta}} = -1.3494 \qquad \textbf{Eq. 23}$$

Using linear interpolation in Table 2, a value of β=0.331 (apart from a misprint of 0.314 in **Owen and Rogers [64]**) is obtained which is in reasonable agreement with the value β=0.314 obtained by **Dijkstra and Heijst [27]** for the laminar flow between infinite disks solving the full Navier-Stokes equations numerically. In fact, the only coupling between these two solutions is the continuity equation which shows that the two boundary layers are virtually independent of each other.

The flow model that most consistently explains the flow physics is the four layer model proposed by **Senoo and Hayami [85]**. For example, angular momentum is truly conserved in each layer since differential equations in the radial and tangential direction are formulated for each single layer. However, this model is very complicated to use for design applications since seven differential equations have to be solved in a coupled manner. **Senoo and Hayami [85]** solve the resulting system of equations numerically using an iterative technique. Since eight unknowns are present and only seven differential equations are available, the thickness of the outward flow layer is assumed to be twice the wall layer thickness. Additionally, the shear stress between the wall layer and the outward flow layer is modelled as a two-dimensional turbulent jet in a stagnant surrounding. Furthermore, in terms of the prediction of engineering magnitudes such as the pressure distribution, the core swirl ratio or the disk friction torque, the four layer model is not expected to give more accurate results than other models which are easier to handle. For example, **Hamkins [36]** shows comparisons between experimentally deduced (from the static pressure distribution) and computed core rotation factors. The results agree qualitatively but with large differences in the numerical values.

Kurokawa et al. [44][45][46][47] discuss the flow in the impeller side gap in several papers. The analysis includes a theoretical model that basically remains the same, except slight modifications, in all publications. The theoretical results are supported by measurements. This flow model is widely used in the industry and is based on the assumption of flow regime IV with core region and two boundary layers (three-layer-model). The general flow structure for a wide gap is given on the left hand side in Fig. 6.

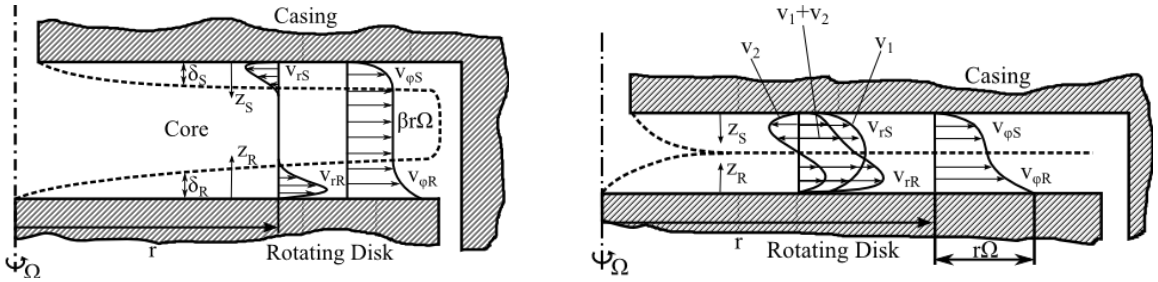

Fig. 6: Non-interference (left) and interference gap flow (right) according to Kurokawa and Sakuma [47]

The momentum equations are integrated across the gap width assuming that the local boundary layer structure depends uniquely on the local core rotation distribution. Equations for the boundary layer thickness as a function of the radius are necessary for both rotor and stator boundary layer. For the rotor, the equation given by **Daily et al. [25]** is used and the thickness of the stator boundary layer is determined from the continuity equation assuming that the entire radial flow takes place in the boundary layers. Further on, velocity profiles according to the classical 1/7 power law are presumed. With these simplifications, the equations can be integrated to yield two differential equations for the radial pressure and core rotation distribution, respectively. **Kurokawa and Toyokura [44]** emphasize that not the mere leakage flow rate but rather the angular momentum flux it carries has the most dominant effect on the flow field in the side chamber. The width of the side gap is mentioned to have only a small influence if the leakage flow contains angular momentum but if not, the axial spacing has a much greater effect on the radial pressure distribution.

Kurokawa and Sakuma [47] give the following equation for the derivative of the core rotation factor with the radius in case of separated boundary layers that has been adjusted to the present notation:

$$\frac{\partial\beta}{\partial\bar{r}} = \left\{ 0.0256 \left[\frac{(a_R^2+1)^{0.375}}{0.54^{0.25}} \left(1-\beta(\bar{r})\right)^{1.125} - \frac{((a_S^2+1)^{0.375})}{f'^{\frac{1}{4}}} \beta(\bar{r})^{\frac{7}{4}} \right] - \frac{5}{6}\frac{\varphi_G}{\bar{r}^{2.6}} Re_\varphi^{0.2} \beta(\bar{r}) \right.$$
$$\left. - \frac{1127}{3600} a_R 0.54 \left(1-\beta(\bar{r})\right)^{3.5} - \frac{49}{720} 0.54 \left(1-\beta(\bar{r})\right)^{3.5} \bar{r} \left(\frac{da_R}{d\bar{r}}\right) \right\} \qquad \textbf{Eq. 24}$$
$$\cdot \left\{ \bar{r} \left[\frac{5}{12}\frac{\varphi_G}{\bar{r}^{2.6}} Re_\varphi^{0.2} - \frac{343}{1480} a_R 0.54 |1-\beta|^{2.5} \right] \right\}^{-1}$$

The constant 0.0256 results from the empirical description of the wall shear stresses in analogy to the flow in hydraulically smooth pipes. This approach is based on the one-seventh-power law for the velocity distribution. In the basic model (**Kurokawa and Toyokura [44]**), the same value amounts 0.0225 instead of 0.0256. The origin and reason for this discrepancy is discussed in chapter 4.4.
In Eq. 24 two constants (α_R, α_S) appear to which values from experiments are assigned. The velocity parameters α_R and α_S are fixed in **Kurokawa and Toyokura [44]** whereas in **Kurokawa and Sakuma [47]** empirical correlations for the flow angle are used to improve the analysis:

$$a_S = 1.03 \left(\frac{Re_l}{10^5} + 2 \right)^{-0.387} \qquad \textbf{Eq. 25}$$

$$a_R = 1.18 \left(\frac{Re_l}{10^5} + 2 \right)^{-0.490} \qquad \textbf{Eq. 26}$$

The function f´ follows from the continuity equation and writes:

$$f' = \frac{\left(a_R c (1-\beta)^{3.5} - \frac{120}{98}\frac{\varphi_G}{\bar{r}^{2.6}} Re_\varphi^{0.2} \right)}{a_s \beta} \qquad \textbf{Eq. 27}$$

For a known core rotation distribution, the pressure can be successively calculated from the assumption of radial equilibrium between pressure and centrifugal forces in the core region.
In **Kurokawa and Sakuma [47]**, the method is extended to the flow with merged boundary layers since in case of a small axial gap distance or a large radial outflow, the conventional method yields larger errors. The statement that a radial through-flow affects the boundary layers confirms that the different regimes according to **Daily and Nece [24]** are strictly valid only for the enclosed rotating disk. In the general case of a rotor-stator cavity with leakage flow, the borders between the different regimes are likely to be different.
In the case of merged boundary layers or "interference gap flow" the derivative of the core rotation (i.e. the dimensionless rotational velocity in the middle of the side gap) with respect to the radius and the respective pressure gradient are written as:

$$\frac{\partial\beta}{\partial\bar{r}} = -\frac{1+16\beta}{\bar{r}} - \frac{49}{1440}\left(4\alpha^{\#} + \bar{r}\frac{\partial\alpha^{\#}}{\partial\bar{r}}\right) \cdot \left(\frac{9}{4}\frac{\bar{r}}{\varphi_G}\frac{s}{b}\right) + 0.0256 \left(\frac{2\bar{r}^3}{Re_\varphi \left(\frac{s}{b}\right)^5} \right)^{2.5}$$
$$\cdot \left(\frac{9}{4}\frac{\bar{r}}{\varphi_G}\frac{s}{b}\right) \left[(1-\beta) \cdot \left\{ (1-\beta)^2 + \left(\frac{4}{7}\frac{\varphi_G}{\bar{r}^2\left(\frac{s}{b}\right)} + \alpha^{\#} \right)^2 \right\}^{\frac{3}{8}} \right. \qquad \textbf{Eq. 28}$$
$$\left. - \beta \left\{ \beta^2 + \left(\frac{4}{7}\frac{\varphi_G}{\bar{r}^2\left(\frac{s}{b}\right)} - \alpha^{\#} \right)^2 \right\}^{\frac{3}{8}} \right]$$

$$\frac{\partial p^*}{\partial \bar{r}} = \frac{56\beta^2 + 7\beta + 1}{36}\bar{r} - \frac{343}{828}\alpha^{\#}\bar{r}\left(3\alpha^{\#} + 2\bar{r}\frac{\partial \alpha^{\#}}{\partial \bar{r}}\right) + \frac{128}{63}\bar{r}\left(\frac{\varphi_G}{2\bar{r}^2\left(\frac{s}{b}\right)}\right)^2 - 0.0512\bar{r}\left(\frac{2\bar{r}^3}{Re_\varphi\left(\frac{s}{b}\right)^5}\right)^{2.5}$$
$$\cdot\left[\left(\frac{4}{7}\frac{\varphi_G}{\bar{r}^2\left(\frac{s}{b}\right)} + \alpha^{\#}\right)\cdot\left\{(1-\beta)^2 + \left(\frac{4}{7}\frac{\varphi_G}{\bar{r}^2\left(\frac{s}{b}\right)} + \alpha^{\#}\right)^2\right\}^{\frac{3}{8}}\right. \qquad \textbf{Eq. 29}$$
$$\left. + \left(\frac{4}{7}\frac{\varphi_G}{\bar{r}^2\left(\frac{s}{b}\right)} - \alpha^{\#}\right)\left\{\beta^2 + \left(\frac{4}{7}\frac{\varphi_G}{\bar{r}^2\left(\frac{s}{b}\right)} - \alpha^{\#}\right)^2\right\}^{\frac{3}{8}}\right]$$

The function $a^{\#}$ formulates:

$$\alpha^{\#} = 0.0646\left(\frac{s}{b}\right)^{-0.693}\left(\frac{Re_l}{10^5} + 2\right)^{-0.0285\left(\frac{s}{b}\right)^{-0.693}} \qquad \textbf{Eq. 30}$$

Comparing the two equations for the radial core rotation distribution indicates that the axial gap width now has a strong influence on the core rotation and the pressure distribution in the case of flow regime III.

Some test calculations have been performed with Eq. 24 for the limiting cases of zero and infinite high through-flow. Fig. 7 shows a parameter combination of the inlet rotation and zero leakage. For β values around 0.45, the solution almost corresponds to a constant core rotation. A variation of the core rotation is observed for higher inlet rotation (β_e) of the fluid. Even with no leakage, a momentum exchange with the impeller outflow can be present (e.g. **Schubert [83]**). This causes a change in the core rotation that would not be present for an isolated side chamber.

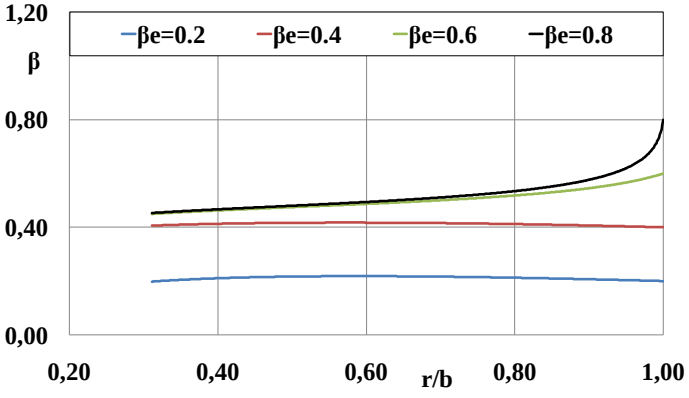

Fig. 7: Core rotation distribution according to Eq. 24 in case of zero leakage and different boundary values

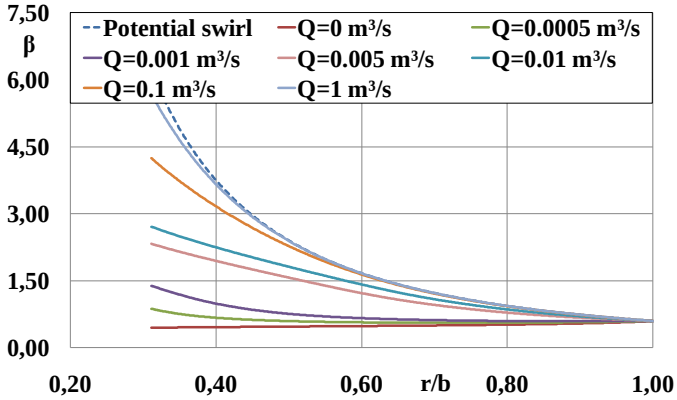

Fig. 8: Core rotation distribution according to Eq. 24 in case of constant entrance rotation (β_e=0.6) and different leakage flow rates

Fig. 8 illustrates the influence of the leakage flow rate while the inlet rotation is kept constant (β_e=0.6). For increasing angular momentum fluxes, the curves approach the limiting potential swirl distribution.
Baibikov and Karakhan'yan [7] and **Baibikov [8]** suggest another integral method for calculation of the turbulent flow in the impeller side gap. In contrast to most of the other flow models in the literature, the assumed velocity profiles correspond to the case of merged boundary layers. The integration of the profiles leads to the Eulerian integral of the first kind (the so called beta function) which appears in the final expressions for the radial distribution of the velocity parameters.
Zilling [109] examines effects on the axial thrust in a single centrifugal pump stage. The influence of the through-flow, the gap width, the radial clearance at the outer diameter and the inlet conditions are considered. For the case of zero leakage, an equation for the core rotation is developed based on the idea that the angular momentum of the rotating core is in equilibrium with the torques of the confining walls. Interestingly, the final equation for solid body core rotation is based on geometrical magnitudes only. If a leakage flow is present, a differential equation for the radial gradient of the core rotation is developed based on the momentum balance for a small cylindrical volume element. The formulation accounts for turbulence effects using an eddy viscosity formulation.
Möhring [59] extends the same model by additionally including the effects of the secondary flows (in the rotor and stator boundary layer) in the momentum balance for the cylindrical volume element. He argues that the radial gradient of the turbulent shear stress is much smaller than the axial gradients of the flow quantities in the boundary layers and can thus be neglected. His experimental results cover the influence of a superposed through-flow without a swirl component. In this case, his theoretical model shows a good agreement with the experimentally determined core rotation from the radial equilibrium relation.
Owen [63] develops a flow model to calculate the core rotation factor and the frictional resistance by solving the Ekman equations for flow regime IV in terms of an application in the secondary air systems of gas turbines. In such a configuration, the flow direction is usually radially outwards (e.g. **Rabs et al. [76], Da Soghe et al. [23]**) The Ekman equations are a simplified, linearized form of the equations of motion. The functional relation for the core rotation in case of laminar flow is finally obtained by use of the continuity equation disregarding the outer cylindrical wall:

$$\beta = 0.25\left[-1+\sqrt{\left(5-4\varphi_G\frac{\sqrt{Re_\varphi}}{\bar{r}^2}\right)}\right]^2 \qquad \textbf{Eq. 31}$$

For zero through-flow it follows from Eq. 31 that β=0.382 which is in very good agreement with the measurements of **Daily et al. [25]**. The core rotation is completely suppressed for a critical value of the through-flow coefficient ($\varphi_G\frac{\sqrt{Re_\varphi}}{\bar{r}^2}=1$) which is approximately 16% greater than the entrainment rate for laminar flow over the free disk. It appears thus as if an external leakage flow rate equal to the entrainment rate of the free disk is sufficient to completely suppress the core rotation. For higher values, a flow structure according to **Stewartson [93]** is present. For turbulent flow, **Owen [63]** uses the integral method according to **Van Kármán [42]** to solve the non-linear equations of motion for the rotor boundary layer. This solution is combined with a simplified (linear) approach on the stator side. Balancing the flow rates finally yields an equation for moderate through-flow rates ($\pi\varphi_G {Re_\varphi}^{0.2}\bar{r}^{2.6} < 0.1$):

$$(1-\beta)^{\frac{8}{5}}\cdot(1-0.51\beta)-0.638\beta^{\frac{4}{5}}=4.57\varphi_G\frac{\pi Re_\varphi^{\frac{1}{5}}}{\bar{r}^{\frac{13}{5}}} \qquad \textbf{Eq. 32}$$

In the case of zero leakage, Eq. 32 implies that β=0.426 which is again in reasonable agreement with the experiments by **Daily et al. [25]**. The core rotation completely diminishes when the leakage flow rate is equal to the entrainment rate of the free disk under turbulent conditions predicted by Van Kármán ($\varphi_G=0.0697\frac{\bar{r}^{\frac{13}{5}}}{Re_\varphi^{\frac{1}{5}}}$). The results obtained with Eq. 32 are in fair agreement with the

experimental and numerical data of **Vaughan [99]** and the proposed empirical correlation (Eq. 19) by **Daily et al. [25]**. Nonetheless, the approximation becomes worse as the through-flow rate increases.
Lauer [50] includes the influence of indentions in the side gap geometry and picks up the eddy viscosity concept used by **Zilling [109]**. He notes that employing this concept models the same effect as exchange flows present between the impeller main flow and the side gap in the case of zero leakage. Nevertheless, the proper specification of a general appropriate value for the eddy viscosity remains an open question and complicates the numerical solution using a finite difference procedure.

3.4 Computational Fluid Dynamics

In the beginning of the sixties, increasing computing powers gave rise to the numerical solution of the Navier-Stokes equations. Since then, numerous numerical studies have been devoted to rotating disk flows. Features such as strong streamlines curvature, thin boundary layers or transitional zones pose a challenging task for numerically modeling this kind of flow. Especially turbulence modeling turns out to be a key feature. Besides, these flows are very well suited to study the effects of rotation on turbulence.
Morse [57] studies the effects of radial inflow and outflow in a rotating cavity with a peripheral shroud using an elliptical solver with a modified low Reynolds number k-ε model proposed by Launder and Sharma. Especially in the stator boundary layer, the computations show a tendency of the flow to laminarize under conditions which are known from experiments to be turbulent. **Chew and Vaughan [18]** compute the flow in a rotor-stator cavity using a finite difference method in combination with a mixing length formulation. The results are compared to the experimental data by **Daily and Nece [24]** and show a fair agreement with some discrepancies in the core and the relaminarization region close to the rotation axis, where the local Reynolds numbers are small. The computations indicate that the prediction of laminarization is too strong. **Morse [58]** extends his computations to the enclosed rotating disk case without superimposed flow by applying an anisotropic low Reynolds number k-ε turbulence model. To trigger transition, a small fraction of the turbulent viscosity calculated from a mixing length model is added to the energy production term. A delayed transition from laminar to turbulent flow is observed on the rotor with reference to the experimental data of **Daily and Nece [24]**. In contrast, turbulence is well established in the stator boundary layer characterized by a significantly thicker boundary layer and thinner outflow layer at the corresponding radius. Furthermore, the moment coefficient is slightly under-predicted compared to the measured value as a consequence of the delayed transition. **Iacovides and Theofanopoulus [37]** accomplish computations of different co-rotating and enclosed disk configurations (with and without through-flow) applying several turbulence models. In the fully turbulent regions, a k-ε and an algebraic stress model are used while in the near wall regions a Van-Driest modified version of the mixing length model is adapted. The modeling of the wall regions turns out to be of much greater importance compared to the outer region. Regarding the results, some deficiencies concerning the rotor boundary layer thickness and core rotation are observed. The authors claim that an anisotropic model may be necessary to reach a general validity. Furthermore, neither of the two near wall models employed in their study appears to be universally applicable to all rotating disk flows. **Iacovides and Toumpanakis [38]** solve the axisymmetric Navier-Stokes equations in case of an enclosed rotating disk using four different turbulence models: A k-ε model coupled with an one-equation model, the Launder and Sharma k-ε model, a k-ω model and a low Reynolds number differential stress model. The k-ε and the k-ω model fail to correctly predict the size of the laminar region in the rotor boundary layer. But the results indicate that a Reynolds stress model might be the adequate choice of closure. **Elena and Schiestel [30]** perform a numerical study based on the finite volume method for rotor-stator systems with and without through-flow. Their study includes a low Reynolds number k-ε model, a zonal modeling approach based on an algebraic stress model linked to the k-ε model close to the walls and a Reynolds stress model. The latter model is modified to account for the implicit effect of rotation on the turbulence field. The authors state that Reynolds stress models are an adequate closure assumption for correctly predicting the flow in rotor-stator systems. **Launder et al. [52]** note that at that time, it turned out that the second moment closure approach has to fulfill the two-component limit, a state that is asymptotically reached as one approaches the wall. The implementation of the two component limit constraint in modeling mean strain rate effects on the pressure-strain term turns out to be very important (**Launder and Li [51]**) because pressure reflection impacts are embedded in the basic model rather than being modeled separately as an empirical correlation. **Randriamampianina et**

al. [79] investigate the effect of the rotational Reynolds number for a fixed aspect ratio. The geometry corresponds to a variant studied earlier by **Daily and Nece [24]** while the outer radial shroud is either rotating or stationary. For the sake of comparison, a standard k-ε model and a Reynolds stress model are used. For flow regime II (separated boundary layer and laminar flow), the influence of the radial shroud is limited to its close vicinity. Instabilities in terms of vortices are found between the two boundary layers. Further, the authors emphasize the characteristic of the k-ε model to be blind to any rotation effect on the turbulence field and the ability of the Reynolds stress model to give more accurate predictions. **Haddadi and Poncet [35]** calculate the flow in a rotor-stator cavity for small gap clearances either with or without a superposed through-flow using a low Reynolds number second-order full stress closure. The results show that, depending on the local Reynolds number, different flow regimes can coexist in the case of an enclosed rotating disk. For example, the flow changes from flow regime II to III in dependance on the radial position which is clearly evident from the velocity profiles. In this case, a coexistence of two flow regimes, as well as transition from laminar to turbulent flow, is present. Separated boundary layers always occur close to the hub which is assigned to the characteristics of the boundary layers to increase with radius. Moreover, in contrast to the classical Batchelor flow, turbulence is distributed in the axial direction. In Batchelor flow, turbulence is concentrated in the boundary layers, while the Reynolds stress components vanish in the core. Another noticeable difference is that the flow on the rotor becomes turbulent for smaller Reynolds numbers than the stator which contradicts the separated boundary layer flow structure (see **Itoh et al. [40]**). When a centrifugal flux is employed the flow pattern changes to Stewartson flow and turbulence is mainly confined in the rotor boundary layer. In presence of a centripetal flux, turbulence is mainly confined to the stator boundary layer and the flow resembles flow structure IV. The authors emphasize that the mean tangential velocity profile is very similar to the profiles found in flows with separated boundary layers but the radial velocity is of a very different shape. In the case of flow regime IV, the radial velocity must become zero in the core region whereas in case of torsional Couette flow, the radial velocity varies almost linearly across the gap width.

Meanwhile, a large body of literature is devoted to the transitional state in rotor-stator cavities. A comprehensive review is given by **Launder et al. [52]**. Several different instability mechanisms can occur in rotor-stator cavities depending on the values of the gap width and the Reynolds number. For very small axial gap widths, the merged boundary layer case resembles the classical Taylor-Couette problem. In the case of separated boundary layers, the stability is mainly determined by the boundary layers. Furthermore, the presence of a hub or a radial shroud can significantly influence the global stability of the flow. **Schouveiler et al. [82]** give a transition diagram that shows the various types of instabilities that can occur for the enclosed rotating disk in dependance on the axial gap width and the circumferential Reynolds number Re_φ.

So far, nearly all studies cited above assume stationary flow conditions. This means that the coherent structures present in the laminar and transitional state have disappeared. The reason could be that these structures have simply vanished due to being drowned out by fine-scale turbulence or that their effect is at least somehow accounted for in the turbulence model (**Craft et al. [21]**). **Owen [65]** for example remarks that his research group encountered problems when trying to model the flow in an enclosed system using the RANS model under certain parameter combinations. He suspects that under these conditions the flow cannot be treated as axisymmetric and steady any more. **Czarny et al. [22]** use dye traces in an experimental setup similar to the one by **Owen [65]** to visualize large scale rotating structures in the core. The structures rotate with approximately half of the rotor speed. Based on their results they conclude that the number of vortices decreases as the Reynolds number increases which means that the influence of the vortices on the overall transport of momentum and heat is reduced at high Reynolds numbers.

Wu and Squires [106] accomplish large eddy simulations for the statistically three-dimensional flow over a rotating disk. Their study supports **Littell and Eaton's [53]** observations regarding the mechanisms promoting sweeps and ejections (that is when high momentum fluid is transported either to the wall or away from it by velocity gradients) that contribute to the shear stress production (i.e. turbulent kinetic energy). **Anderson and Lygren [4]** perform a direct numerical solution of a rotor-stator system (G=0.02) similar to that of **Itoh et al. [41]** to investigate the effect of mean-flow three-dimensionality on the turbulence structure. The model consists only of a sector segment in order to achieve a sufficiently fine mesh capable of resolving even the smallest eddies. The authors find only a modest misalignment of the shear stress vector and the mean flow gradient vector in the near wall

regions, indicating that isotropic eddy viscosity models might produce reliable results. The coherent structures in both boundary layers are remarkably similar to each other, but no spiral vortices resulting from laminar-turbulent transition are discovered. Later, **Anderson and Lygren [5]** compute the flow between a rotating and a stationary disk in case of a wide and a narrow gap using LES (large eddy simulation). The model assumes full periodicity in the tangential direction and represents an idealized model of an unshrouded rotor-stator system. For decreasing axial gap distance, the core rotation factor in the middle of the cavity approaches the limiting case of β=0.5 characteristic for plane Couette-flow. It is further confirmed that the mean flow three-dimensionality affects the near-wall vortices and their ability to generate shear stresses stated by **Littell and Eaton [53]**. **Séverac et al. [86]** perform LES computations of the flow resulting from an enclosed rotating disk using a spectral-vanishing-viscosity approach. The results coincide very well with measurements using LDV. In contrast to the idealized model studied by **Anderson and Lygren [4] [5]**, the three-dimensionality of both boundary layers is much greater. Large scale rotating structures, present in the experiments, are not reproduced by the numerical approach. This is attributed (**Launder et al. [52]**) to the presence of an inner, frictionless hub in the computation in order to save computational costs. However, this hub was not present in the experiment. **Craft et al. [21]** report unsteady RANS computations of the flow initiated by an enclosed rotating disk. A low-Reynolds number k-ε model is employed and resolves the spiral coherent structures in both boundary layers. Despite the excessive grid clustering required in the near wall region, no large scale structures are present in the core region as expected from the experiments of **Czarny et al. [22]**. In order to increases the grid density in the core region, a new analytical wall function is embedded that accounts for the skewing of the wall parallel velocity vector with the wall distance. This approach successfully resolves both the near-wall structures and the large scale rotating structures in the core. Nevertheless, the simulations show that the structures exhibit an evolution in time to a state that finally appears to be axisymmetric. In contrast to this, the structures in the experiments are time-independent.

Poncet et al. [72] use a low Reynolds number Reynolds stress model to predict the flow field in a rotor-stator configuration with either centrifugal or centripetal through-flow and a fixed aspect ratio (G=0.036, $Re_\varphi=1\cdot10^6$). The grid has 140 divisions in the radial and 80 divisions in the axial direction. Both the mean velocities and the corresponding Reynolds stresses are measured using the LDV technique. In the case of a centripetal flow, the leakage enters the cavity with a swirl leading to an increase of the core swirl ratio at a fixed radial position for increasing through-flow rate. The centripetal flux passes the cavity in the Bödewald layer increasing the boundary layer thickness and compressing the core region. As soon as the core rotation is equal to one, the centrifugal force in the Ekman layer is no longer strong enough to pump the fluid radially outwards. Consequently, the radial velocity is directed radially inwards in both layers. In none of the cases considered by **Poncet et al. [72]** the streamlines (Fig. 9) show the vortex pair as predicted by **Radtke and Ziemann [78]** for a core rotation coefficient greater one (see Fig. 94).

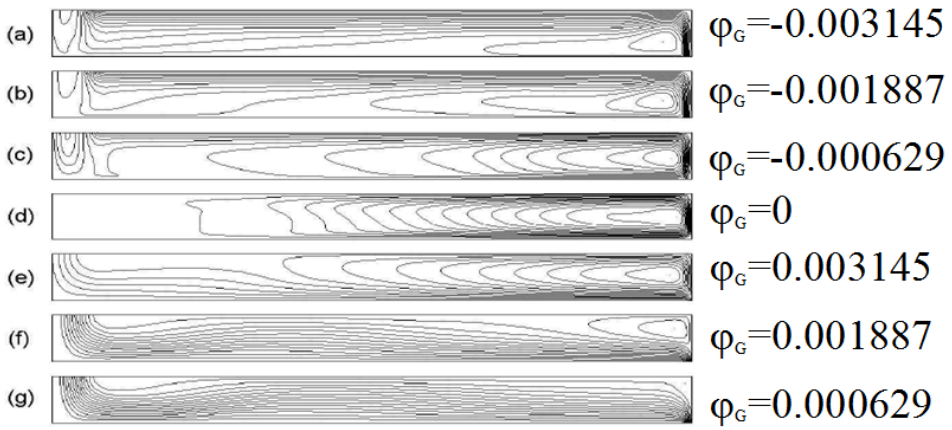

Fig. 9: Streamline patterns computed by Poncet et al. [71] for centripetal (negativ) and centrifugal (positiv) flow

In the case of centrifugal flow, the core rotation is slowed down with increasing flow rate until higher circumferential velocities appear only in the rotor boundary layer. This flow case corresponds to the

Stewartson solution discussed above. Comparisons of the measured and computed Reynolds stresses confirm that the k-ε model is in less good agreement than the Reynolds stress model.

Poncet et al. [74] present benchmark calculations using the commercial CFD solvers Ansys Fluent and Ansys CFX. Three different configurations are considered: A rotating cavity (both walls rotating) with a centrifugal outflow investigated by **Owen and Pincombe [62]**, the flow in the annular space between two concentric cylinders (Taylor-Couette-Poiseuille flow) and the rotor-stator cavity discussed before by **Poncet et al. [71]**. For the second and the third case, all models are found to predict the mean flow field quite well, whereas larger discrepancies remain for the turbulent quantities. The k-ω SST model is finally recommended for industrial use as a good compromise between accuracy and computational effort. Interestingly, this is valid for either the high and low-Re formulations of the model.

When using Reynolds stress models, the solution is extremely complicated because of stability reasons. Several researchers have reported the use of various stabilizing techniques in order to obtain a stable solution (**Poncet et al. [73], Elena and Schiestel [30]**). This is a clear disadvantage of the Reynolds stress approach and results from the "stiffness" of the underlying equations.

4 Theoretical Analysis

4.1 General Flow Structure in Rotor-Stator Cavities

In this chapter, qualitative aspects of the flow fields encountered in rotor-stator cavities are discussed. Details for this chapter are assembled from the literature review. In general, boundary layer type flow structures are to be expected. Fig. 10 shows the most frequently encountered flow pattern when the gap width is large enough to allow a formation of two boundary layers on rotor and stator.

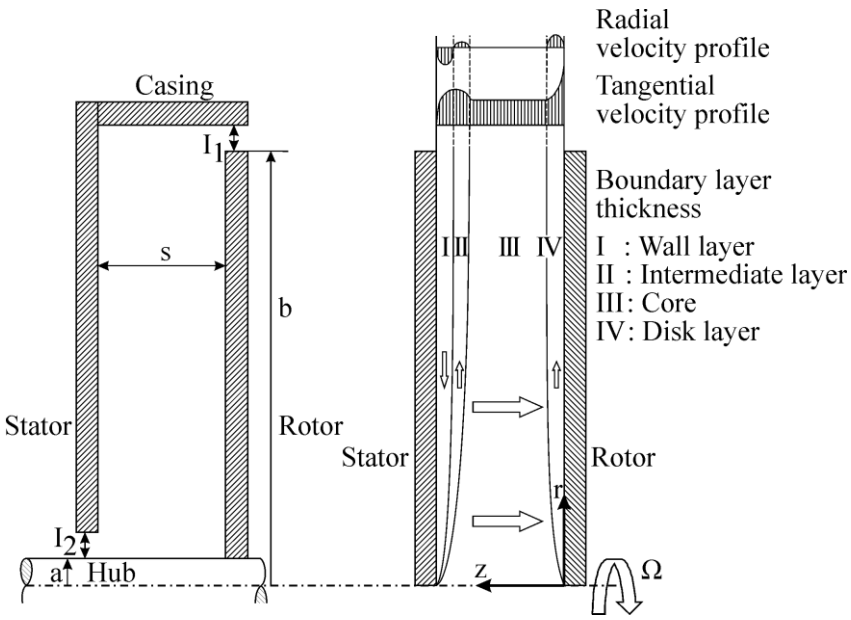

Fig. 10: Idealized cavity model and principal flow structure for a wide gap

The overall flow structure can be described as follows using cylindrical coordinates: due to viscosity the fluid in the cavity is set into motion by the rotation of the impeller. The no-slip condition requires that the fluid matches the circumferential velocity at the rotating disk and is at rest at the stationary wall. The velocity course between the two walls depends on the axial gap size. **Daily and Nece [24]** measure the velocity distribution in the axial gap of an enclosed rotating disk and distinguish between four different flow regimes (Fig. 5).

For a wide gap an intermediate velocity establishes between the walls, which is referred to as "core region". The circumferential velocity in the core is generally characterized using the core rotation coefficient β which represents the ratio of the angular velocity of the fluid to the angular velocity of the impeller. Due to the dominant tangential motion, a radial pressure gradient establishes with the maximum pressure value at the outer radius of the cavity.

In the core, centrifugal and pressure forces can balance each other without any additional forces. This state is usually known as radial equilibrium. At the stationary wall the tangential velocity is reduced to zero and therefore a radial inflow develops in the stator boundary layer caused by the dominant pressure forces. Near the rotor surface dominant centrifugal forces lead to a radial outflow. Since the main fluid motion is in circumferential direction the radial velocity component is often referred to as "secondary flow".

The boundary layers can either be merged or not; the flow can be laminar or turbulent. In case of flow regimes II or IV, which is supposed to apply in the majority of practical applications (**Gülich [34], Hamkins [36]**), the basic structure is indicated in Fig. 10 (**Senoo and Hayami [85]**): A boundary layer on rotor (IV) and stator (I), a core region (III) and an intermediate layer (II) between stator boundary layer and core with a small radial outflow of fluid. Due to mass conservation, an axial convection of fluid from the stator to the rotor takes place. Although the axial velocity itself is very small, the axially convected angular momentum is not (**Hamkins [36]**).

The circumferential velocity distribution in the core region essentially dictates the pressure distribution and frictional resistance of the rotor. The torque is affected by the circumferential velocity gradient in axial direction while the pressure is determined by the magnitude of the circumferential velocity. In centrifugal pumps the pressure in the side cavities decreases with decreasing radial coordinates

depending on the core rotation. For a constant core rotation (solid body rotation) the pressure decreases parabolically while the decrease for a superposed centripetal flow can be significantly higher with a completely different characteristics. Consequently, the determination of the radial evolution of the tangential velocity component, respectively the core rotation coefficient, is one of the major tasks in rotor-stator cavity problems in case of flow regime IV.

Bennet [11] argues that the frictional resistance of the rotor is determined by the difference of angular momentum flux between the radial exiting and the axial incoming flow in the rotor boundary layer. The axial incoming flow in the rotor boundary layer carries a significant amount of angular momentum and therefore the torque for the enclosed rotating disk must be smaller than for the free disk.

In addition, the core rotation balances the secondary flows in the boundary layers. More precisely, the difference in circumferential speed between the core layer and the boundary layers on rotor and stator determines the radial volume flow rates. For this reason, the core rotation can be understood as an equilibrium parameter for the cavity flow.

As already mentioned, in general, a leakage flow which can be directed in centrifugal (hub to casing) or centripetal (casing to hub) direction, passes the cavities. The fluid leaving the impeller can have a considerable amount of angular momentum. Due to momentum exchange, the flow entering the cavity lowers the core rotation if the tangential velocity of the incoming flow is lower than in the core or accelerates it in the opposite case. The angular momentum of the incoming flow is certainly one of the most important magnitudes since the principle of conservation of angular momentum requires an increase of the tangential velocity with decreasing radius for centripetal leakage.

Another important aspect can be concluded from the diagram in Fig. 5. For increasing Reynolds numbers the limit for the occurrence of flow regime III decreases. Consequently, this means that the thickness of the boundary layers must also decrease for increasing Re_{φ}.

4.2 Dimensionless Parameters

A dimension analysis according to the π-Theorem of Buckingham was performed for the idealized cavity model in Fig. 10. The purpose was to reveal the main dimensionless parameters encountered in rotor-stator flow problems. The basic idea behind this method is that every physical quantity with dimensions can be described using a product of powers of the basic dimensions length, time, mass and temperature. Consecutively, all dimensionless quantities follow from a product of powers of magnitudes with dimensions (**Will and Benra [102]**).

The dimensionless equation obtained for the enclosed cavity writes:

$$F\left(\frac{\Delta p}{b^2 \cdot \Omega^2 \cdot \rho}, \frac{\mu}{b^2 \cdot \Omega \cdot \rho}, \frac{\omega}{\Omega}, \frac{s}{b}, \frac{a}{b}, \frac{k_S}{b}\right) = 0 \qquad \textbf{Eq. 33}$$

The resulting quantities can be finally written in a more familiar way:

$$\Delta\bar{p} = \frac{\Delta p}{\frac{\rho}{2} \cdot \Omega^2 \cdot b^2} \qquad \text{Pressure coefficient} \qquad \textbf{Eq. 34}$$

$$Re_{\varphi} = \frac{\Omega \cdot b^2 \cdot \rho}{\mu} \qquad \text{Global Reynolds number} \qquad \textbf{Eq. 35}$$

$$\beta = \frac{\omega}{\Omega} \qquad \text{Core rotation coefficient} \qquad \textbf{Equ.36}$$

$$G = \frac{s}{b} \qquad \text{Dimensionless gap width} \qquad \textbf{Eq. 37}$$

$$\frac{a}{b} \qquad \text{Ratio of hub and rotor radius} \qquad \textbf{Eq. 38}$$

$$\frac{k_S}{b} \qquad \text{Relative surface roughness} \qquad \textbf{Eq. 39}$$

Analogous, the same procedure is applied to a cavity subjected to an external leakage flow. In this case, some additional parameters are of importance:

$\varphi_G = \frac{Q}{\pi \cdot \Omega \cdot b^3}$	Dimensionless through-flow rate	**Eq. 40**
$\beta_e = \frac{v_{\varphi e}}{\Omega \cdot b}$	Entrance rotation factor	**Eq. 41**
$\frac{l_1}{b}$	Clearance ratio between radial gap height and rotor radius	**Eq. 42**
$\frac{l_2}{b}$	Clearance ratio between hub and radial casing	**Eq. 43**

As already pointed out above, the major parameters for a rotor-stator cavity subjected to a through-flow are the Reynolds number, the gap width and the entering angular momentum flux. The importance of the gap height of the cavity anteroom is confirmed by the measurements of **Lauer [50]**. The gap height controls the degree of coupling between the impeller side gap and the main flow path. Small gap heights increase the resistance of the anteroom. In fact, this decouples the outer and the side chamber flow, since the incoming leakage is homogenized by the anteroom.
The influence of the Reynolds number compared to the angular momentum flux can be seen in the following picture according to the measurements of **Schubert [83]**.

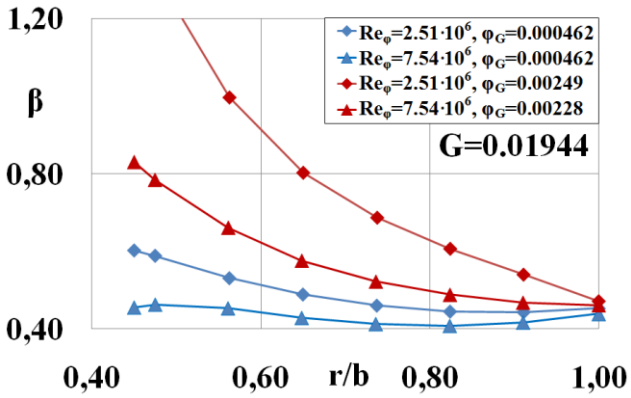

Fig. 11: Influence of Reynolds number and angular momentum flux (Schubert [83])

The figure nicely highlights the dominant influence of the leakage flow compared to the Reynolds number effect. Increasing the angular momentum flux leads to a sharp drop of the core rotation towards the inner radii as also shown by the experiments of **Altmann [2]**. **Schubert [83]** mentions that in case of high Reynolds numbers, the agreement between computed and measured core rotation is generally better. This can be ascribed to the homogenizing effect of the increased inertia to viscosity ratio. Depending on the operating point, relatively high entrance rotation factors can occur in centrifugal pumps (**Lauer [50]**). If the leakage fluid contains only a small swirl component, the core rotation is slowed down due to momentum exchange. This situation is often encountered in radial compressors when the leakage flow in the rearside chamber is directed in centrifugal direction. Since the leakage enters the cavity through a labyrinth seal it has only a small amount of rotation.
The dimensionless gap width is mainly important to distinguish between the different flow regimes. For the case of separated boundary layers, the influence of the gap width is reduced to the retarding effect of an outer stationary shroud for example. In other words, the gap width influences the flow only indirectly by the outer boundary condition for flow regime IV. The core rotation can also be completely suppressed by a superposed through-flow and the flow can change from Batchelor to Stewartson flow where higher circumferential velocities occur only in the rotor boundary layer.
The global Reynolds number and the axial gap width can be combined into the so called Ekman number:

$$Ek = \frac{1}{G^2 Re_\varphi} \qquad \textbf{Eq. 44}$$

In the common case of cavities with large aspect ratios and high Reynolds numbers, the Ekman number is usually very small (e.g. Ek=1.16·10^{-4} for the shroud side chamber of the centrifugal pump in chapter 5).
In some papers, another definition of the through-flow coefficient can be found (**Poncet et al. [71]**):

$$\varphi_G = \frac{\mathrm{Q}}{2\pi\Omega r^3} Re_l^{\frac{1}{5}} \qquad \textbf{Eq. 45}$$

The same definition is used by **Kurokawa and Toyokura [44]**, except that the radial coordinate is replaced with the outer rotor radius. **Eq. 45** contains the radius in the denominator as well as in the Renyolds number. This definition prohibits a global characterization of the leakage. Moreover, due to its minor influence in flow regime IV, the axial gap distance is not recommended to be used in a definition of a through-flow coefficient (**Schubert [83]**).

4.3 Basic Equations

The fundamental equations for any analytical treatment are the conservation laws for mass, momentum and energy. Some of the successive derivations are given in **Will and Benra [103]**.
The continuity equation expresses the principle of conservation of mass. The rate of change of mass per unit volume is equal to the inflowing minus the outflowing mass over the surface of a control volume element. This leads to the universal formulation of the continuity equation using the tensor notation according to Einstein for a compressible, unsteady flow:

$$\frac{\partial \rho}{\partial t} + \frac{\partial (\rho v_i)}{\partial x_i} = 0 \qquad \textbf{Eq. 46}$$

The momentum equations express Newton's second law and relate the acceleration of a fluid particle to the surface and body forces experienced by the fluid. The rate of change of momentum per unit volume plus the outflowing minus the inflowing momentum over the surface equals the sum of forces acting on a control volume element. The universal momentum equation for an unsteady and compressible flow is written as:

$$\frac{\partial (\rho v_i)}{\partial t} + \frac{\partial \left(\rho v_i v_j\right)}{\partial x_j} = f_i - \frac{\partial p}{\partial x_i} + \frac{\partial \tau_{ij}}{\partial x_j} \qquad \textbf{Eq. 47}$$

The left hand side represents the inertia terms while the right hand side includes the impact of pressure, friction and external forces. For compressible Newtonian fluids the stress tensor can be written using the hypothesis of Stokes which is basically a generalization of Newton's one dimensional shear stress approach (e.g. **Schlichting [81]**):

$$\tau_{ij} = \mu \left(\frac{\partial v_i}{\partial x_j} + \frac{\partial v_j}{\partial x_i} - \frac{2}{3} \delta_{ij} \frac{\partial v_l}{\partial x_l} \right) \qquad \textbf{Eq. 48}$$

The Euler equations result by neglecting the viscous terms in **Eq. 47**. These equations are still non-linear due to the convective terms.

$$\frac{\partial (\rho v_i)}{\partial t} + \frac{\partial \left(\rho v_i v_j\right)}{\partial x_j} = f_i - \frac{\partial p}{\partial x_i} \qquad \textbf{Eq. 49}$$

Due to the geometrical shape of rotor-stator cavities, the equations are best expressed using cylindrical coordinates. Since the flow is assumed to be isothermal and incompressible with constant density, the energy equation can be omitted in the following analysis. Without making closure assumptions for the shear stresses the full equations can be formulated as:

Radial momentum

$$\rho\left(\frac{\partial v_r}{\partial t}+v_r\frac{\partial v_r}{\partial r}+\frac{v_\varphi}{r}\frac{\partial v_r}{\partial \varphi}-\frac{{v_\varphi}^2}{r}+v_z\frac{\partial v_r}{\partial z}\right) = f_r-\frac{\partial p}{\partial r}+\frac{1}{r}\frac{\partial(r\tau_{rr})}{\partial r}+\frac{1}{r}\frac{\partial(\tau_{r\varphi})}{\partial \varphi}-\frac{\tau_{\varphi\varphi}}{r}+\frac{\partial(\tau_{rz})}{\partial z} \quad \textbf{Eq. 50}$$

Tangential momentum

$$\rho\left(\frac{\partial v_\varphi}{\partial t}+v_r\frac{\partial v_\varphi}{\partial r}+\frac{v_\varphi}{r}\frac{\partial v_\varphi}{\partial \varphi}+\frac{v_r v_\varphi}{r}+v_z\frac{\partial v_\varphi}{\partial z}\right) = f_\varphi-\frac{1}{r}\frac{\partial p}{\partial \varphi}+\frac{1}{r^2}\frac{\partial}{\partial r}\left(r^2\tau_{\varphi r}\right)+\frac{1}{r}\frac{\partial(\tau_{\varphi\varphi})}{\partial \varphi}+\frac{\partial(\tau_{\varphi z})}{\partial z} \quad \textbf{Eq. 51}$$

Axial momentum

$$\rho\left(\frac{\partial v_z}{\partial t}+v_r\frac{\partial v_z}{\partial r}+\frac{v_\varphi}{r}\frac{\partial v_z}{\partial \varphi}+v_z\frac{\partial v_z}{\partial z}\right) = f_z-\frac{\partial p}{\partial z}+\frac{\partial(\tau_{zr})}{\partial r}+\frac{\tau_{zr}}{r}+\frac{1}{r}\frac{\partial(\tau_{z\varphi})}{\partial \varphi}+\frac{\partial(\tau_{zz})}{\partial z} \quad \textbf{Eq. 52}$$

The continuity equation writes:

Continuity

$$\frac{1}{r}\frac{\partial(rv_r)}{\partial r}+\frac{1}{r}\frac{\partial(v_\varphi)}{\partial \varphi}+\frac{\partial(v_z)}{\partial z}=0 \quad \textbf{Eq. 53}$$

These equations are valid for general flows even when they do not have Newtonian viscosity. Several assumptions can be made in order to simplify the equations:

- Steady flow conditions $\frac{\partial}{\partial t}=0$
- Axisymmetric flow $\frac{\partial}{\partial \varphi}=0$
- Disregarding body forces
- Normal stresses due to viscosity (τ_{rr},$\tau_{\varphi\varphi}$) cancel out in **Eq. 50**
- The shear stress due to gradients of the tangential velocity with radius can be neglected ($\tau_{\varphi r}$)

Turbulence effects are neglected in order to enable the derivation of a comparatively simple calculation method that focuses on the prediction of the radial core rotation distribution. Otherwise, the Reynolds averaged Navier-Stokes equations should be considered. This would result in extra terms accounting for the turbulent stresses and a solution would require additional assumptions in terms of a turbulence model.
The simplified equations can be formulated as (see also **Owen [63]**):

Radial momentum

$$\rho\left(v_r\frac{\partial v_r}{\partial r}-\frac{{v_\varphi}^2}{r}+v_z\frac{\partial v_r}{\partial z}\right)=-\frac{\partial p}{\partial r}+\frac{\partial(\tau_{rz})}{\partial z} \quad \textbf{Eq. 54}$$

Tangential momentum

$$\rho\left(v_r\frac{\partial v_\varphi}{\partial r}+\frac{v_r v_\varphi}{r}+v_z\frac{\partial v_\varphi}{\partial z}\right)=\frac{\partial(\tau_{\varphi z})}{\partial z} \quad \textbf{Eq. 55}$$

Axial momentum

$$\rho\left(v_r\frac{\partial v_z}{\partial r}+v_z\frac{\partial v_z}{\partial z}\right)=-\frac{\partial p}{\partial z}+\frac{\tau_{rz}}{r}+\frac{\partial \tau_{rz}}{\partial r} \quad \textbf{Eq. 56}$$

The continuity equation now becomes:

Continuity $$\frac{\partial v_r}{\partial r} + \frac{v_r}{r} + \frac{\partial v_z}{\partial z} = 0$$ **Eq. 57**

These are the simplified momentum and continuity equations for steady, axisymmetric flow in rotor-stator cavities.
Outgoing from these equations, some general aspects of the core region in case of flow regime IV can be analyzed. Neglecting the axial velocity, the tangential momentum equation for the inviscid core region reduces to:

$$\rho\left(v_r \frac{\partial v_\varphi}{\partial r} + \frac{v_r v_\varphi}{r}\right) = 0$$ **Eq. 58**

This relation can also be written in the following form:

$$\frac{v_r}{r}\frac{\partial}{\partial r}\left(v_\varphi r\right) = 0$$ **Eq. 59**

Excluding the arbitrary case of $v_\varphi \neq 0$, only two possible solutions remain. Zero radial velocity in the core corresponds to an axially constant core rotation. In this case the pressure distribution can be evaluated using the radial balance between centrifugal and pressure forces following from **Eq. 54**:

$$\frac{\partial p}{\partial r} = \rho \frac{{v_\varphi}^2}{r}$$ **Eq. 60**

Allowing for a radial velocity results in a radial transport of angular momentum and the solution as a potential swirl ($v_\varphi \cdot r = constant$) must take over. Hence, the determination of the pressure distribution requires an additional term taking into account the radial convection:

$$\frac{\partial p}{\partial r} = \rho\left(\frac{{v_\varphi}^2}{r} - v_r \frac{\partial v_r}{\partial r}\right)$$ **Eq. 61**

The influence of the radial velocity on the pressure calculation will be discussed later.
In order to enable an approximate analytical calculation of the flow in the impeller side gap, a common method is the integral boundary layer theory as mentioned before. To do so, the equations have to be integrated in the axial direction. In this approach, the integral relations are only fulfilled for integrated values across the boundary layer thicknesses, not for every single location in each layer. The equations can be applied to each single layer according to Fig. 10 with regard to the specific simplifications (**Senoo and Hayami [85], Hamkins [36]**). Then, the resulting system consists of seven differential equations while one additional relation needs to be assumed since eight unknowns are present. **Senoo and Hayami [85]** assume the thickness of the outward (or intermediate) flow layer to be twice the stator boundary layer thickness. The solution is reported to be little affected by this assumption. A numerical solution of this equation system in presence of a radial through-flow requires a complex iterative procedure. For example, **Hamkins [36]** uses a Newton-Raphson method to solve the system. Generally, the model only applies for core rotation factors smaller than one.
To obtain an easier model for estimation purposes, some further steps are necessary. The integral boundary layer method requires the specification of velocity profiles a priori. The profiles are assumed rather than being found as a part of the solution. Accordingly, the quality of the solution depends on the assumed profiles. Nevertheless, integral quantities such as the frictional resistance or the axial force can be well predicted by the method because the main velocity component is in circumferential direction. For example, the transverse velocity profiles contribute only a small fraction to the tangential shear stress.
The following identities are valid for the simplified radial and tangential momentum equations which will be central to the further derivations (see **Owen and Rogers [64]**):

$$v_r\frac{\partial v_r}{\partial r}-\frac{v_\varphi^2}{r}+v_z\frac{\partial v_r}{\partial z}=\frac{1}{r}\left[\frac{\partial}{\partial r}(rv_r^2)+\frac{\partial}{\partial z}(rv_rv_z)-v_\varphi^2\right] \quad \textbf{Eq. 62}$$

$$v_r\frac{\partial v_\varphi}{\partial r}+\frac{v_rv_\varphi}{r}+v_z\frac{\partial v_\varphi}{\partial z}=\frac{1}{r^2}\left[\frac{\partial}{\partial r}\left(r^2v_rv_\varphi\right)+\frac{\partial}{\partial z}\left(r^2v_zv_\varphi\right)\right] \quad \textbf{Eq. 63}$$

The radial and tangential momentum can now be written as:

$$\frac{\partial}{\partial r}(rv_r^2)+r\frac{\partial}{\partial z}(v_rv_z)-v_\varphi^2=-\frac{r}{\rho}\frac{\partial p}{\partial r}+\frac{r}{\rho}\frac{\partial(\tau_{rz})}{\partial z} \quad \textbf{Eq. 64}$$

$$\frac{\partial}{\partial r}\left(r^2v_rv_\varphi\right)+\frac{\partial}{\partial z}\left(r^2v_zv_\varphi\right)=\frac{r^2}{\rho}\frac{\partial\left(\tau_{\varphi z}\right)}{\partial z} \quad \textbf{Eq. 65}$$

These equations are now integrated in z-direction for a control volume from z_1 to z_2. To take into account a possible variation of the limits z_1 and z_2 with radius, the application of the Leibniz rule for a general variable X yields:

$$\int_{z=z_1}^{z=z_2}\frac{\partial X(r,z)}{\partial r}dz=\frac{\partial}{\partial r}\left(\int_{z=z_1}^{z=z_2}X(r,z)dz\right)+\frac{\partial z_1}{\partial r}X(r,z_1)-\frac{\partial z_2}{\partial r}X(r,z_2) \quad \textbf{Eq. 66}$$

Application of this rule to **Eq. 64** and **Eq. 65** leads to the general integrated forms of the radial and tangential momentum equations:

$$\frac{\partial}{\partial r}\left(r\int_{z=z_1}^{z=z_2}v_r^2\,dz\right)+r\frac{\partial z_1}{\partial r}v_{r1}^2-r\frac{\partial z_2}{\partial r}v_{r2}^2+rv_{r2}v_{z2}-rv_{r1}v_{z1}-\int_{z=z_1}^{z=z_2}v_\varphi^2\,dz = -\frac{r}{\rho}\int_{z=z_1}^{z=z_2}\frac{\partial p}{\partial r}dz+\frac{r}{\rho}\int_{z=z_1}^{z=z_2}\frac{\partial(\tau_{rz})}{\partial z}dz \quad \textbf{Eq. 67}$$

$$\frac{1}{r^2}\frac{\partial}{\partial r}\left(r^2\int_{z=z_1}^{z=z_2}v_rv_\varphi\,dz\right)+\frac{\partial z_1}{\partial r}v_{r1}v_{\varphi1}-\frac{\partial z_2}{\partial r}v_{r2}v_{\varphi2}+v_{z2}v_{\varphi2}-v_{z1}v_{\varphi1} = \frac{1}{\rho}\int_{z=z_1}^{z=z_2}\frac{\partial\left(\tau_{\varphi z}\right)}{\partial z}dz \quad \textbf{Eq. 68}$$

In the following, the existence of a plane rotor-stator cavity is assumed. **Zilling [109]** shows that for inclination angles smaller than 12 degree, conical walls have no significant influence and can thus be treated as parallel walls.

For a plane rotor-stator system with z_1=0 and z_2=s, the following equations are obtained since the velocity components v_z and v_r are zero on the walls (no slip condition):

$$\frac{1}{r}\frac{\partial}{\partial r}\left(r\int_{z=0}^{z=s}v_r^2\,dz\right)-\frac{1}{r}\int_{z=0}^{z=s}v_\varphi^2\,dz=-\frac{1}{\rho}\int_{z=0}^{z=s}\frac{\partial p}{\partial r}dz+\frac{1}{\rho}(\tau_{rzS}-\tau_{rzR}) \quad \textbf{Eq. 69}$$

$$\frac{1}{r^2}\frac{\partial}{\partial r}\left(r^2\int_{z=0}^{z=s}v_rv_\varphi\,dz\right)=\frac{1}{\rho}\left(\tau_{\varphi zS}-\tau_{\varphi zR}\right) \quad \textbf{Eq. 70}$$

These are the integral momentum relations expressed in cylindrical coordinates for a steady, incompressible and axially symmetric flow field. They are central to most analytical flow models in the literature (e.g. **Kurokawa et al. [44] [45] [46] [47], Baibikov and Karakhan'yan [7], Baibikov [8]**). A further solution requires the specification of velocity profiles and suitable expressions for the wall shear stresses.

4.4 The Blasius Law for the Wall Shear Stress

One major step towards a further evaluation is to find proper expression for the shear stresses in the integral momentum equations. A widespread approach is the so called pipe flow analogy which allows, under compliance of certain criteria, to convey the insights from pipe flows to boundary layer flows.

The universal logarithmic law of the wall is a self-similar solution for the mean velocity parallel to a solid wall and can be derived in several ways, e.g. from empirical models and dimensional analysis or the so called velocity defect law (see **Oberlack [60]**). **Oberlack [60]** derives the logarithmic law directly from the Reynolds averaged Navier-Stokes equations for the first time. A similar profile is apparent for the velocity distribution in turbulent pipe flows. Prandtl derives a friction law based on the logarithmic law which agrees very well with available experimental data over the entire range of turbulent Reynolds numbers (see Fig. 12, **Truckenbrodt [98]**):

$$\frac{1}{\sqrt{\lambda}} = 2lg\left(Re_{Pipe}\sqrt{\lambda}\right) - 0.8 \qquad \textbf{Eq. 71}$$

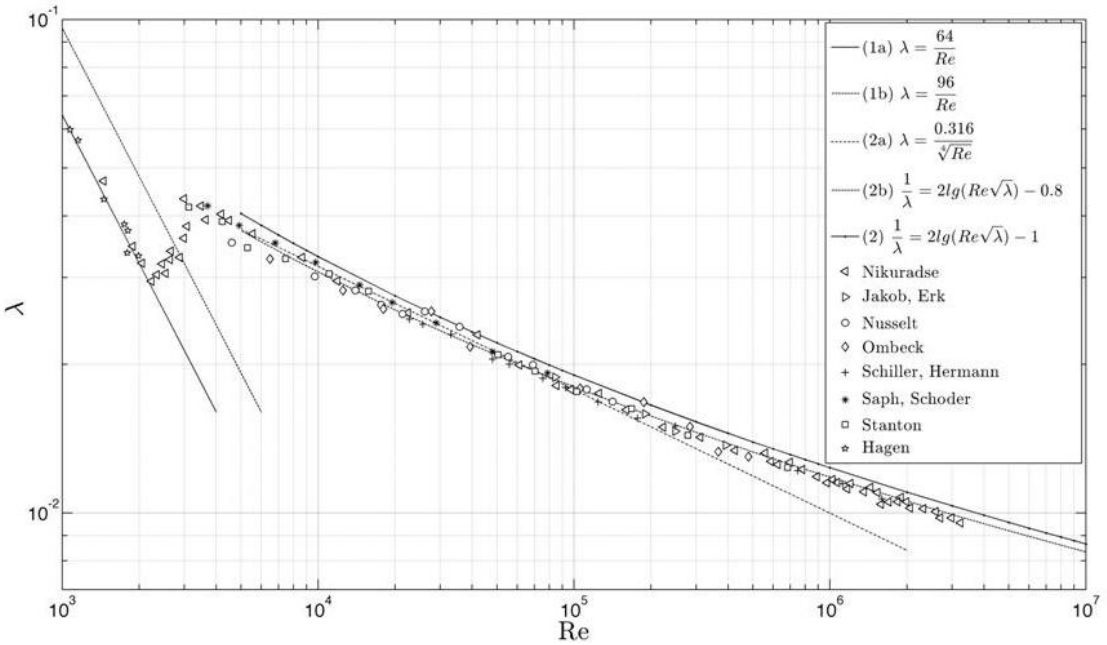

Fig. 12: Pipe friction coefficients for hydraulically smooth pipes and gaps (1a: Laminar pipe flow, $Re_{Pipe}<Re_{crit}$; 1b: Laminar gap flow; 2a: Turbulent pipe flow, $Re_{crit}<Re_{Pipe}<10^5$; 2b: Turbulent pipe flow, $Re_{crit}<Re_{Pipe}<\infty$; 2: Turbulent gap flow)

The pipe friction factor for turbulent flow in hydraulically smooth pipes can be expressed in a Reynolds number range $Re_{cr}<Re_{Pipe}<10^5$ using a relation given by Blasius:

$$\lambda = \frac{0.3164}{\sqrt[4]{Re_{Pipe}}} \qquad \textbf{Eq. 72}$$

This empirical formula is obtained by correlating the measured data of different experimentalists and agrees with the Prandtl-law to within 3% for $10^4<Re_{Pipe}<10^5$. Outside its scope, the errors can be severe, for example 30% at $Re_{Pipe}=10^7$ (**Pope [75]**).

The wall shear stress for a pipe flow can be formulated as:

$$\tau = \lambda \frac{\rho}{8} v_{mean}^2 \qquad \textbf{Eq. 73}$$

Introducing the Blasius formula (**Eq. 72**) results in an expression for the wall shear stress for smooth pipe flows:

$$\tau = 0.03955 \rho v_{mean}^{\frac{7}{4}} \left(\frac{\nu}{D}\right)^{\frac{1}{4}} \qquad \textbf{Eq. 74}$$

This relation can be used to approximately calculate the turbulent boundary layer on a flat plate assuming that the velocity profile close to the solid surface is the same as in the pipe flow case. A fundamental difference between the flow in a pipe and across a flat plate is that the pipe flow is related to a pressure drop (dp/dx<0) and the radius is constant whereas the boundary layer increases with distance from leading edge. The boundary layer thickness corresponds to the pipe diameter and the mean velocity must be expressed in terms of the free stream velocity which corresponds to the maximum velocity in the pipe. Therefore the following power law is used as an explicit approximation for the velocity distribution (**Truckenbrodt [98]**):

$$\frac{v(r)}{v_{max}} = \left(\frac{y}{R}\right)^n = \left(1 - \frac{r}{R}\right)^n \; or \; \frac{v}{v_{max}} = \left[1 - \left(\frac{r}{R}\right)^m\right]^n \qquad \textbf{Eq. 75}$$

In this relation, y=R-r denotes the wall distance. It is worth mentioning that the velocity gradient close to the wall according to **Eq. 75** tends towards infinity for exponents smaller than one. Because of this, the viscous sublayer is not correctly captured by this relation and cannot be used for the evaluation of shear stresses. The mean velocity for a pipe can be written as:

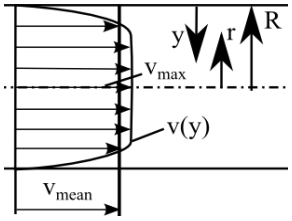

$$v_{mean} = K \cdot v_{max} = \frac{Q}{A} = \frac{1}{A} \int_{r=0}^{r=R} v(r) 2\pi r dr = \frac{2}{R^2} \int_{r=0}^{r=R} v(r) r dr \qquad \textbf{Eq. 76}$$

The relationship between the mean and the maximum velocity (K factor) is obtained by introducing **Eq. 75** into **Eq. 76**:

$$K = \frac{v_{mean}}{v_{max}} = \frac{2}{(n+1)(n+2)} \qquad \textbf{Eq. 77}$$

According to **Eq. 77**, the following table results for different exponents of the velocity profile:

Re	$4 \cdot 10^3$	$2.3 \cdot 10^4$	$1.1 \cdot 10^5$	$1.1 \cdot 10^6$	$(2 \ldots 3.2) \cdot 10^6$
n	1/6	1/6.6	1/7	1/8.8	1/10
K	0.791	0.807	0.817	0.85	0.865

Table 3: Exponent n and K factor in dependance on the Reynolds number

It is obvious that the proper choice of the exponent for the velocity profile depends on the Reynolds number. **Schlichting [80]** introduces a value of 0.8 for K in **Eq. 76** for the mean velocity and the radius (respectively the diameter) is replaced with the boundary layer thickness to obtain a relation for the wall shear stress on a flat plate:

$$\tau = 0.0225 \rho v_\infty^{\frac{7}{4}} \left(\frac{\nu}{\delta}\right)^{\frac{1}{4}} \qquad \textbf{Eq. 78}$$

This is the empirical Blasius law for the wall shear stress on a flat plate in turbulent flow which is central to all analytical calculation procedures in rotor-stator cavity problems (see e.g. **Hamkins [36], Daily and Nece [24], Schultz-Grunow [84], Owen [63]**). Since it depends on the Blasius relation correlated for pipe flows, **Eq. 78** is limited for Reynolds numbers $5 \cdot 10^5 < Re_{Plate} < 10^7$ (**Truckenbrodt [98]**) for which experiments show a good agreement with the theoretical values.
A more exact value for K in case of a 1/7 power law is apparent from Table 3. Using K=0.817 instead of K=0.8 gives:

$$\tau = 0.02335 \rho v_\infty^{\frac{7}{4}} \left(\frac{\nu}{\delta}\right)^{\frac{1}{4}} \qquad \textbf{Eq. 79}$$

The choice of the K factor is probably the reason in discrepancies for different numerical values which occurred in the literature (e.g.: 0.0225 in **Kurokawa and Toyokura [44]** or 0.0256 in **Kurokawa and Sakuma [47]**) but the majority of researchers utilizes a value of 0.0225. The advantage of **Eq. 78** is that an explicit relation for the wall shear stress can be obtained. Nevertheless, the correlation is strictly empirical which limits its range of application.

4.5 1D Flow Model for the Radial Core Rotation Distribution

A simplified flow model for the radial distribution of the core rotation factor can be deduced from **Eq. 70** under assumption of a constant value for the circumferential velocity ("mean value theorem") according to **Lomakin [54]** along the axial gap width. v_φ can then be taken outside the integral sign. The idea is that the circumferential velocity is almost constant in the core region and a significant change appears only within the thin boundary layers. The axial distance with a significant change of v_φ, compared to the region with an almost constant value, can thus be neglected. Obviously, this assumption restricts the model validity in case of stronger variations in the velocity profiles for example in case of flow regime III. Nevertheless, numerical simulations as well as numerous experimental studies have shown that this is an admissible assumption for most cases.
If the assumption of figuring out the tangential velocity in **Eq. 70** is dropped, velocity profiles have to be assumed in order to accomplish the integration across the gap width. In principle, variable limits could be used to account for geometrical changes of the cavity in radial direction. For example, the integral can be written using the interval additivity rule and assuming three layers:

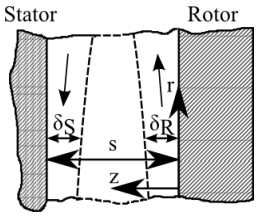

$$\int_{z=0}^{z=s} v_r v_\varphi \, dz = \int_{z=0}^{z=\delta_R} v_r v_\varphi \, dz + \int_{z=s-\delta_s}^{z=s-\delta_s} v_r v_\varphi \, dz + \int_{z=s-\delta_s}^{z=s} v_r v_\varphi \, dz \qquad \textbf{Eq. 80}$$

If the radial velocity in the core is considered as zero, the second term becomes equal to zero. The volume flow rate passing through the cavity is defined as follows:

$$Q = 2\pi r \int_{z=0}^{z=S} v_r \, dz \qquad \textbf{Eq. 81}$$

Expanding **Eq. 70** with 2π and introducing the core rotation factor leads to a differential expression for the radial gradient of the core rotation:

$$\frac{d\beta}{d\bar{r}} = \frac{2\pi b}{\dot{m}\Omega}\left(\tau_{\varphi zs} - \tau_{\varphi zR}\right) - \frac{2\beta}{\bar{r}} \qquad \textbf{Eq. 82}$$

In the previous chapter a relation for the wall shear stress on a flat plate is deduced using the pipe flow analogy. To convey this relationship to rotor-stator cavities, various adjustments are necessary:

$$\tau = \lambda \frac{\rho}{8} v_{mean}^2 \qquad \textbf{Eq. 83}$$

The mean velocity needs to be adjusted for the rotor and stator boundary layer, respectively:

$$\begin{matrix} v_{meanR}^2 = r^2\Omega^2(1-\beta)^2 \\ v_{meanS}^2 = r^2\Omega^2\beta^2 \end{matrix} \qquad \textbf{Eq. 84}$$

Introducing these results into **Eq. 82** leads to a correlation for the radial gradient of the core rotation coefficient dependent on the friction coefficients for rotor and stator:

$$\frac{d\beta}{d\bar{r}} = \frac{\bar{r}^2}{4\varphi_G}(\lambda_S\beta^2 - \lambda_R(1-\beta)^2) - \frac{2\beta}{\bar{r}} \qquad \textbf{Eq. 85}$$

For equal friction coefficients ($\lambda_R = \lambda_S$), the limits of this correlation can be easily seen by considering a vanishing small through-flow and the opposite case of an infinite high leakage:

$$\begin{matrix} \varphi_G \to 0: \quad \beta = \frac{1}{2} \to Solid\ body\ rotation\ (free\ vortex) \\ \varphi_G \to \infty: \quad \beta \cdot \bar{r}^2 = const. \to Potential\ swirl\ (forced\ vortex) \end{matrix}$$

The limits correspond to the two classical vortex distributions namely a free and a forced vortex. Especially the solid body assumption is still used today as a rough guess for estimation purposes because of its easy handling. However, solid body rotation with a core rotation of half the angular speed of the rotor is only possible in case of rotor-stator cavities with infinite radial extent (e.g. **Cooper and Reshotko [20]**). The other limit agrees with the findings from the core analysis for which the forced vortex distribution becomes dominant as the through-flow (in other words the angular momentum flux) increases. In practice the magnification of the core rotation will always be less due to the influence of friction on the bounding walls.
On the previous pages **Eq. 85** is derived directly from the basic Navier-Stokes equations using several simplifications. Usually, the derivation in the literature is performed by applying the principle of conservation of angular momentum to a cylindrical control volume (Fig. 13).

$$dM_I + dM_{Rotor} + dM_{Stator} = 0 \qquad \textbf{Eq. 86}$$

The torques on rotor and stator are formulated as follows using the above mentioned shear stress analogy:

$$dM_{Rotor} = -\lambda_R \frac{\pi}{4} \rho r^4 (\Omega - \omega)^2 dr \qquad \textbf{Eq. 87}$$

$$dM_{Stator} = -\lambda_S \frac{\pi}{4} \rho r^4 \omega^2 dr \qquad \textbf{Eq. 88}$$

Both frictional moments tend to retard the disk as long as the core rotates slower than the rotor and are therefore defined negative. In the case of core rotation higher than one, the whole flow structure is different and the flow in the rotor boundary layer becomes centripetal too. Dominant pressure forces (caused by the high rotation in the core) drive the flow radially inwards even in the Ekman layer. In this case the core tends to accelerate the rotor and therefore the sign needs to be reversed.
The change in angular momentum over the infinitesimal radius dr can be expressed as:

$$dM_I = \rho Q r(2\omega dr + r d\omega) \qquad \textbf{Eq. 89}$$

Using these three relations together with **Eq. 86** leads to **Eq. 85**. Note that this formulation does not include any effects or conditions at the outer periphery, e.g. an outer radial shroud. From the literature

review it is clear that for a cavity according to Fig. 10 a retarding influence can be present. Disk friction and axial force are essentially influenced by the flow conditions at the outer radius and therefore a correction function will be introduced later to account for the influence of a stationary outer shroud.

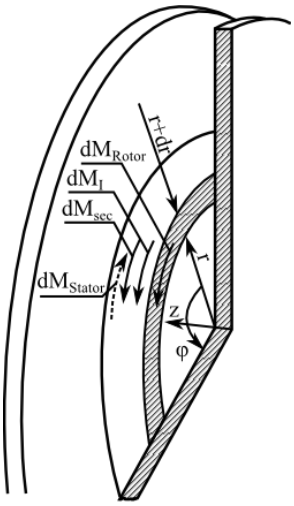

Fig. 13: Torques on an annular volume element

In general, the friction factors λ_R, λ_S are neither constant nor equal on rotor and stator. A common approach (e.g. **Schultz-Grunow [84], Daily and Nece [24], Zilling [109], Möhring [59], Senoo and Hayami [85], Kurokawa et al. [44] [47], Lauer [50]**) is the implementation of the Blasius law, discussed in the previous chapter, for a velocity distribution according to the 1/7 power law for pipe flow. Further evaluations require information about the boundary layer thickness. Commonly, the dependencies for the free disk are used. In contrast to the laminar case, the boundary layer thickness of a rotating disk in a quiescent environment under turbulent conditions is not constant, but increases with the 3/5 power of the radius (**Dorfman [29]**):

$$\delta_R = \gamma_R \cdot r^{\frac{3}{5}} \left(\frac{\nu}{\Omega}\right)^{\frac{1}{5}} \qquad \textbf{Eq. 90}$$

$$\delta_S = \gamma_S \cdot r^{\frac{3}{5}} \left(\frac{\nu}{\Omega}\right)^{\frac{1}{5}} \qquad \textbf{Eq. 91}$$

The proportionality factors are now different from the free disk value (0.526). Insertion of **Eq. 90** and **Eq. 91** into **Eq. 79** and afterwards into **Eq. 83** gives the friction factors for rotor and stator in dependency upon the local Reynolds number:

$$\lambda_R = \underbrace{\frac{0.18}{\gamma_R^{\frac{1}{4}}}}_{C_R} \cdot Re_l^{-\frac{1}{5}} \left(\frac{1}{1-\beta}\right)^{\frac{1}{4}} \qquad \textbf{Eq. 92}$$

$$\lambda_S = \underbrace{\frac{0.18}{\gamma_S^{\frac{1}{4}}}}_{C_S} \cdot Re_l^{-\frac{1}{5}} \left(\frac{1}{\beta}\right)^{\frac{1}{4}} \qquad \textbf{Eq. 93}$$

The radial gradient of the core rotation now becomes:

$$\frac{d\beta}{d\bar{r}} = \frac{\bar{r}^2}{4\varphi_G Re_l^{\frac{1}{5}}} \left(C_S \beta^{\frac{7}{4}} - C_R (1-\beta)^{\frac{7}{4}}\right) - \frac{2\beta}{\bar{r}} \qquad \textbf{Eq. 94}$$

Möhring [59] proposes the inclusion of the angular momentum difference resulting from the secondary flow on rotor and stator. The extended momentum balance is then written as:

$$dM_I + dM_{Rotor} + dM_{Stator} + dM_{secR} + dM_{secS} = 0 \qquad \textbf{Eq. 95}$$

The momentum of the secondary flow can be estimated by assuming equilibrium between the torque on the walls and the momentum difference of the secondary flow in case of zero leakage. An implementation is reasonable by increasing the frictional resistance of the casing C_S (**Möhring [59]**):

$$C_S = C_R \left(\frac{1-\beta_0}{\beta_0}\right)^{\frac{7}{4}} \qquad \textbf{Eq. 96}$$

Möhring [59] determines the constant C_R by comparison of the impeller torque with the results of **Schultz-Grunow [84]** and adjustment with his own results:

$$C_R = 0.315 \qquad \textbf{Eq. 97}$$

The dimensionless differential equation for the core rotation finally becomes:

$$\frac{d\beta}{d\bar{r}} = \frac{0.079}{\varphi_G Re_\varphi^{\frac{1}{5}}} \bar{r}^{\frac{8}{5}} \left(\left(\frac{1-\beta_0}{\beta_0}\beta\right)^{\frac{7}{4}} - \left|(1-\beta)^{\frac{7}{4}}\right| \right) - \frac{2\beta}{\bar{r}} \qquad \textbf{Eq. 98}$$

The first term on the right side prescribes the influence of friction and therefore the deviation from the free-vortex distribution. The leakage here is negative for centripetal flow. For zero through-flow, the fluid is in solid body rotation. **Zilling [109]** deduces a formula for the core rotation of the enclosed rotating disk from the torque equilibrium between the angular momentum of the core and the bounding walls which can be used to calculate β_0. For parallel walls and equal friction factors the formula is written as:

$$\beta_0 = \frac{1}{1 + \sqrt{\dfrac{\left(\frac{b+l_1}{b}\right)^5 - \left(\frac{a}{b}\right)^5 + 5\frac{s}{b}\left(\frac{b+l_1}{b}\right)^4}{1 - \left(\frac{a}{b}\right)^5 + 5\frac{s}{b}\left(\frac{a}{b}\right)^4}}} \qquad \textbf{Eq. 99}$$

In the case of solid body rotation, it is interesting to note that the core rotation only depends on geometric magnitudes. For $l_1 \approx 0$ and negligible hub radius, the formula can be further simplified:

$$\beta_0 = \frac{1}{1 + \sqrt{1 + 5\frac{s}{b}}} \qquad \textbf{Eq. 100}$$

For $b \to \infty$ (infinite disks) the fluid would rotate with half the angular velocity of the rotor according to **Eq. 100**. The calculation of the cavity flow mainly depends on the determination of the core rotation. Successively, the pressure distribution and the frictional resistance can be determined as magnitudes of engineering interest. A boundary condition for the core rotation coefficient and the leakage flow rate have to be provided for the calculation. The distribution of β can then be determined via numerical integration of **Eq. 98** which is accomplished in the present work using a fourth-order Runge-Kutta method.

4.6 New 1D Flow Model

The further considerations refer **Eq. 85** but account for different friction factors on rotor and stator.

$$\frac{d\beta}{d\bar{r}} = \frac{\bar{r}^2}{4\varphi_G}(\lambda_S\beta^2 - \lambda_R(1-\beta)^2) - \frac{2\beta}{\bar{r}} \qquad \textbf{Eq. 101}$$

In the previous chapter, a flow model is derived under assumption of the validity of the empirical Blasius law for the prescription of the wall shear stresses. The major disadvantages are that the shear stress in the viscous sublayer tends towards infinity if they are determined with this relation and a discontinuity in the middle of the pipe. Moreover, this correlation is strictly empirical and therefore limited in its application range.
A more general approach can be implied by starting from the logarithmic law of the wall which is a self-similar solution for the mean velocity parallel to the wall. It is valid in the boundary layer region outside the viscous affected sub regions and semi empirical since two constants (A^*, B^*) have to be determined from experiments.
According to **Spurk [90]** the following law known as "Van Kármán relation" can be obtained for the friction factor in smooth pipes and channels:

$$\frac{1}{\sqrt{\lambda}} = \underbrace{2.03}_{A^*} lg\left(Re\cdot\sqrt{\lambda}\right) - \underbrace{0.8}_{B^*} \qquad \textbf{Eq. 102}$$

To apply this correlation to the cavity flow, the Reynolds numbers for rotor and stator can be defined as follows in analogy to pipe flows:

$$Re_R = \frac{(\Omega-\omega)r2\delta_R}{\nu} \qquad \textbf{Eq. 103}$$

$$Re_S = \frac{\omega r2\delta_S}{\nu} \qquad \textbf{Eq. 104}$$

If the same boundary layer thicknesses are assumed as before (**Eq. 89** and **Eq. 84**), the following implicit formulas for the dependance of the friction factors with the radius can be derived:

$$\lambda_R = \frac{1}{\left[A^*\cdot lg\left[(1-\beta)Re_l^{0.8}\cdot\gamma_R 2\sqrt{\lambda_R}\right] - B^*\right]^2} \qquad \textbf{Eq. 105}$$

$$\lambda_S = \frac{1}{\left[A^*\cdot lg\left[\beta^{0.8}Re_l^{0.8}\cdot\gamma_S 2\sqrt{\lambda_S}\right] - B^*\right]^2} \qquad \textbf{Eq. 106}$$

The determination of the friction factors requires an iterative cycle as it is known for example from pipe flow calculations. The constants γ_R and γ_S can be either be determined from **Eq. 95** and **Eq. 96** or adapted by using experimental data. The friction factors for rotor and stator depend on the local Reynolds number. This agrees with the experimental study of **Itoh et al. [40]** who confirm that the velocity profiles in the boundary layers depend on the local Reynolds number.
If it is assumed that the velocity profiles evolve according to the 1/7 power law in the boundary layers then the friction coefficient Cf_{mean} can be expressed by Dean's formula (according to **Poncet et al. [71]**):

$$C_{fmean} = 0.073Re_{mean}^{-0.25} \qquad \textbf{Eq. 107}$$

Herein Re_{mean} denotes the Reynolds number based on the mean velocity at the cross-section. In the present case, the mean velocity in the Ekman layer is chosen in accordance with **Eq. 84** and the Reynolds number can be formulated as:

$$Re_{mean} = \frac{2\Omega r(1-\beta)\delta_R \rho}{\mu} \qquad \textbf{Eq. 108}$$

The characteristic length in the Reynolds number is the boundary layer thickness δ_R. The friction coefficient and thus the effective shear stress become:

$$C_{fmean} = \frac{\tau_{res}}{\frac{\rho}{2} v_{mean}^2} \sim \left(2\Omega r(1-\beta)\right)^{-\frac{1}{4}} \left(\frac{\delta_R}{\nu}\right)^{-\frac{1}{4}} \qquad \textbf{Eq. 109}$$

Due to the cross-flow, the total wall shear stress composes of a radial and a tangential component illustrated in Fig. 14. Generally, the wall shear stresses are always opposite to the direction of movement of a fluid particle.

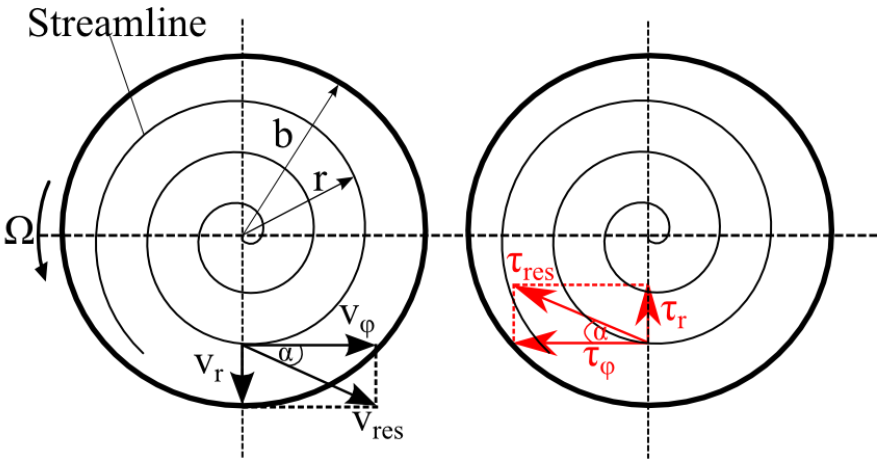

Fig. 14: Velocity and shear stress on a streamline in the rotor boundary layer

The tangential wall shear stress can be written using the angle α as:

$$\tau_\varphi = \tau_{res} cos\alpha \sim \rho\left(2\Omega r(1-\beta)\right)^{\frac{7}{4}} \left(\frac{\nu}{\delta_R}\right)^{\frac{1}{4}} \qquad \textbf{Eq. 110}$$

The radial wall shear stress is in equilibrium with the centrifugal force in a volume element with the height δ_R.

$$\tau_r = \tau_{res} sin\alpha = \rho\Omega^2 r\delta_R \qquad \textbf{Eq. 111}$$

Equating the expressions **Eq. 110** and **Eq. 111** eliminates the shear stresses and results in a general expression for the boundary layer thickness on the rotor:

$$\delta_R = A^+ \frac{r}{Re_l^{0.2}} (1-\beta)^{\frac{7}{5}} \qquad \textbf{Eq. 112}$$

This equation resembles the relation proposed by **Daily et. al. [25]**:

$$\delta_R = B^+ \frac{r}{Re_l^{0.2}} (1-\beta)^m \qquad \textbf{Eq. 113}$$

Some of the parameter combinations for the constants B^+ and m which have occurred in the literature are given in the following table:

	B^+	m
Daily et al. [25]	0.4	2
Kurokawa and Toyokura [44]	0.526	2
Kurokawa and Sakuma [47]	0.54	2.5

Table 4: Values for the parameters B and m

Almost all flow models that emerge from the integral boundary layer theory require information about the radial evolution of the boundary layer thickness on the rotating disk and the stationary casing. The boundary layer thickness essentially influences the rotation of the core and the friction coefficient. In principle, smaller boundary layer thicknesses result in higher frictional resistances because of stronger velocity gradients. Previously, an explicit expression for the rotor boundary layer thickness has been deduced from the friction coefficient for the flow over a flat plate. Several different formulations for the boundary layer thickness have occurred in the literature and some of them are mentioned in this text. Unfortunately, no experimental data are available to validate and compare these theoretical expressions.

The proportionality constant A^+ in **Eq. 112** can be determined for example by comparison with the results of **Schultz-Grunow [84]**. In the following sections, a value of A^+=0.3035 is adopted. As already briefly discussed in the description of the general flow structure, the boundary layer thickness of the disk decreases for increasing Reynolds numbers. This can also be seen from **Eq. 112** and agrees with the principal relations found by **Daily and Nece [24]**.

A relation for the radial evolution of the stator boundary layer thickness can be obtained from the continuity equation. The relation formulates under assumption of zero radial velocity in the core:

$$\int_{z=0}^{z=\delta_S} v_{rS}\, dz_S + \int_{z=0}^{z=\delta_R} v_{rR}\, dz_R = \frac{Q}{2\pi r} \qquad \textbf{Eq. 114}$$

The axial coordinates for the respective boundary layers are counted positive from the corresponding walls. To further evaluate this relation assumptions about the velocity profiles are necessary. The following profiles are assumed for the radial velocity components in the rotor and the stator boundary layer (see e.g. **Kurokawa and Sakuma [47]**):

$$v_{rS} = -a_S \beta r \Omega \left(1 - \frac{z_S}{\delta_S}\right)^n \cdot \left(\frac{z_S}{\delta_S}\right)^{\frac{1}{m}} \qquad \textbf{Eq. 115}$$

$$v_{rR} = a_R r \Omega (1-\beta) \left(1 - \frac{z_R}{\delta_R}\right)^n \cdot \left(\frac{z_R}{\delta_R}\right)^{\frac{1}{m}} \qquad \textbf{Eq. 116}$$

The radial profiles are shown in Fig. 15 for the assumption of a velocity distribution according to the 1/7 power law and two different exponents n. For the successive considerations n=2 is used since the profile appears to be closer to the actual flow physics. **Kurokawa and Sakuma [47]** for example use n=1.

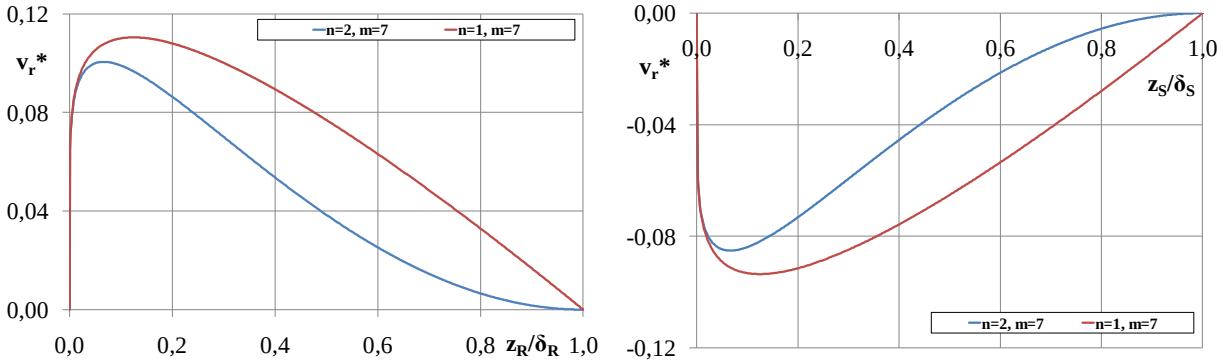

Fig. 15: Radial velocity profiles in dependance on the chosen form function

The velocity factors a_S and a_R can be determined from the empirical relations given by **Kurokawa and Sakuma [47]** based on flow angle measurements for the flow regime IV:

$$a_S = 1.03\left(\frac{Re_l}{10^5}+2\right)^{-0.387} \qquad \textbf{Eq. 117}$$

$$a_R = 1.18\left(\frac{Re_l}{10^5}+2\right)^{-0.49} \qquad \textbf{Eq. 118}$$

Several different formulations for the velocity profiles can be found in the literatures (e.g. **Daily and Nece [24], Schultz-Grunow [84], Kurokawa et al. [44] [47]**) which basically differ in the chosen form function.
Introducing these profiles in the continuity equation and solving for the stator boundary layer thickness finally yields:

$$\delta_S = A\frac{a^*}{a}\frac{(1-\beta)^{\frac{12}{5}}}{\beta}\frac{r}{Re_l^{0.2}} - \frac{Q}{C^+ a 2\pi r^2 \Omega \beta} \qquad \textbf{Eq. 119}$$

The value for the constant C^+ depends uniquely on the form function chosen and in the present case amounts to C^+=0.408. For centripetal flow, the volume flow rate is negative and therefore the stator boundary layer thickness increases since the flow passes the cavity in the vicinity of the stator.
Tests with the flow model in its original form indicate that in case of lower entrance rotation and large axial gap width, the computed curves show a slightly too strong increase in the core rotation compared to the available measurements performed by **Lauer [50]**. The decelerating effect of a radial shroud onto the core rotation, especially at the outer radius, has yet not been accounted for in the present flow model. The basic formulation of the model is derived both from the general Navier-Stokes equations as well as from the principle of conservation of angular momentum for a small cylindrical volume element. In the latter case it is clearly obvious that the influence of an outer casing is not taken into consideration. The overall decelerating influence of an outer (stationary) shroud on the core rotation can be observed for the enclosed rotating disk where usually both measured and computed values are markedly below the theoretical maximum of 0.5. If a centripetal through-flow is present, the shear stress created by the interaction of the entering leakage with the shroud gives rise to an additional "dynamic stress" whose influence decreases at lower radial locations. To include both effects in the flow model, a correction function f* for the friction factor of the stator is introduced.

$$\frac{d\beta}{d\bar{r}} = \frac{\bar{r}^2}{4\varphi_G}\left(f^* \cdot \lambda_S \beta^2 - \lambda_R (1-\beta)^2\right) - \frac{2\beta}{\bar{r}} \qquad \textbf{Eq. 120}$$

The function is defined as follows:

$$f^* = 1 + \left(\frac{s}{b + l_1 - a} + 5\bar{r}^4 \left|1 - \frac{\beta}{0.58}\right|^{\frac{6}{5}}\right) \qquad \textbf{Eq. 121}$$

The first term in the correction function can be considered as a static influence and results from the general decelerating effect of the outer shroud. The second term accounts for the dynamic influence resulting from interaction of the shroud with the leakage flow in the outer cavity region.
Zilling [109] and **Lauer [50]** account for a torque resulting from a turbulent shear stress acting on the lateral area of the control volume shown in Fig. 13. **Möhring [59]** argues that this effect can be neglected because the velocity gradient within the boundary layers in the axial direction (which determines for example the wall frictional torque) is much greater than the velocity gradient in the radial direction responsible for the turbulent shear stress.

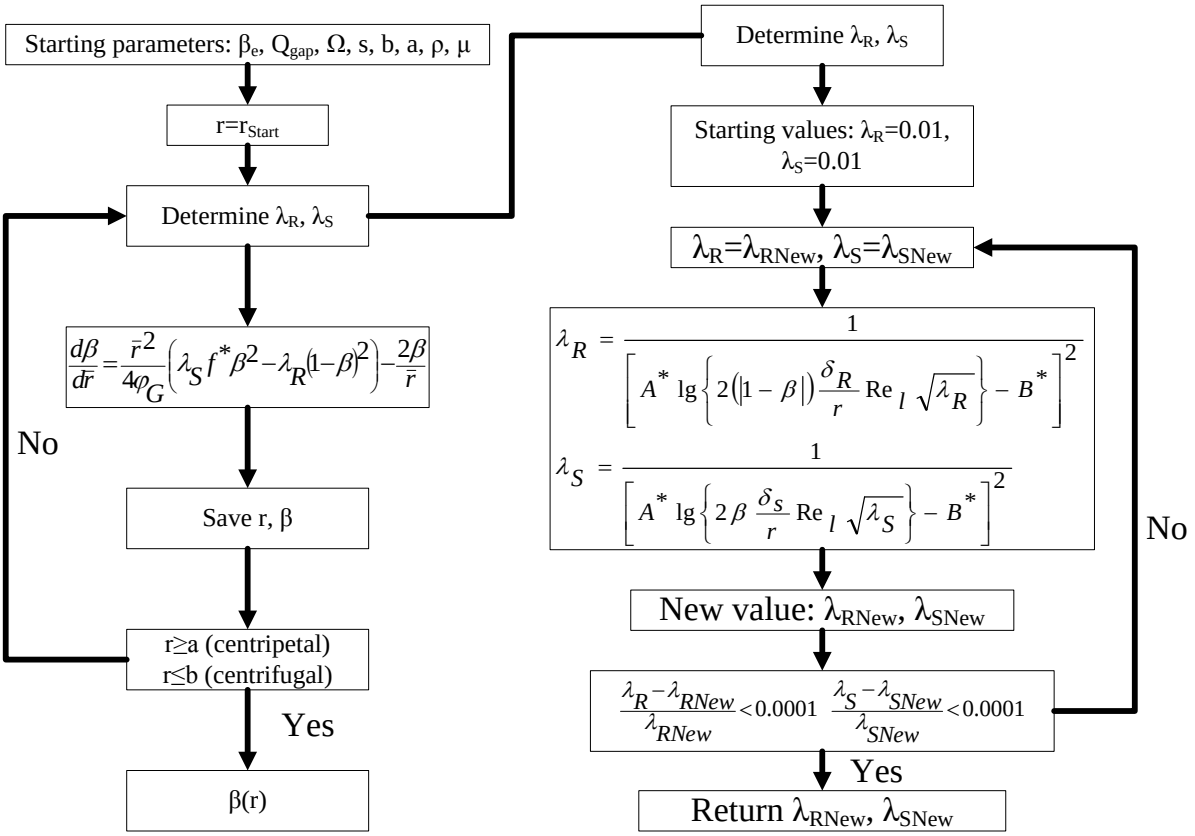

Fig. 16: Solution procedure for β(r)

The flow model according to **Eq. 98** and the proposed modified form are applicable for both centripetal ($\varphi_G>0$) and centrifugal ($\varphi_G<0$) flow directions. Moreover, the model can principally handle values for the core rotation greater than one. In this case, the core rotates faster than the impeller at inner radii for a centripetal through-flow. However, for rotation faster than the disk the assumptions in the theoretical derivation are no longer valid. Nevertheless, the outer radius is by far the dominant region with respect to disk friction and axial force.

4.7 Comparison with Experimental Results

Lauer [50] examines the flow in the impeller side gap with respect to the influence of the cavity anteroom. In his experiments, he measures the radial core rotation distribution using Laser-Doppler Anemometry. These results are used for comparison with the theoretical model because the "non-invasive" measuring technique does not introduce errors resulting from a velocity probe in the flow field. The comparisons for the plane rotor-stator cavity include different leakage flow rates, gap widths and entrance rotation values as they typically occur in centrifugal pumps. In addition, the calculated curves from the flow models of **Möhring [59]** and **Kurokawa and Sakuma [47]** are included.
A drawing of the investigated cavity with different axial gap distances is given in the following figure.

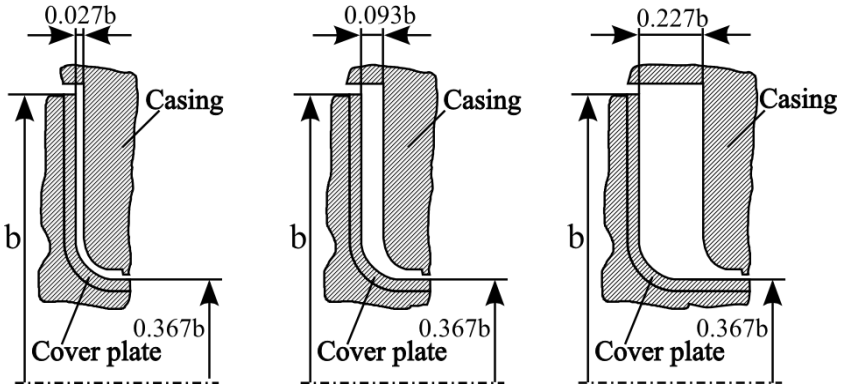

Fig. 17: Different gap sizes experimentally investigated by Lauer [50]

The different parameter variations used for comparisons are outlined in Table 5.
One dimensional flow models can also be used to predict the frictional resistance of the rotating surface. Unfortunately, not many results are available for comparison. Some comparisons with the torque obtained from the CFD simulation will be given in the discussion of the flow in the centrifugal pump later in chapter 5.

Re_φ	G	φ_G
$3.5 \cdot 10^6$	0.027	0.0003
		0.0006
		0.0009
	0.093	0.0003
		0.0006
		0.0009
	0.227	0.0003
		0.0006
		0.0009

Table 5: Experimentally investigated parameter combinations by Lauer [50] used for the computational results in Table 7

The comparison shows a significant improvement in the case of increasing gap widths. Especially at the outer radius, which is of predominant importance for the resulting axial force and the frictional resistance, the modified model yields better results. In the formulation of **Möhring [59]**, the influence of the gap width in terms of β_0 is overrated and the calculated curves are considerably smaller than the experimental data.
In order to demonstrate the versatility of the method, the model has been used to determine the core rotation and the resulting pressure distribution in the front side chamber of a radial compressor. Note that this particular study extends the usually investigated range of circumferential Reynolds numbers. The pressure measurements have been performed at the Siemens Company in Duisburg / Germany in a research project primarily devoted to acoustic resonances occurring in the side chambers. Details about the compressor and the test rig, as well as further information, can be found in **Petry et al. [70]**. The basic test rig parameters and a sketch of the compressor are given in Table 6 and Fig. 18 respectively.

Number of impeller blades	17
Number of diffuser vanes	10
Number of inlet guide vanes	18
Number of return guide vanes	22
Outer diameter of the impeller	350 mm
Max. speed of rotation	15900 rpm
Circumferential Reynolds number Re_φ (π=1)	$5 \cdot 10^7$
Circumferential Reynolds number Re_φ (π=1.2)	$5.3 \cdot 10^7$
Circumferential Reynolds number Re_φ (π=1.3)	$5.3 \cdot 10^7$

Table 6: Test rig parameters of the centrifugal compressor

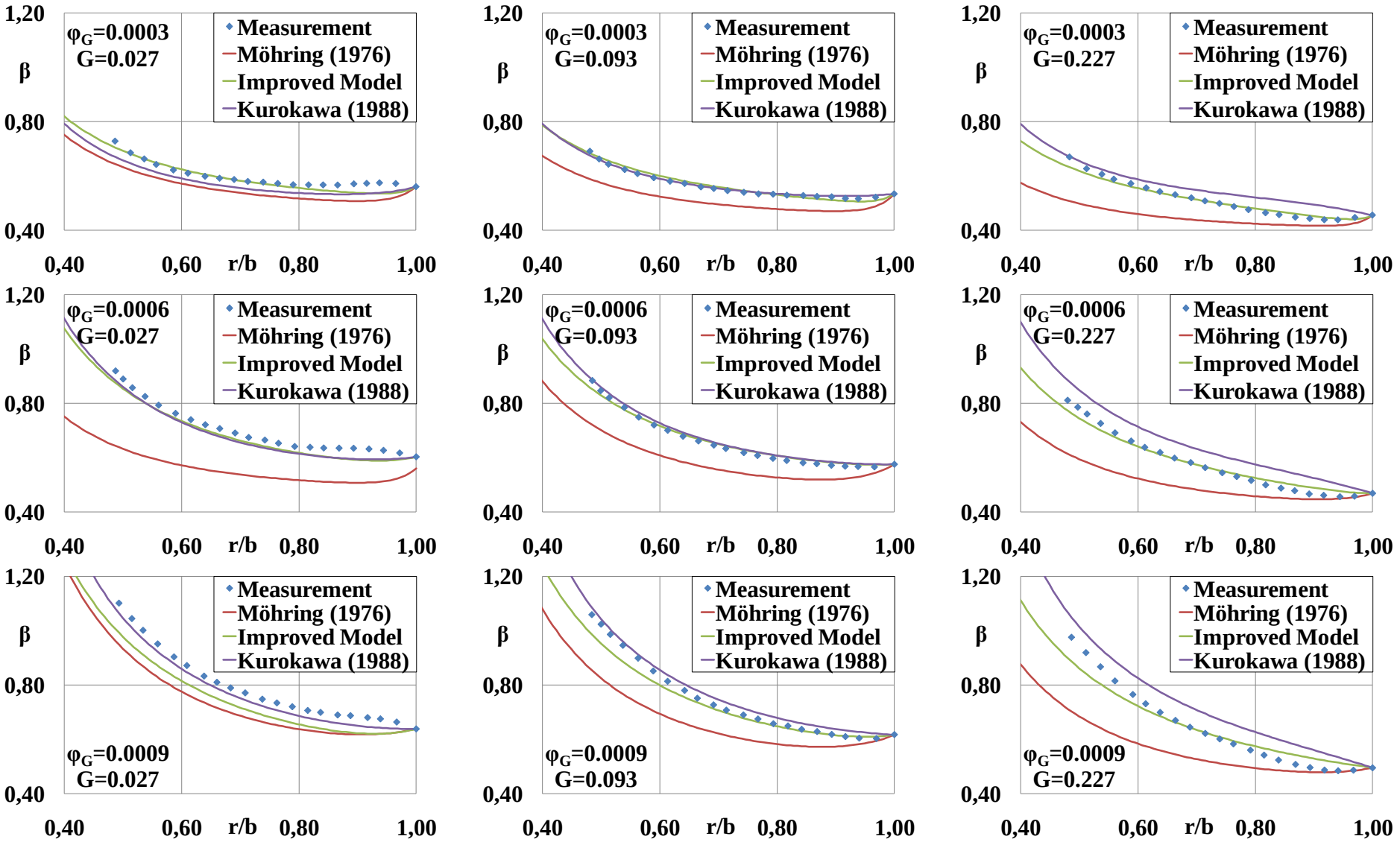

Table 7: Comparison of the radial core rotation distribution for different flow models (Eq. 120, Kurokawa and Sakuma [47], Möhring [59]) and parameter combinations

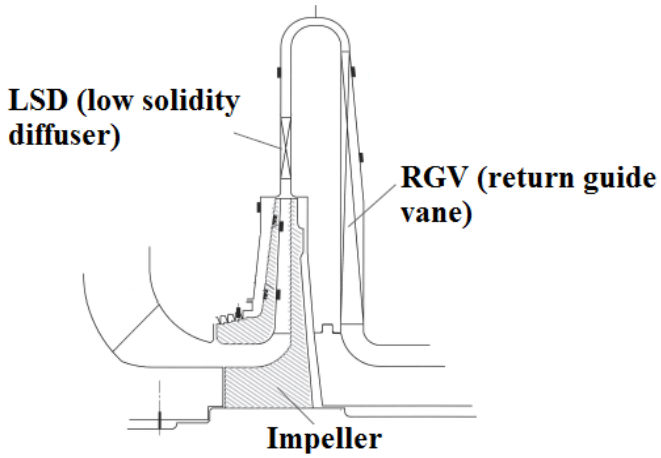

Fig. 18: Sketch of the compressor stage

The outer boundary condition for the core rotation is set equal to the corresponding value at the impeller outlet due to absence of additional information. The source of this value is an internal Siemens design code. Further, the leakage is determined using the measured pressures in front of and behind the labyrinth seal with an internal calculation method.
The results calculated with **Eq. 120** indicate a good agreement with the measured points for all three investigated pressure ratios of the stage (Fig. 19). It is clearly noticeable that the pressure profile is more curved for the higher pressure ratios while for the "blue" curve the pressure decreases almost linearly with the radius. The reason is that the leakage respectively the angular momentum flux in the front side chamber increases for higher pressure ratios. This leads to a sharper pressure drop towards the inner radii. It must be mentioned at this point that the side gap width is not constant. At the outer radius, the axial distance between the rotating and the stationary wall amounts to 9.5mm and decreases to 6.6mm close to the hub. As already pointed out, the larger radii are mostly responsible for the frictional torque and the axial force. Therefore, the axial gap width is assumed to have a constant value of 9.5mm for the calculation. The results give further evidence that the circumferential velocity at the impeller outlet is a sufficient estimate in the present configurations for the radial boundary condition due to the very close overlap of the radial casing and the outer impeller shroud. Further on, the leakage flow rate in the side chamber comes directly from the impeller outlet in contrast to the centrifugal pump investigated later on.
In modern centrifugal compressors, very high circumferential Reynolds numbers can be present. At the present state, not much is known about the flow structure under these conditions. However, high Reynolds numbers represent an increased ratio of inertia to viscosity forces. If other parameters such as the entering angular momentum flux increase less compared to the Reynolds number, then the flow structure is likely to approach a state similar to a solid body rotation which would be very convenient with respect to an analytical calculation.

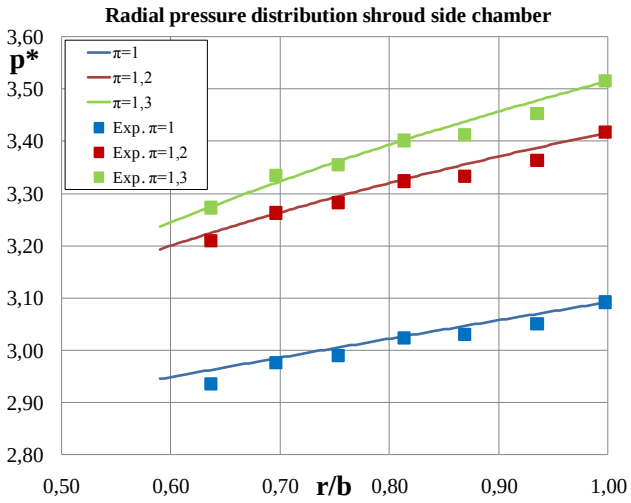

Fig. 19: Radial pressure distributions in the front side chamber of a radial compressor for three pressure ratios

4.8 Boundary Conditions for the Flow Models

The above presented flow models allow for a simplified calculation of the flow in rotor-stator cavities assuming that a flow structure with separated boundary layers establishes. However, the use of these models requires adequate input parameters such as the entrance rotation of the fluid and the leakage flow rate that must come from the outer flow field. In contrast to the centrifugal flow case, the leakage can contain a considerable amount of angular momentum in case of centripetal flow direction. This originates from the circumferential velocity component of the main flow and has a severe effect on the overall flow conditions.

If the pressure has to be determined, the entrance pressure is additionally required as a boundary condition for the differential equation that relates the radial pressure to the core rotation. In summary, three parameters are required (β_e, φ_G, p_e) and the quality of the solution depends strongly on the accuracy of the available boundary information. Since the pressure and the leakage are strongly dependent on each other, an iterative procedure is necessary to determine both the pressure distribution and the leakage flow rate emerging from an assumed, initial radial pressure profile.

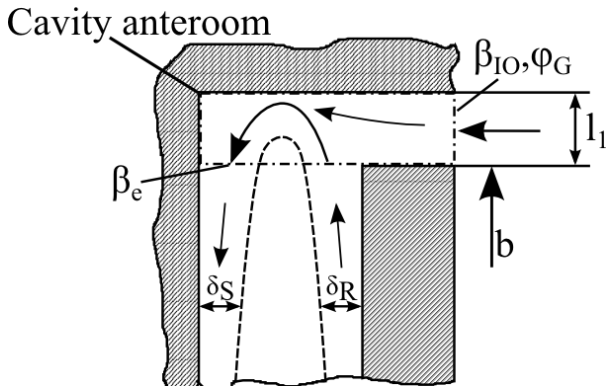

Fig. 20: Entrance conditions for the enclosed rotating disk model

The idealized rotating disk model with a cylindrical casing does not accurately represent the flow conditions in all real machines. The reason is that, depending on the type of machine, many different geometrical configurations can occur at the outer radius that determine the coupling of the side chamber flow with the flow in the adjacent components. For example, the inflow conditions for a centrifugal pump with spiral casing are strongly affected by the secondary flow in the volute.

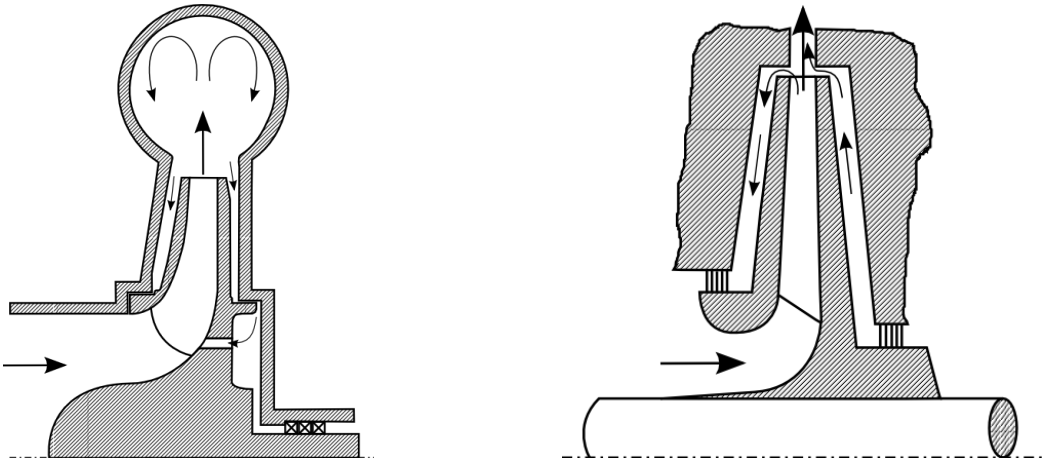

Fig. 21: Typical geometrical configuration for a centrifugal pump with volute casing (left) and a compressor stage (right)

In centrifugal compressors, the side cavities are more isolated due to the narrow gap between the outer shroud of the rotor and the casing. Consequently, the inflow conditions on the shroud side are mainly determined by the impeller outflow which resembles the rotating disk model with conical casing depicted in Fig. 20 more closely.

Usually, only the circumferential velocity component of the fluid at the impeller outlet is known. This velocity component does not necessarily agree with the component at the inlet of the cavity required for the calculation procedure in all cases. For example, **Lauer [50]** shows that the cavity anteroom can have a severe influence on the velocity component depending on the inflow parameters. For a geometry similar to Fig. 20, he gives the following empirical relation between the fluid rotation at the impeller outlet and the entrance condition in the side chamber:

$$\beta_e - \beta_{IO} = \beta_{IO}(125.7\varphi_G - 0.72) - 38.9\varphi_G + 0.33 \qquad \textbf{Eq. 122}$$

Other methods to determine the entrance swirl are summarized by **Wiederuh and Lingelbach [101]**. All models apply for a geometry similar to Fig. 20 but with a large general scatter in the results. However, due to the absence of suitable experimental data, no general conclusion about the accuracy can be drawn.

The influence of the cavity anteroom has been investigated numerically using the commercial CFD code Fluent 6.3.24. A reference case has been an experimental setup studied by **Schubert [83]**. The computational domain including the grid is shown in Fig. 22.

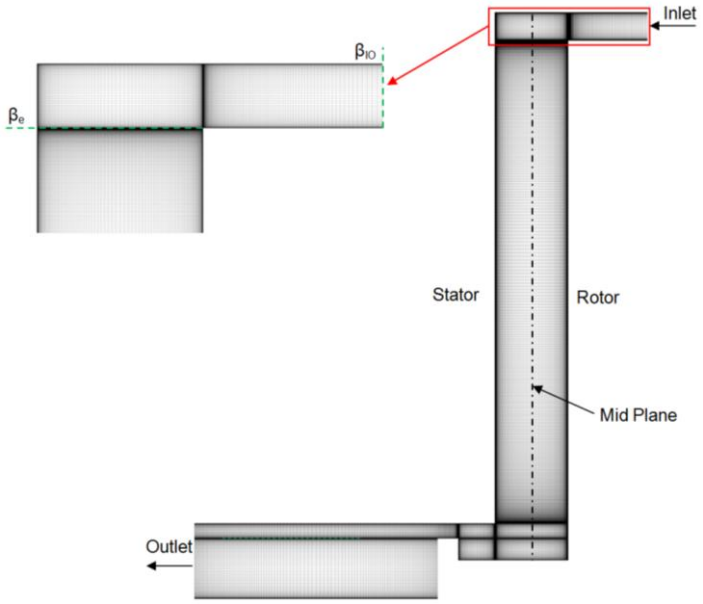

Fig. 22: Numerical model for the cavity according to Schubert [83]

To ensure grid independance, several different dense meshes have been tested. The final mesh consists of 197800 cells and ensures that y+ is about one for the first wall adjacent grid point on rotor and stator in order to resolve the boundary layers. The leakage flow enters the cavity at the upper right and leaves at the lower left so that a centripetal through-flow establishes. At the inlet, the axial and the angular velocity components are specified. Due to absence of detailed information at the outlet, a pressure outlet boundary condition with a target mass flow rate is used. Then, the exit pressure is automatically calculated to satisfy the specified mass flow rate. The pressure based segregated solver is applied with a SIMPLE scheme for the pressure velocity coupling. Spatial discretization is of second order. To model turbulence, two variants of the RSM are used, namely the linear pressure-strain and the omega-stress variant. Table 8 shows the two investigated configurations for different values of the incoming swirl β_{IO}:

$\beta_{IO} = 0.43$	$\beta_{IO} = 1.63$
$\varphi_G = 0.000462$	
$Re_\varphi = 2.51 \cdot 10^6$	
$G = 0.0972$	

Table 8: Computed configurations

The entrance rotation values determined from the CFD calculations and **Eq. 121** are summarized in Table 9:

	$\boldsymbol{\beta_{IO} = 0.43}$	$\boldsymbol{\beta_{IO} = 1.63}$
CFD (RSM - linear pressure strain)	$\beta_e = 0.496$	$\beta_e = 0.59$
CFD (RSM - omega stress)	$\beta_e = 0.41$	$\beta_e = 0.79$
Eq. 121 according to **Lauer [50]**	$\beta_e = 0.457$	$\beta_e = 1.28$
Experiment **Schubert [83]**	$\beta_e = 0.45$	$\beta_e = 0.98$

Table 9: Calculated entrance rotation values

In the moderate entrance swirl case, the tangential fluid velocity changes only slightly across the cavity anteroom. A greater scatter is present in the case of strongly rotating inward leakage. Fig. 23 compares the computed stream functions. Both cases show a noticeable change of the flow structure in the cavity anteroom, near the shroud of the rotor. In the case of moderate incoming swirl, the flow structure at the outer radius between rotor and stator is not much affected by the incoming flow. The accelerating (rotor shroud) and decelerating (radial casing) friction forces are almost in equilibrium in the anteroom since the relative velocities are approximately equal. As a result, the boundary value for the calculation does not differ significantly from the inlet value. It can be further noticed that the entering flow is slightly accelerated for β_{IO}=0.43. The counter rotating structures between the shroud of the rotor and the cylindrical casing in this case are called Taylor vortices and result from the principle instability of the flow in this region. A more detailed explanation about this phenomenon will be given later.
In contrast, the whole upper region is affected by the entering volume flow in case of very strong inlet rotation. The incoming fluid is immediately entrained into the radial casing boundary layer because of dominant centrifugal forces. Both bounding walls (the shroud of the rotor and the radial casing) have now a decelerating effect on the flow and therefore a strong gradient of the circumferential velocity in axial direction establishes.

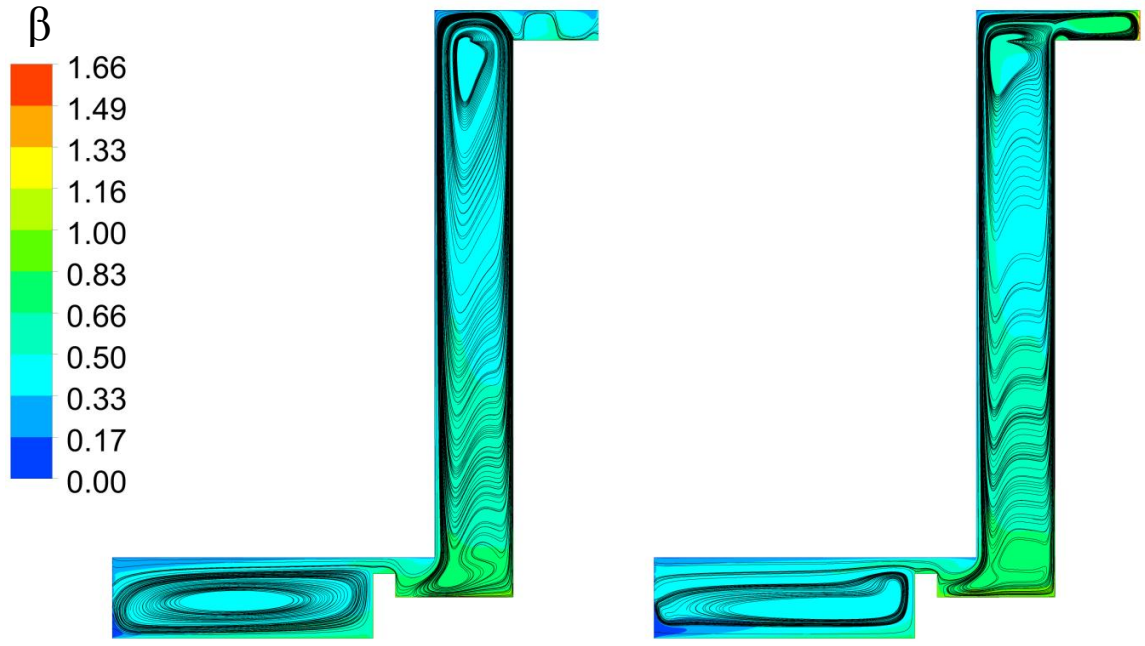

Fig. 23: Stream functions and contours of the core rotation (RSM - linear pressure-strain model) for β_{IO}=0.43 (left) and β_{IO}=1.63 (right)

For a configuration such as the one depicted in Fig. 22, one can assume that the fluid rotation does not change significantly along the cavity anteroom as long as the accelerating and decelerating forces are in equilibrium. This is the case when the relative velocities between incoming fluid and impeller shroud as well as incoming fluid and stationary radial casing are approximately equal. This condition is exactly fulfilled for β_{IO}=0.5. However, for increasing through-flow rates, inertial effects increase too because the time which a fluid particle is exposed to the shear forces decreases. Because of this, the

change in the fluid velocity is less marked. In summary, the investigated cavity anteroom has a homogenizing effect on the flow. For strong inflow rotation the flow is retarded. Otherwise it is accelerated. As pointed out before, the major parameter for the flow is the angular momentum flux entering the side cavity. Moreover, the choice of the turbulence model significantly affects the results. Fig. 24 displays the results for the two turbulence models and the measured values from **Schubert [83]**.

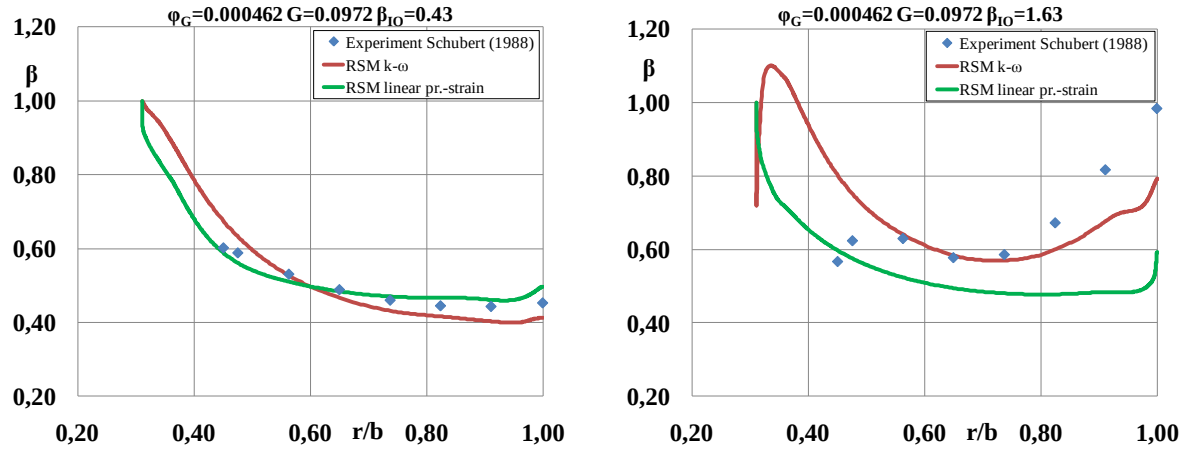

Fig. 24: Comparison between linear pressure-strain RSM and omega-stress model

For moderate entrance rotation both models give quite comparable results and it seems that they actually cover the flow physics correctly. For very strong inlet swirl, much greater deviations are observable. The omega-stress model predicts a stronger gradient especially at the outer radius which approaches the measured data. However, the measurements are performed with a velocity probe and the accuracy of applying such a method for strongly rotating flows is questionable.

4.9 Pressure Calculation

The radial pressure distribution on the rotating disk is one of the most important magnitudes for engineering purposes in radial turbomachinery. Integrating the pressure distribution in the radial direction yields the corresponding axial force. Especially in case of separated boundary layers, the pressure and the core rotation are inseparably coupled. To derive an equation for the pressure distribution, it is convenient to accomplish a force balance for a small annular fluid element shown in Fig. 25.

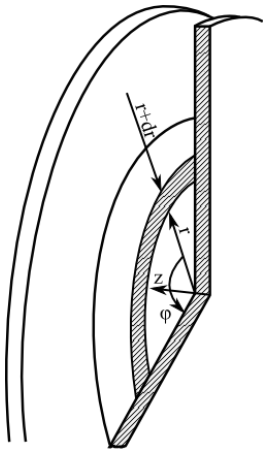

Fig. 25: Small annular fluid element in a rotor-stator cavity

The force balance can be expressed as:

$$\underbrace{pA_1 - \left(p + \frac{\partial p}{\partial r}dr\right)A_1}_{Pressure\ forces} + \underbrace{I - \left(I + \frac{\partial I}{\partial r}dr\right)}_{Momentum\ forces} + \underbrace{dm \cdot r\omega^2}_{Centrif.\ force} + \underbrace{\tau'}_{turb.\ shear\ stress} dA_2 = 0 \qquad \textbf{Eq. 123}$$

Simplifying the relation by canceling out identical terms leads to:

$$\frac{\partial p}{\partial r} dr A_1 + \frac{\partial I}{\partial r} dr + dm \cdot r\omega^2 + \tau' dA_2 = 0 \qquad \textbf{Eq. 124}$$

The following identities are valid for the momentum, the gradient of the momentum in radial direction and the mass of the element:

$$\begin{aligned} I &= \rho A_1 v_r^2 = 2\pi\rho r dz v_r^2 \\ \frac{\partial I}{\partial r} &= 2\pi\rho dz \frac{\partial (r v_r^2)}{\partial r} \\ dm &= \rho A_1 dr \\ A_1 &= 2\pi r s \\ dA_2 &= 2\pi r dr \end{aligned} \qquad \textbf{Eq. 125}$$

Neglecting the turbulent shear stress and introducing the foregoing expression yields the following relation for the radial pressure gradient:

$$\frac{\partial p}{\partial r} = \rho \left[\frac{v_\varphi^2}{r} - \frac{1}{r} \frac{\partial (r v_r^2)}{\partial r} \right] \qquad \textbf{Eq. 126}$$

Expanding the gradient on the right hand side leads to:

$$\frac{\partial p}{\partial r} = \rho \left[\frac{v_\varphi^2}{r} - v_r \left(\underbrace{\frac{\partial v_r}{\partial r} + \frac{v_r}{r}}_{=0\ (Continuity\ equation)} + \frac{\partial v_r}{\partial r} \right) \right] \qquad \textbf{Eq. 127}$$

Since the continuity equation is identically zero, the pressure gradient in radial direction becomes:

$$\frac{\partial p}{\partial r} = \rho \left(\frac{v_\varphi^2}{r} - v_r \frac{\partial v_r}{\partial r} \right) \qquad \textbf{Eq. 128}$$

This equation is identical to **Eq. 61** obtained directly from the radial momentum equation.
In a rotor-stator cavity, the cross sectional area changes in radial direction. Consequently, the pressure must also change since the mean velocity changes in radial direction according to the continuity equation. For centrifugal through-flow direction, the cross sectional area increases and the mean radial velocity decreases (radial diffuser effect). In the contrary case, the mean radial velocity increases towards smaller radii. The radial velocity can be replaced using the leakage flow rate $\left(v_r = \frac{Q}{A} = \frac{Q}{2\pi r s}\right)$ and the circumferential velocity component can be replaced using the core rotation coefficient:

$$\frac{\partial p}{\partial r} = \rho \beta^2 \Omega^2 \mathrm{r} + \frac{\rho \mathrm{Q}^2}{4\pi^2 \mathrm{s}^2 \mathrm{r}^3} \qquad \textbf{Eq. 129}$$

Integrating between r=b and r=r leads to:

$$p(r) = p(b) + \frac{\rho Q^2}{8\pi^2 s^2 b^2} \left[1 - \frac{b^2}{r^2} \right] + \rho \Omega^2 \int_b^r r \beta^2 dr \qquad \textbf{Eq. 130}$$

If dimensionless quantities are introduced the equation is transformed to:

$$\Delta\bar{p}(r) = \underbrace{\frac{\varphi_G^2}{4G^2}\left[1 - \frac{1}{\bar{r}^2}\right]}_{leakage\ flow} + \underbrace{2\int_1^{\bar{r}} \bar{r}\beta^2 d\bar{r}}_{core\ rotation} \qquad \textbf{Eq. 131}$$

Herein, the dimensionless pressure $\Delta\bar{p}$ (similar to **Eq. 34**) is defined as:

$$\Delta\bar{p}(r) = \frac{p(r) - p(b)}{\frac{\rho}{2}\Omega^2 b^2} \qquad \textbf{Eq. 132}$$

The first term on the right hand side of **Eq. 131** accounts for the influence of the leakage flow magnitude on the pressure distribution. The second term covers the influence of the core rotation. For small leakage flow rates, the first term is expected to be much smaller than the second one and the equation simplifies to the well known radial equilibrium relation:

$$\Delta\bar{p}(r) = 2\int_1^{\bar{r}} \bar{r}\beta^2 d\bar{r} \qquad \textbf{Eq. 133}$$

To solve the integral, the radial distribution of the core rotation factor has to be known. Since this is the major parameter in case of flow regime IV, analytical flow models focus on the prediction of this parameter. Assuming that the fluid rotates as a solid body with a constant angular velocity, the pressure distribution becomes a quadratic function with the radius since β can be taken out of the integral sign.

4.9.1 Influence of a Through-flow on the Pressure Distribution

In principle, the pressure distribution is determined from the rotation of the fluid in the side gap and the leakage flow rate. To distinguish between the relevance of these two parameters, the inviscid flow between two concentric disks is considered. With this assumption, the pressure distribution and the axial force can be evaluated analytically allowing for a relative comparison of the influence of the through-flow and the fluid rotation. Disregarding the frictional influence excludes the formation of boundary layers on the walls and therefore disk rotation is of no influence. An externally applied momentum flux causes the inviscid fluid to evolve according to a free vortex since no other velocity distribution is compatible when a radial velocity component is present. For the sake of comparison, CFD solutions of the Euler equations have been obtained on an axis symmetric setup shown in the following figure.

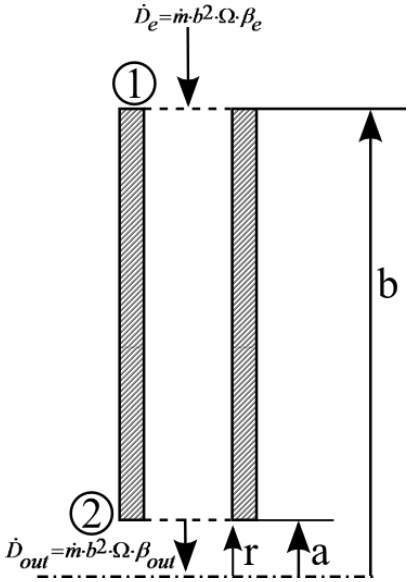

Fig. 26: Coaxial disks with entering and exiting angular momentum flux

The pressure drop resulting from a potential swirl velocity distribution is the theoretical upper limit that can occur. Consequently, the resulting axial force is minimal. According to the potential swirl, the core rotation evolves radially according to the following formula:

$$\beta(r) = \beta_e \frac{b^2}{r^2} \qquad \textbf{Eq. 134}$$

The axial force results from the integration of the pressure distribution across the radius:

$$F_{ax} = 2\pi \int_{r=a}^{r=b} p(r) r dr \qquad \textbf{Eq. 135}$$

For a circumferential velocity distribution according to a free vortex, the radial pressure distribution becomes (see **Eq. 130**):

$$p(r) = p_e + \frac{\rho}{2}\beta_e^2 \Omega^2 \mathrm{b}^2 \left(1 - \frac{\mathrm{b}^2}{\mathrm{r}^2}\right) + \frac{\rho}{8}\frac{Q^2}{\pi^2 s^2}\left(\frac{1}{b^2} - \frac{1}{r^2}\right) \qquad \textbf{Eq. 136}$$

Consequently, the corresponding axial force writes:

$$\begin{aligned} F_{ax} = \pi p_e (b^2 - a^2) + \frac{\rho}{2}\pi\beta_e^2\Omega^2\mathrm{b}^2(b^2 - a^2) - \rho\pi\beta_e^2\Omega^2\mathrm{b}^4\left(\ln\frac{\mathrm{b}}{\mathrm{a}}\right) \\ + \frac{\rho}{8}\frac{Q^2}{\pi b^2 s^2}(b^2 - a^2) - \frac{\rho}{4}\frac{Q^2}{\pi s^2} ln\left(\frac{b}{a}\right) \end{aligned} \qquad \textbf{Eq. 137}$$

If the through-flow is omitted, the pressure distribution can be simplified to:

$$p(r) = p_e + \frac{\rho}{2}\beta_e^2 \Omega^2 \mathrm{b}^2 \left(1 - \frac{\mathrm{b}^2}{\mathrm{r}^2}\right) \qquad \textbf{Eq. 138}$$

Accordingly, the axial force now becomes:

$$F_{ax} = \pi p_e (b^2 - a^2) + \frac{\rho}{2}\pi\beta_e^2\Omega^2\mathrm{b}^2(b^2 - a^2) - \rho\pi\beta_e^2\Omega^2\mathrm{b}^4\left(\ln\frac{\mathrm{b}}{\mathrm{a}}\right) \qquad \textbf{Eq. 139}$$

Both formulas highlight that at least the entrance pressure and the radial core rotation distribution are necessary to evaluate the axial force, even for an inviscid flow. To account for the influence of the radial velocity component on the pressure, the leakage flow rate must be known.
Numerical calculations solving the inviscid Euler equations have also been performed to verify the validity of the previously derived equations. At the domain entrance (position 1), the radial and circumferential velocity components are specified while at the exit (position 2) the static pressure is given as the boundary condition. The inviscid flow between two parallel, coaxial disks is a flow with constant total pressure and Bernoulli's equation can be used to relate pressure and velocity between the entrance and the exit of the computational domain:

$$p + \frac{\rho}{2}v^2 = const. \rightarrow p_1 = p_2 + \frac{\rho}{2}(v_2^2 - v_1^2) \qquad \textbf{Eq. 140}$$

The absolute velocity in the present case is comprised of a radial and a tangential component:

$$v^2 = v_r^2 + v_\varphi^2 \qquad \textbf{Eq. 141}$$

The component $v_{\varphi 2}$ can be expressed with the potential swirl distribution. This yields for the entrance pressure:

$$p_1 = p_2 + \frac{\rho}{2}\left[\left(v_{r2}^2 + v_{\varphi 1}^2 \frac{b^2}{a^2}\right) - \left(v_{r1}^2 + v_{\varphi 1}^2\right)\right] \qquad \textbf{Eq. 142}$$

This equation can be used to determine the pressure at the entrance of the domain knowing the values of the velocity components at this position. The radial velocity component at position 2 simply follows from the continuity equation:

$$v_{r2} = v_{r1} \frac{b}{a} \qquad \textbf{Eq. 143}$$

The results for the axial force obtained from **Eq. 137** almost exactly agree with the numerical solution while the deviations for **Eq. 139** increase with increasing through-flow. For this reason, **Eq. 137** can be termed as an exact solution for the inviscid flow case.
A comparison between the two analytical formulas (**Eq. 136** and **Eq. 140**) for the radial pressure distributions has been accomplished using the boundary conditions from the centrifugal pump described later on. Two parameters are checked. First, the circumferential velocity is halved successively. Secondly, the mass flow rate, respectively the radial velocity component at the cavity entrance, is successively doubled. The resulting pressure distributions are shown in Table 10 in dependance on the velocity ratio at the cavity entrance.
The curves show the expected decrease for smaller radii. If the circumferential velocity is decreased and the mass flow rate kept constant, the resulting pressure distribution flattens. The differences between the two equations remain negligible since the same parameter is changed in both equations. In the other case, when the leakage flow rate is increased, the deviations becomes greater with increasing $v_{re}/v_{\varphi e}$ ratio.

Decrease of the tangential velocity component ($v_{\varphi e}$)	Increase of the leakage flow (v_{re})	$v_{re}/v_{\varphi e}$
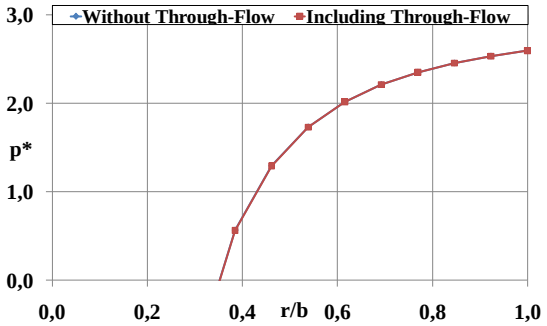	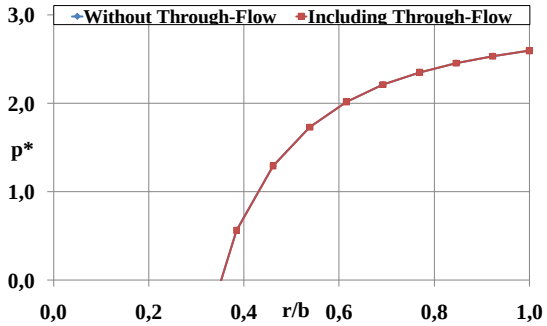	0.03876
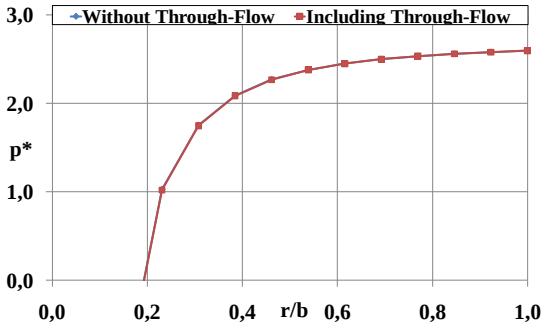	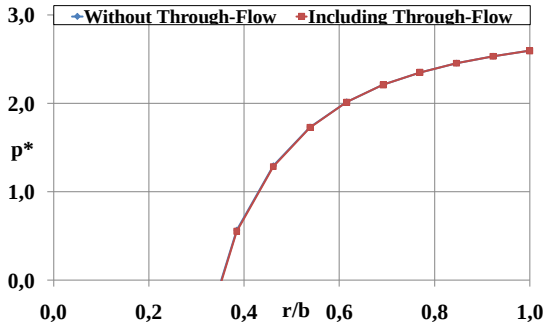	0.0775

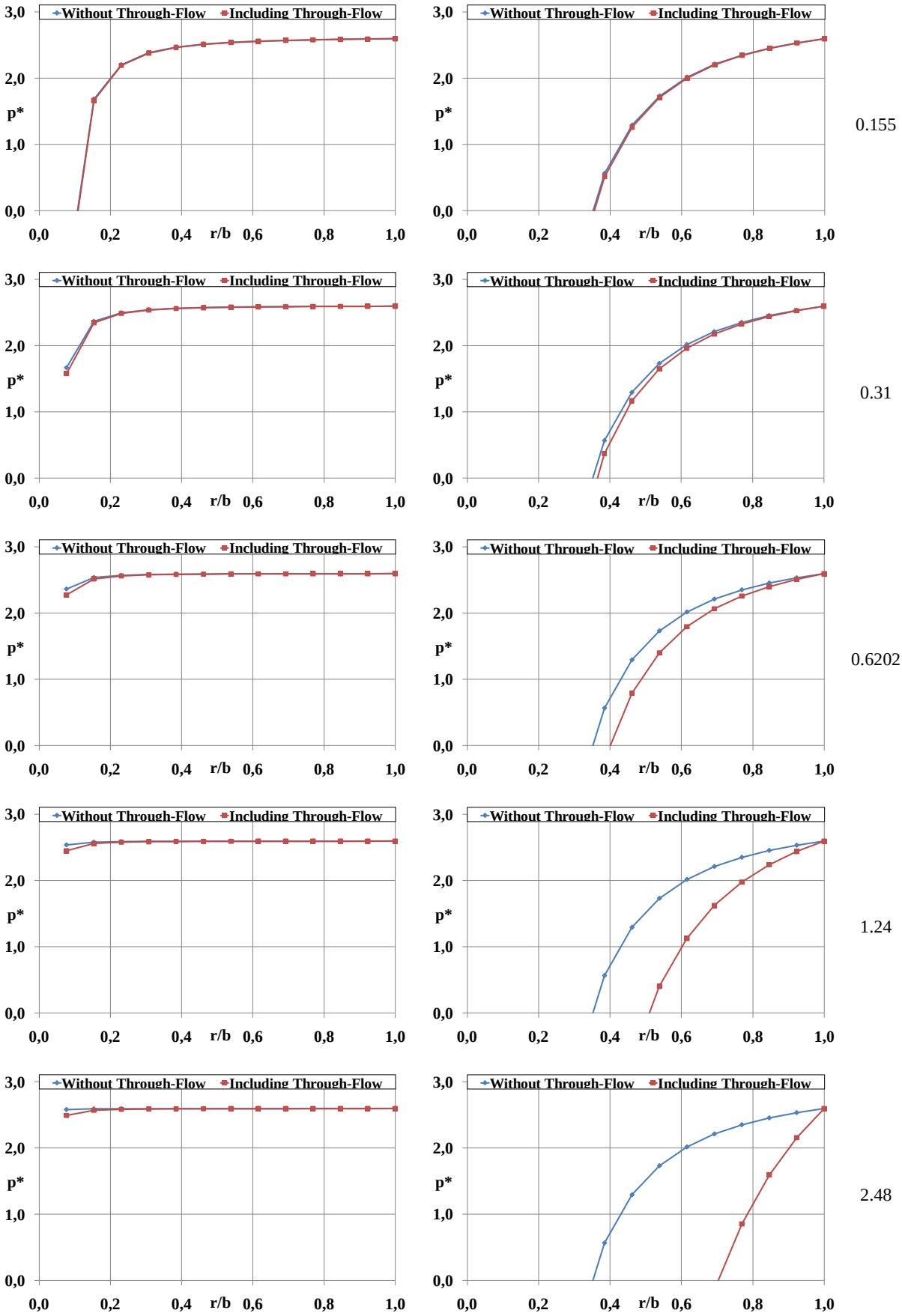

Table 10: Influence of the through-flow on the pressure distribution (without through-flow: Eq. 138, with throughflow: Eq. 136)

In the majority of practical cases, the ratio $v_{re}/v_{\varphi e}$ will be small. According to the previous results, the validity of the radial equilibrium relation is confirmed for practical applications. The resulting axial forces are summarized in the next two tables.
The error resulting from omitting the radial through-flow on the pressure distribution is shown in Fig. 27. Greater errors in the resulting axial force are apparent only for large leakage flow rates. If the tangential velocity at the inlet is decreased, the pressure distribution flattens and the characteristic curve evolution vanishes. The resulting error is comparatively small and remains approximately constant because the lowering of the circumferential velocity influences both equations.

Decreasing $v_{\varphi e}$			
$v_{re}/v_{\varphi e}$	F [N] (without through-flow)	F [N] (incl. through-flow)	Relative Error [%]
0.03876	8319.4	8318.1	0.015626127
0.0775	8970.3	8969	0.014492269
0.155	9133.09	9131.8	0.014124464
0.31	9173.77	9172.49	0.013952824
0.62	9183.95	9182.66	0.014046244
1.24	9186.49	9185.2	0.01404236
2.48	9187.12	9185.84	0.013932549

Table 11: Axial force in dependance on the velocity ratio for decreasing v_{φ}

Increasing v_{re}			
$v_{re}/v_{\varphi e}$	F [N] (without through-flow)	F [N] (incl. through-flow)	Relative Error [%]
0.03876	8319.4	8318.1	0.015626127
0.0775	8319.4	8314.27	0.061663101
0.155	8319.4	8298.83	0.247253408
0.31	8319.4	8237.05	0.989855038
0.62	8319.4	7989.95	3.960021155
1.24	8319.4	7001.53	15.84092603
2.48	8319.4	3047.88	63.36418492

Table 12: Axial force in dependance on the velocity ratio for increasing v_r

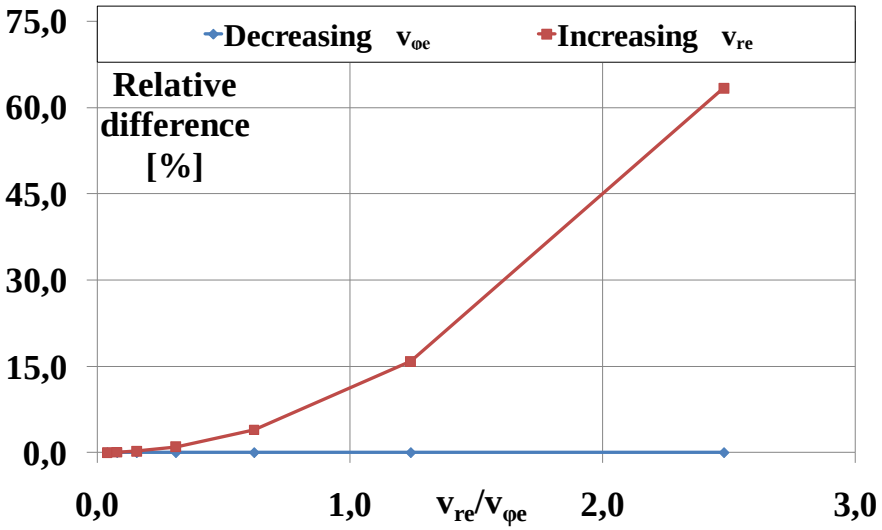

Fig. 27: Influence of the velocity ratio on the error on the calculated axial force

4.9.2 Radial Equilibrium

If the influence of a superposed through-flow is neglected on the pressure distribution, the formula for the radial gradient of the pressure writes:

$$\frac{\partial p}{\partial r} = \rho \frac{v_\varphi^2}{r} \qquad \textbf{Eq. 144}$$

The equation holds in the frictionless core region and states that pressure and centrifugal forces balance each other. This relation is central to the calculation of the resulting pressure distribution from a known core rotation distribution. If the core rotation distribution is calculated using one of the above mentioned flow models, the pressure distribution is obtained by integration of **Eq. 144**. To do so, polynomial functions can be used to approximate the radial core rotation distribution. In general, third-order polynomial curves are sufficient to approximate the usual core rotation distributions:

$$\beta(r) = C_1 r^3 + C_2 r^2 + C_3 r + C_4 \qquad \textbf{Eq. 145}$$

Conversely, the radial equilibrium equation can also be used to evaluate the core rotation from a measured static pressure distribution. In this case, polynomial curves have to be fit to the measured data and the derivatives with respect to the radius must be calculated.
Lauer [50] compares the core rotation determined from static pressure measurements with direct measured data using LDA. The general agreement is found to be good except in the case of large momentum exchange with a superposed through-flow. **Altmann [2]** observes a good agreement between direct measurements using a velocity probe and the values determined from the pressure distribution except for slight differences at the smallest radii in case of radial outward directed flow.

5 Computational Fluid Dynamics

Numerous numerical simulations using the commercial CFD codes Ansys Fluent and CFX have been performed in the course of this work. In general, the calculations focused on an economic prediction of the mean flow quantities using the RANS approach. The goal was to gather experience in how far the predictions depend on different numerical setups and the derivation of best practice guidelines for the successive calculation of the flow in the centrifugal pump. The major and most interesting results are described in the following.

5.1 Transition on the Enclosed Rotating Disk

Itoh et al. [40] perform detailed measurements of both mean and turbulent quantities for a rotating disk in a closed casing. The experimental apparatus is shown in Fig. 28.

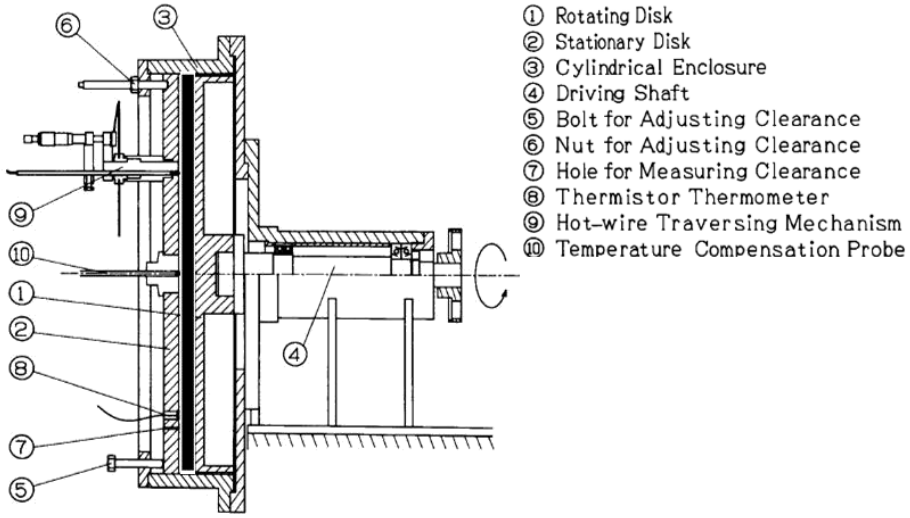

Fig. 28: Experimental configuration of Itoh et al. [40]

A lot of studies have dealt with the numerical treatment of flow in rotor-stator cavities. Examples are **Elena and Schistel [30], Poncet and Schiestel [73]** or **Haddadi and Poncet [35]**. One of the most influential parameters in a numerical computation is the choice of the turbulence model. The reasons

are, for example, the confinement of the flow in a narrow gap, a strong influence of rotation onto turbulence and the possible existence of both laminar and turbulent flow regimes (**Elena and Schiestel [30]**). **Itoh et al. [40]** emphasize that the flow is basically more turbulent near the stationary wall than near the rotating disk. In their experiments, the flow is laminar at small radii in the Ekman layer but turbulent in the Bödewald layer and hence a coexistence of both laminar and turbulent regimes is present.

To address this problem, three different turbulence models have been employed and compared with the mean measured velocity components. More precisely, the realizable k-ε model, the kω SST model and the new transition SST model proposed by **Langtry [49]** are used for the calculation. The latter model is a correlation based transition model which is strictly confined to local variables. Basically, the model links the vorticity Reynolds number to the momentum thickness Reynolds number. The latter comes from an empirical correlation that accounts for the different modes of transition such as natural, bypass or separated flow transition. In rotating flows, the cross-flow is the major instability source for transition from laminar to turbulent flow. For example, transition on the free disk is purely cross-flow induced. Besides, cross-flow plays a crucial role in the transition process on swept wings.

The computations are accomplished on a two-dimensional grid in the r-z plane and the flow is assumed to be axisymmetric. The first grid point is placed within the viscous sublayer which is mandatory for the transition model to yield good results (**Langtry [49]**). Post-processing of the results focuses on the comparison of the predicted and measured mean velocity profiles. The discretization of the advection terms is of second order for all quantities and the PRESTO scheme is employed for the pressure-velocity coupling. Convergence is controlled by monitoring integral parameters like the pressure or the torque on the rotating wall and the velocity in several single points.

Computations using the realizable k-ε model (Fig. 29 and Fig. 30) reveal an over-prediction of the core rotation. All curves fall very close to each other while the largest differences with respect to the experimental values are present at the smallest radius (≈28%) where the Ekman layer is laminar. A core rotation value of approximately 0.31 is characteristic for laminar flow. For instance, **Cooper and Reshotko [20]** give a value of 0.3135 in case of laminar flow between infinite disks. For increasing radii, the agreement with the experimental data clearly improves. The boundary layer attached to the rotor undergoes a noticeable change. At r/b=0.4 and r/b=0.6 the boundary layer thickness is quite small with a high peak in the radial velocity which is characteristic for a laminar boundary layer. The peak is markedly reduced at r/b=0.8 and r/b=0.94 due to turbulent flow conditions. Consequently, mass conservation requires that the boundary layer thickness must increase. The conditions on the stationary wall are different. No indications of laminar flow are visible and the general agreement with the numerical results is much better. The reason is probably that the turbulent conditions simply apply better to the turbulence model.

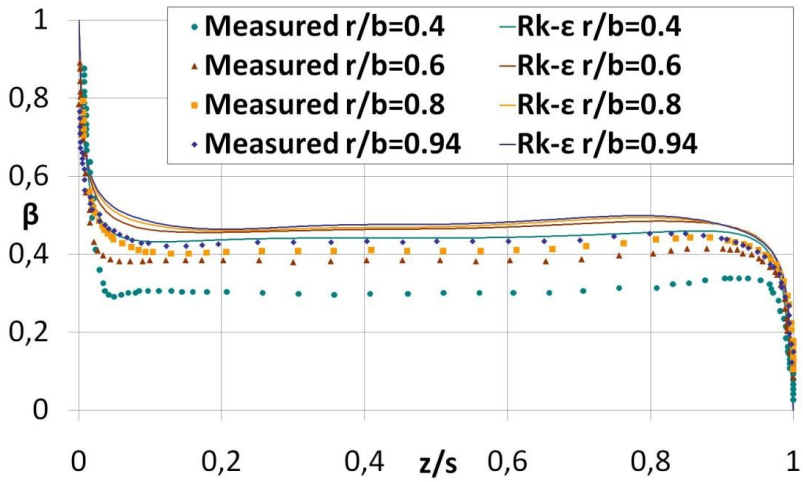

Fig. 29: Comparison of the core rotation distribution - experimental and CFD results for the realizable k-ε model

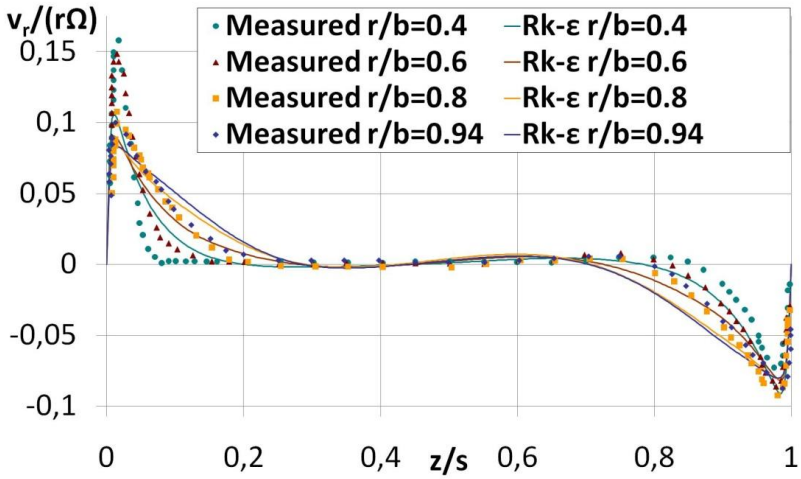

Fig. 30: Comparison of the dimensionless radial velocity distribution - experimental and CFD results for the realizable k-ε model

Using the kω SST model instead significantly improves the predictions (Fig. 1 and Fig. 32). Now the core rotation at r/b=0.4 is reduced below 0.4 and the radial velocity profiles are in a much better agreement with the experiments. A markedly reduced thickness of the boundary layer accompanied with a higher velocity peak is also clearly visible. According to the measurements, the flow is in a transitional state at r/b=0.6 while the turbulence model already seems to predict turbulent conditions.

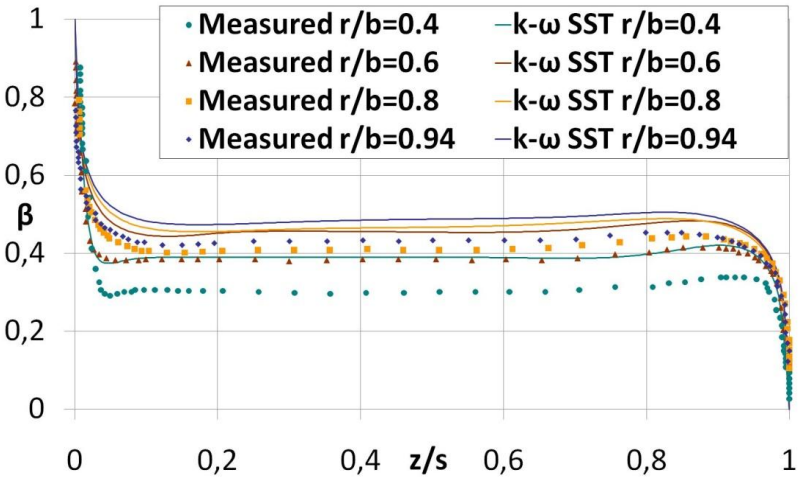

Fig. 31: Comparison of the core rotation distribution - experimental and CFD results for the kω SST model

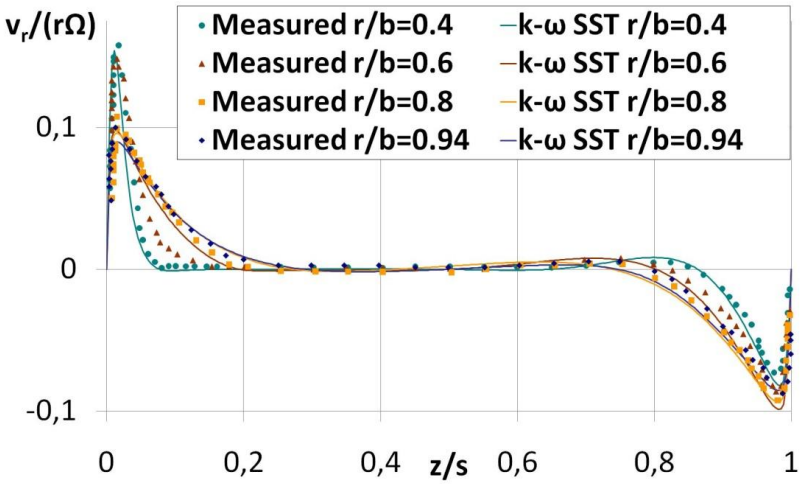

Fig. 32: Comparison of the dimensionless radial velocity distribution - experimental and CFD results for the kω SST model

Finally, the results obtained with the transition kω SST model are closest to the experiments for this kind of flow (Fig. 33 and Fig. 34). The core rotation at r/b=0.4 is now approximately 0.35 which is nevertheless still slightly too high. In contrast to the standard kω SST model, the transitional state at r/b=0.6 appears to be additionally captured by the model. In fact, the results are somewhat surprising since the model in its original state is not able to reflect transition due to cross-flow instabilities. This means that in the present case some additional effects must trigger the model. Apart from beforehand considerations, this study shows that the idea of the fluid in solid body rotation is not necessarily appropriate for the enclosed rotating disk. Here, the core rotation is a function of radius caused by laminar-turbulent transition.

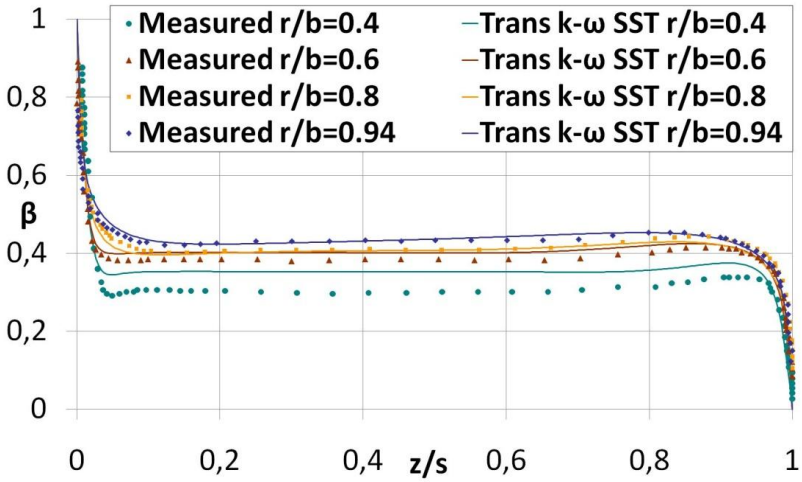

Fig. 33: Comparison of the core rotation distribution - experimental and CFD results for the transition kω SST model

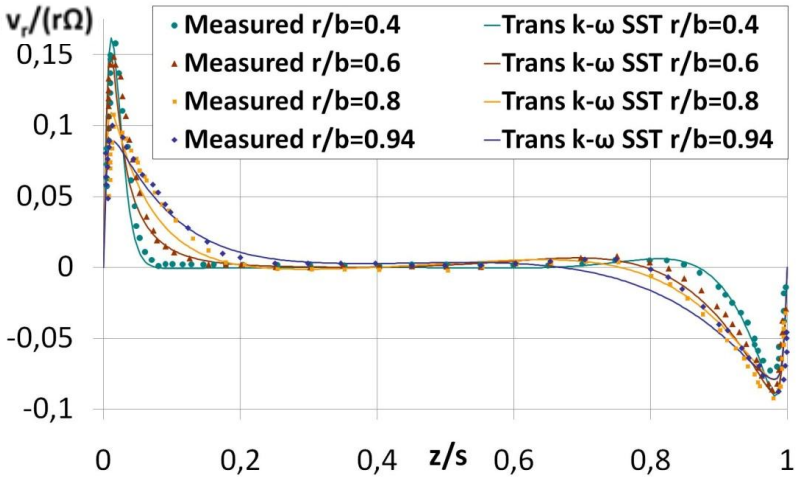

Fig. 34: Comparison of the dimensionless radial velocity distribution - experimental and CFD results for the transition kω SST model

In addition to the steady RANS solutions presented above, a two dimensional LES simulation has been performed. The results give some interesting insight in the flow physics. An exemplary picture of the stream function is given in Fig. 35.

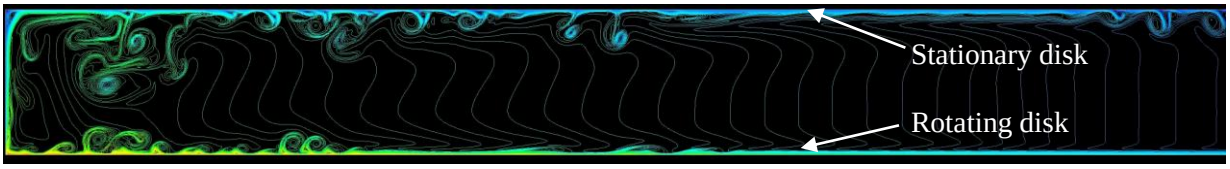

Fig. 35: Stream function in the r-z plane obtained by a 2D LES solution

In this figure, the lower boundary is the rotating disk. At smaller radii, the flow close to the rotor is undisturbed whereas for increasing radial location the boundary layer becomes wavy and vortices roll

up towards the outer stationary shroud. Moreover, it appears as if the turning of the fluid at the radial shroud (a region of high shear) enforces the instabilities. Further downstream along the stator, the flow is characterized by small vortices travelling towards the axis of rotation. These vortices are not confined to the Bödewald layer and extend through the core to affect the Ekman layer. This suggests that cross-flow transition is not the only instability source for this kind of problem. In fact, the disturbances created by the turning at the outer radial casing seem to significantly affect the stability of the rotor boundary layer which supports the reasoning by **Cheah et al. [17]**. At lower radial positions, the flow leaving the stator boundary layer passes to the core region which is characterized by negligible strain rates. This leads to a rapid decay of turbulence before the fluid is entrained into the Ekman layer.

5.2 Transition on the Free Disk

The flow structure in case of the enclosed rotating disk discussed before is surprisingly well modeled with the transition SST model. Pure cross-flow transition occurs on the free disk and **Gregory et al. [32]** intensively investigate this case as a simplified example for transition in real three-dimensional boundary layers with respect to swept wings. To test the transition model in case of pure cross-flow transition, the free disk case is simulated. In the transition zone, vortices form standing waves with a characteristic angle ($\varepsilon \approx 14$ deg) and number (28-31) depicted in Fig. 36 according to **Dorfmann [29]**.

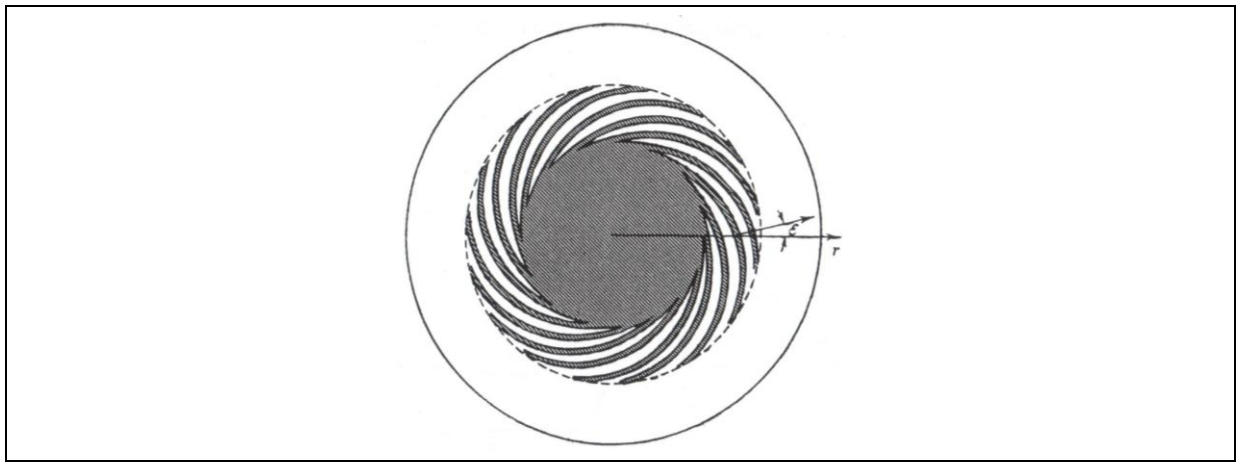

Fig. 36: Vortices in the transition zone on a rotating disk (Dorfmann [29])

The computational domain including the grid for the simulation is shown in Fig. 38. The geometrical shape of the surrounding domain is not arbitrary because the possible creation of an artificial shear layer can lead to erroneous results and should therefore be avoided. After a grid independence study, first some computations with different laminar Reynolds numbers have been performed in order to compare the frictional resistance with the analytical solution given in **Eq. 2**. The values obtained for the moment coefficients are summarized in Table 13.

Re_φ	c_m - Analytical	c_m - Numerical	Relative Deviation [%]
6.85	0.7393	1.5997	116.39
10.00	0.6119	1.0190	66.54
68.50	0.2338	0.2705	15.69
100.00	0.1935	0.2126	9.87
685.00	0.0739	0.0718	-2.83
1000.00	0.0612	0.0626	2.28
6025.70	0.0249	0.0252	1.21
8004.00	0.0216	0.0219	1.03
10271.00	0.0191	0.0193	0.90
50000.00	0.0087	0.0087	0.45

Table 13: Comparison between analytical and numerical solution for the moment coefficient

For very small Reynolds numbers (creeping flow), the deviation between the two solutions becomes large. This originates from the fact that in case of dominant viscous forces the flow structure does not match the assumptions in the analytical derivation any more. For increasing laminar Reynolds numbers the agreement substantially improves.
The adequacy of the numerical solution can also be shown by comparing the dimensionless velocity profiles from the simulation and the solution according to **Lance and Rogers [48]** who numerically solve the Van Kármán equations for a rotating disk in a stationary fluid. The dimensionless velocity profiles are defined as (see **Van Kármán [42]**):

Radial $$F = \frac{v_r}{\Omega r}$$ **Eq. 146**

Tangential $$G = \frac{v_\varphi}{\Omega r}$$ **Eq. 147**

Axial $$H = \frac{v_z}{\sqrt{\Omega \nu}}$$ **Eq. 148**

The profiles are a function of the dimensionless wall distance ζ:

Dimensionless wall distance $$\zeta = z\sqrt{\frac{\Omega}{\nu}}$$ **Eq. 149**

According to Fig. 37, both solutions perfectly match for all three velocity components.

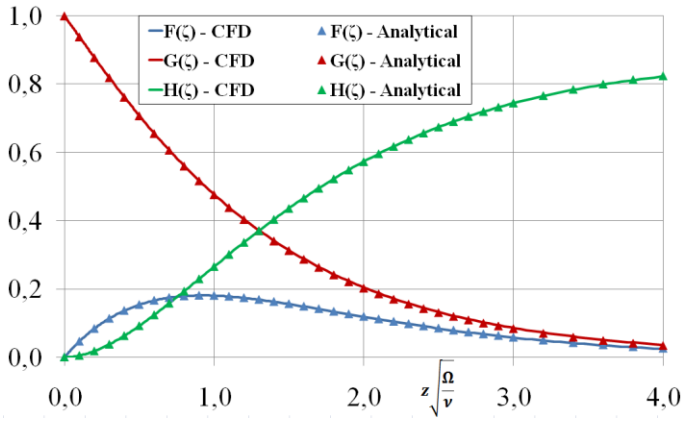

Fig. 37: Exemplarily comparison of the velocity profiles for laminar flow on the free disk (r/b=0.5, Re_φ=50000; "analytical" values according to Lance and Rogers [48])

In conclusion, the numerical setup including the grid is considered sufficient to adequately model the case. The final axisymmetric, structured mesh consists of about 1 million cells with y+ below 2.5 everywhere on the disk in case of transitional flow. The circumferential Reynolds number is $2.07 \cdot 10^6$ according to the experiments of **Gregory et al. [32]**.

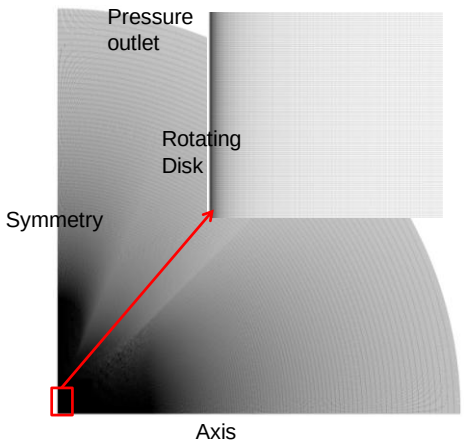

Fig. 38: Computational Domain and grid for the free disk case

Regarding the computational results (Fig. 39), neither the wall shear stress nor the intermittency indicate transition whereas the experimentally observed loss of stability point is at r/b≈0.29 and transition to fully turbulent flow takes place at r/b≈0.36.

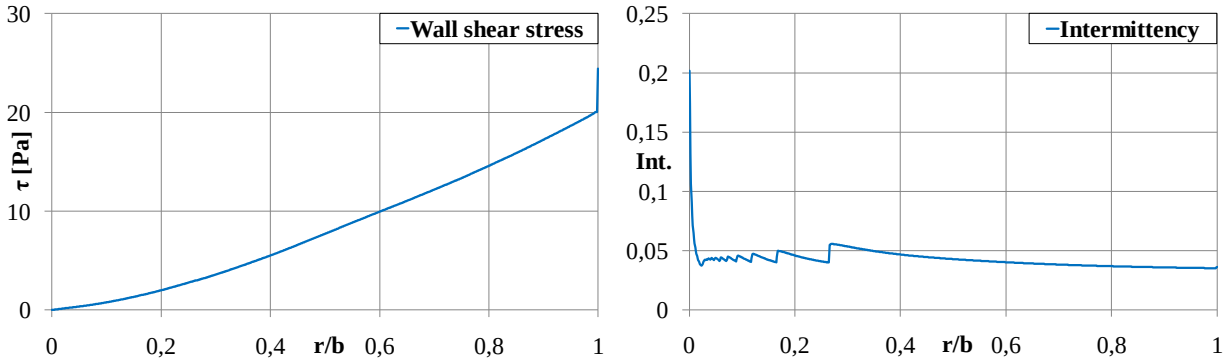

Fig. 39: Wall shear stress (left) and intermittency (right) on the rotating disk

The same becomes clear displaying the resulting velocity profiles. The turbulent profile agrees very well with the experimental one. However, both profiles from the CFD simulation are very similar to each other and obviously no sign of laminar flow is present.

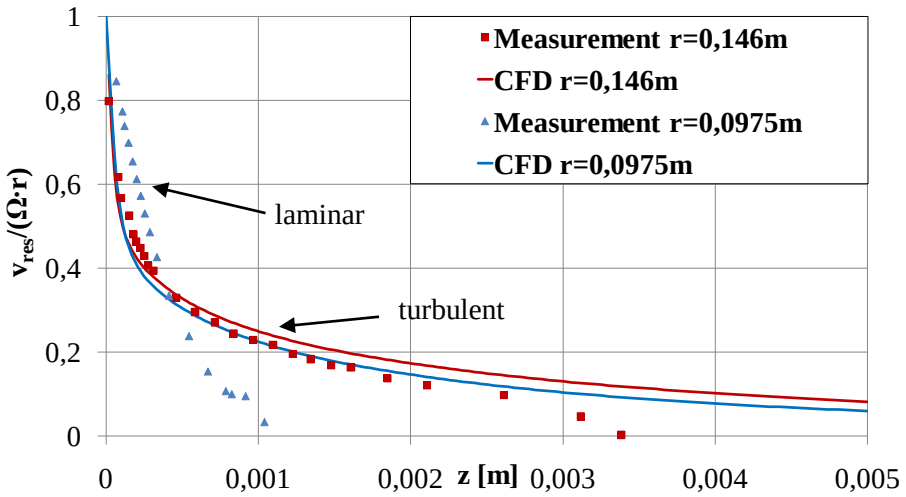

Fig. 40: Comparison of the velocity profiles for the free disk, CFD - experiment (Gregory et al. [32])

Finally, the moment coefficient is considered. For values of rotational Reynolds numbers up to $7 \cdot 10^6$, the moment coefficient for one side of the disk is known as (**Dorfman [29]**):

$$c_m = 0.491\left(logRe_\varphi\right)^{-2.58} \qquad \textbf{Eq. 150}$$

For the present case, the following values result:

Experimental (**Dorfman, 1963**)	Numerical
0.004226	0.004466

Table 14: Comparison of the moment coefficients for the free disk

The numerical value is slightly higher than the one obtained from the experimental correlation as a consequence of the fact that the laminar flow regime is not resolved in the numerical simulation. Consequently, the entirely turbulent flow across the disk surface leads to a higher frictional resistance. In summary, the transition SST model does not resolve transition due to pure cross-flow instabilities on the free disk. This confirms that in the case of the enclosed rotating disk considered before, other transition mechanisms must be present. It is worth mentioning that the choice of the modeling domain is not arbitrary in case of the free disk. If a flow domain according to Fig. 41 is chosen, an artificial

shear layer is created across the diagonal from the upper right to the lower left originating from the disk pumping effect. This shear layer increases the intermittency and the model misleadingly predicts transition.

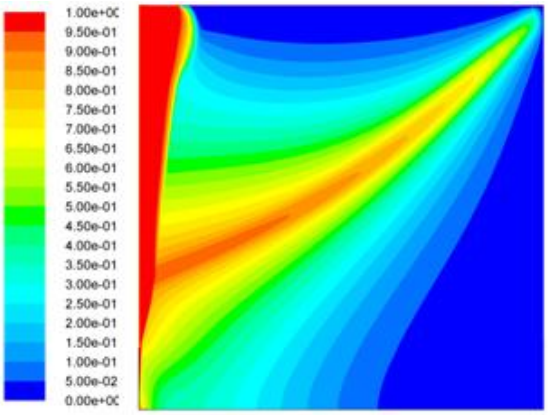

Fig. 41: Creation of a false shear layer in case of a rectangular computational domain for the free disk (contours of intermittency)

5.3 Simulation of the Flow in Rotor-Stator Cavities

The numerical study of the flow in rotor-stator cavities is quite a challenging problem using commercial CFD codes. In the following chapter, a numerical study is described with the goal of finding the best practice guidelines for industrial use with Ansys CFX. For this purpose, multiple test calculations were performed. In order to enable comparisons, the extensive experimental study performed by **Radtke and Ziemann [78]** (FVV - report nr. 213) is used. Their measurements include mean velocity profiles, disk friction coefficients and radial pressure distributions. Due to the massive amount of data, only the most relevant results are presented here.

5.3.1 Enclosed Rotating Disk

5.3.1.1 Basic Flow Structure and Temperature Influence

The basic geometry and mesh for the study of the enclosed rotating disk is shown below in Fig. 40. Since CFX is basically a three-dimensional solver, only one computational cell is specified in the circumferential direction in order to allow for a virtually 2D simulation. Both planar faces are specified as periodic in the tangential direction implying that the flow is axisymmetric. The dimensionless gap width G amounts 0.1375 in the present case with a circumferential Reynolds number of approximately $4.2 \cdot 10^6$. It is further proven that the results are virtually independent whether the governing equations are solved in a rotating or a stationary frame of reference. Unless otherwise mentioned, the SST turbulence model is used together with the curvature correction option.

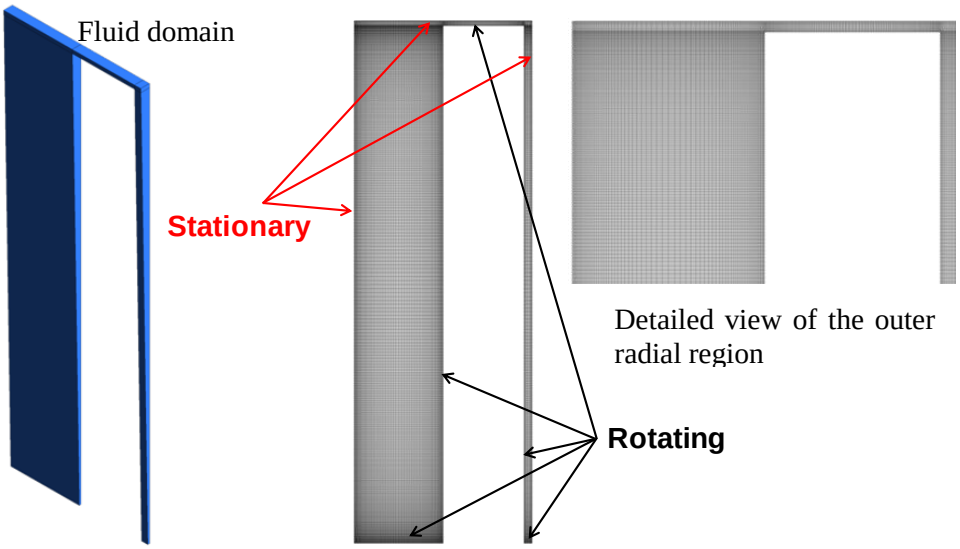

Fig. 42: Basic model and mesh for the enclosed rotating disk

Based on the above mesh, several different simulations are accomplished. For example, a 30 deg, 90 deg and 360 deg model has been created to investigate the influence of three-dimensionality on the flow structure. The fluid is treated as compressible and the ideal gas relation is used to model density. To include the temperature dependance of the viscosity, the Sutherland law is employed:

$$\mu = \mu_0 \frac{T_0 + C}{T + C} \left(\frac{T}{T_0}\right)^n \qquad \textbf{Eq. 151}$$

The reference conditions used in this formula correspond to Table 15:

T_0	μ_0	Sutherland constant	Exponent n
291.15 K	$18.27 \cdot 10^{-6}$ Pas	120 K	1.5

Table 15: Reference values used in the sutherland law

Since viscous shear in the present case is large, the option "include viscous work term" is activated which adds an additional term in the energy equation. If this term is not included, the solver ignores the work performed by the fluid on the moving wall, and instead adds this work to the dissipated amount of heat energy erroneously increasing the temperature. Further on, the heat transfer across the stationary walls is accounted for by specification of the heat transfer coefficient and the outer temperature. The outer temperature and the heat transfer coefficient are finally determined as 293K and 1000W/(m^2K) respectively from several test calculations. With these inputs a volume averaged temperature of approximately 300K establishes in the cavity.

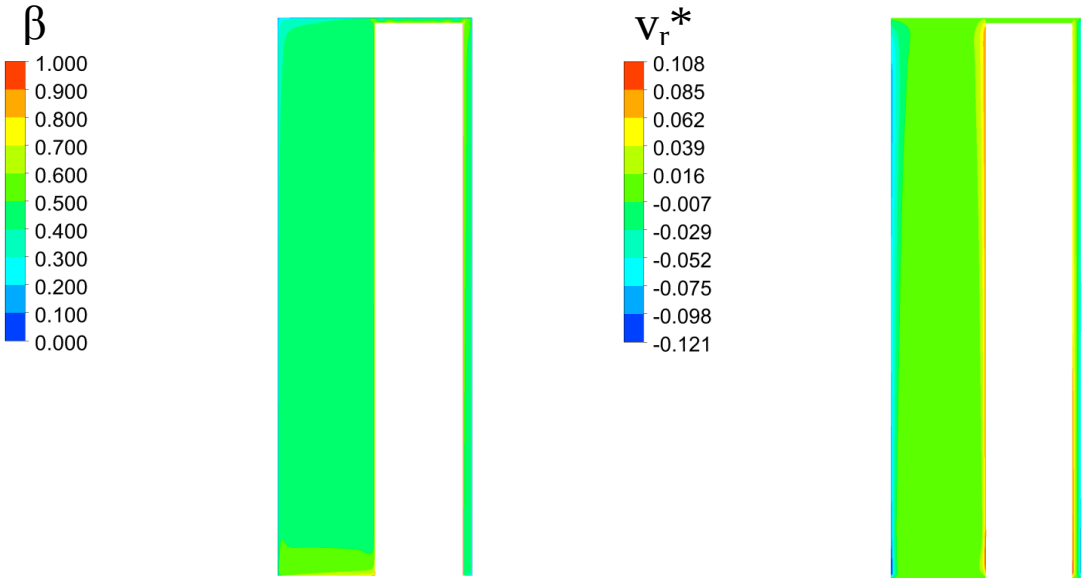

Fig. 43: Contours of the core rotation coefficient (left) and the dimensionless radial velocity (right)

The flow structure described beforehand can be clearly identified in Fig. 43. A boundary layer close to the rotor with a radial outflow of fluid (disk pumping effect) and a boundary layer close the stator with a radial inflow of fluid. The fluid pumped out at the rotating disk is turned at the outer shroud towards the stator boundary layer. Between these two narrow layers, the radial velocity vanishes which is characteristic for the core region. Because of mass conservation, an axial exchange flow from the stator to the rotor is present. A detailed view of the flow conditions at the outer periphery is given in Fig. 44 including the velocity vectors.

The frictional torque from the numerical simulation and the measurement is given in dimensionless form using the torque respectively moment coefficient c_m. The present 2D simulations consist of a 1 degree element in circumferential direction. Therefore, the computed torque has to be multiplied with 360 deg in order to allow a comparison with the measured data.

$$c_m = 360 \cdot c_{m1deg} \qquad \textbf{Eq. 152}$$

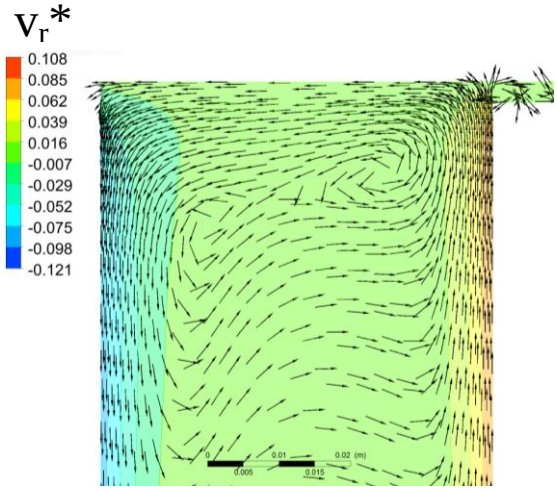

Fig. 44: Contours of the dimensionless radial velocity and velocity vectors at the outer cavity radius

In order to allow for a comparison, volume averaged values of the density, as well as the dynamic viscosity, are used in the case of provision of heat transfer in order to determine the c_m value. **Daily and Nece [24]** correlate their torque measurements for flow regime IV in the following empirical formula:

$$c_m = 0.051 \cdot G^{0.1} Re_\varphi^{-0.2} \qquad \textbf{Eq. 153}$$

Kreith [43] later proposes a slight correction to this formula by setting the constant to 0.0545:

$$c_m = 0.0545 \cdot G^{0.1} Re_\varphi^{-0.2} \qquad \textbf{Eq. 154}$$

The resulting values for the moment coefficients are compared in the following table:

Measurement	CFD (isothermal)	CFD (with heat flux)	**Daily and Nece [24]**	**Kreith [43]**
$c_m=2.05\cdot10^{-3}$	$c_m=1.9\cdot10^{-3}$	$c_m=1.9\cdot10^{-3}$	$c_m=1.98\cdot10^{-3}$	$c_m=2.12\cdot10^{-3}$

Table 16: Moment coefficients for the enclosed disk

The correlation according to **Kreith [43]** gives somewhat greater values than the experimental one whereas the correlation of **Daily and Nece [24]** results in a smaller value. The difference between the two numerical values is negligible small while the discrepancy with the experimental value, as will be discussed later, mainly results from the resolution of the circumferential velocity gradient in axial direction. This gives rise to the wall treatment applied in the numerical simulation. Basically, two approaches can be distinguished: On one hand the explicit resolution of the boundary layer using low Reynolds variants of the implemented turbulence models and on the other hand the bridging of the near wall region using wall functions. The wall shear stress in the circumferential direction on the disk is mainly responsible for the frictional resistance. It can be simply formulated as:

$$\tau_\varphi = \mu \frac{\partial v_\varphi}{\partial z} \qquad \textbf{Eq. 155}$$

The moment coefficient as an integral parameter is relatively insensitive to the radial flow profile. The major velocity components and gradients are present in the circumferential direction and therefore the radial velocity profiles have only a small influence on the tangential wall shear stress. Exactly this insensitivity of integral parameters like the axial force or the frictional resistance in terms of the radial profiles is the reason why integral calculation procedures can yield quite sufficient results.
Volume averaged quantities for the fluid properties are compared for the two simulations in Table 17:

	Isothermal	Heat flux
Temperature [K]	300	298.64
Density [kg/m3]	1.16	1.16
Dyn. Viscosity [Pas]	$1.831 \cdot 10^{-05}$	$1.863 \cdot 10^{-05}$

Table 17: Fluid properties in case of the isothermal and the heated case

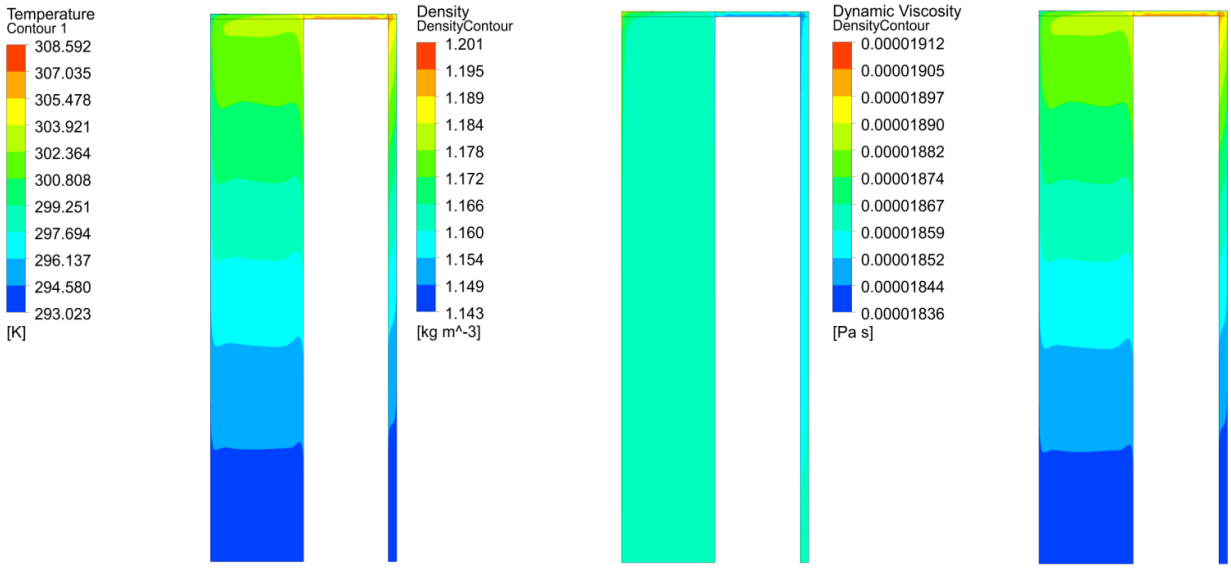

Fig. 45: Temperature (left), density (middle) and dynamic viscosity (right) distribution in the r-z plane

Fig. 45 shows a plot of the resulting temperature, density and dynamic viscosity distribution in the r-z plane. It can be observed that the variations are quite small. Nevertheless, the strongest changes occur at the outer radius, especially in the small radial gap (gap height 3mm) above the rotor. This region is of special importance concerning the occurrence of Taylor vortices which result from the principle flow instability in this region. The instability arises from the fact that the centrifugal force is higher at the inner radius, namely at the outer shroud of the rotor and decreases towards the stationary casing. In fact, this is an example of the classical Taylor-Couette problem (flow between two concentric cylinders). The mesh size according to mesh no. 2 employs 14 cells in the radial direction which is not sufficient to resolve these structures yet. It will be shown that with increasing mesh size these structures become clearly visible.

Next, the radial static pressure distribution measured on the stator wall is examined. Fig. 46 shows the trend of the measured and computed pressure curve in radial direction. According to the basic boundary layer theory, the pressure is axially constant across gap width for flow regime IV and the pressure in the core region is imposed onto the boundary layers.

At the outer radius, the agreement between computed and measured pressure is very good, while some small differences are visible at smaller radii. The pressure can also be estimated analytically assuming that the fluid rotates as a solid body with a certain fraction of the rotor angular velocity. According to **Zilling [109]**, the magnitude of the solid body rotation can be determined from **Eq. 99**. Now, a relation between the pressure and the fluid rotation is necessary. If the radial equilibrium relation is used together with a constant core rotation value according to **Eq. 133**, the radial pressure distribution becomes:

$$p(r) = p(b) + \frac{\rho}{2}\Omega^2 b^2 \beta_0^2 \left[\left(\frac{r}{b}\right)^2 - 1\right] \qquad \textbf{Eq. 156}$$

The static pressure distribution essentially determines the axial force exerted on the wall in the axial direction:

$$F_{ax} = 2\pi \int_{r=a}^{r=b} p(r) r dr \qquad \textbf{Eq. 157}$$

Since the resulting axial force and the frictional resistance are both resulting from the integration of the pressure and the shear stress across the radius, the outer region of the disk is of significant importance. The previously introduced correction function for the 1D flow model exactly addresses this demand. For the fluid in solid body rotation the pressure drops parabolically with the radius. The dimensionless pressure coefficient c_p is defined in the FVV report as follows:

$$c_p = \frac{p(b) - p(r)}{\rho \Omega^2 b^2} \qquad \textbf{Eq. 158}$$

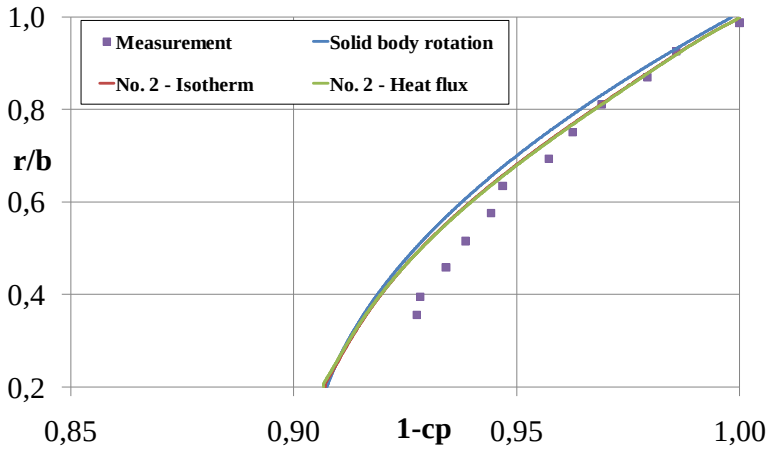

Fig. 46: Comparison between computed, analytical (Eq. 151**, denoted as "solid body rotation") and measured pressure distribution**

It is interesting to note, that the pressure distribution according to the simple analytical model falls very close to the curve determined from the CFD solution. However, some small discrepancies are present at lower radial locations. This indicates that a change in the core rotation is likely to occur which could be a consequence of transition from laminar to turbulent flow. Laminar flow in the rotor boundary layer leads to a lower core rotation and consequently to a decreased pressure drop. This in turn leads to a smaller c_p and the pressure curve (1-cp) is shifted to larger values in Fig. 46 as the experimental values indicate.

The velocity profiles for the dimensionless tangential (core rotation) and radial velocities are given in the following figures together with the measured data. It can be seen that the principal flow structure from the numerical simulation agrees with the experimental one. Nevertheless, some discrepancies remain. The tangential velocity obtained from the CFD simulation over-predicts the value of the core rotation at r/b=0.456 and r/b=0.691 by about 8%. At the outer radius (r/b=0.985), the braking influence of the stationary shroud becomes dominant and lowers the core rotation. Further on, the shape of the curve is altered which is founded in the turning of the fluid at the outer casing. The radial profiles show a major difference between the measured and the computed profiles. In the CFD simulations the radial velocity completely vanishes in the core region while the measured profiles clearly indicate a nonzero, positive value. A nonzero value in the core means that a radial transport of angular momentum must take place. But this strictly contradicts the measured and the computed tangential core rotation distributions and indicates that some systematic errors might have occurred during the measurements. The only possible region with a nonzero radial velocity is at the outer measuring location (r/b=0.985) caused by the turning of the fluid at the stationary shroud. Consequently, the radial velocity becomes negative as predicted by the CFD calculation. This in turn changes the profile of the core rotation which cannot be constant any more in the axial direction for a nonzero v_r^* (**Owen and Rogers [64]**).

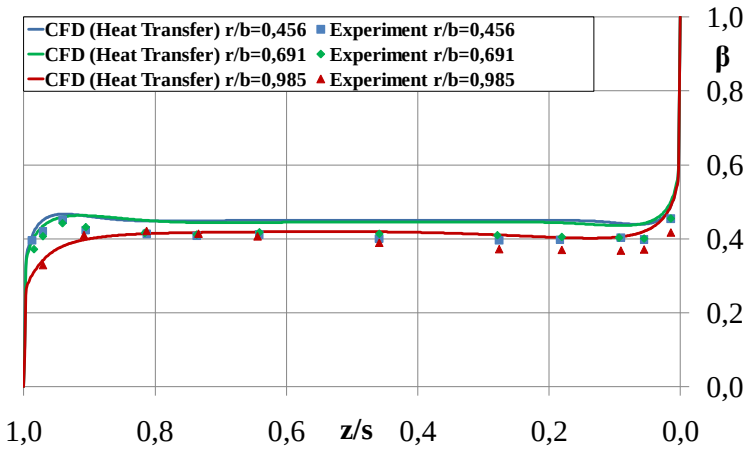

Fig. 47: Core rotation distribution

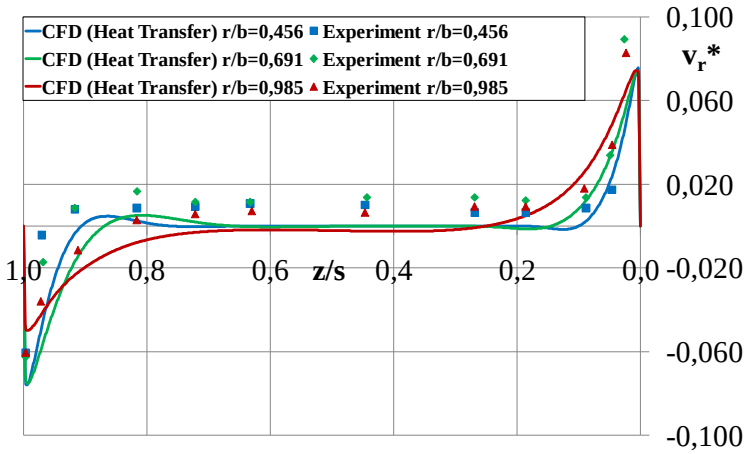

Fig. 48: Dimensionless radial velocity distribution

It must be pointed out that the radial profiles are of special importance in case of a superposed through-flow because the externally entering fluid is entrained in the respective boundary layer according to the flow direction. In the case of centripetal flow, the fluid passes the stator boundary layer while for centrifugal flow direction the fluid enters the rotor boundary layer.
The performance of every turbulence model depends strongly on the ability of predicting the radial flow profiles. Validation purposes in turn require more accurate measurements.

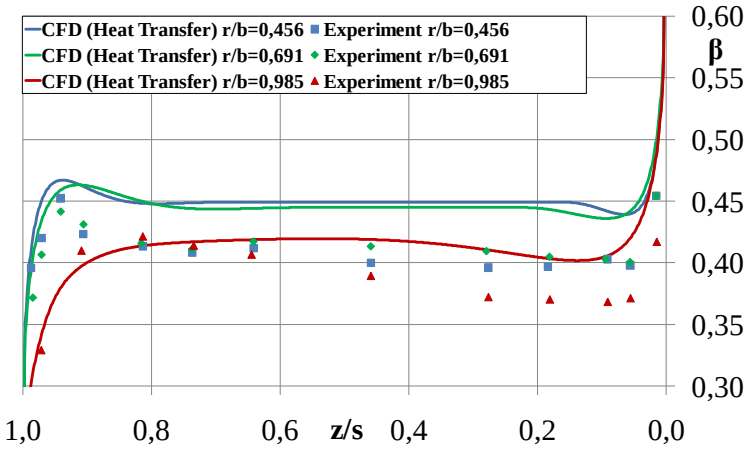

Fig. 49: Detailed view of the core rotation distribution

The comparison of the profiles from the thermal and isothermal simulation confirms that thermal effects on the flow field are negligible. The obtained profiles exactly match each other and will not be shown here due to space restrictions. Instead, a difference plot of the dimensionless absolute velocity

is shown in Fig. 50 which clearly brings out that the inclusion of heat transfer effects leads to only negligible changes in the flow field. For this reason, all successive calculations have been performed assuming isothermal conditions.

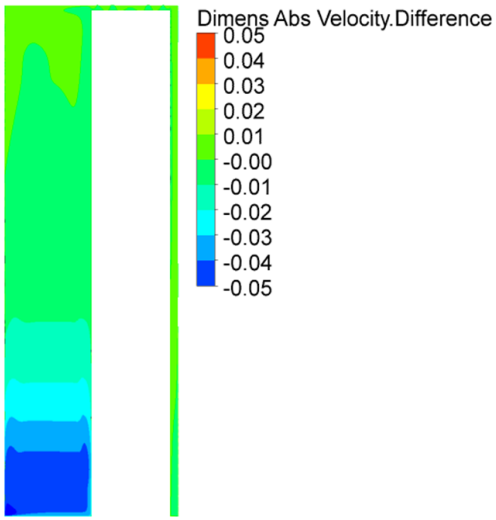

Fig. 50: Differences of the absolute velocity between isothermal and non-isothermal computation

5.3.1.2 3D Segment Studies

The aforementioned investigations are based on the assumption of axisymmetric flow conditions. For a standalone cavity with through-flow and fully turbulent flow conditions, this is a reasonable assumption. However, in a complete machine, the flow in the side cavity is indivisibly coupled with the flow in other adjacent parts which can lead to strong variations of the flow parameters around the circumference. Apart from an externally imposed three-dimensionality, the flow in a cavity can become three-dimensional due to the formation of vortex structures in the transitional flow regimes. For example, fine scale near-wall spiral structures have been observed experimentally by **Czarny et al. [22]** and numerically by **Gant (cited in Craft et al. [21])**:

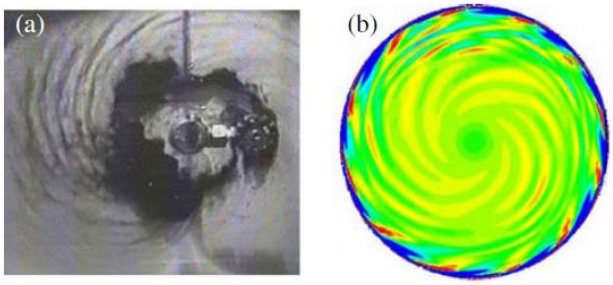

Fig. 51: Fine scale near-wall spiral structures; experiments by Czarny et al. [22] and computations by Gant cited in Craft et al. [21] (≈2.115 Mio. Cells)

These structures are also known as Ekman (on the rotating disk) or Bödewald (on the stationary disk) spirals and are confined to the near wall vicinity. Moreover, large scale rotating structures can also occur in the core region as exemplarily illustrated in form of an S-shaped vortex pair in Fig. 52.

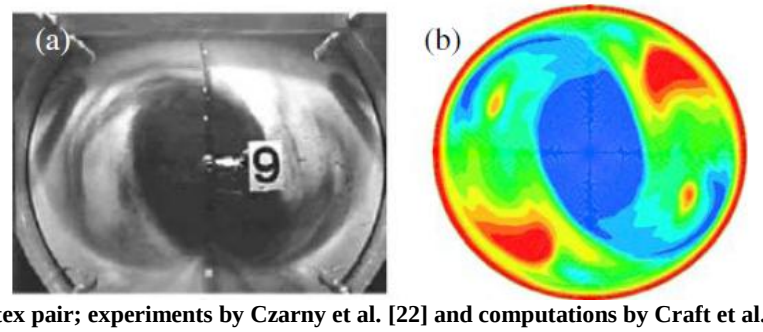

Fig. 52: S-shaped vortex pair; experiments by Czarny et al. [22] and computations by Craft et al. [21]

Craft et al. [21] incorporate an economical calculation method using a modified wall function approach which accounts for the strong skewing of the velocity vector in the boundary layers. Large scale rotating structures have also been observed by **Rabs [77]** in a gas turbine rim seal cavity depicted in Fig. 53.

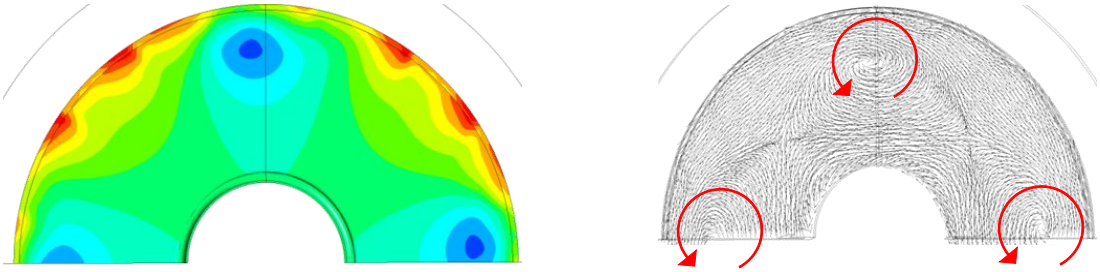

Fig. 53: Large scale rotating structures in a gas turbine rim seal cavity (Rabs [77])

Craft et al. [21] notice that the structures seem to diminish with increasing number of revolutions to a steady state solution with no vortex patterns as shown by computations of **Zacharos [107]**. The structures observed by **Rabs [77]** seem to be caused by the interplay of the cavity and the hot gas path while the majority of the other structures result from the flow instability during transition from laminar to turbulent flow. Nevertheless, the extensive computational costs for resolving such phenomena restrict the feasibility for industrial applications. Strictly spoken, a proper strategy would include time dependent computations with very fine grids and time steps to account for the steep gradients of the turbulent quantities. However, for all the cases considered in this study, a two dimensional model seems to be sufficient with respect to the mean flow quantities.
The three-dimensional segments consist of the above presented mesh with 40456 elements in the r-z plane and is rotated around the rotation axis providing one element per 1 deg. Accordingly, 1.213.680 elements result for the 30 deg model. The element number for the 360 deg model amounts approximately 14 million and takes a considerable amount of computing resources. To start the calculation, half of the circumferential velocity at the outer disk radius has proven as a good initial guess. A comparison between the 3D and the 2D computations will be given next. First, the frictional resistance in terms of the moment coefficient is compared in the following table:

c_m (2D model)	c_m (3D - 30deg - model)	c_m (3D - 360deg - model)
$1.9 \cdot 10^{-3}$	$1.9 \cdot 10^{-3}$	$1.92 \cdot 10^{-3}$

Table 18: Comparison of the moment coefficient between 2D and 3D models

No significant differences are noticeable from the results. The contour plots of important variables like the pressure coefficient or the dimensionless absolute velocity show circular lines. This means that no gradients in circumferential direction are present (Fig. 54, Fig. 55, Fig. 56, Fig. 57), independent of the axial position.

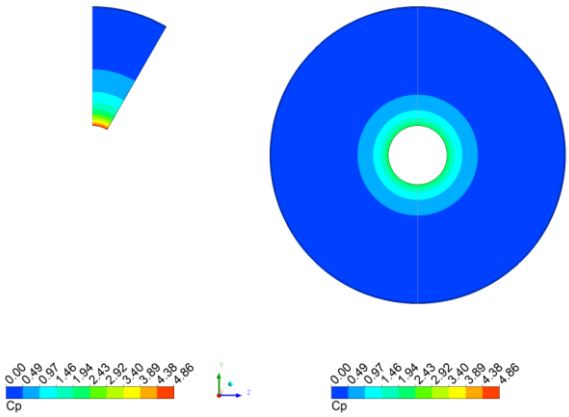

Fig. 54: Contours of the pressure coefficient c_p for the 30 deg segment model (left) and the 360 deg model (right) in the middle of the cavity

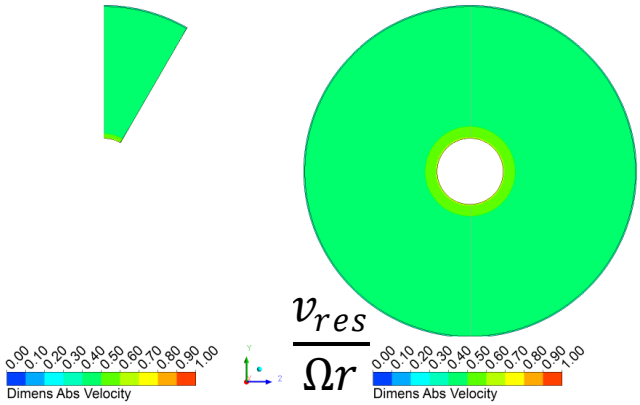

Fig. 55: Contours of the dimensionless absolute velocity for the 30 deg segment model (left) and the 360 deg model (right) in the middle of the cavity

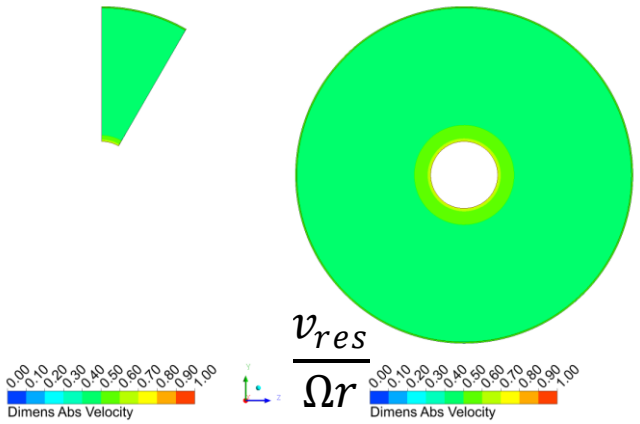

Fig. 56: Contours of the dimensionless absolute velocity for the 30 deg segment model (left) and the 360 deg model (right) in the rotor boundary layer

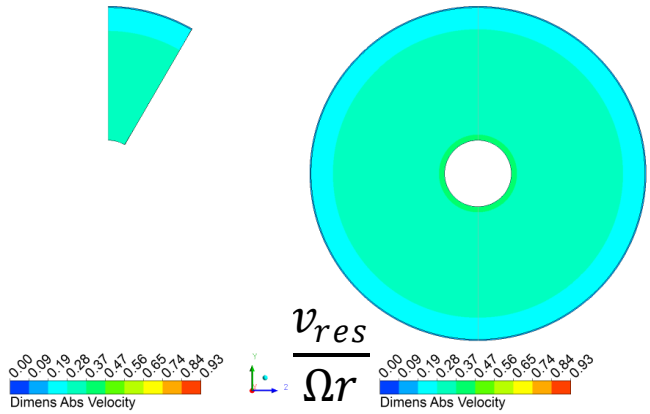

Fig. 57: Contours of the dimensionless absolute velocity for the 30 deg segment model (left) and the 360 deg model (right) in the stator boundary layer

A quantitative comparison of the pressure distribution on the stator is given in Fig. 58. The full 360 deg model gives some greater values for cp at the inner radius which leads to a shifting of the curve 1-cp to smaller values.
The reason is that the computation was broken off when the maximum residuals were below $1 \cdot 10^{-5}$ due to the massive computational effort. However, the averaged pressure on the stator wall, as a measure of physical convergence, was not completely converged at that point. For a longer computation time, the pressure is expected to be identical to the two other models. In conclusion, the comparison of the 3D and the 2D case proves that the use of 2D models in combination with the numerical setup for the present study appears to be sufficient.

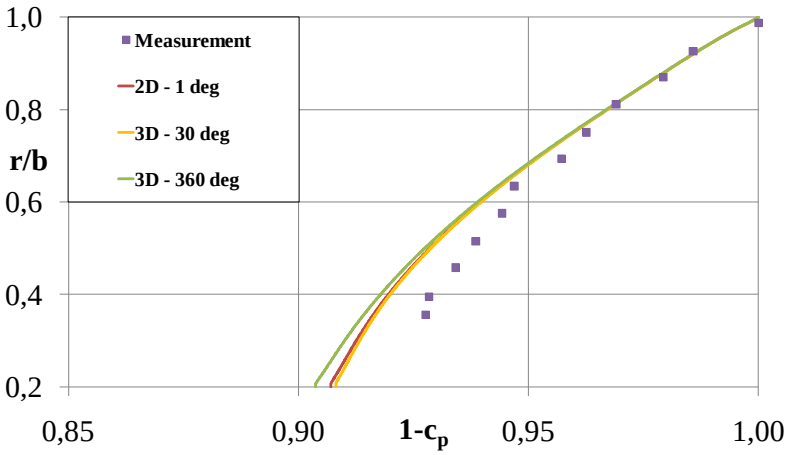

Fig. 58: Comparison of the pressure distributions for the 30 deg, 360 deg and 2D model

5.3.1.3 2D Grid Independence Study

To check the dependance of the 2D solution on the grid size, meshes of different refinement levels have been generated. CFD mesh has been used as meshing tool and the corresponding resulting maximum y+ values for the different meshes are summarized in Table 19.

Mesh No.	1	2	3	4	5	6	7
Elements	10114	40456	161824	647296	647296	647296	647296
Max. y+ rotor	153.24	50.24	15.84	4.7	3.4	2.59	1.97
Max y+ stator	106.17	35.4	11.3	3.4	2.7	2.26	1.48

Table 19: Moment coefficient in dependance on grid size

The refinement strategy was to double the number of divisions and the bias factor on the specified edges for every new grid, starting from a rough basic mesh. Consequently, the total amount of computational elements increased by the factor 4 for the 2D mesh. For the models denoted as mesh no. 5, 6 and 7 the amount of elements was kept constant and the near wall cells were successively moved closer to the wall in order to reduce the y+ values.
Next, the influence of the grid size on the moment coefficient is given in Table 20 and also visualized in Fig. 59:

Mesh No.	1	2	3	4	5	6	7	Measurement
c_m	$1.75 \cdot 10^{-3}$	$1.9 \cdot 10^{-3}$	$2 \cdot 10^{-3}$	$1.91 \cdot 10^{-3}$	$1.88 \cdot 10^{-3}$	$1.87 \cdot 10^{-3}$	$1.87 \cdot 10^{-3}$	$2.05 \cdot 10^{-3}$
Deviation CFD-Exp.[%]:	14.6	7.3	2.4	6.8	8.2	8.8	8.8	

Table 20: Moment coefficient in dependance on grid size

As expected, the moment coefficient predicted by the numerical simulation first approaches the experimental value with increasing grid size. For closer wall proximity, the deviations increase again which is somewhat surprising since mesh no. 7 provides the closest wall proximity that should enable an explicit boundary layer resolution. Usually, the SST model requires a y+ value lower than two to switch to a low Reynolds number formulation using the automatic wall treatment (**Menter et al. [55]**). However, the smallest deviation between measured and computed moment coefficient exists for mesh no. 3 where the maximum y+ at the outer rotor radius is about 15.84. Nonetheless, the predictions can still be regarded as quite good with respect to the difficulties arising from an accurate experimental determination of the disk friction torque.
It is further noticeable from Table 19, that the y+ value is always higher on the rotor compared to the stator. This is plausible because the relative velocity in the rotor boundary layer is higher than in the stator boundary layer as long as the core rotation is smaller than 0.5. Assuming that the core rotates

with a value of approximately 0.44, then the rotor senses a velocity difference of 0.56 while the stator senses the value 0.44. Consequently, as long as the core rotates with β smaller than 0.5, the relative velocity for the rotor will always be higher than for the stator and so will the y+ values.

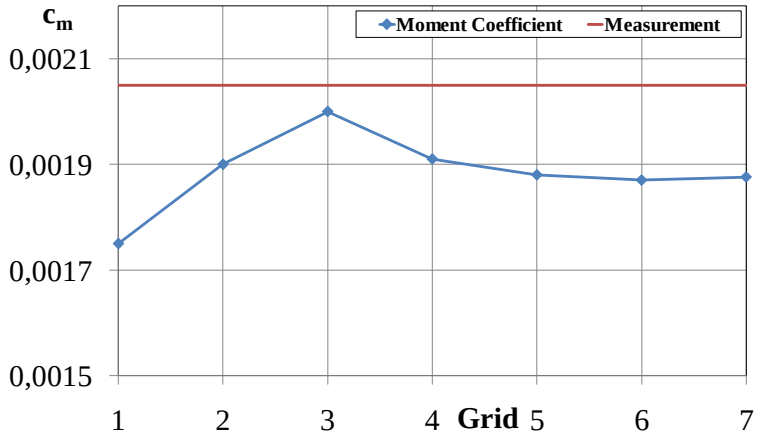

Fig. 59: Dependance of the moment coefficient on the grid size

The trend of the pressure distributions is shown in Fig. 60.

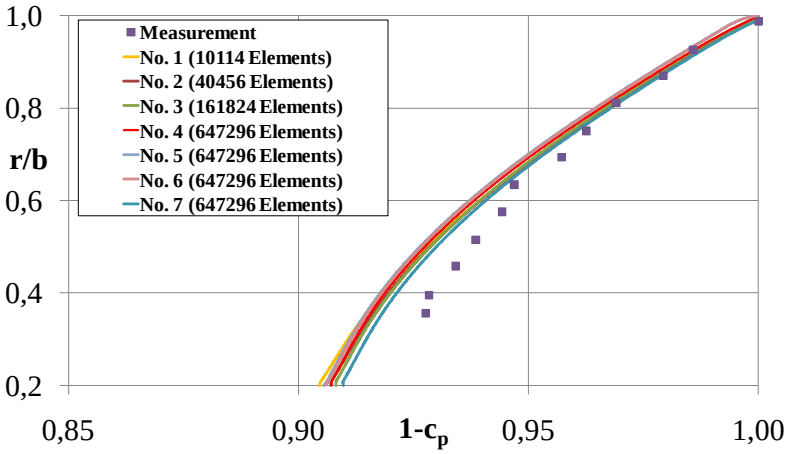

Fig. 60: Pressure distributions for different 2D grids

It is obvious that the calculated pressure distributions do not differ very much from each other. This makes sense because according to the basic boundary layer theory, the pressure is imposed from the core region which seems to be sufficiently resolved even for a moderate number of computational elements. It is not expected that for increasing grid size the pressure distribution dramatically changes. Comparatively, the pressure distribution computed with finest mesh (no. 7) is closest to the experimental values.
It is further noticed that for increasing grid size vortex structures occur in the small radial gap at the outer rotor radius (Fig. 61).

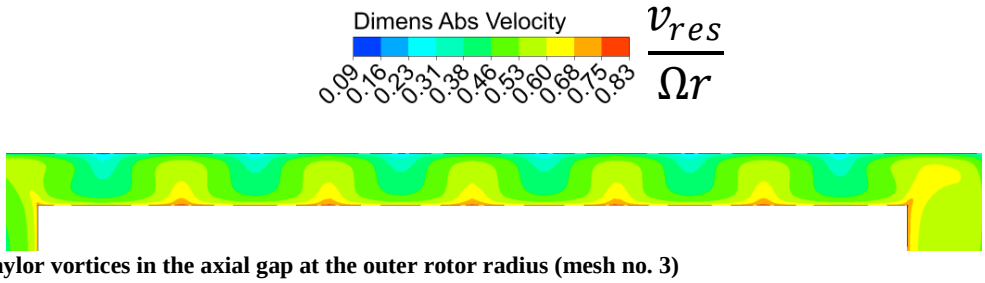

Fig. 61: Taylor vortices in the axial gap at the outer rotor radius (mesh no. 3)

These structures are the aforementioned Taylor vortices caused by inherent flow instability in this region. The instability originates from the decrease of the centrifugal forces with radius in the radial gap. Due to the no slip conditions, the fluid must have the same circumferential speed at the rotor surface. With increasing radial distance the fluid is retarded and the centrifugal forces decrease. The first grid fine enough to resolve these vortex structures properly is mesh no. 3.

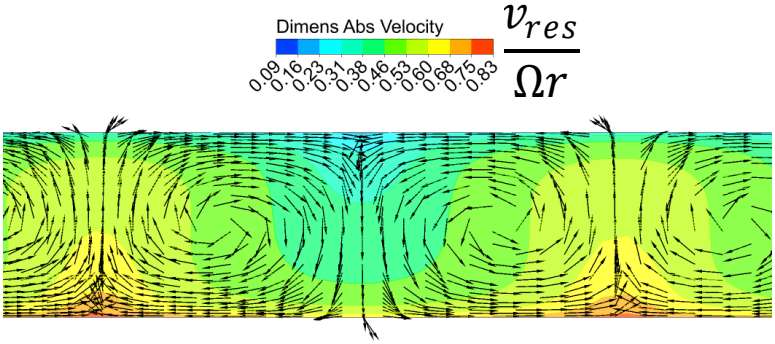

Fig. 62: Detailed view of a pair of Taylor vortices in the radial gap between outer rotor radius and casing (mesh no. 3)

Next, the influence of the grid size on the velocity distributions is shown in the subsequent figures. First of all, it can be noticed that the core velocity itself is predicted to be very similar in all cases. Only the coarsest mesh shows a slightly higher value than the other models. This agrees with the good overall prediction of the radial pressure distribution.

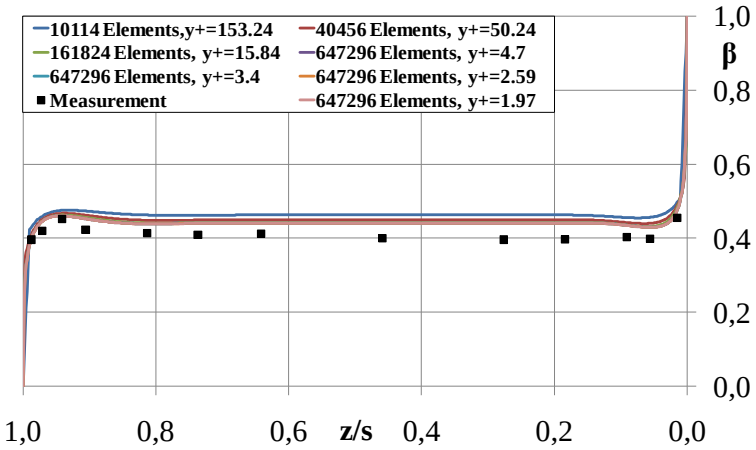

Fig. 63: Core rotation distribution at r/b=0.456 for different dense grids

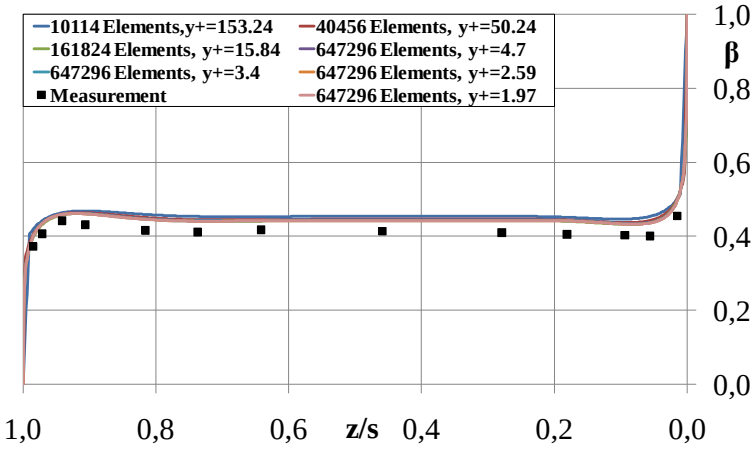

Fig. 64: Core rotation distribution at r/b=0.691 for different dense grids

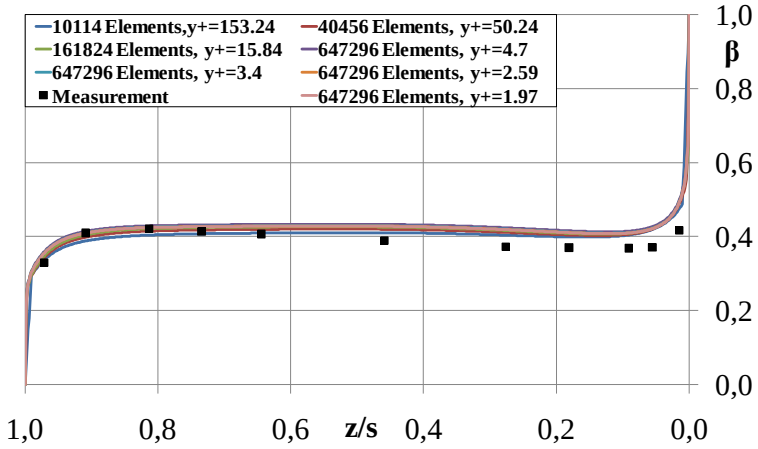

Fig. 65: Core rotation distribution at r/b=0.985 for different dense grids

The radial profiles reveal somewhat larger discrepancies especially with regards to the velocity maximum in the respective boundary layer. Nevertheless, finer grids than mesh no. 3 differ only insignificantly in the calculated profiles. Besides, the occurrence of a radial outward flow layer close to the stationary wall according to **Senoo and Hayami [85]** is clearly visible in the radial profiles between z/s≈0.9 and z/s≈0.8. An oscillatory behavior of the radial and tangential velocity components with increasing axial distance for a rotating fluid over a stationary wall has also been noticed in the solution of **Bödewald [12]**. **Owen [63]** shows that the velocity profiles derived from the linearized Ekman equation show the same behavior, although of smaller magnitude.

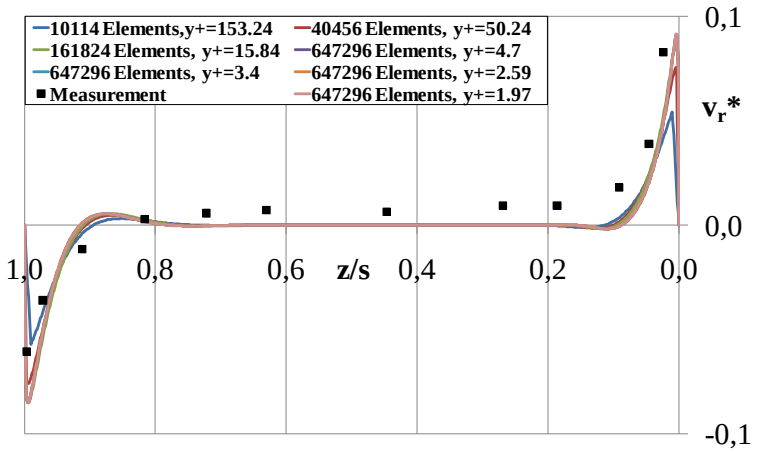

Fig. 66: Dimensionless radial velocity distribution at r/b=0.456 for different dense grids

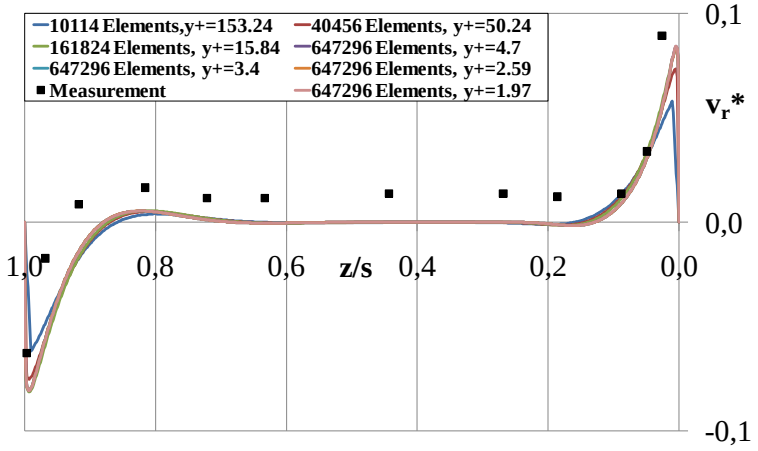

Fig. 67: Dimensionless radial velocity distribution at r/b=0.691 for different dense grids

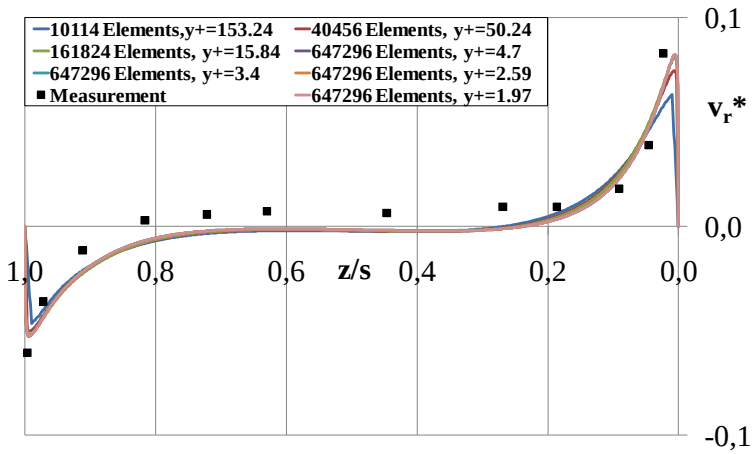

Fig. 68: Dimensionless radial velocity distribution at r/b=0.985 for different dense grids

These results allow the conclusion that grid no. 2, combined with the SST turbulence model, provides the best compromise between accuracy and computational effort. Some small improvements are visible from the more refined grids but are disproportionate to the increased computational demands.
Further studies for a 90 degree segment with a refined mesh near the outer radial casing revealed the occurrence of periodic vortex structures in circumferential direction. It is expected, that these vortices are similar to the Taylor vortices found in the radial gap above the shroud of the rotor. The structures persist only in case of the enclosed rotating disk and diminish as soon as a superposed through-flow is applied.

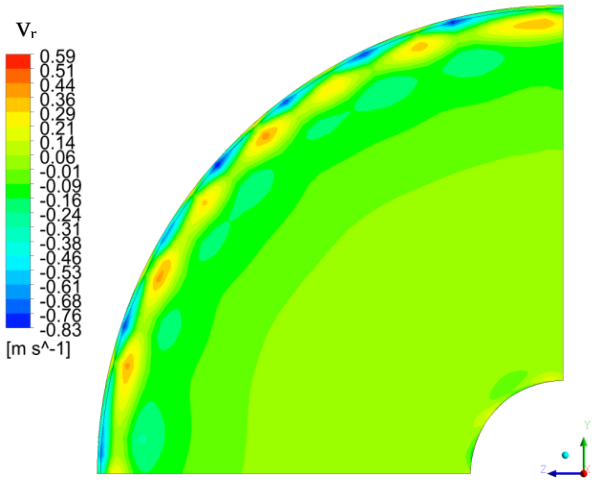

Fig. 69: Circumferential distribution of the radial velocity (r-φ plane) at z/s=0.25 from the rotor surface

5.3.1.4 Turbulence Modeling

The SST turbulence model includes an advanced option called “curvature correction” according to **Menter and Smirnov [56]**. This option is expected to improve the predictions in the case of strong rotating flows because basically eddy viscosity models are insensitive to streamline curvature and system rotation. The curvature correction uses an empirical function as a multiplier for the production terms in the SST model. The multiplier is based on a function originally developed by **Spalart and Shur [89]** and is limited within a certain range from strong convex curvature (stabilized flow - no production) to strong concave curvature (enhanced production). Further details can be found in the respective paper or the CFX user guide.
During this study, the curvature correction option turned out to be generally useful. Although the results for the enclosed rotating disk do not differ significantly whether the option is activated or not, the convergence behavior of the simulations improves. Therefore, the use of this feature is recommended for further studies. Besides, the curvature correction option is also available for the RNG k-ε model.
Basically four different turbulence models are compared with each other on mesh no. 2 in the following section. These are in particular:

- SST model with and without curvature correction
- Standard k-ε model
- RNG k-ε model with curvature correction
- Omega-stress model (RSM)

These models represent standard closure nowadays and are known to give reasonable results for a wide range of flows. In principle, Reynolds stress models can provide better predictions for rotating flows as they account for the additional anisotropy due to Coriolis forces in the rotating frame of reference. However, to exploit the benefits of Reynolds stress models very fine grids are necessary that allow for an explicit resolution of the boundary layers in flow regime IV. Furthermore, a considerable amount of extra computing time is necessary due to the additional transport equations. Moreover, the numerical solution of the resulting equations often results in very poor convergence behavior. Several stabilizing techniques are necessary in order to achieve a stable solution (e.g. **Poncet and Schiestel [73]**).

The omega-stress model is based on the ω-equation and allows for a more accurate near wall treatment with an automatic switch from a wall function approach to a low Reynolds number formulation based on the grid spacing. For all turbulence models based on the ω-equation, the automatic near wall treatment implemented in CFX is used in the calculations. This technique automatically switches from wall functions to a low-Re approach as the mesh is refined. K-ε models usually require y+<0.2 and complex damping functions to handle near wall turbulence. The k-ω model is more generous concerning the flows close to solid walls and requires y+<2 for a near wall resolution. Since even this cannot always be guaranteed at all walls in the simulations, the automatic near wall treatment assures a smooth transition from a low-Re formulation to a wall function approach.

The turbulent stress transport is very sensitive to streamline curvature even for weak amounts of curvature. Streamline curvature is generally accompanied by secondary flows and usually the eddy viscosity based turbulence models take the local turbulent stresses directly proportional to the local strain rates. This practice is known to be very insensitive to streamline curvature and is the main reason why for many cases the accuracy can be very low.

The obtained moment coefficients for the different turbulence models on grid no. 2 (40456 elements) are given in the following table:

Turbulence Model	SST	SST (curvature correction)	k-ε	RNG k-ε	Omega-stress (RSM)	Measurement
c_m	$1.9 \cdot 10^{-3}$	$1.9 \cdot 10^{-3}$	$1.88 \cdot 10^{-3}$	$1.74 \cdot 10^{-3}$	$1.89 \cdot 10^{-3}$	$2.05 \cdot 10^{-3}$

Table 21: Comparison of the moment coefficient c_m for different turbulence models on mesh no. 2

The values for the SST model with and without curvature correction are identical. The omega-stress model deviates little from the value of the SST model while the RNG k-ε model shows the biggest deviation from the experimental value. Next the pressure distributions will be compared to each other.

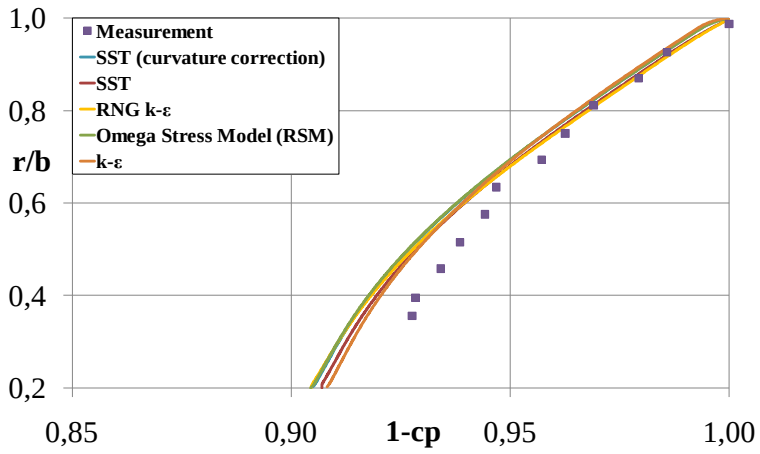

Fig. 70: Presure distributions for different turbulence models on mesh no.2

Again, all computed radial pressure distributions fall very close to each other. But as before, slight differences remain at smaller radii. It is important to notice here, that for this particular test case, the choice of the turbulence model has no major influence on the pressure distributions. Nevertheless, it must be kept in mind that the boundary layers are not explicitly resolved but rather modeled using wall functions. Since the turbulent shear stresses vanish in the core region (**Poncet et al. [72]**), turbulence modeling has no significance here.
In the next diagrams, the affiliating velocity profiles are compared.

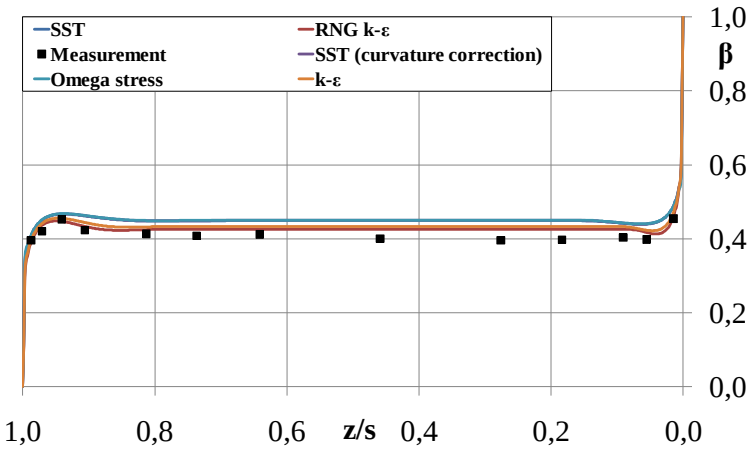

Fig. 71: Core rotation distribution at r/b=0.456

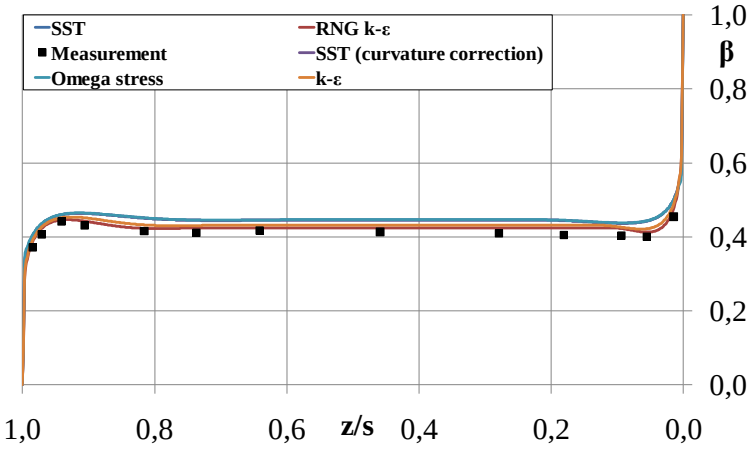

Fig. 72: Core rotation distribution at r/b=0.691

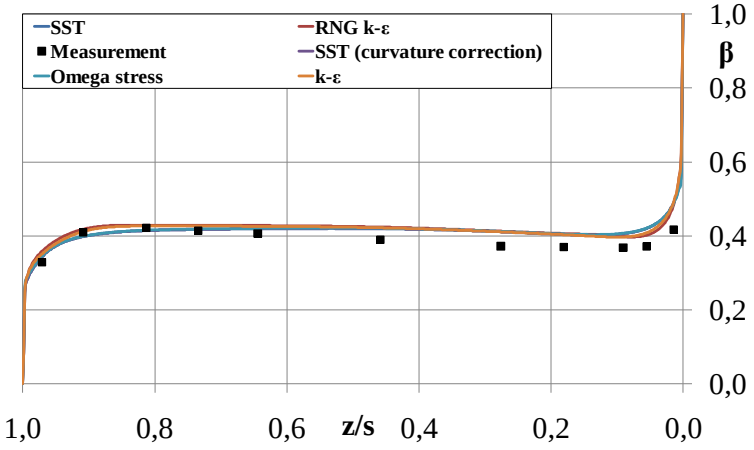

Fig. 73: Core rotation distribution at r/b=0.985

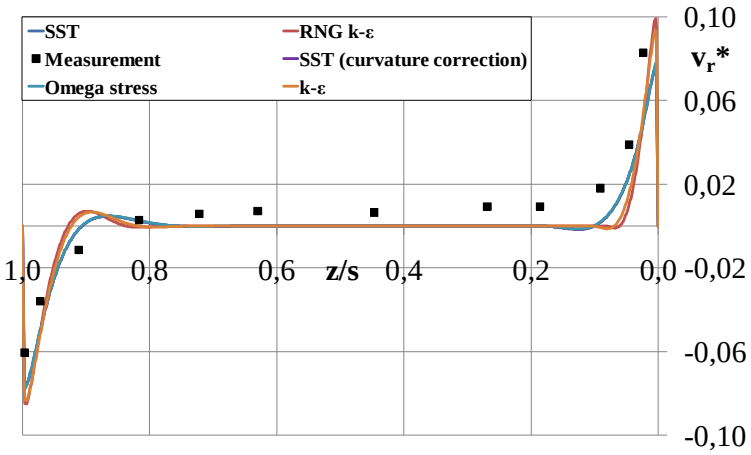

Fig. 74: Dimensionless radial velocity distribution at r/b=0.456

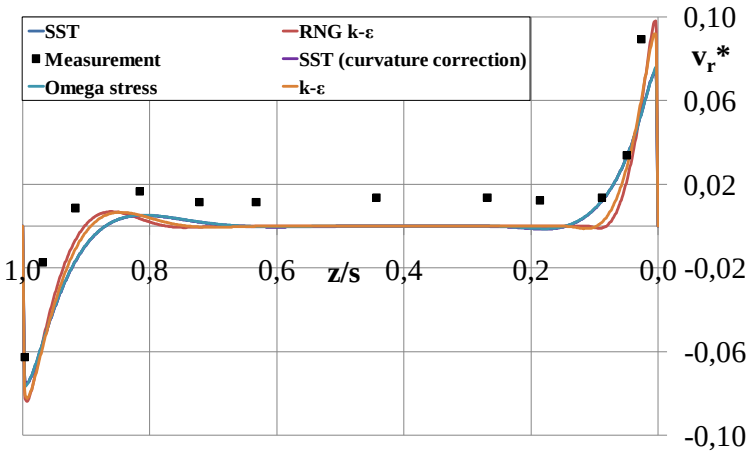

Fig. 75: Dimensionless radial velocity distribution at r/b=0.691

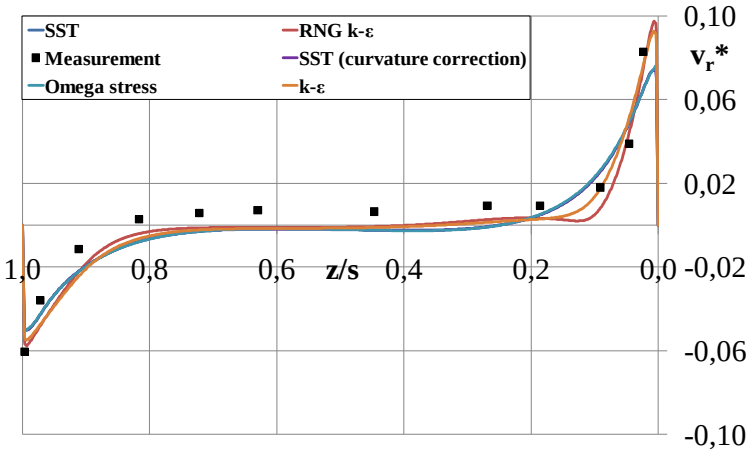

Fig. 76: Dimensionless radial velocity distribution at r/b=0.985

For the SST and the omega-stress model, the plotted velocity profiles for the radial and tangential velocity component are identical. This is certainly founded in the formulation for the wall function which is basically the same for both models in the present configuration. The RNG model and the standard k-ε model deviate slightly from each other. The core rotation distribution is slightly smaller at r/b=0.456 and r/b=0.691 while at r/b=0.985 the trend of the curve almost exactly coincides with the ones computed with the omega-stress and SST model. Larger deviations are also present in the rotor boundary layer for the radial velocity profiles. The velocity peak is higher and consequently the boundary layer thickness is reduced. The same tendency applies for the stator boundary layer but with smaller overall differences.

The y+ values for mesh no.2 do not allow for an explicit resolution of the boundary layers close to the walls. The SST model requires at least y+<2 which requires an appreciable amount of computational elements when the element quality in terms of the cell aspect ratio should not be significantly altered. The circumferential Reynolds numbers encountered in rotor-stator cavities are usually very large which leads to the formation of very thin boundary layers. However, resolving the boundary layers generally improves the prediction capability of near wall effects like separation or shear. The highest rotational velocities are present at the outer rotor radius and therefore the maximum y+ values occur exactly in this region.
y+ is defined as:

$$y+= \frac{y \cdot v_\tau}{\nu} = \frac{y \cdot \sqrt{\frac{\tau}{\rho}}}{\nu} \qquad \textbf{Eq. 159}$$

The shear results mainly from the circumferential velocity gradient as expressed in **Eq. 155**. Thus, y+ can be transformed to:

$$y+= y\sqrt{\frac{1}{\nu}\frac{dv_\varphi}{dz}} \qquad \textbf{Eq. 160}$$

The maximum velocity gradient occurs in the rotor boundary layer at the outer radial location where the circumferential velocity at the wall reaches its maximum. According to **Eq. 160**, y+ develops accordingly. This is also verified by the numerical solution exemplarily shown as an example in Fig. 77. For a known velocity gradient, the beforehand formula can be used to estimate the wall distance during the grid generation process necessary for a specific y+ value.

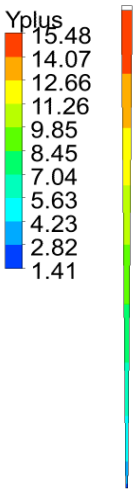

Fig. 77: Exemplary y+ distribution on the rotor (mesh no. 3)

Another interesting effect is that the resolution of the Taylor vortices in the radial gap between the rotor shroud and the radial casing does not depend solely on the mesh density but also on the employed turbulence model. The RNG k-ε model already resolves theses vortices clearly for mesh no. 2 while the SST model shows only the faintest signs of their appearance. A difference plot between these two calculations clearly emphasizes this tendency (Fig. 79).

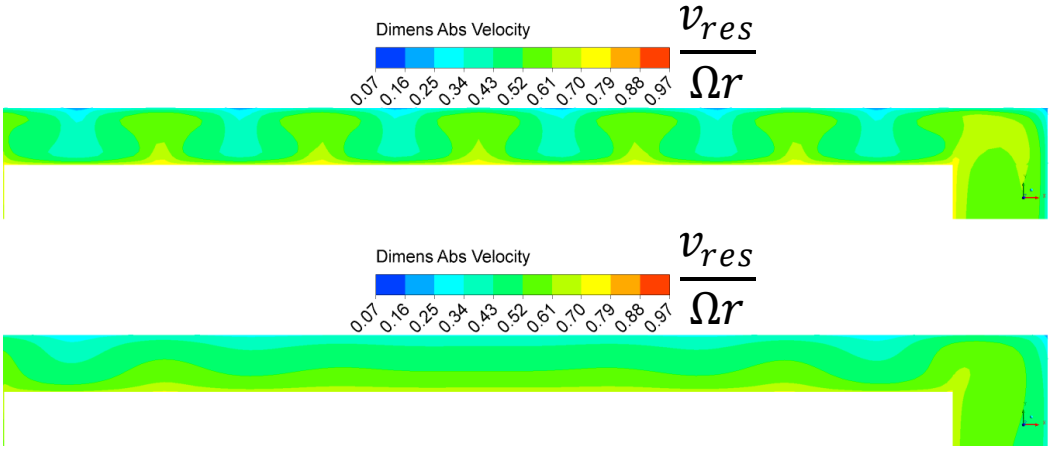

Fig. 78: Comparison of the computed dimensionless absolute velocity between RNG k-ε (up) and SST (down) turbulence model in the radial gap above the rotating disk

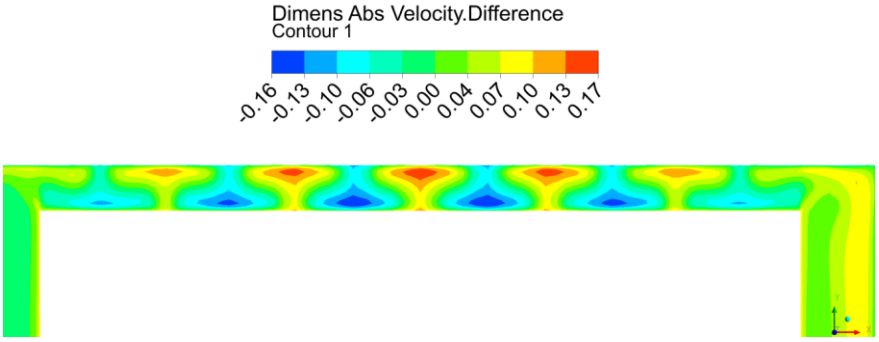

Fig. 79: Differences in the dimensionless absolute velocity between the RNG k-ε und SST turbulence model in the radial gap above the rotating disk

5.3.2 Influence of a Superposed Through-Flow

One of the most influential parameters in rotor-stator cavity flow problems is an external leakage flow which passes the cavity. In general, the leakage contains a circumferential velocity component and thus introduces additional angular momentum into the side chamber. In this study, first a superposed through-flow without swirl component is considered according to the FVV case 1.03. Afterwards, the additional involvement of a swirling through-flow is studied. The computation in such a case becomes more complicated because two effects interact with each other:

- The externally applied leakage flow rate
- The "natural" rotation-induced flow resulting from the rotation of the disk

The influence of the disk rotation is determined by the magnitude of the leakage flow. For high through-flow rates, the flow structure in the cavity will be predominantly determined by the leakage flow. In the opposite case, the rotation of the disk will be of significant importance for low through-flow.

If the disk is stationary, the cavity alternately behaves like a radial diffuser, or a nozzle depending on the through-flow direction. Therefore, for a centripetal flow, the pressure decreases as the radius decreases while the velocity increases. In case of a centrifugal flow, the contrary prevails. The inclusion of a superposed leakage flow considerably influences the flow conditions in the axial gap, especially with respect to the core rotation. For a non-swirling leakage, the core rotation is reduced in the whole gap and reaches higher values only within the Ekman layer due to the no slip condition.

In case 1.03, the geometry is extended in the radial direction in order to enable a through-flow. The grid resolution corresponds to mesh no. 2 from the study of the enclosed rotating disk. If no leakage is applied and the geometries for 1.03 and 1.02 are compared, the core rotation values for case 1.03 are lower. This is caused by the braking effect of the additional surfaces. Therefore, the core rotation decreases with increasing radius. In case of a small gap width with interacting boundary layers viscous effects damp out the influence of the discarding surfaces. Comparatively, the influence of the additional radial extent is only obvious at the outer radii and does not reach as far as in the case of separate boundary layers.

A limitation with respect to the setup of the numerical model are the available boundary conditions given in the FVV report to define the inlet and outlet adequately. Only the flow coefficient is known precisely. It is assumed that the pressure at the exit of the system corresponds to the ambient pressure. A more or less stable configuration of boundary conditions finally used in the computations is summarized in the following table:

	Boundary type	Frame type	Mass and Momentum	Turbulence
Inlet	Inlet	Stationary	Mass flow rate	Intensity 1%
Outlet	Outlet	Stationary	Static pressure 0 Pa	-

Table 22: Boundary Conditions for the case FVV 1.03

For very small through-flow rates, the boundary condition at the outlet is changed to a mass flow outlet to improve convergence.

5.3.2.1 Centripetal Through-Flow

In the case of a centripetal through-flow, the flow enters the cavity at the outer radial casing and exits in axial direction right above the rim. Since the fluid contains no circumferential velocity component, the core flow is decelerated due to momentum exchange. Three through-flow rates are considered and the resulting moment coefficients are summarized in the following table:

Through-flow coefficient c_D‘	Through-flow direction	c_m - CFD	c_m - Experiment
$14 \cdot 10^4$	Centripetal	0.0036	0.003297
$7 \cdot 10^4$	Centripetal	0.003088	0.00276
$0.8 \cdot 10^4$	Centripetal	0.00202	Not available

Table 23: Moment coefficients for centripetal through-flow without swirl

The deviations for the frictional resistance are now somewhat larger than for the enclosed disk. The through-flow rates are chosen with respect to the available results in the FVV report. Not all of the measured data are given in the report which limits the comparability. With respect to the available boundary conditions, the agreement can be judged as good although the numerical simulations tend to over-predict the measured values.

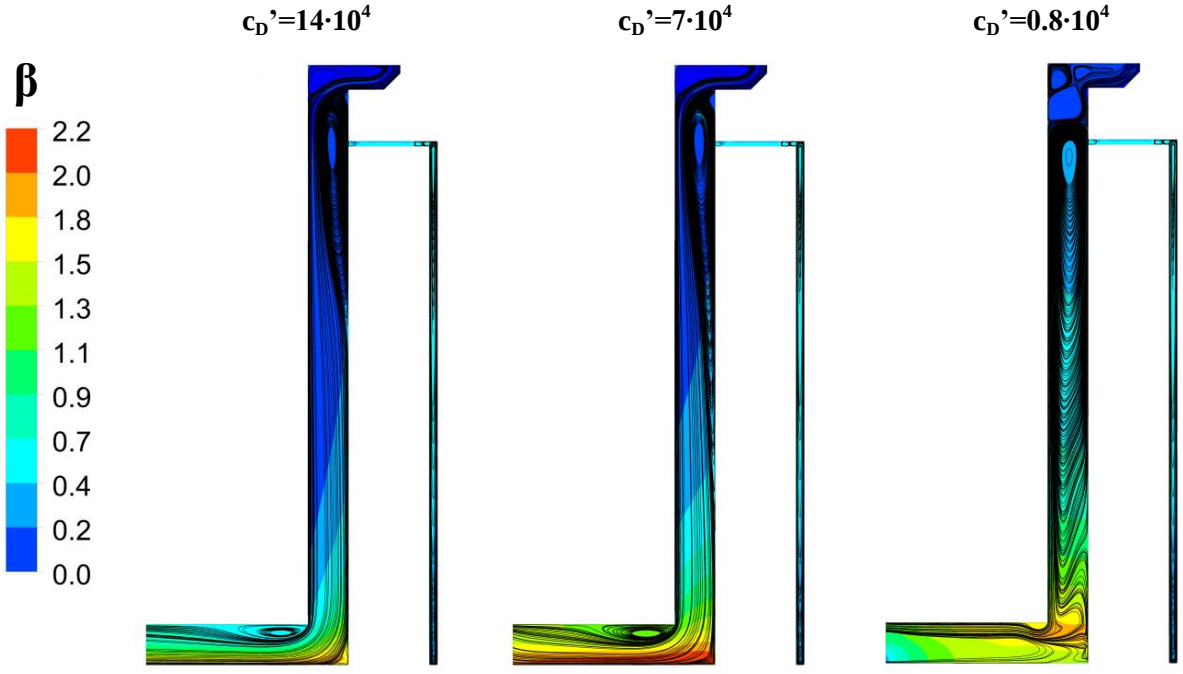

Fig. 80: Surface streamlines in case of centripetal through-flow coloured by the core rotation magnitude

To gain a qualitative survey of the flow in the meridional plane, Fig. 80 shows the respective surface streamlines for all three cases including the contours of the core rotation. For high through-flow rates, the flow structure is very similar. A recirculation area is formed close to the rotating disk whose size depends on the magnitude of the leakage flow. For maximum through-flow, the recirculation region is confined to the upper part. In this region, the leakage flows radially inwards close to the stator. The recirculation region results from the rotation of the disk and the turning of the fluid from axial to radial direction. However, when the through-flow is reduced this region reaches further radially inwards which underlines its origin from the disk rotation. For the smallest through-flow rate, the streamline pattern is obviously very similar to case of the enclosed rotating disk. In conclusion, the influence of the disk rotation on the flow structure is dominant for small leakage flow rates. It is worth noting that this particular calculation has been very difficult to converge in contrast to the other cases, where the flow structure is clearly dictated by the outer through-flow.
The resulting maximum y+ values at the outer rotor radius for the present grids are given in the following table:

	c_D‘=14·10^4	c_D‘=7·10^4	c_D‘=0.8·10^4
$y+_{max}$	33.19	31.19	29.49

Table 24: Maximum y+ on the rotor in dependance on the through-flow coefficient

These values match mesh no. 2 from the study of the isolated cavity. In the case of a centripetal flow, the meridional velocity component increases for decreasing radii as a consequence of the decrease of the through-flow area. This results in smaller core rotation values.
Velocity measurements are only given for c_D’=14·10^4. The comparison with the CFD results is presented in Fig. 81 and Fig. 82. The core rotation agrees with the experiment in an acceptable range while the discrepancies in the radial velocities are larger.

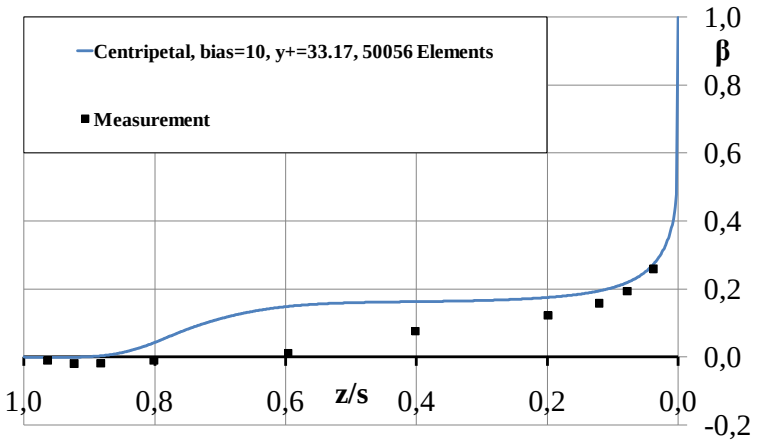

Fig. 81: Core rotation distribution in case of centripetal through-flow without swirl (c_D'=14·10^4) at r/b=0.985

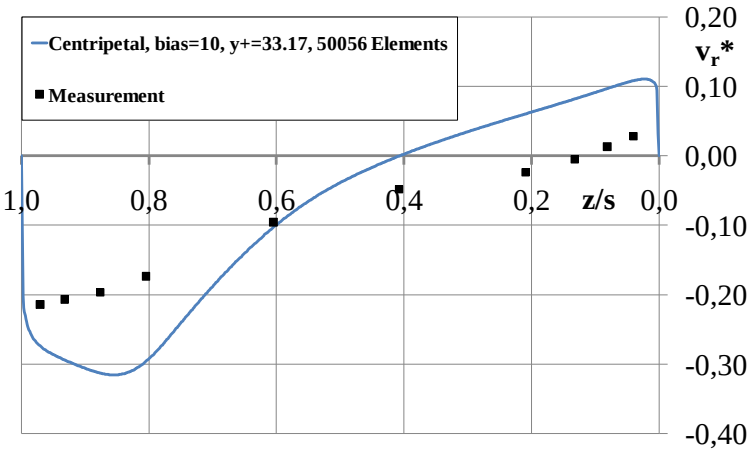

Fig. 82: Dimensionless radial velocity distribution in case of centripetal through-flow without swirl (c_D'=14·10^4) at r/b=0.985

The diagrams underline that the through-flow suppresses the core rotation. Even at the outer radius, the circumferential velocity component diminishes when approaching the stator. In the middle of the cavity the core rotation predicted by the simulation is about 50% smaller than for the enclosed rotating disk. No typical signs of Batchelor type of flow are apparent. For example, the radial velocity does not become zero which indicates that no distinct core region is present. However, the measured radial velocity data appear to be somewhat too small especially in the rotor boundary layer. This might be a result of the measuring method. **Hamkins [36]** remarks that "…several authors have reported systematic deviations between the integrated measured radial velocity profiles and the separately measured volumetric through-flow" when multiple-hole hydrodynamic velocity probes are used.
The radial pressure distributions for the three different leakage flow rates are shown in Fig. 83. No measured profile is available for the lowest through-flow rate and therefore the pressure distribution for zero leakage is included instead.

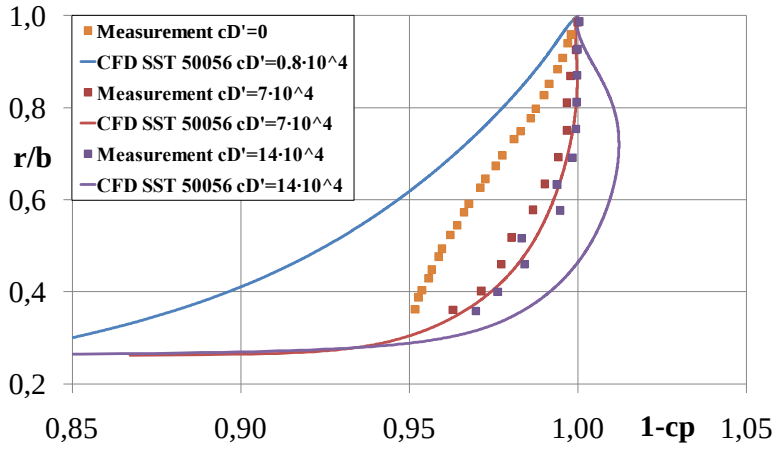

Fig. 83: Pressure distributions for non-swirling centripetal through-flow

The overall agreement is still satisfactory, especially for c_D'=$7 \cdot 10^4$. It can be clearly seen from the shape of the curve that the through-flow alters the pressure distribution. The core rotation is slowed down and the pressure drop is reduced. This leads to smaller c_p values. The turning of the fluid at the lower radius from radial to axial direction further decreases the pressure.
The fact that the pressure distribution in Fig. 83 reaches higher values than one for 1-c_p can be explained from the streamline pattern. The recirculation pattern for the through-flow coefficient c_D'=$14 \cdot 10^4$ shows that the typical flow structure which is known from enclosed rotating disk case is confined to the outer disk radius. The incoming through-flow is compressed in this region which leads to an acceleration of the fluid and thus a decrease in the local pressure. Since the expansion of the recirculation pattern becomes smaller with decreasing radius, the superposed flow is retarded and the pressure increases. This leads to negative c_p values and thus 1-c_p can become greater than one.

5.3.2.2 Centrifugal Through-Flow

The moment coefficients for centrifugal flow direction are compared in the following table:

Through-flow coefficient c_D'	Through-flow direction	c_m - CFD	c_m - Experiment
$14 \cdot 10^4$	Centrifugal	0.0051	0.0044
$7 \cdot 10^4$	Centrifugal	0.004236	0.0038
$0.8 \cdot 10^4$	Centrifugal	0.0027	Not available

Table 25: Moment coefficients for centrifugal through-flow without swirl

The deviations are of the same order as for centripetal flow. As in the centripetal through-flow case, the frictional resistance of the rotating disk increases with increasing leakage flow rate since the through-flow suppresses the fluid rotation induced by the rotor.
From the plot of the surface streamlines in Fig. 84, a large recirculation region is apparent which is now attached to the stator and the flow passes the cavity in the vicinity of the rotating disk. The flow in this case can be divided into four different regions: A source region in the inner part of the cavity,

the recirculation bubble, the boundary layers on the rotor (Ekman layer) and stator (Bödewald layer) and finally the exiting region where the flow leaves the cavity. **Elena and Schiestel [30]** observe similar structures in their study, although their configuration is slightly different at the exiting region. These flow conditions lead to a non-uniform velocity distribution in the axial gap which homogenizes towards outer radii and to low pressure in this region. For the lowest flow rate, the through-flow influence is dominant only in the lower part whereas the flow pattern in the upper part is strongly determined by the disk rotation. As before, this case is very difficult to converge. Another noticeable difference is that the core rotation distribution is substantially lowered. In case of centripetal flow, the inward flowing leakage is accelerated in tangential direction by the disk. Thus, the leakage contains angular momentum that magnifies for lower radial positions.

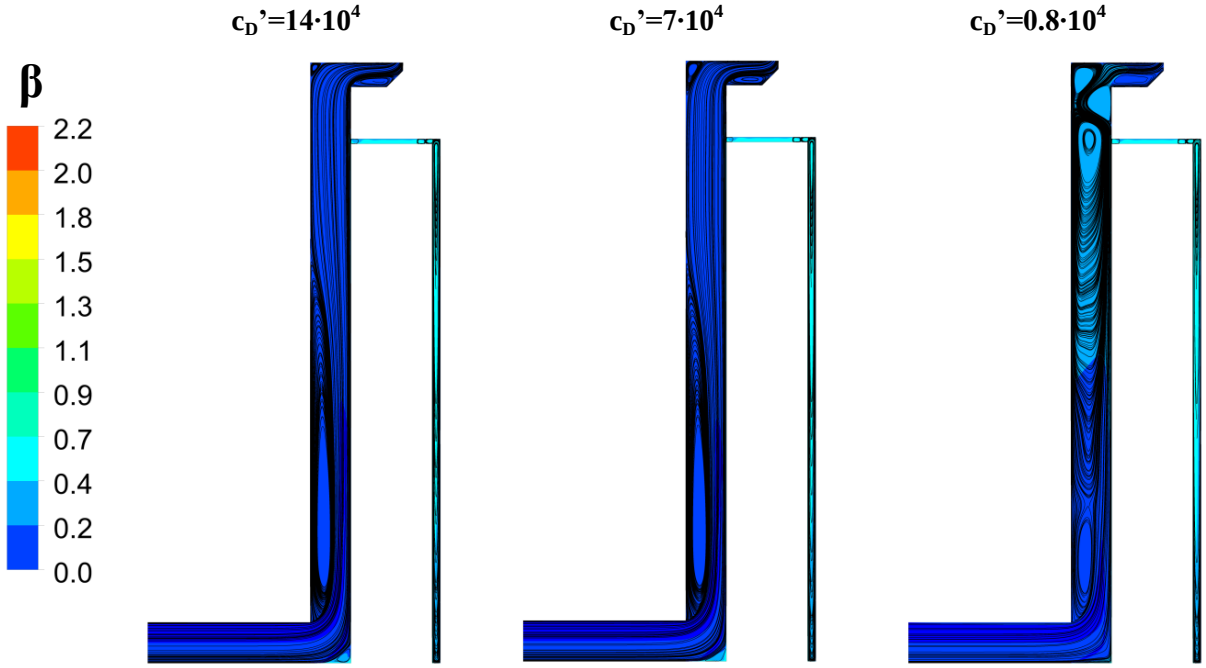

Fig. 84: Surface streamlines in case of centrifugal through-flow coloured by the core rotation magnitude

The velocity profiles are presented in Fig. 85 and Fig. 86. They give clearly evidence that in case of large through-flow, the flow becomes Stewartson-like at the outer disk radius with radial outflow across the whole gap width. This agrees with the findings of **Poncet et al. [72]**. High circumferential velocities remain only in the vicinity of the rotating disk. Besides, an excellent agreement between the measured and the computed core rotation factor is observed. For weak leakage, the flow structure resembles the case of a closed cavity as in the centripetal case. With increasing through-flow the radial velocity distribution resemble a Poiseuille profile.

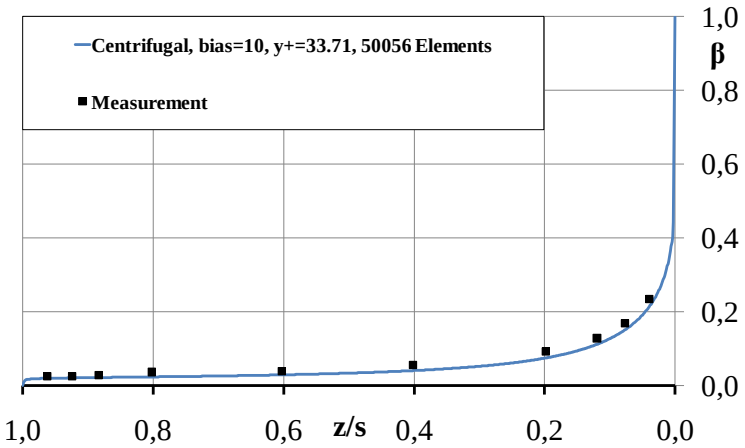

Fig. 85: Core rotation distribution in case of centrifugal through-flow without swirl (c_D'=14·10^4) at r/b=0.985

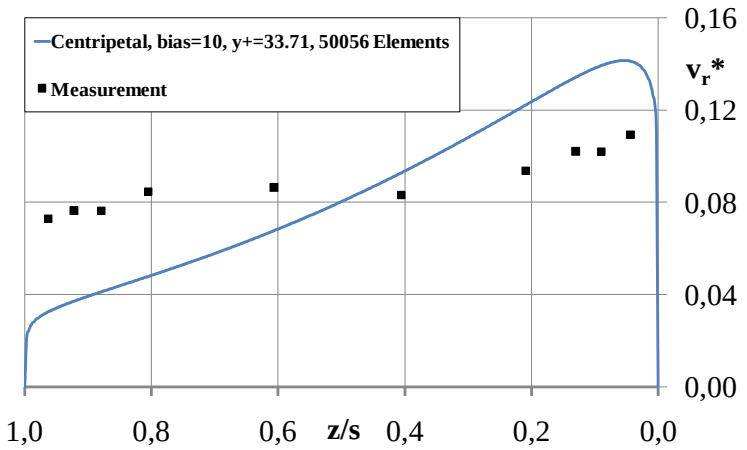

Fig. 86: Dimensionless radial velocity distribution in case of centrifugal through-flow without swirl (c_D'=14·10^4) at r/b=0.985

The resulting radial pressure distributions are displayed in Fig. 87. For the smallest flow rate the curvature of the curve is completely different compared with the other two cases. This can be regarded as a clear indication that the pressure is mainly determined by rotation rather than the through-flow in contrast to the other cases. The closest agreement with the measured results is again obtained for c_D'=7·10^4.

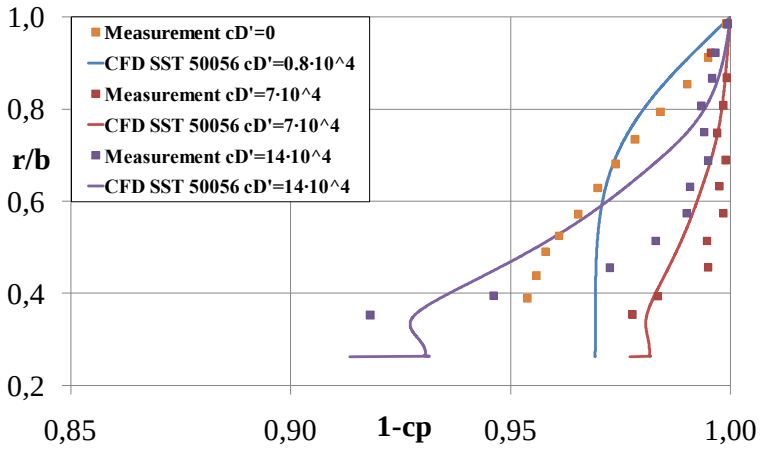

Fig. 87: Pressure distributions for non-swirling centrifugal through-flow

The fact that the cross sectional area increases linearly with the disk radius leads to a deceleration of the fluid (diffuser effect) causing "fuller" profiles.
Additional computations with refined grids close to the rotor and stator wall have not shown any changes in the above presented results. This confirms the robust and accurate formulation of the near wall treatment embedded in the SST model in dependance on the near wall grid density mentioned by **Menter et al. [55]**.

5.3.3 Influence of a Superposed Through-Flow with Swirl

In real turbomachinery applications, the entering leakage flow can contain a significant amount of angular momentum resulting from the impeller outflow. **Kurokawa and Toyokura [44]** for example show that not the mere volume flow rate but rather the angular momentum flux has the most significant effect on the axial thrust.
One major issue in this investigation has been the specification of proper boundary conditions, especially with respect to the swirl component of the leakage flow. Guide vanes, oriented either in radial (centripetal flow) or axial (centrifugal flow) direction are used in the experiments to deflect the fluid in the circumferential direction. Since no explicit information about the respective flow magnitudes are given in the report, the circumferential velocity component must be estimated from the blade angle of the guide vanes (flow angle = blade angle). The meridional component is calculated from the continuity equation disregarding the obstruction by the guide vanes. However, as mentioned

in the report, the flow angle does not correspond to the geometrical angle of the profile and further varies in the axial direction. Measurements just beyond the vanes are not available, only at a lower radial location at r/b=0.985. The flow angle is said to depend on the geometrical angle of the profile, the superposed volume flow rate and the different circumferential velocities from the core and the rotating disk. According to Fig. 88, the tangential and radial velocities are calculated from the following relationships:

$$\dot{m} = \frac{c_D'}{Re_\varphi}\rho\Omega b^3$$
$$v_r = \frac{\dot{m}}{\rho A} \qquad \textbf{Eq. 161}$$
$$tan(90° - \alpha) = \frac{v_\varphi}{v_r}$$

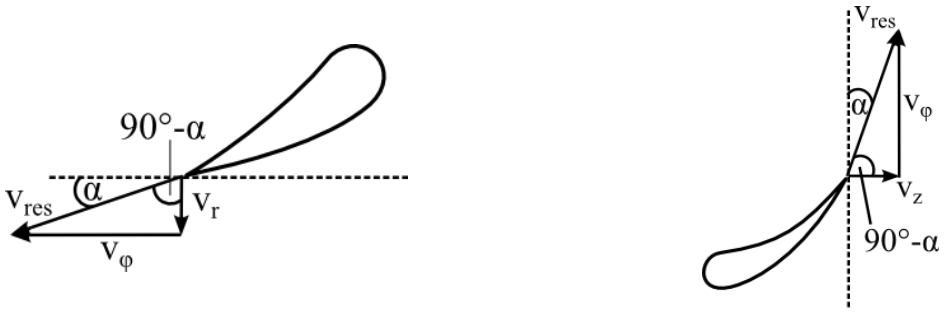

Radial guide vanes Axial guide vanes

Fig. 88: Velocity triangles for specification of swirl component

All numerical calculations presented below have been performed for the highest mass flow rate in the experiments because most experimental data are available for this particular case.
The inclusion of the swirl requires some modifications of the model. In the experiment, guide vanes are used to deflect the fluid in the tangential direction. A specification of a circumferential velocity component at a radial domain boundary is not useful because no convergence can be obtained for such a configuration. The reason is that the boundary is placed in a region where high flow gradients occur. To solve the problem, the outer L-shaped part is included and, instead of modeling the guide vanes explicitly, a momentum source is defined at the respective region.

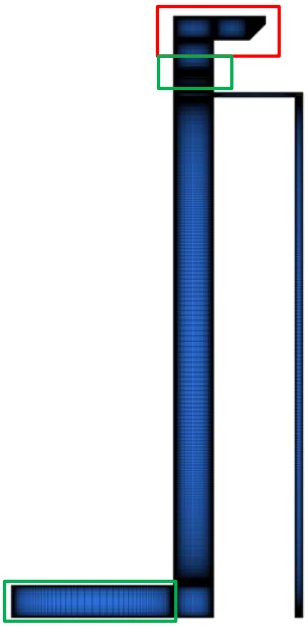

Fig. 89: Modified modeling domain with L shaped upper part (red) and position of the momentum source region (green)

The inlet region is closed and the momentum source is defined as a mass source. This allows the definition of both the velocity components and the mass flow rate which resolves the problem of deviations between calculated and theoretical mass flow rates due to alternating density. The definition as mass source adds an additional source term in the momentum equations. For a uniform setup, the same strategy is applied for the centrifugal through-flow case. In case of centripetal through-flow with swirl, stronger gradients of the flow variables occur in radial direction. Therefore, the aspect ratio of the cells should be kept below 500 to ensure a stable solution.
A more detailed view of the mesh structure is given in Fig. 90. It is designed for high Re computations and consists of 80x300x1 divisions in the axial, radial and tangential direction (G=0.0625). **Poncet et al. [74]** simulate a similar case. Their mesh resolution is quite comparable (70x240x1, G=0.036). The relative distance of the first wall adjacent mesh point is $\Delta z/s=7\cdot10^{-4}$ which ensures y+ values between 1 and 33.

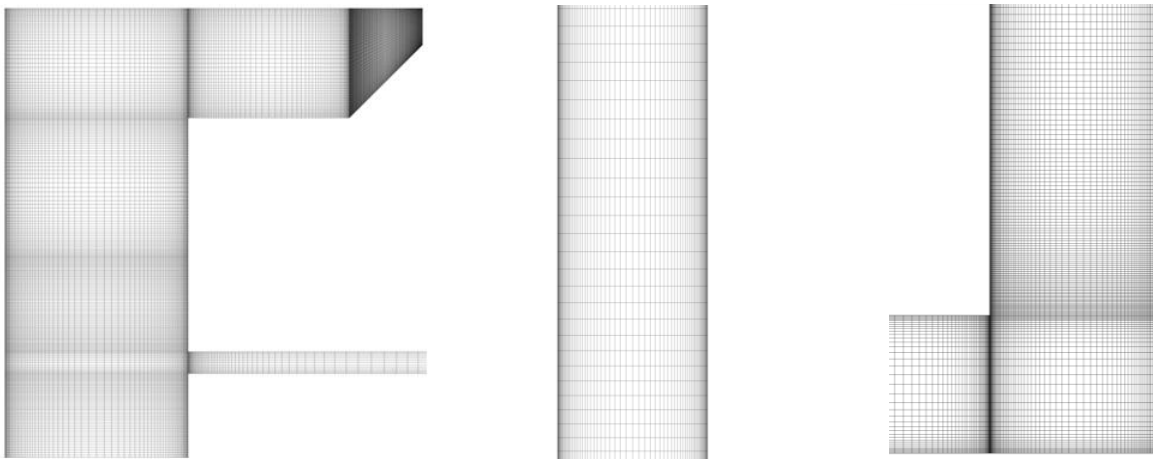

Fig. 90: Detailed views of the computational mesh in case of swirling through-flow

5.3.3.1 Centripetal Through-Flow

In Fig. 91, the results of the through-flow without (left) and with swirl (right) are compared.

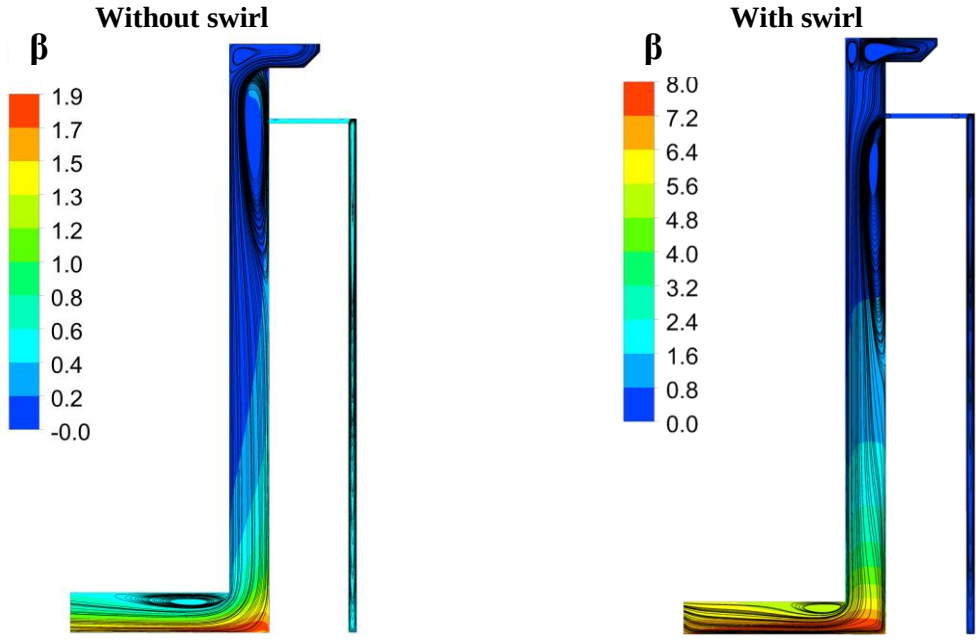

Fig. 91: Influence of a centripetal swirling through-flow on the flow field

The circumferential velocity component amounts to 66 m/s at the momentum source and the mass flow rate is approximately 1 kg/s. Of course, the swirl-free leakage flow strongly lowers the core rotation throughout the whole flow domain as discussed before. Higher core rotation factors occur

only towards lower radii in the vicinity of the hub and along the rotating disk. In contrast, the core rotation magnifies with decreasing radius for the swirling through-flow and becomes even greater than one. In case of strong incoming angular momentum, the overall flow structure is largely determined by the conservation of angular momentum in the radial direction. Furthermore, both cases show the appearance of recirculation regions near the rotating disk. On the left hand side in Fig. 91, the turning of the leakage from axial to radial direction is the major reason for the recirculation. In addition, the disk pumping effect appears only at the outer disk radii and is suppressed by the radial leakage flow at lower radii. On the right hand side, the recirculation pattern develops further downstream at the outer rotor radius and ends just at the point where the core rotation becomes equal to one. In this case, the rotation induced effects are clearly dominant for the flow field.
The comparison with the measured velocity profiles is given in the following two diagrams:

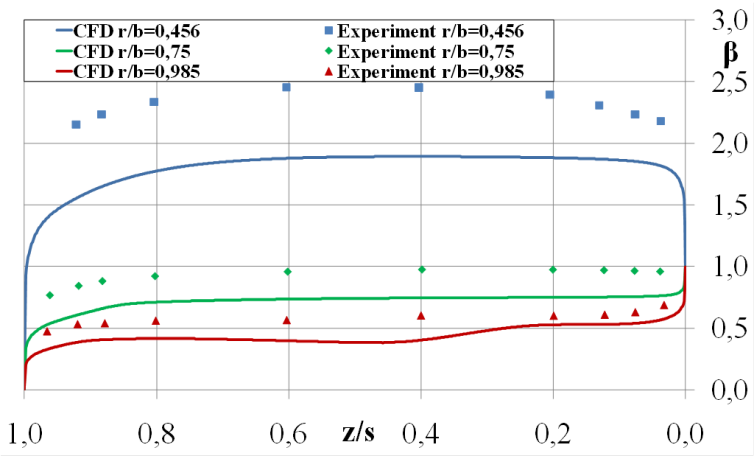

Fig. 92: Core rotation distribution at three different radial positions

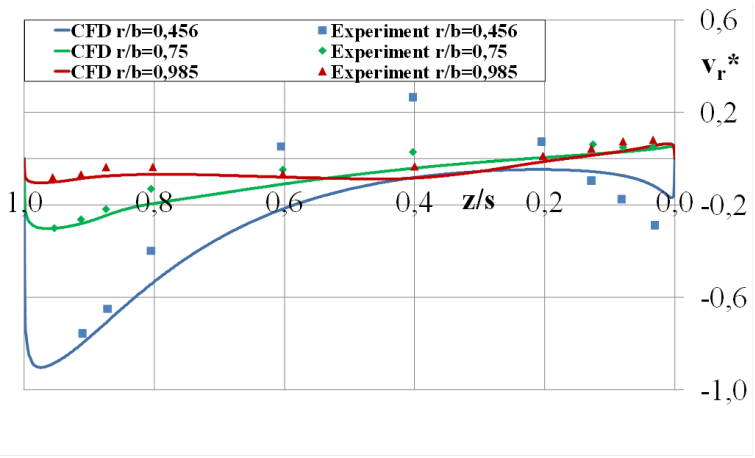

Fig. 93: Dimensionless radial velocity distribution at three different radial locations

The core rotation is consistently under-predicted at all three radial locations. Surprisingly, the agreement for the radial velocity component is much better despite one aspect. At the lowest radial location, the measured points become positive in the middle of the cavity. This is not reproduced by the numerical simulation. As already mentioned, the core rotates faster than the disk at lower radii which results in a breakdown of the common flow structure and the creation of an attachment line where fluid and rotor rotate at the same speed. Outgoing from this point, the dominant pressure gradient drives the fluid radially inwards even in the rotor boundary layer for decreasing radii.
Based on the measured profiles, **Radtke and Ziemann [78]** give a qualitative streamline pattern of the flow structure for rotation faster than the disk. According to their measurements, two counter rotating vortices are formed with radial outflow in the core region. **Owen and Rogers [64]** also discuss this issue. Their theoretical streamline pattern does not show any sign of positive radial outflow. The fluid is directed radially inwards along the complete gap width for rotation faster than the core. This is also confirmed by the streamline patterns found by **Poncet et al. [72]** in Fig. 9 who use a more elaborate

Reynolds stress model which is in good agreement with the measured velocity and turbulence data. The present results also support the flow pattern according to **Owen and Rogers [64]**.

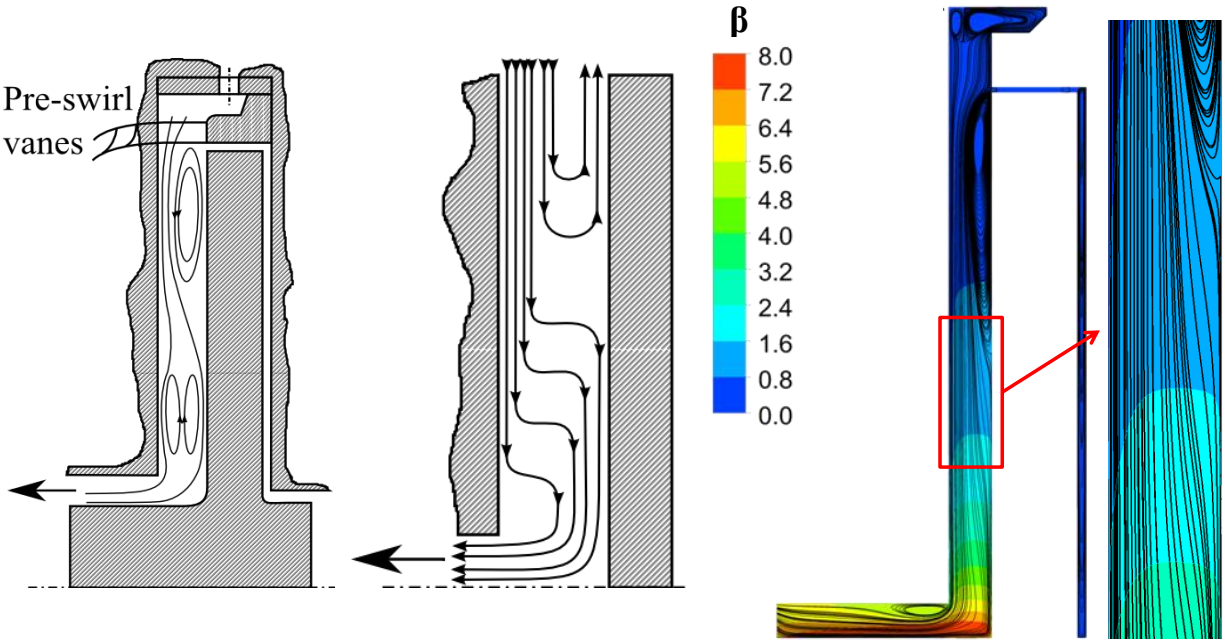

Fig. 94: Flow strucutre in the case of rotation faster than the core; left: Streamline pattern according to Radtke and Ziemann [78], middle: Streamline pattern according to Owen and Rogers [64], right: Computed streamline pattern and contours of the core rotation

The radial pressure distribution (Fig. 95) is basically correctly predicted but with some quantitative differences that are related to the underestimation of the core rotation. This also brings out the strong coupling between these two parameters in the case of flow regime IV.

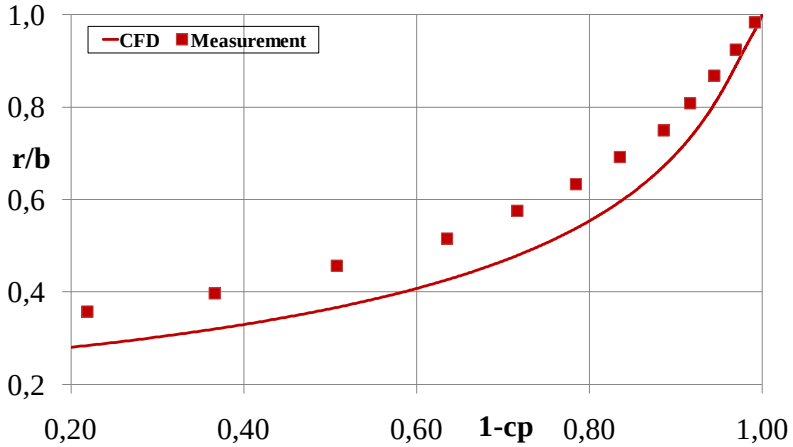

Fig. 95: Pressure distribution distribution in case of swirling centripetal through-flow (entrance rotational velocity 66 m/s)

High rotation rates of the fluid lead to a much lower frictional resistance of the rotating disk since the difference between the angular momentum flux entering and leaving the boundary layer is significantly reduced. This is confirmed by the measured moment coefficient which is considerably lowered in the case of swirling centripetal through-flow. For the present case, no reliable information about the experimental value of the moment coefficient could be obtained from the project report.

c_m - CFD
$4.39 \cdot 10^{-5}$

Table 26: Moment coefficient in case of swirling centripetal flow

The previously given results indicate that the core rotation is somewhat underpredicted. For this reason, a second calculation has been performed with a higher circumferential entrance velocity (83 m/s). For this boundary value, the agreement between numerical and experimental data improves which can be seen from the next two diagrams.

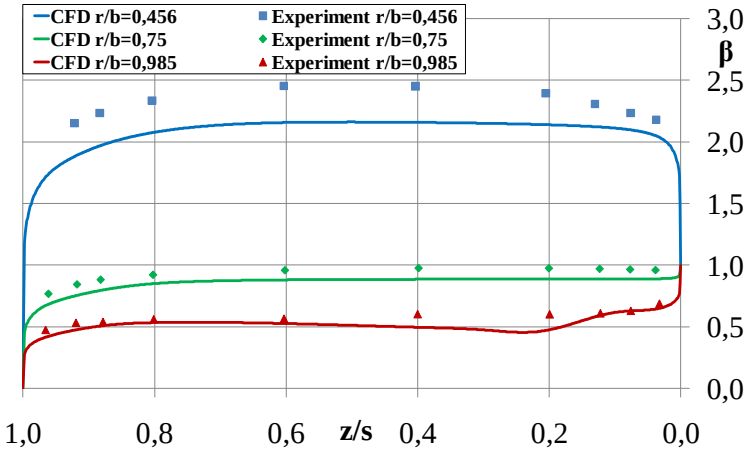

Fig. 96: Core rotation distribution at three different radial positions (entrance rotational velocity 83 m/s)

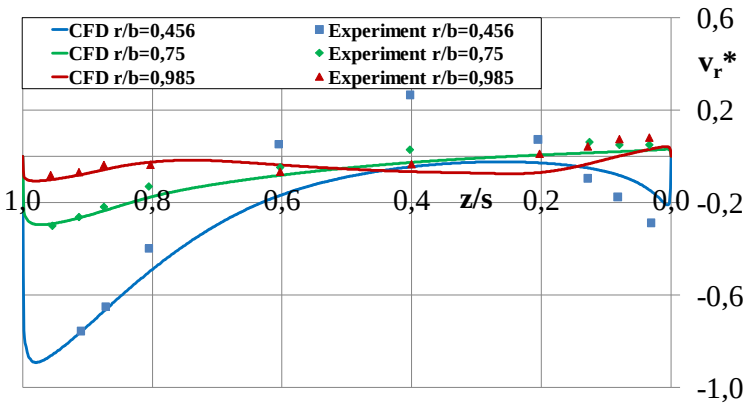

Fig. 97: Dimensionless radial velocity distribution at three different radial locations (entrance rotational velocity 83 m/s)

Despite the closer agreement with the measured curves, no sign of a positive radial velocity is present in the core region for the lowest radial location. The same applies as well for all additional calculations performed with higher entrance swirl.

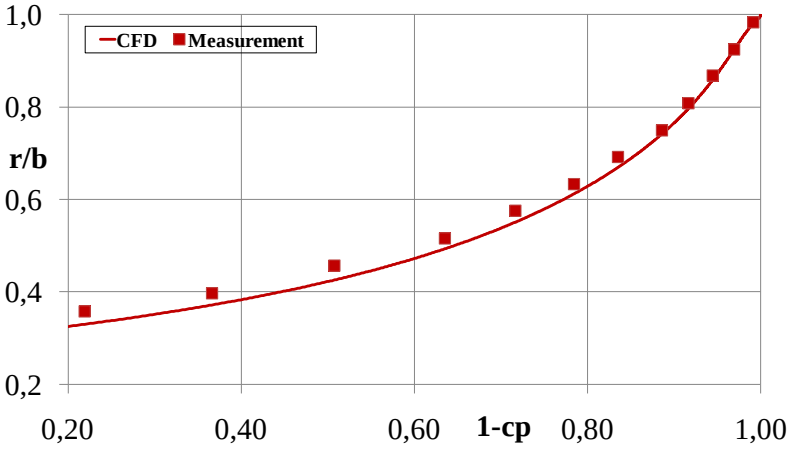

Fig. 98: Pressure distribution (entrance rotational velocity 83 m/s) in case of swirling centripetal through-flow

For the latter reason, the disagreement between the numerical and experimental conditions concerning the fluid rotation in the core does not seem to be responsible for the occurrence of positive outward flow in the core. As expected, the computed and measured pressure distributions are brought closer together for the increased entrance rotation of the fluid. A strong swirling centripetal through-flow causes a much greater pressure drop across the cavity, significantly reducing the resulting axial force.

5.3.3.2 Centrifugal Through-Flow

In case of centrifugal flow, the core rotation decreases with increasing radius. A momentum source is again used as the inlet condition for the entering leakage. The estimated entrance rotation amounts to 289 m/s while a mass flow rate of 1 kg/s is retained. A comparison of the resulting flow pattern with the non-swirling case is given in Fig. 99.

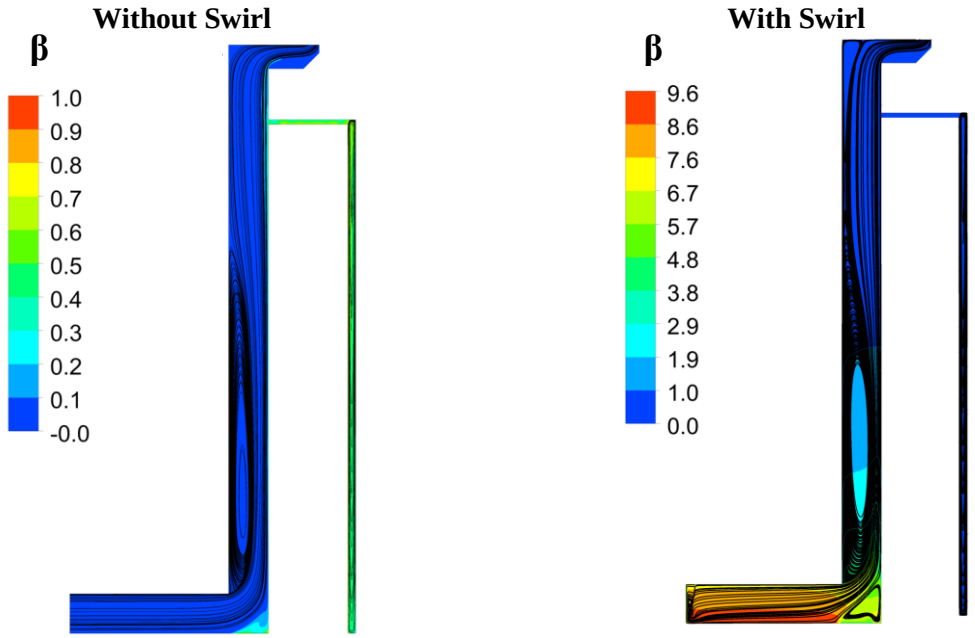

Fig. 99: Influence of centrifugal swirling through-flow on the flow field

The general relationships are similar to those in the centripetal flow case. For swirl-free through-flow, the fluid rotation is almost completely suppressed except for a small region close to the rotating wall and the hub. In both configurations, the through-flow takes place in the vicinity of the rotating disk.
The agreement between computed and measured moment coefficient is quite good with respect to the uncertainties resulting from the unknown flow conditions in the experiments.

c_m - CFD	c_m - Experiment
$8 \cdot 10^{-4}$	$1.8 \cdot 10^{-3}$

Table 27: Moment coefficient in case of swirling centrifugal flow

Fig. 100 and Fig. 101 depict the velocity profiles for the core rotation and the dimensionless radial velocity. The core rotation is now overestimated with respect to the experimental values which causes lower pressure levels. Again, the agreement between experimental and numerical data improves for raising radial coordinates. Due to the high mass flow rate, the flow is directed radially outwards over almost the entire gap width. Negative values are only present in the close vicinity of the stationary wall. As expected from the over-prediction in the core rotation, the pressure is lower than the measured values (Fig. 102).
Aside from the previously mentioned results, the importance of turbulence modeling can be shown for the centrifugal flow case. In Fig. 103, the dimensionless radial velocity distributions calculated with the SST and the BSL turbulence model are compared. Especially at the lower radii (r/b=0.75), the BSL model totally fails to mimic the general flow structure.

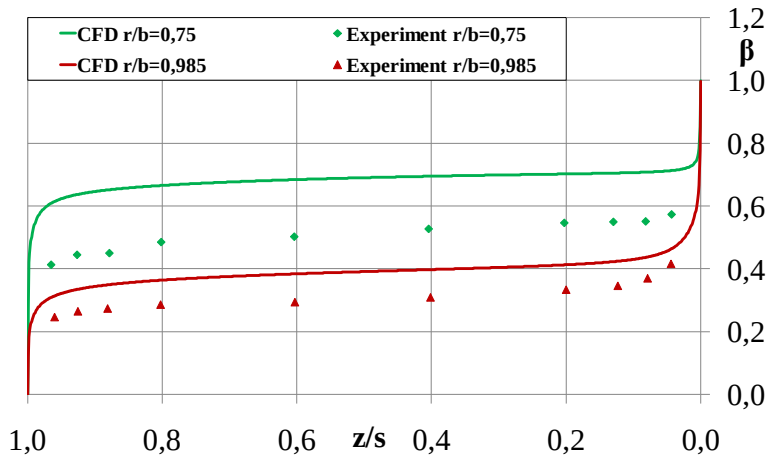

Fig. 100: Core rotation distribution at two different radial positions (entrance rotational velocity 289 m/s)

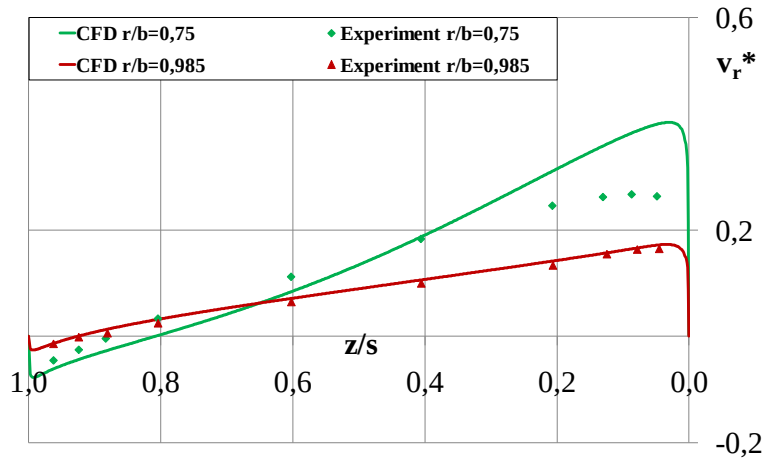

Fig. 101: Dimensionless radial velocity distribution at two different radial locations (entrance rotational velocity 289 m/s)

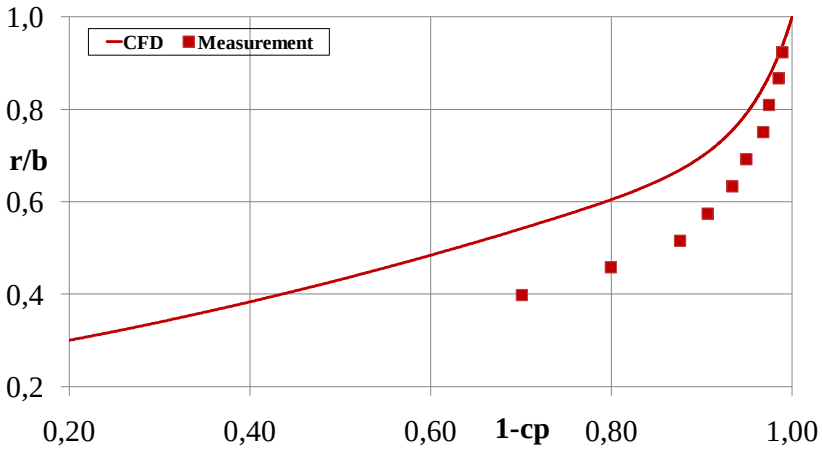

Fig. 102: Pressure distribution (entrance rotational velocity 289 m/s) in case of swirling centrifugal through-flow

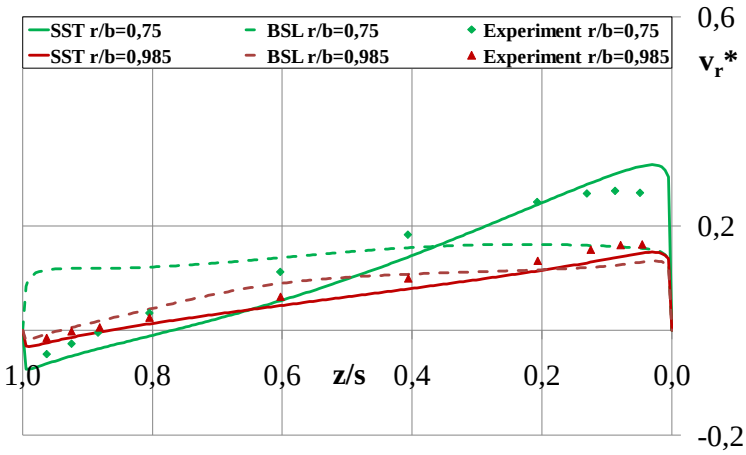

Fig. 103: Dimensionless radial velocity distribution at two different radial locations for the for SST and the BSL turbulence model

5.4 Concluding Remarks

The previous results clearly indicate the importance of the incoming angular momentum flux as a major parameter in rotor-stator cavity flows. For strong non-swirling leakage flow rates, the Batchelor-type flow structure can break down and turn into Stewartson-type of flow. Then, high circumferential velocities occur only in the vicinity of the rotating disk. The influence of the angular momentum flux on the flow field increases according to its magnitude. For higher leakage flow rates the overall flow structure is mainly determined by the external leakage flow rather than by the rotation of the disk. This becomes obvious for example from the pressure distribution which has a totally different shape compared to the natural flow in case of the enclosed rotating disk. Another break up in the flow structure can be caused by the incoming angular momentum flux when the core rotation becomes greater than one. Then, the flow is directed radially inwards over the complete axial gap width. In such a case, the obtained results confirm the principal streamline pattern discussed by **Owen and Rogers [64]** and also the streamline patterns computed by **Poncet et al. [72]**. Both authors observe no radial outward directed flow in the core region when the fluid rotates faster than the disk as proposed by **Radtke and Ziemann [78]**.

Three-dimensional simulations of the enclosed rotating disk using eddy viscosity based turbulence models show the appearance of vortex like structures at the outer periphery in the circumferential direction. A certain threshold of the mesh density is necessary to resolve these structures which are suspected to be Taylor vortices. However, these structures do not seem to significantly influence the overall mean flow field and are absent as soon as an outer leakage flow is applied.

Including the side chambers into a complete 3D and transient computation of a radial turbomachinery still prohibits an explicit boundary layer resolution due to the extensive computational costs. Based on the previous results, it can be concluded that the SST model can be expected to give reasonable results for the radial pressure distribution and also the velocity profiles, even if the grid is comparatively rough. A general statement about the accuracy of the computed moment coefficients is not possible since detailed information about the flow conditions in the experiments are unknown and the values given in the diagrams printed in the report cannot be directly transferred to the present calculations because the dimensionless parameters differ for several reasons. For example, the density used in the CFD calculations of the moment coefficient is obtained from a volume average. If the Reynolds number is calculated with the flow parameters from the CFD calculations, deviations from the experimental values are apparent that complicate direct comparisons. Especially in case of a swirling through-flow, the moment coefficient changes sharply with the Reynolds number. In the centripetal flow case, only one experimental value is given which does not correlate with the flow conditions in the simulation. This permits a direct comparison.

6 Side Chamber Flow in a Centrifugal Pump

6.1 Preliminary Considerations

The design process of radial fluid machines requires reliable information about the fluid dynamics in every single component of the machine. Aside from the flows which are responsible for the energy transmission in the main parts of a machine, such as the blade passages in the impeller or the volute casing, the flow in regions resulting from construction conversion are of great importance. These parts, such as the side cavities between the rotating impeller and the stationary casing, do not serve the purpose of increasing the energy level of the fluid. Rather they lead to a reduction of the machine efficiency and can affect the operational reliability, for example in case of axial thrust reversal. In the side chambers, the frictional resistance (drag losses or disk friction losses) of the side walls has a great impact on the required power of the machine. Especially for low specific speed impellers, this is an inherent problem. **Gülich [33]** mentions that for low specific speed machines (n_q=10) disk friction losses can amount up to 50% of the useful power and the leakage losses can make up to 12% of the nominal flow rate (**Surek, 1966; cited in Bahm [6]**). Furthermore, in general a leakage flow is present which passes the sealing clearances and leads to a reduction of the hydraulic efficiency.

The flow in the side chambers directly influences the mechanical design of the pump because the resulting axial force, whose knowledge is necessary for the design of the bearing, is essentially determined by the static pressure distribution on the outer side walls of the impeller. The pressure distribution depends on the rotation of the fluid in the side chamber which is strongly influenced by the incoming swirling leakage flow. The leakage again is a function of the operating point of the machine. Besides, the central role of the leakage flow with respect to the axial thrust had already been noticed in the early literature (e.g. **Lawaczek, 1932; cited in Bahm [6]**).

In this work, the flow in the wheel spaces of a single stage centrifugal pump with volute casing is investigated in order to gather insight into the cavity flow under real operating conditions. Furthermore, the present configuration of a centrifugal pump with a narrow axial gap in the rearside chamber, volute casing and balancing holes has yet not been discussed in the literature to the knowledge of the author. For this sake, numerical and experimental efforts have been performed. Two configurations of the impeller are investigated: Either with or without balancing holes. Balancing holes are a common method to reduce the resulting axial thrust on the impeller but lower the hydraulic efficiency. The basic idea is to create the same flow conditions (respectively pressure drop) in the rearside chamber as in the front side chamber so that the resulting static pressure distributions on the impeller walls cancel each other. This requires that both the inflow conditions and the flow structure are similar.

Investigations devoted to the isolated study of the flow in rotor-stator cavities give detailed insight into the actual flow physics. However, the flow in the side chambers of a real machine depends on the interplay of many different parameters. The flow between the outer impeller wall and the casing is inseparably coupled with the flow at the impeller outlet and in the volute. Especially the determination of the outer boundary conditions that establish as a kind of equilibrium condition, determined by the inflow and outflow condition of the impeller, pose a severe problem.

The flow structure in the volute depends on the operating point and an axisymmetric pressure distribution is usually only present for design flow conditions (**Pavesi [68]**). According to **Binder and Knapp (1936; cited in Bahm [6]**), the volute acts like a diffuser at part load. Consequently, the flow in the volute is retarded and the pressure increases in tangential direction. For overflow conditions, the volute acts like a nozzle accelerating the fluid in the tangential direction. This leads to a pressure decrease in the circumferential direction. Further, the authors observe an inward directed flow close to the wall whose velocity and direction depend on the circumferential position. This imbalance results in a radial load which deflects the impeller into an eccentric position. As a result, the line of influence of the axial force does not coincide with the rotation axis leading to an additional torque (**Ris et al., 1963; cited in Bahm [6]**).

In centrifugal pumps, part load recirculation is a well-known problem. **Gülich [34]** notices that especially low energy backflow fluid entering the side chambers significantly dampens the fluid rotation and thus affects the axial force. A reduced fluid rotation leads to a smaller pressure drop which results in a higher pressure force. In dependance on the axial displacement of the impeller, the recirculation region can occur close to either of the side chambers at part load conditions. Under certain circumstances, this can even cause a reversal of the resulting axial force in multi-stage pumps.

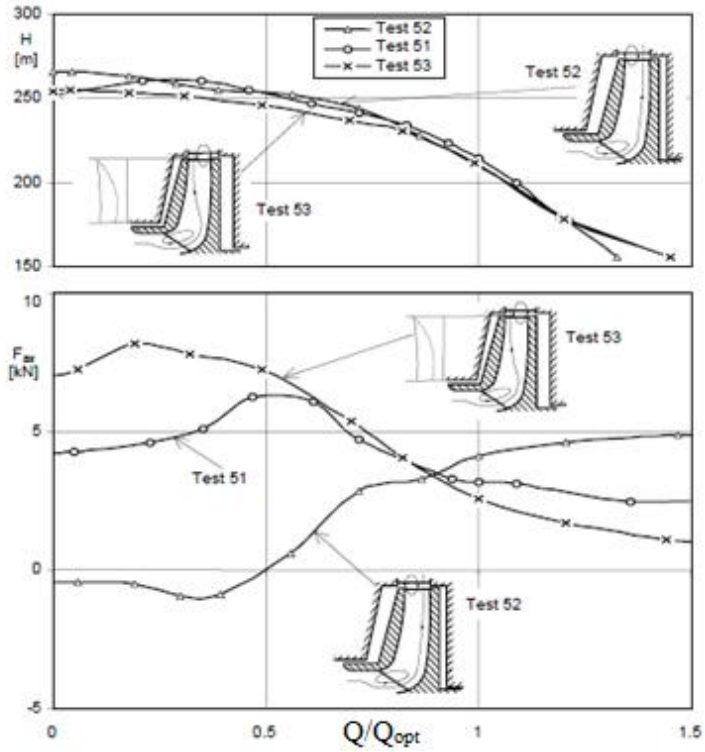

Fig. 104: Influence of axial rotor position on Q-H-curve and axial thrust, n_q = 22, Sulzer Pumps; Test 51: Rotor position centered; Test 52: Rotor shifted to discharge side; Test 53: Rotor shifted to suction side (Gülich [34])

The pressure distribution at the impeller outlet is non-stationary (**Gülich [34]**) due to the complex interaction of the rotating impeller and the stationary casing or the guide vanes. This causes a fluctuating behavior of the flow magnitudes that even extends into the side cavities.
In order to obtain simplified equations for the analytical calculation, the assumption of steady, axisymmetric flow conditions is fundamental to nearly all publications concerning rotor-stator cavities. At best, this condition applies to a centrifugal pump with volute casing only in the design point. Despite the above mentioned difficulties, the ability of one-dimensional calculation methods to predict at least an average estimate of the pressure distribution in the side chambers will be discussed in the following chapters.
Little is known about the flow in the side chambers of a centrifugal pump with volute casing under real operating conditions and different pump flow rates. Therefore, the following study tries to shed some light on this aspect. Furthermore, only little information is available about the influence of the balancing holes on the flow structure. Of course, the transferability of the previously obtained results on the flow in the pump will be evaluated.

6.2 Investigated Pump

The centrifugal pump under investigation is a standard commercial pump in compliance with the guidelines of the International Organization for Standardization (ISO). The specific speed is n_q=22.8 min^{-1} for which impellers with a relatively large radial extent are common, causing high disk friction and leakage losses. The impeller is shrouded and has seven three-dimensional shaped and strongly backward curved blades. The flow leaving the impeller is collected by a volute casing. The main geometric data and operating conditions are depicted in Table 28.
In order to reduce the axial force, the impeller has seven balancing holes, one in each blade channel. This leads to a radial inwardly directed flow in the rearside chamber. In the second configuration, the balancing holes are closed so that no leakage flows through the rearside cavity.

Impeller	
Number of blades	7
Outlet width	14 mm
Outlet radius	130 mm
Number of balancing holes	7
Diameter of the balancing holes	5.5 mm
Volute casing	
Basic circle radius	140 mm
Volute width at the basic circle	25 mm
Design operating conditions	
Volume flow rate	80 m^3/h
Speed of rotation	1450 min^{-1}
Side cavities	
Re_φ	$2.57 \cdot 10^6$
Width of shroud side chamber	7.57 mm (G=0.058)
Width of hub side chamber	3 mm (G=0.023)

Table 28: Main geometric data and operating conditions of the pump

6.3 Numerical Model

Transient, fully 3D computations of the Reynolds-averaged Navier-Stokes equations using the commercial CFD code Ansys CFX 12 are conducted in order to predict the flow field in the whole pump including both side chambers. A block structured mesh is used with an overall amount of approximately 12.8 million nodes (12.2 million elements). Following the preliminary studies, the grid is designed in order to keep the y^+ magnitudes below 30 in the whole flow domain. Fig. 105 shows two cross sectional views of the computational mesh in an axial and in the meridional plane.

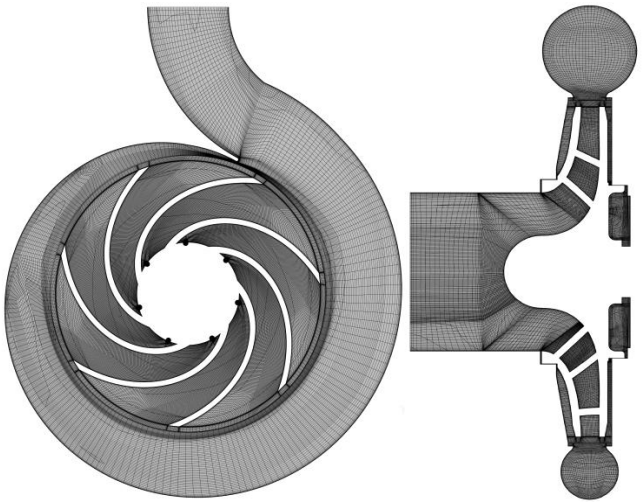

Fig. 105: Numerical model of the pump (left: axial plane, right: meridional plane)

Close to the inlet radius of the impeller, the balancing holes can be seen. To model turbulence, the SST model is used since it offers a good compromise between accuracy and computational effort, both for the side chambers and the main flow in the pump. Moreover, this model proved to give good results in the aforementioned numerical study. **Poncet et al. [74]** also notice that this model seems to be a good compromise for industrial use. At the inlet, the total pressure and the direction of the absolute velocity vectors are specified while the mass flow rate is defined as outlet boundary condition. The no-slip condition is applied at all wall boundaries in the relative frame of reference.
A detailed view of the computational grids in the side cavities is given in Fig. 106. Both cavities are divided in the axial direction with 22 nodes. In the front side chamber, 76 nodes are employed in radial direction while 106 nodes are used in the rearside chamber. These limitations in the spatial resolution are necessary in order to limit the computational costs for the calculation.

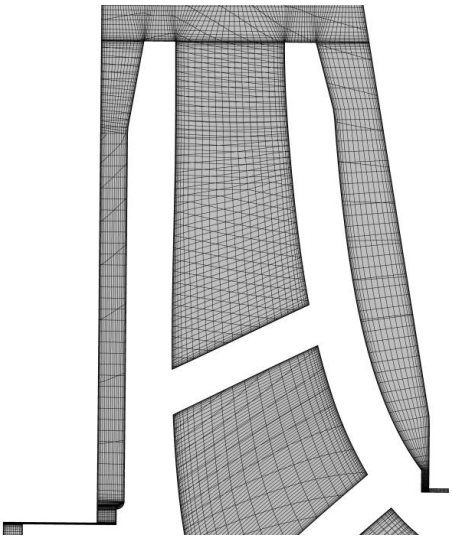

Fig. 106: Numerical grid for the side chambers in the meridional plane

6.4 Experiments

In the experiments, the delivery head is obtained from the total pressure difference between the inlet and outlet of the pump:

$$H = \frac{p_{tot.outlet} - p_{tot.inlet}}{\rho g} \qquad \textbf{Eq. 162}$$

With the total pressure being the sum of the static and dynamic pressure:

$$p_{tot} = p + \frac{\rho}{2}\vec{v}_{mean}^{2} \qquad \textbf{Eq. 163}$$

In order to determine the radial pressure distribution in both side chambers, static pressure measurements at different radial locations are accomplished by pressure holes in the casing wall. The pressure transducers for the side cavities have an accuracy of 0.25% of the full scale value. To determine the delivery head of the pump, the absolute pressures at the pump entrance and behind the volute casing are additionally measured. These transducers have an accuracy of 0.5% of the full scale range. The signals from the transducers are digitalized by a Goldammer data acquisition device and recorded using a self-programmed Matlab program. In order to capture enough samples, tests proved that a measuring interval of 200 seconds per measuring location is sufficient. After recording, the data are averaged arithmetically.
The desired volume flow is adjusted using a sphere valve and an inductive flowmeter in order to measure the flow rate. The radial locations for the pressure measurements are listed Table 29. Due to manufacturing constraints, unfortunately no pressure measurements have been available at the outer impeller radius (r/b=1).

Relative radial position (r/b)	Shroud side chamber	Hub side chamber
0.354		X
0.431		X
0.508		X
0.558		X
0.608	X	
0.649	X	X
0.740	X	X
0.832	X	X
0.923		X

Table 29: Measuring locations for the static pressure in the side cavities

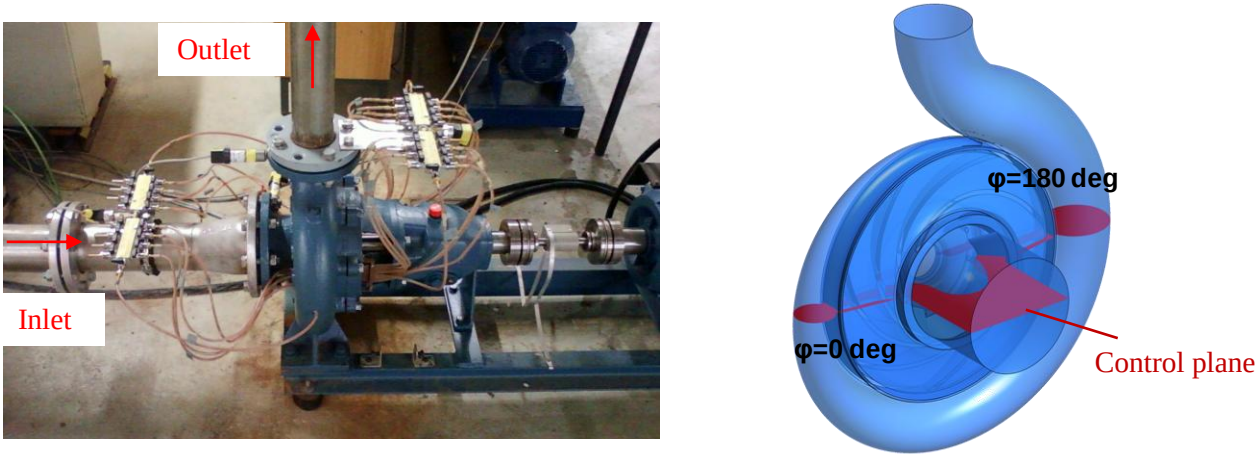

Fig. 107: Experimental setup and control plane

On the left hand side of Fig. 107, the experimental setup is shown. Starting from a tank, the fluid enters the pump through a straight pipe on the left and exits in the vertical direction. Radial pressure measurements haven been performed at two circumferential positions outlined on the right hand side. Consequently, the numerical results obtained in this study are basically evaluated on the same perimeter coordinates as in the experimental setup. The perimeter coordinate is expressed using the angle φ.

6.5 Results for Design Flow Rate

6.5.1 Influence of the Sealing Gap Height

The sealing gaps in centrifugal pumps are usually very narrow in order to keep the leakage flow rate as low as possible. During operation, the gap height can change due to wear or vary in the tangential direction because of a possible eccentricity of the rotor. Due to the small gap height (increased ratio of roughness to gap height), roughness effects are of great importance in this region. In conclusion, the sealing gap height is influenced by several parameters. Furthermore, a reliable determination of this parameter is very difficult under operating conditions. To investigate the effect of the sealing gap height in the rearside chamber, two different combinations are tested:

	Config. 1	Config. 2
Gap height shroud side chamber	0.5 mm	0.5 mm
Gap height hub side chamber	0.48 mm	0.24 mm

Table 30: Sealing gap heights in the two investigated configurations

Fig. 108 shows the comparisons of the computed and measured pressure distributions in the side cavities using the non-dimensional pressure p*. The results for the front side cavity are very satisfactory while in the rearside cavity bigger deviations occur.

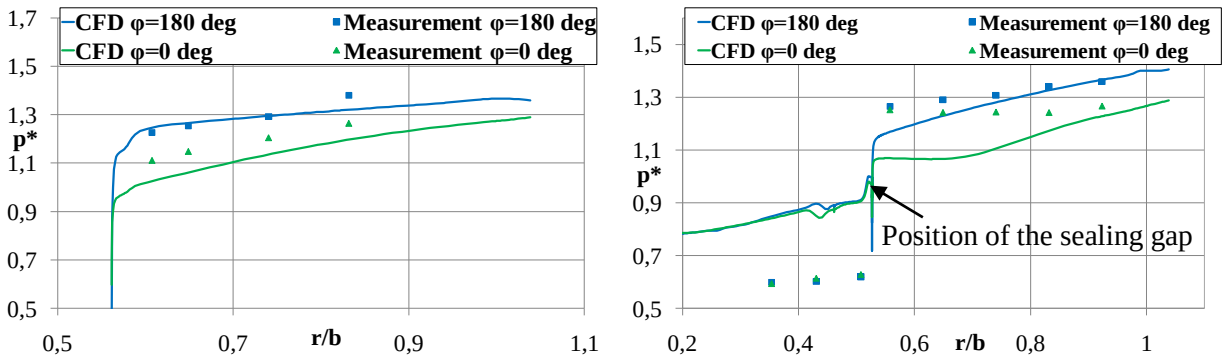

Fig. 108: Comparison between experimental and numerical results for the shroud side chamber (left) and the hub side chamber (right) in case of 0.48mm clearance gap height

To estimate the expected flow regimes in both side chambers, the diagram according to Fig. 107 is used:

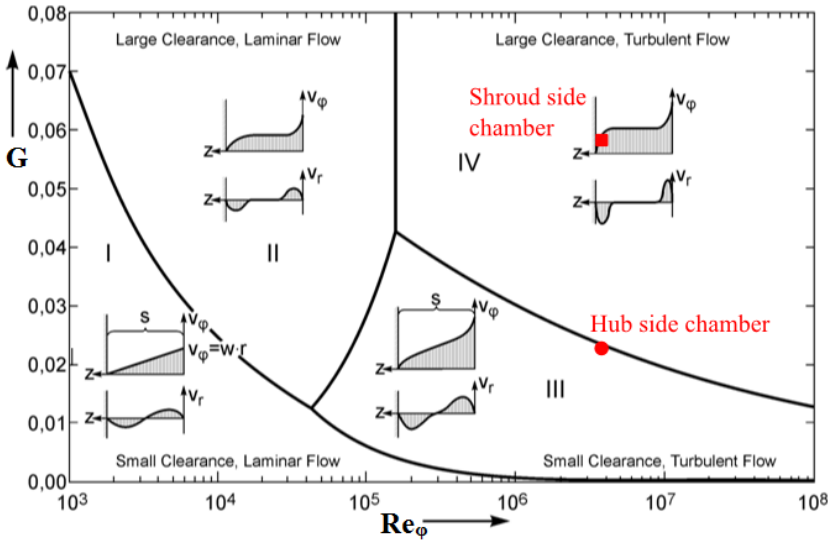

Fig. 109: Estimation of the flow regimes in the shroud and hub side chamber of the pump according G and Re_φ

In the shroud side chamber, the expected Batchelor flow is likely to be present whereas in the hub side chamber, the point is just below the limiting curve in flow regime III with merged boundary layers. However, the influence of the leakage flow rate is not taken into consideration in this figure.
Due to the balancing holes in the impeller, the leakage is directed centripetally in both side chambers. For single stage pumps without balancing holes, this applies only in the front side chamber. Consequently, the principal physical relations in the present investigation are the same for both side chambers.
The results in the front side chamber reflect the expected decrease of the pressure towards the inner radii resulting from an increase in the core rotation. This is caused by the incoming angular momentum flux at the outer disk radius. According to the principle of conservation of angular momentum, the circumferential velocity must increase when the radius decreases as demonstrated in the numerical study of the rotor-stator cavity subjected to an external angular momentum flux.
Especially in the hub side chamber, larger deviations between numerical and experimental values are apparent across the sealing gap. The sealing gap controls the amount of leakage that passes through the cavity and vice versa determines the pressure difference across the gap. Mechanical energy conveyed to the fluid in the impeller is dissipated into heat by the choking effect of the sealing which directly influences the efficiency of the pump. The value of the pressure drop across the sealing predicted by the numerical simulation has a much lower magnitude compared to the values obtained from the experiments.

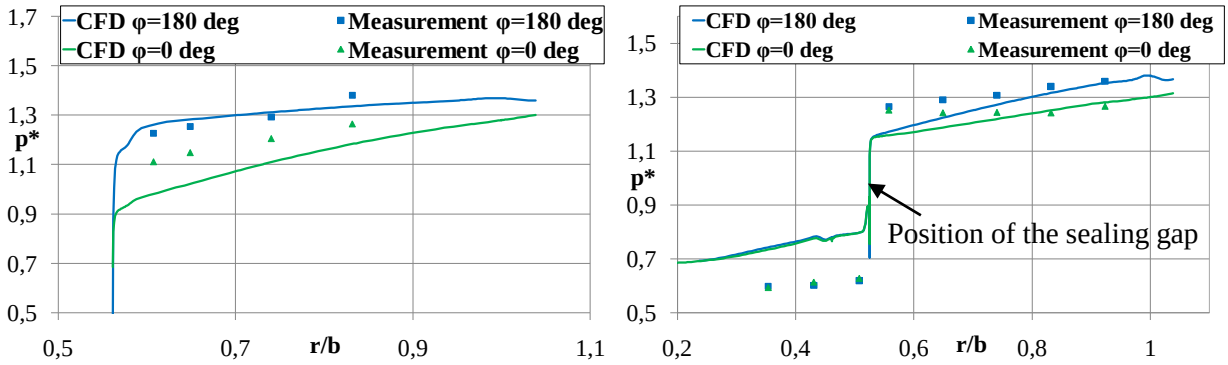

Fig. 110: Comparison between experimental and numerical results for the shroud side chamber (left) and the hub side chamber (right) in case of 0.24mm clearance gap height

One major parameter for the pressure drop is the gap height which is also pointed out by **Iino et al. [39]** for multistage pumps. In order to reduce the leakage losses, the gap height is generally very small and therefore difficult to determine under operating conditions. Examining the present data suggests that the employed gap height is too large and therefore a second simulation is performed with halved gap height. The modified results can be seen in Fig. 110.
As expected, the pressure drop considerably increases and the agreement with the experimental data improves. Unfortunately, some discrepancies are still apparent behind the sealing gap which might be attributed to an insufficient resolution of the flow in the gap itself. Currently, the flow is only resolved by 8 cells in the radial direction in the shroud side cavity and by 13 cells in the hub side cavity. For example, **Tamm [95]** uses 6 cells and notes that doubling the number does not change the results. He mentions that smaller gap heights cause increased pressure differences but increase the inaccuracy in the calculation as well. To address this issue, another separate study of the rearside chamber is initiated which will be described in the successive chapter.
According to **Gülich [34]** the flow in the gap is unstable because the circumferential velocity, respectively the centrifugal forces decrease from the inside (rotating shaft) to the outside (stationary casing). A similar situation is present in the radial gap between the shroud of the rotating disk and the radial casing in the numerical study of the enclosed rotating disk (e.g. Fig. 61). The stability criterion for the formation of Taylor-vortices in the gap resulting from this instability is the Taylor number:

$$Ta = \frac{v_{gap} t}{\nu} \sqrt{\frac{t}{r_{gap}}} = Re_p \sqrt{\frac{t}{2 d_{gap}}} \qquad \textbf{Eq. 164}$$

For Ta≥41.3, counter-rotating Taylor vortices are expected in the sealing between the rotating shaft and the stationary casing which strongly influence the pressure drop and energy dissipation in the gap. To determine whether the flow is turbulent or not, both rotational and axial velocities have to be taken into account considering the gap Reynolds number:

$$Re_{gap} = \sqrt{\left(\frac{2 t v_{axgap}}{\nu}\right)^2 + 0.25 \left(\frac{2 t v_{gap}}{\nu}\right)^2} \qquad \textbf{Eq. 165}$$

Transition to turbulent flow takes place at Re_{gap}=2000 while the flow will always be turbulent for Re_{gap}=4000 (**Gülich [34]**). For turbulent flow in the gap, the friction factors for the sealing additionally depend strongly on the wall roughness due to the very small gap height (the relative roughness ε is comparatively large). In the present simulation, all walls have been treated as hydraulically smooth which might not apply for the small sealing gaps. Unfortunately, no information about the surface roughnesses in this region are available.
An estimation of the Taylor number and the gap Reynolds number for both cavities indicates that the flow is turbulent and Taylor vortices are to be expected (Table 31). However, the results of the numerical simulation do not show any sign of these vortices. This issue will be further discussed in chapter 6.6.

	Shroud disk cavity	Hub disk cavity
Re_{gap}	12841	4450
Ta	457	147

Table 31: Estimation of gap Reynolds and Taylor number

Besides, it is noteworthy that even the pressure distribution in the front side chamber changes slightly for the reduced sealing gap width in the rearside chamber which demonstrates the interdisciplinary character of the side chambers as part of the whole system.
Further on, both simulation and measurement indicate a slightly transient behavior of the pressure (pressure fluctuations at the order of ~3%) in the wheel spaces resulting from the blade rotation. For this reason, the pressure in the side cavities depends on the position of the impeller relative to the casing. This small side-effect is eliminated in the measurements by arithmetically averaging the

samples taken over a measuring interval of 200 seconds (corresponds to numerous impeller revolutions).

6.5.2 Impeller with and without Balancing Holes at Design Flow Rate

All further computations are carried out with the small sealing gap height in the rearside chamber since it obviously better represents the actual flow conditions in the pump. In the beginning of the study, a double manifold was mounted in front of the pump causing a contra rotating swirl of the entering volume flow. According to Euler's basic formula of turbomachinery, a counter rotating swirl increases the specific work. This led to somewhat higher values in the measured delivery head compared to the CFD results. Consequently, the overall pressure level in the pump increased. For the present study, the experimental setup consisted of a long pipe in front of the pump to avoid pre-swirl effects.

Exp. with balancing holes	18.5m
CFD with balancing holes	18.3m
Exp. without balancing holes	18.74m
CFD without balancing holes	19m

Table 32: Comparison of delivery heads at design flow rate (Q=80m^3/h)

A comparison of all delivery heads for the design flow rate is given in Table 32. Both experimental and numerical values are in excellent agreement indicating that the overall flow in the pump is sufficiently captured by the simulation. The balancing holes lead to a reduction of the delivery head due to increased losses. These losses are a result of reentering leakage from the balancing holes which disturbs the main flow in the blade channels. Further on, the use of balancing holes magnifies the seal gap losses. This is reflected both in the delivery heads from the experiment and the numerical simulations since the head is slightly higher in the absence of balancing holes.
A very important result is that the pressure in the volute casing increases in the streamwise direction which means that a circumferential pressure gradient exists (Fig. 111).

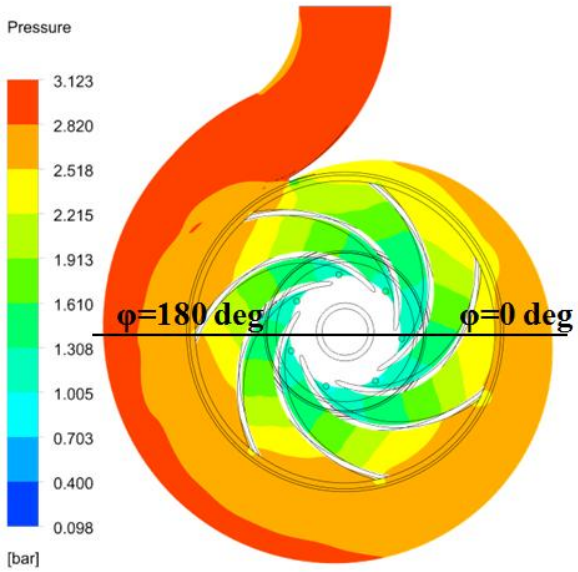

Fig. 111: Static pressure distribution at the middle section of the pump

The reason for this is that the volute and the impeller are obviously designed for different flow rates. This causes a radial force on the impeller and variable flow conditions for the blade channels during each rotation. Similar pressure distributions are observed in the experimental investigations of **Bahm [6]** for a volute casing or **Bubelach [15]** for a ring casing.

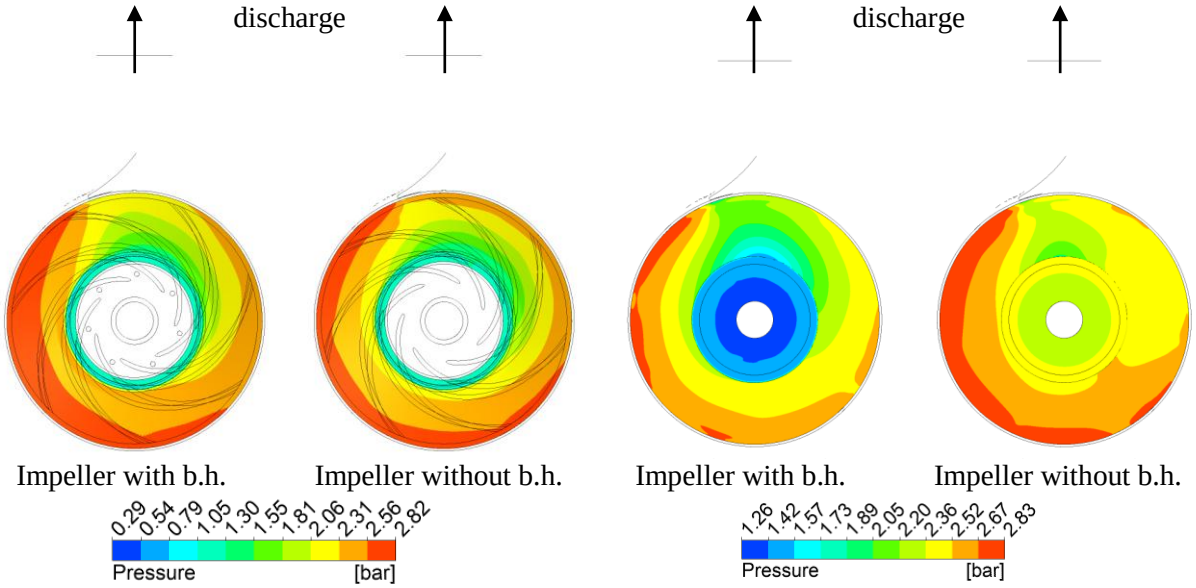

Fig. 112: Pressure distribution on the casing walls in the front side cavity (left) and rearside cavity (right)

Furthermore, the inflow conditions for the side cavities are now dependent on the angular coordinate. The side cavities in pumps with volute casing are relatively open at the outer radius which leads to a strong interaction between the flow in the volute, the impeller outflow and the side chambers. As a result, the pressure in the cavities also varies in circumferential direction (Fig. 112). The comparison between the radial static pressure distribution on the casing wall in the side cavities either with or without balancing holes in the impeller is given in the following diagrams.

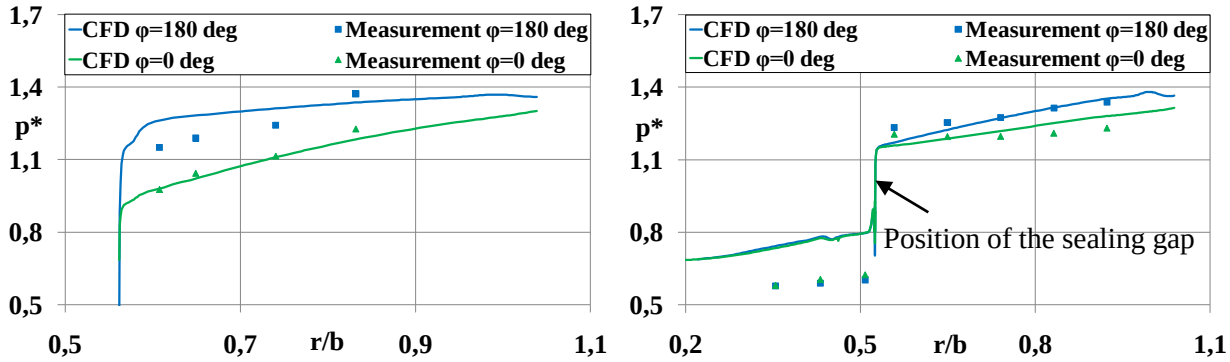

Fig. 113: Comparison between experimental and numerical results for the front side chamber (left) and rearside chamber (right) - impeller with balancing holes

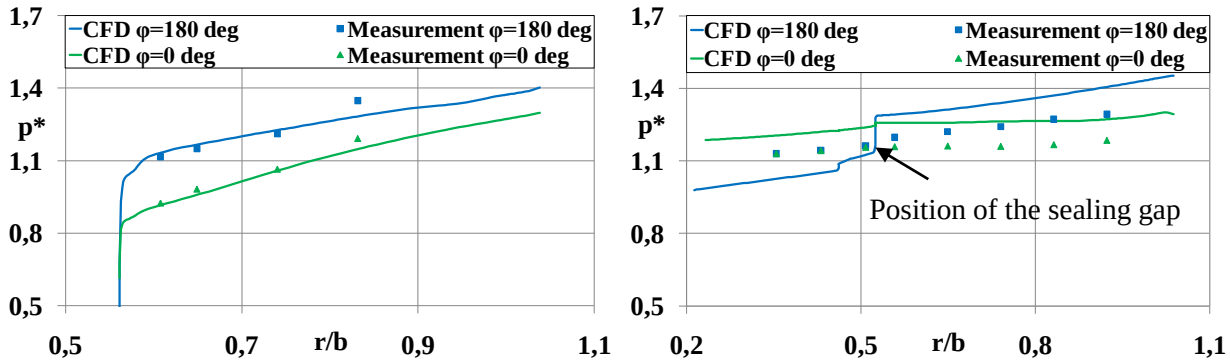

Fig. 114: Comparison between experimental and numerical results for the front side chamber (left) and rearside chamber (right) - impeller without balancing holes

The overall agreement between measured and numerically predicted curves in the shroud side chamber is quite good in both cases, either with or without balancing holes. The results show the expected decrease of the pressure towards the inner radii which results from an increase in the core

rotation caused by the incoming angular momentum flux at the outer disk radius. According to the boundary layer theory, the pressure is imposed onto the boundary layers from the core region for flow regime IV. Therefore, at least the pressure distribution seems to be sufficiently captured with the present numerical setup. The static pressure distribution in the front side chamber changes slightly for the two configurations. However, if no balancing holes are present, a stronger decrease of the pressure towards the axis of rotation can be observed. This means that the core flow is now accelerated more strongly in the radially inward direction as a result of an increased angular momentum flux entering at the outer radius.
For the impeller with balancing holes, a centripetal inwardly directed leakage flow is present in the rearside chamber too. The pressure drop across the sealing gap predicted by the simulation is somewhat too small (Fig. 113). Reasons for this are, for example, the uncertainty in the determination of the radial gap height, the influence of surface roughness and the grid resolution. To examine the influence of the grid resolution on the obtained pressure distribution, the flow in the rearside chamber is separately simulated in the next chapter.
For zero leakage in the rearside cavity, the sealing gap has much less effect on the flow structure since the axial flow component is of much smaller magnitude and results, if at all, only from recirculation of the flow in the cavity. This can be clearly seen from the measurements and the CFD results. However, a fundamental difference seems to be present at φ=180 deg compared to φ=0 deg in Fig. 114 for the rearside chamber. The shape of the blue curve indicates a non-negligible axial velocity although no general leakage flow is present since the balancing holes are closed.
When the balancing holes are closed, a counter rotating wake region develops in the narrow rearside chamber at the tangential position φ=0 deg. Fig. 115 shows the rotation of the fluid including the streamlines (3D) in the middle of the side chamber. Green indicates rotation in direction of the rotor and red counter rotating.

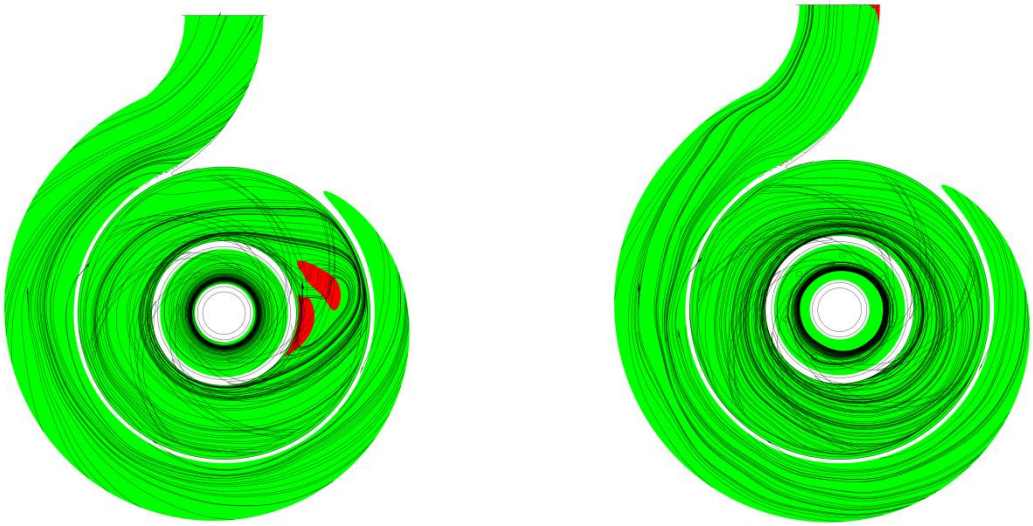

Fig. 115: Fluid rotation direction in the middle plane in the hub side chamber in case of impeller without balancing holes (left) and with balancing holes (right) including 3D streamlines

The red regions indicate recirculation and occur only in absence of through-flow in the side chamber at a fixed position. This phenomenon is directly related to the pressure field respectively the pressure gradient in tangential direction. In fact, the wake region is three-dimensional and the area of counter rotating fluid increases in axial direction with distance from the rotating wall. This is shown in Fig. 116 at different z/s positions.
In the immediate vicinity of the rotating wall, all the fluid rotates in the same direction as the rotor due to the dominant influence of the centrifugal forces. For further wall distance, the influence of the pressure becomes stronger. The location of low static pressure after the tongue of the pump in the hub side chamber accelerates the fluid in the tangential direction. This cannot be counterbalanced by the pressure force in the tangential direction and as a result, a recirculation respectively wake region develops. A pressure difference between the cavity inlet and the balancing holes superposes a radial

flow component which suppresses the creation of the wake by implying a spiral type inward motion. From a global perspective, the formation of the wake in the tangential direction is a direct consequence of the irregular pressure distribution in the circumferential direction.

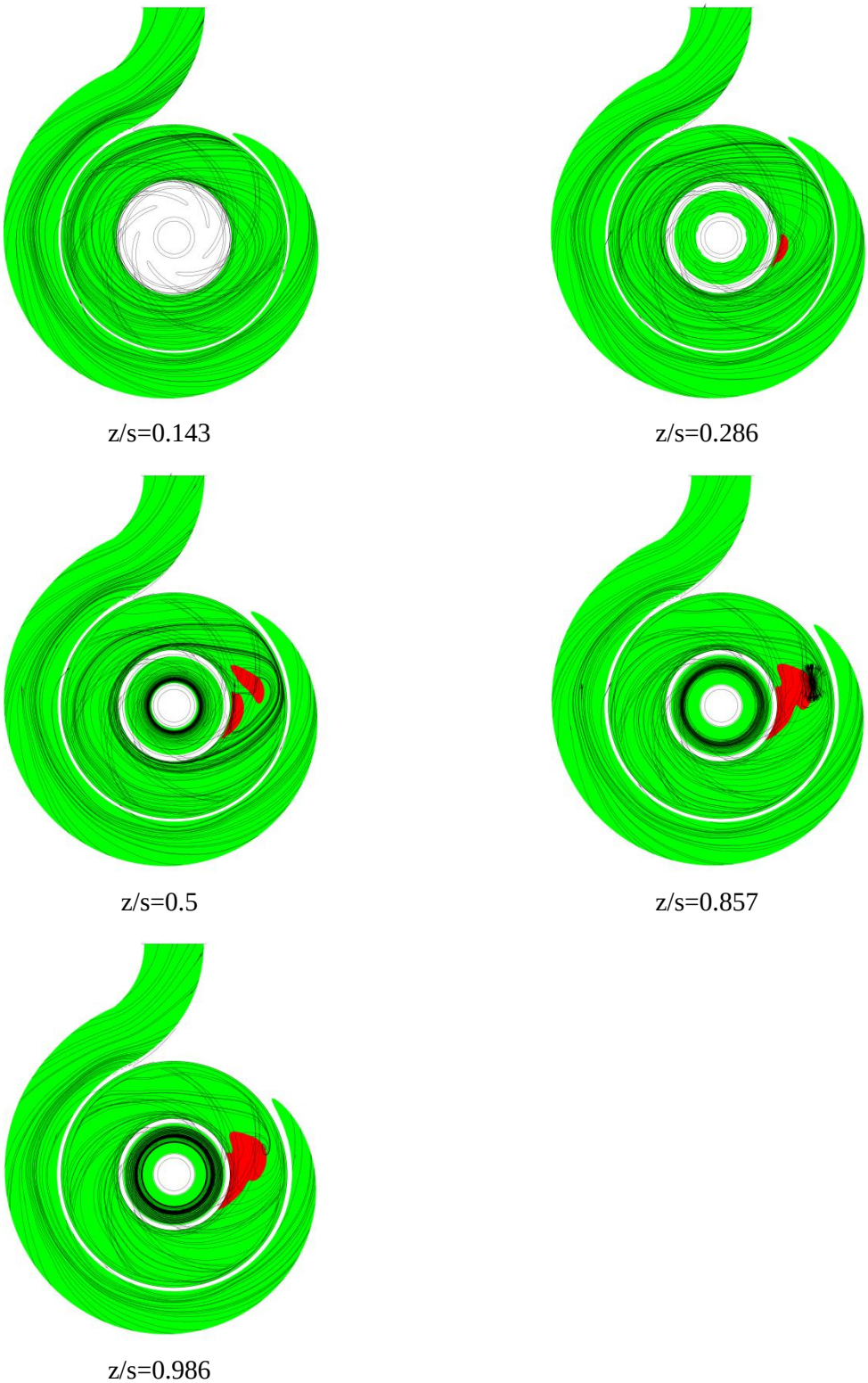

Fig. 116: Axial evolution of the counter rotating fluid region with increasing distance from the rotating wall (z/s is 0 on the rotor and 1 on the stator)

Furthermore, the inflow and outflow into the rearside chamber in the tangential direction is highly non-uniform. After the wake, the fluid is centrifuged out of the cavity into the volute and mixes with

the main flow. Due to the strong pressure gradient at the tongue of the volute, fluid is sucked into the side chamber. Exactly this fluid which is sucked in is responsible for the pressure drop in Fig. 114. This can be seen from the 3D streamlines in Fig. 117. In the wake region, the pressure remains relatively constant in radial direction which explains the almost horizontal course of the measured points in Fig. 114.

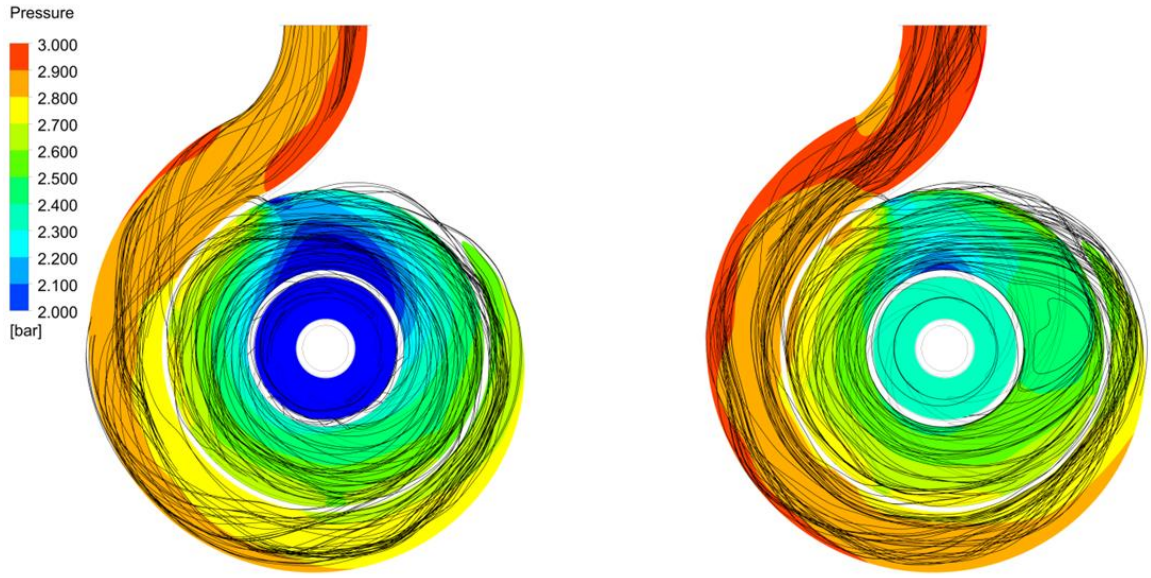

Fig. 117: 3D streamlines and pressure contour at z/s=0.917; impeller with (left) and without (right) balancing holes

In conclusion, there is a strong coupling (mass and momentum exchange) between the outer flow in the volute and the flow in the rearside cavity. No similar effects are observed in the front side cavity due to the inwardly directed leakage flow. The appearance of the wake region applies for both off-design points as well. However, the size of the wake increases for part load operation and decreases for overload conditions.

Investigations of the influence of a leakage flow on the expected Taylor vortices in the axial gap show that even small through-flow rates can completely suppress these vortex structures. In the case of a closed hub side chamber, the pressure level predicted by CFD is somewhat higher (Fig. 114) which agrees with the measured delivery head.

To limit the computational effort, a comparatively rough grid is used in the side chambers as outlined before. In case of a wide gap with separated boundary layers, the core region is essentially free of shear stresses (**Gülich [34], Poncet [72]**). In the present simulations, the near wall region is basically approximated by wall functions and it appears as if the present setup is at least capable of sufficiently predicting the core rotation respectively the pressure distribution. Moreover, the flow conditions are predominantly determined by an external angular momentum flux entering the side chamber which is expected to be adequately determined in the present case as well. The pressure is directly coupled with the core rotation (radial equilibrium) and is imposed onto the boundary layers. In the case of merged boundary layers (rearside chamber), shear forces act along the whole gap width. Thus, the shear stress and the radial expansion of the gap sectional area (**Kurokawa and Sakuma [47]**) essentially influence the pressure distribution whereas for regime IV, the centrifugal forces in the core flow almost uniquely determine the pressure distribution. It can be concluded from the previous results, that the influence of the leakage flow is much weaker in the hub side chamber compared to the shroud side chamber due to the homogenizing effect of the viscous forces.

In the volute, fluid particles follow curved streamlines. Streamline curvature requires a pressure gradient normal to the flow direction. This leads to the formation of secondary flows, which appear, for example, in a curved duct. Fig. 118 shows simplified pictures the velocity vectors for the two locations at φ=0 deg and φ=180 deg and the two corresponding impeller configurations. The colors represent inflow (green) or outflow (red) in the radial direction.

First, it can be observed that the flow fields differ very much from each other according to the circumferential coordinate. The disk pumping effect can be clearly seen for the impeller with

balancing holes (left). The fluid pumped out by the rotating surfaces mixes with the main flow emerging from the impeller. A radial inflow takes place only in the vicinity of the stationary casing walls. This radial inflow emanates from the secondary flow in the volute and therefore contains a lower circumferential velocity component compared to an inflow directly from the impeller. This causes higher disk friction and reduces the pressure drop across the cavity. A decreased magnification of the circumferential velocity with decreasing radius leads to a higher pressure force on the disk.
In the case of closed balancing holes, the secondary flow field shifts towards the suction side of the pump, slightly reducing the inflow in the front disk chamber but increasing the interaction with the main flow from the impeller. This is caused by an axial pressure gradient at the outer impeller radius resulting from the pressure increase in the rearside chamber due to absence of leakage. The overall incoming angular momentum flux in the shroud side chamber increases by about 20% for this configuration which can also be noticed from the gradient of the pressure curve in Fig. 114. A stronger interaction of the secondary flow in the volute with the recirculating flow in the rearside chamber results from the shifting of the flow field and reduces the radial outflow on the disk in the case of the impeller without balancing holes.
The circumstances at φ=180 deg are different for the impeller with balancing holes. The higher pressure level at this peripheral coordinate leads to a much stronger inflow into the side cavities which in return reduces the radial outflow on the rotating surfaces. The strong interaction with the main flow from the impeller results in higher mixing losses. The shifting towards the suction side is again clearly visible for the impeller without balancing holes. The leakage flow at this position is mainly fed from the impeller outflow confirming that the overall angular momentum flux is now higher compared to the balanced impeller.

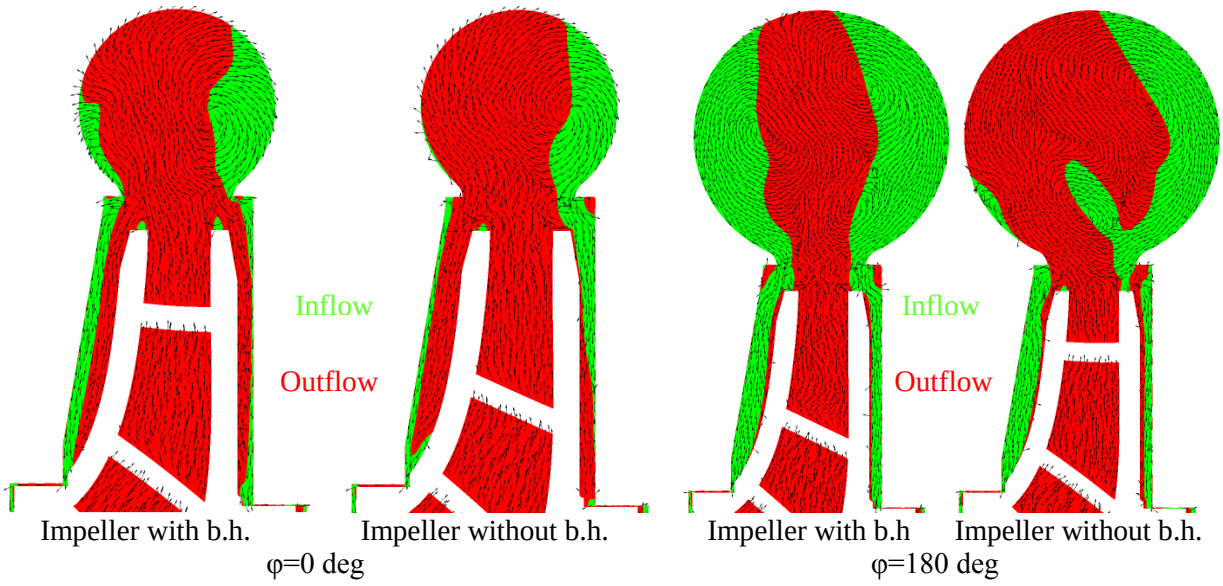

Fig. 118: Comparison of secondary flow patterns

	φ_G	β_e	p_e [Pa]
Impeller with balancing holes			
Shroud side chamber	0.001896	0.42	252737
Hub side chamber	0.0006425	0.395	252528
Impeller without balancing holes			
Shroud side chamber	0.00155	0.566	255263
Hub side chamber	0	0.3975	262627

Table 33: Boundary conditions for the flow models taken from the numerical simulation

Analytical calculations with the previously proposed flow model and the model developed by **Kurokawa and Sakuma [47]** for merged boundary layers are conducted for both side chambers. In the case of flow regime IV, the pressure is calculated from the radial core rotation distribution using the radial equilibrium relation. The necessary input parameters for the calculation are given in Table 33 and are evaluated from the numerical simulation (area averaged values at the outer cavity radius).

In contrast to the impeller with balancing holes, the entrance pressure, as well as the inlet core rotation at the outer cavity radius, are more dissimilar for the impeller with closed holes due to the shifting of the secondary flow field.
The comparison of the proposed flow model with the experimental data (Fig. 119) for the front side chamber, with respect to averaged values between φ=0 deg and φ=180 deg, shows a good agreement either in case with ("bh") or without balancing holes ("wbh"). Using the averaged values as boundary conditions, the analytical curves fall right between the measured data and thus provide a good estimate. However, the variation of the flow in the tangential direction is a direct consequence of the outer flow conditions and cannot be described with such a simplified, axis-symmetric approach.

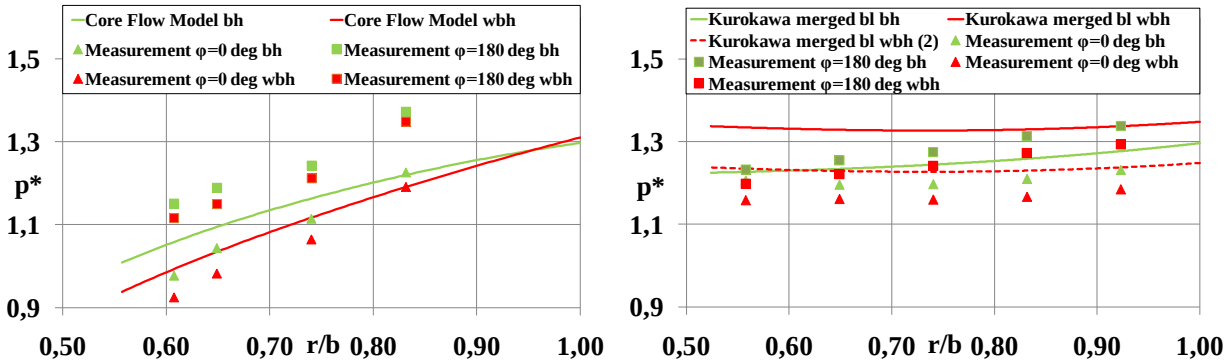

Fig. 119: Comparison between experiments and analytical calculation (left: front side chamber, right: rearside chamber)

If the same model as in the shroud side chamber is used in the rearside chamber, greater discrepancies occur. The general characteristic of the pressure drop towards smaller radii does not correspond to the underlying flow pattern according to regime IV (**Will et al. [104] and Will et al. [105]**). The merged boundary layer case without through-flow in the rearside chamber is computed using a negligible leakage flow rate because the flow model of **Kurokawa and Sakuma [47]** does not allow a numerical value of zero. In the hub side chamber, the agreement for the case with leakage is somewhat worse. This can be attributed to the overall higher pressure level predicted by the CFD simulation used to obtain the pressure at the cavity boundary. This pressure is necessary as a boundary condition for the numerical determination of the radial pressure distribution using the flow model. If an entrance pressure extrapolated from the measurements is used (denoted as "Kurokawa merged bl wbh (2)" in the diagram), the computed curve falls right between the measured points at φ=0 deg and φ=180 deg. The radial trends show that the influence of the incoming angular momentum flux via the leakage flow has much less effect in the case of flow regime III compared to regime IV because the pressure does not drop as sharply as in the front side chamber. The shape of the curve changes only slightly with a different curvature.
So far it can be stated that the flow structure in the rearside chamber is fundamentally different from the flow pattern in the front side chamber. This results in different pressure patterns and the resulting pressure forces do not balance, as intended. The main reason for this discrepancy is the narrow axial gap distance in the rearside chamber which prevents the formation of two boundary layers separated by a core region. Moreover, the magnitudes of the leakage flow rates are very different from each other. The curve shape of the radial pressure distribution is totally different in the rearside chamber. In the front side chamber, the pressure drops off sharply towards the inner radii due to the increased core rotation. In contrast, the pressure gradient in the rearside chamber decreases for smaller radii. Therefore, a measured pressure distribution can yield valuable information about the actual flow regime in the side chamber.
Carefully examining the experimental pressure data shows further that the measured pressure points in front of the sealing gap, at the two different radial locations, differ not only in a parallel shift. At φ=180 deg, clearly a stronger pressure gradient is present than at φ=0 deg. The flat shape of the radial pressure distribution is characteristic for the wake region.
The static pressure is certainly the easiest physical quantity to measure. Nevertheless, a lot of information can be drawn from a measured distribution in combination with a numerical approach as shown beforehand.

6.6 Isolated Study of the Flow in the Rearside chamber

6.6.1 Numerical Model

The previously presented simulations could only be performed with a limited number of computational elements in the side chambers in order to reduce the computational effort. Especially in the rearside chamber, greater differences between the measured and computed values are encountered. To investigate the influence of the spatial discretization in terms of varying the grid density, a segment model (one seventh) of the rearside chamber is simulated separately (**Pastore [67]**). The position of the segment in the whole pump model and the isolated segment are shown in Fig. 120.

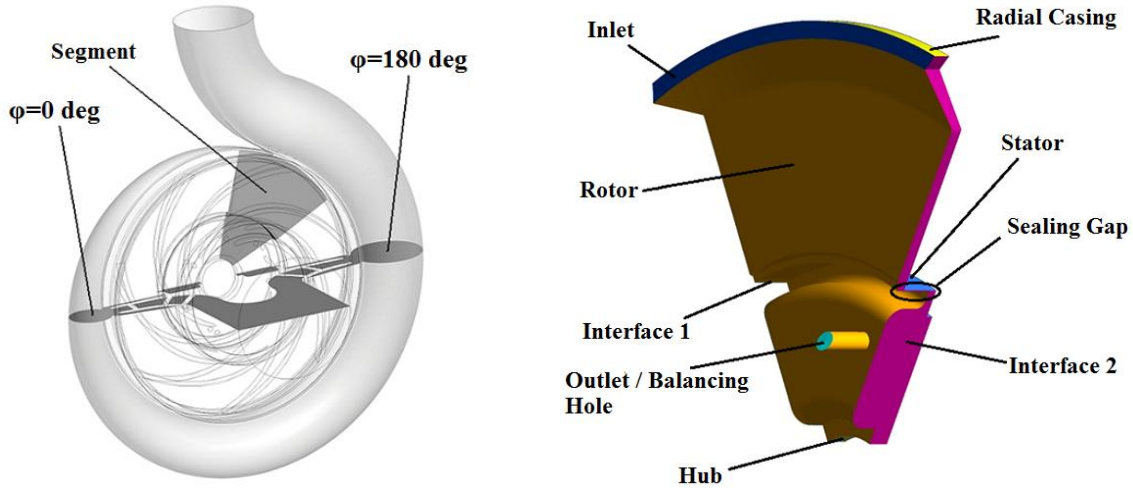

Fig. 120: Position of the segment in the complete pump model (left) and one seventh segment with notations (right)

Grids of different refinement levels haven been generated in order to evaluate both the influence on the simulated flow structure in the upper cavity as well as the resolution of the flow in the sealing gap. Outgoing from the original base mesh with 660000 nodes, two refined variants with approximately 2 respectively 4 million nodes were created. The principal grid structures can be seen in the following picture:

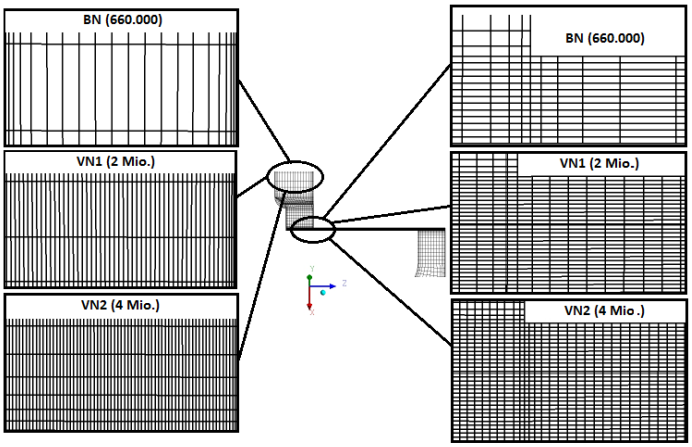

Fig. 121: Base mesh (BN) and refined meshs (VN1, VN2) for the segment model of the rearside chamber

As already mentioned, the flow through the sealing gap is unstable and Taylor vortices are expected to occur. However, it is not clear under which flow conditions these vortices are apparent or not. The clarification of this issue is another important point discussed in the following section.
The determination of adequate boundary conditions turns out to be quite difficult due to the complex flow pattern in the complete pump. As a reference point, the design point of the pump at Q=80 m^3/h is chosen and the following settings are used since they seem to best represent the actual flow conditions:

Inlet	v_z=0.185 m/s v_r=-1.991 m/s v_φ=7.914 m/s
Outlet	p=122534 Pa

Table 34: Boundary conditions for the segment model

In the numerical model, the sealing gap height amounts to 0.25mm and all walls are treated as hydraulically smooth. All simulations are steady state and the y+ of the base mesh is approximately 30 in the whole flow domain. In Fig. 122, the different lines and planes used for the post-processing are depicted.

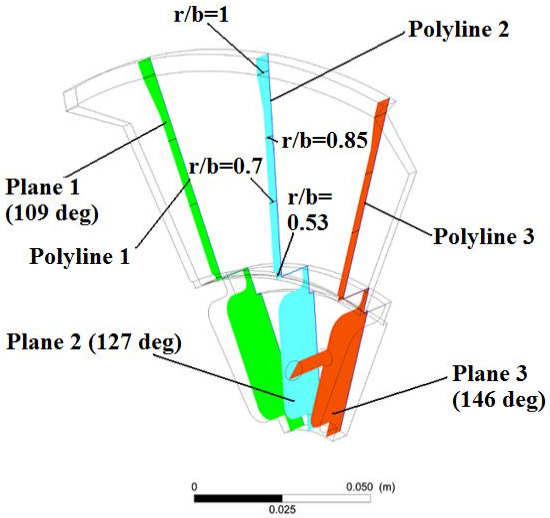

Fig. 122: Planes and lines in the sector model used for post-processing

In contrast to the full model, the flow conditions in the segment model are rotationally symmetric which can be clearly seen from the pressure fields in Fig. 123. According to this picture, the three-dimensionality of the flow in the rearside chamber of the complete pump originates uniquely from the outer flow conditions.

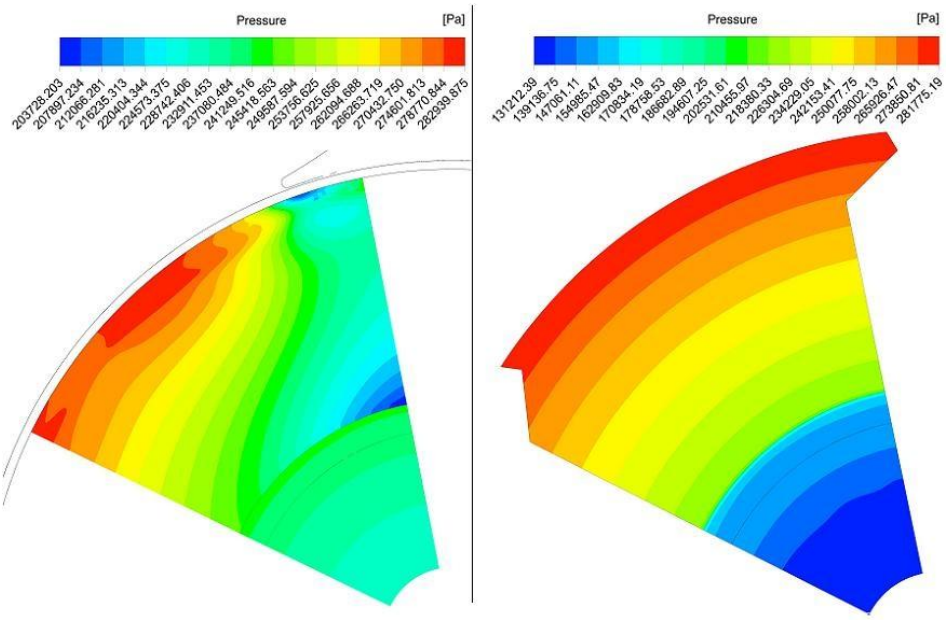

Fig. 123: Comparison of the pressure contours on the casing wall in the full (left) and the segment model (right)

The resulting radial pressure distributions for the base mesh and the refined variants are depicted in Fig. 124. The pressure in the cavity above the sealing gap obtained from the refined grids is somewhat higher than the one obtained from the base mesh. The important thing to notice here is that a further refinement, referring to the base and 2 million mesh, can have an impact on the predicted pressure distribution. No differences are present for a further grid refinement. Although the evaluated velocity distributions change merely for the different grids (see below), the pressure does however. Shear stresses act across the complete cavity width and thus influence the pressure distribution. It is likely that the coupling between the shear stress and the pressure is better resolved in the refined grids although the velocities change hardly. Concluding, the slight differences in the hub side chamber in the simulation of the complete pump compared to the measurements can be ascribed to the grid resolution.

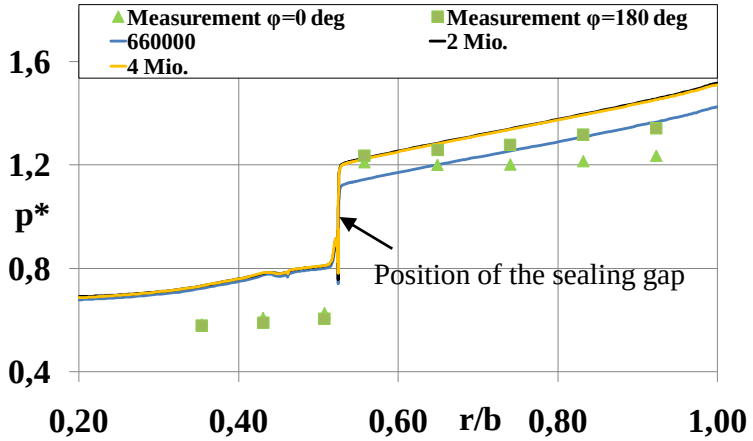

Fig. 124: Comparison of the radial pressure distribution for the segment model with through-flow (φ=127 deg, SST)

6.6.2 Flow Structure with Through-Flow

In order to gain a general survey of the resulting flow pattern, the predicted surface streamlines in the cavity are presented in Fig. 125:

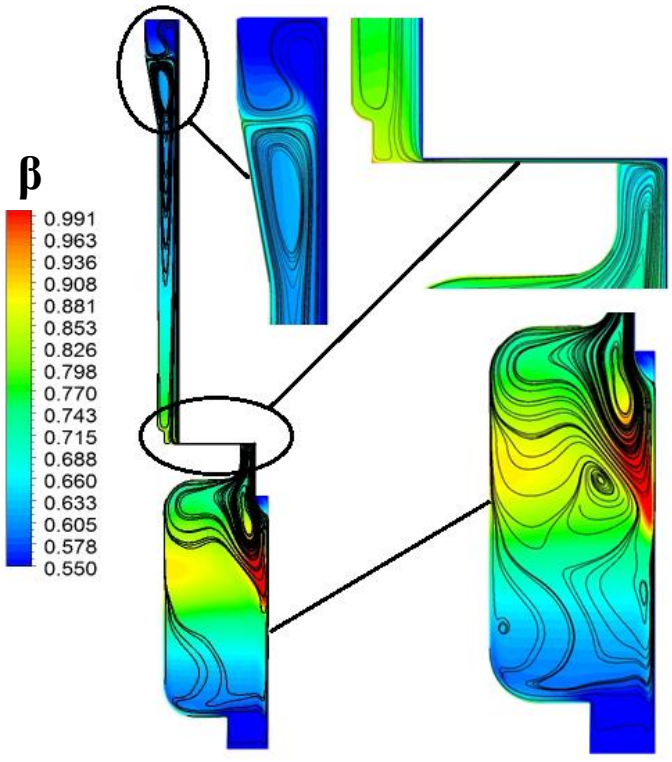

Fig. 125: Streamline pattern in the rearside chamber for the segment model with through-flow (contours of the core rotation factor)

Close to the stator, the fluid is directed radially inwards, while the fluid is pumped out by the rotating surface. The interaction of the externally applied leakage flow with the radially outwards directed flow close to the rotor leads to the formation of a vortex in the meridional plane that directs the leakage towards the stator. A part of the inward flowing leakage passes the sealing gap while the other part recirculates in the upper cavity. Conservation of angular momentum applies again since the contours reveal that the core rotation increases with decreasing radius. Afterwards, the flow enters the balancing drum and leaves through the balancing holes.
In the following picture, the influence of the grid density on the core rotation as a function of the axial distance at four different radial positions is shown. As for the pressure, no velocity gradients are present in the circumferential direction.

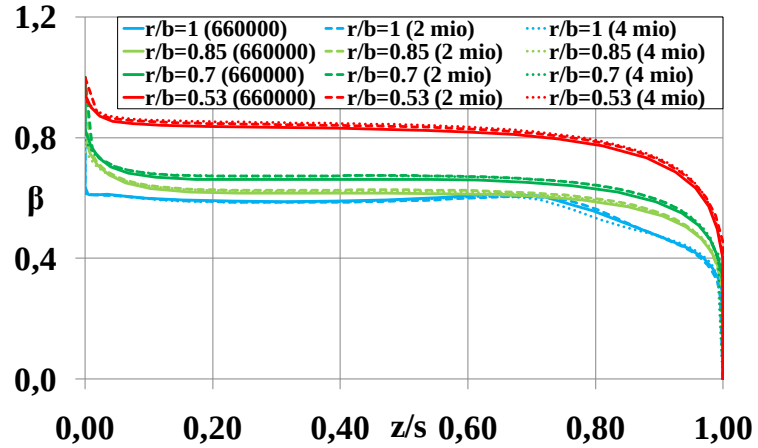

Fig. 126: Core rotation distribution in the hub side chamber for the segment model with through-flow

First of all, it can be noticed that all computed curves fall very close together at the corresponding radii. This means that the base mesh offers quite a good compromise between accuracy and computational costs for the resolution of the velocity distributions. Moreover, the circumferential velocity increases as the radius decreases which follows from the principle of conservation of angular momentum as already noticed from Fig. 125. The predicted profiles are very similar to the profiles encountered in flow regime IV except for the curve at the outer rotor radius which is a consequence of the interaction with the entering leakage flow. The outwardly pumped flow close to the rotor and the entering external leakage lead to the formation of two vortices that redirect the flow towards the stationary casing. **Haddadi and Poncet [35]** observe similar profiles in their numerical study of torsional Couette-flow in a rotor-stator system with superposed through-flow.
In Fig. 127 the associated radial velocity distributions are shown.

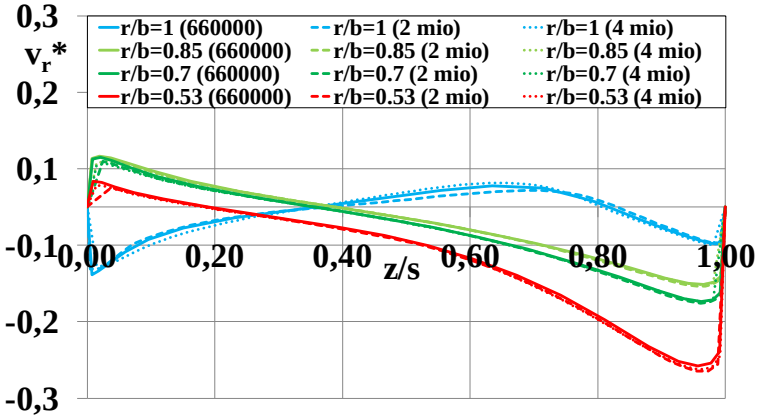

Fig. 127: Radial velocity distribution in the hub side chamber for the segment model with through-flow

The radial profiles are clearly different from the ones encountered in flow regime IV. A characteristic feature for the core region in case of Batchelor-flow is the absent from a radial velocity component.

For flow regime III, the radial velocity varies continuously with the axial coordinate. Except at the cavity entrance (r/b=1) and close to the sealing gap (r/b=0.53), the radial velocity varies almost linearly over most of the axial gap width. As for the circumferential velocity, the influence of the grid density on the resolution of the radial velocity component is negligible. According to the continuity equation, the radial velocity must increase for decreasing radii which can be seen in Fig. 127.

6.6.3 Flow Structure without Through-Flow

The same study as before has been accomplished for the segment without through-flow. To do so, the boundary conditions are changed. The outlet of the balancing hole is defined as a wall and the inlet as an opening. Additional computations with the omega Reynolds-stress (ORE) model are also performed.

First, the obtained radial pressure distributions are compared with the measurements in Fig. 128.

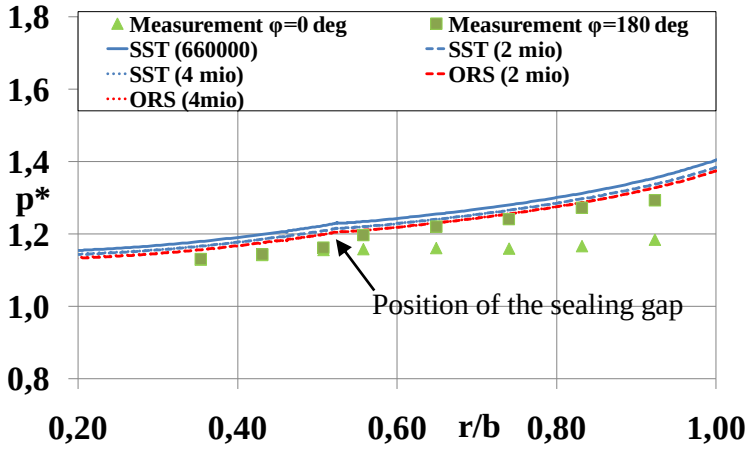

Fig. 128: Comparison of the radial pressure distribution for the segment model without through-flow

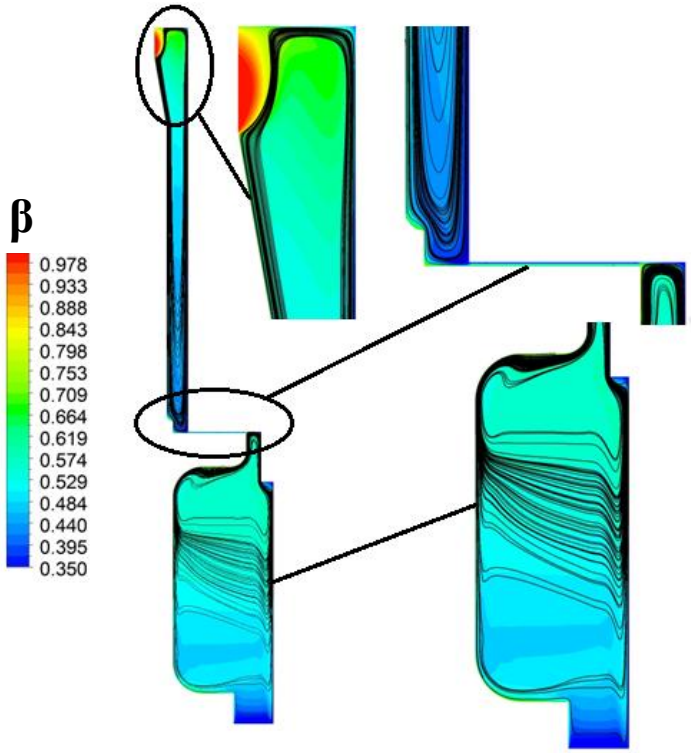

Fig. 129: Streamline pattern in the rearside chamber for the segment model without through-flow (contours of the core rotation)

A close agreement between the computed and the measured pressure distribution at φ=180 deg can be observed. For the closed balancing holes, it has been explained before that the flat course of the measured pressure at φ=0 deg is a direct consequence of the wake that establishes at this position.

Since the wake originates from the circumferential pressure gradient in the spiral casing, such an effect cannot be present in the segment model. A slight vertical shift of the pressure curves can again be observed for the refined variants compared to the base model. Moreover, a very small discrepancy between the two investigated turbulence models exists. As before, a further refinement of the grid does not change the results.
From the resulting streamline pattern in Fig. 129, the recirculation of the flow is clearly evident. Both in the upper part of the cavity as well as in the balancing drum, the flow is like a closed circuit. The radial outwardly pumped flow is turned at the outer radial shroud and flows inwards along the stationary wall. At the position of the sealing gap, the flow is axially redirected towards the rotating wall. The axial core rotation distribution for zero through-flow is depicted in Fig. 130. There are only minor changes between the different grids. Comparing the absolute values of the core rotation, the isolated cavity yields lower values due to the absence of incoming angular momentum. However, the general tendency is different now, namely the core rotation decreases for decreasing radial position.

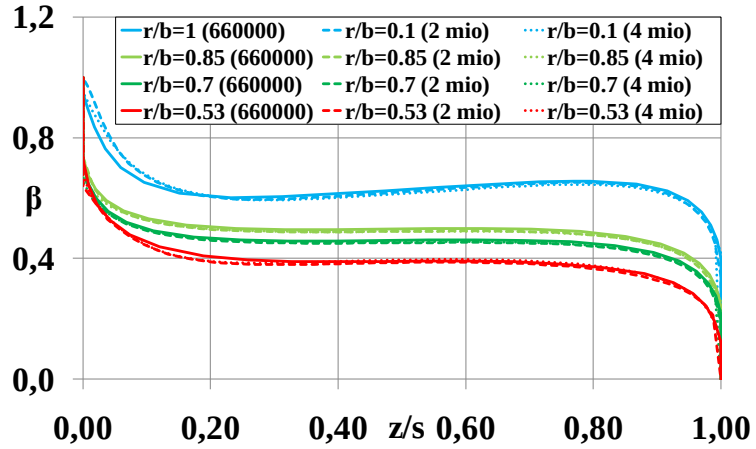

Fig. 130: Core rotation distribution in the hub side chamber for the segment model without through-flow

Haddadi and Poncet [35] notice for a similar case, that for decreasing local Reynolds number and constant gap width G, the flow transitions from flow regime III to regime II at small radial locations. The local Reynolds number in the present case (G=0.023) at r/b=0.53 is about $Re_l=7.2\cdot10^5$ which is still much greater than the critical value. The critical Reynolds number can be taken for a given aspect ratio G from Fig. 109 and defines the border between the different flow regimes. This confirms that the flow remains of torsional Couette type even for small radial positions.
The axial distribution of the radial velocity component is given in Fig. 131. Comparing these results to Fig. 127, the velocity magnitudes close to the stator are smaller due to the absence of a leakage flow. Furthermore, the zero crossing of the radial profiles moves approximately to the middle of the cavity. The radial velocity profile at the outer radius is completely different due to the different boundary condition for this configuration. Since no leakage enters the side gap, no vortex forms that redirects the flow towards the stator.

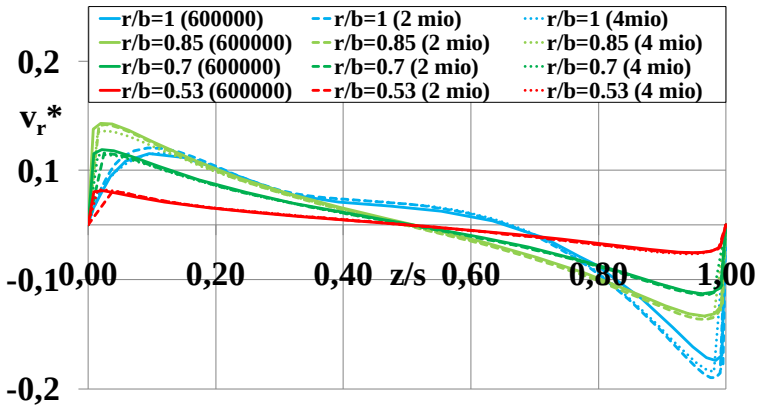

Fig. 131: Radial velocity distribution in the hub side chamber for the segment model without through-flow

On the basis of the previous investigation it is clear that shear flow will always be present whether a leakage flow is present or not. Therefore, the flow in the hub side chamber is strongly influenced by the axial gap width.

6.6.4 Taylor Vortices

As pointed out before, the flow in the sealing gap is unstable and favors the formation of Taylor vortices. An important parameter influencing the flow in the small sealing gap is the external leakage flow. For the segment model with through-flow, the streamline pattern does not show any sign of vortices (Fig. 132) even on the very fine grid with 4 million nodes. To further investigate this detail, a parametric study is performed. The entering leakage flow rate is first set to zero and afterwards successively increased by varying the axial velocity component at the cavity inlet. These simulations are performed with a gap height of 0.8mm to ensure that the resulting Taylor number of Ta=1003 is far above the critical number of Ta=41.3.

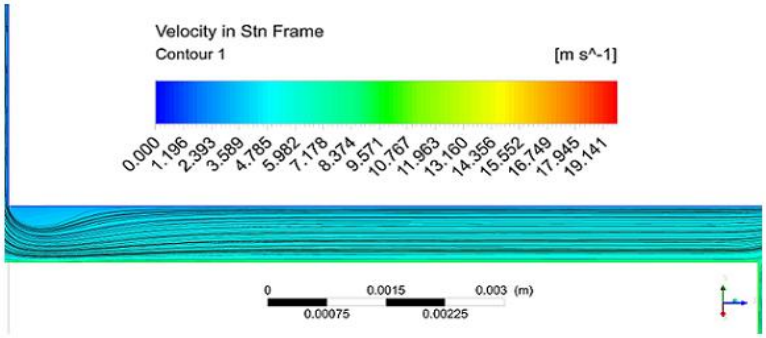

Fig. 132: Flow in the sealing gap (gap height 0.25mm)

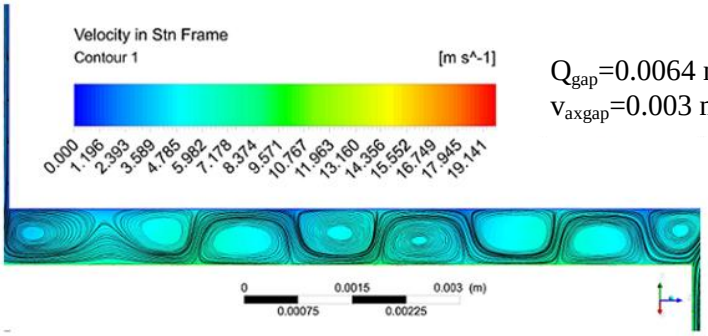

Q_{gap}=0.0064 m^3/h
v_{axgap}=0.003 m/s

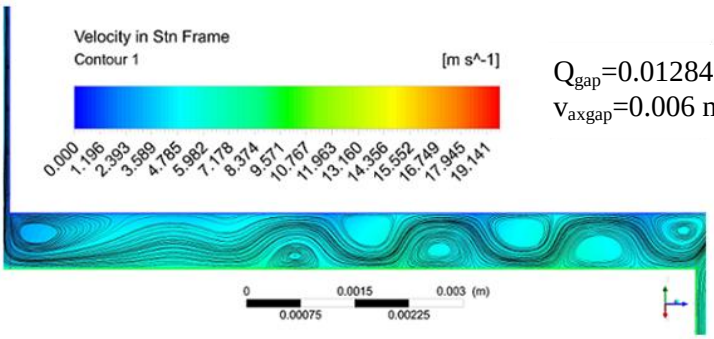

Q_{gap}=0.01284 m^3/h
v_{axgap}=0.006 m/s

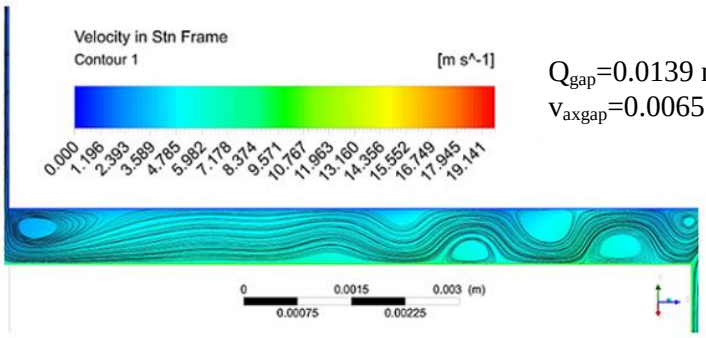

Q_{gap}=0.0139 m^3/h
v_{axgap}=0.0065 m/s

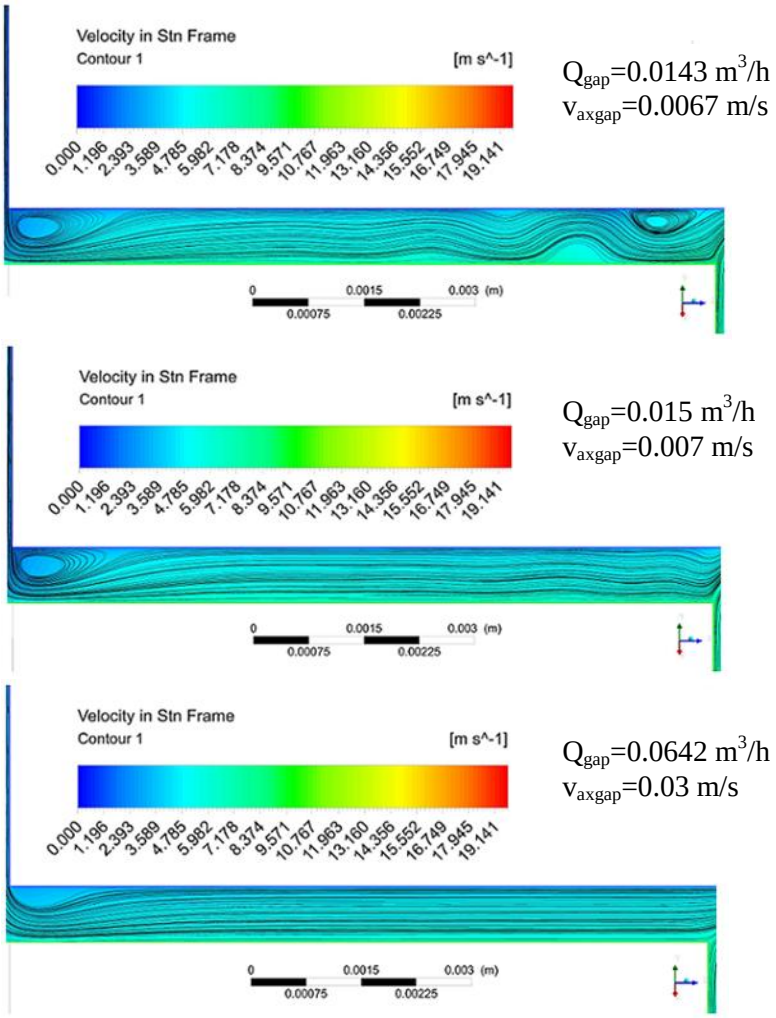

Fig. 133: Flow in the sealing gap (gap height 0.8mm) for different leakage flow rates

The results in Fig. 133 clearly prove the expected dependency of the flow structure on the externally applied leakage flow rate. For a very small flow rate, several vortex pairs are clearly visible in the gap and the flow is dominated by the instabilities rather than the through-flow. If the through-flow rate increases, the vortex pairs gradually diminish. This trend continues with increasing through-flow until the streamlines are perfectly aligned in the axial direction and the flow structure is controlled by the through-flow. The critical through-flow rate in this study amounts approximately 16% of the nominally leakage flow. For greater values no more vortices occur.
Investigations for a smaller gap height of 0.25mm (Ta=182) led to a very unstructured flow pattern in the sealing gap. A possible explanation for this behavior may be that the flow relaminarizes, a process that cannot be sufficiently captured with common eddy viscosity turbulence closures like the SST model.

6.7 Results for Off-Design Conditions

In principle, the flow in the pump at off-design conditions is more complicated. As shown before, even in the operating point a circumferential pressure gradient is present in the volute. The delivery heads obtained from the numerical simulations and the experiments for all three operating points are summarized in Table 35.

	$Q/Q_{opt}=0.6$	$Q/Q_{opt}=1$	$Q/Q_{opt}=1.2$
CFD bh	20.04m	18.3m	16.8m
Exp. bh	20.12m	18.5m	17.1m
CFD wbh	20.3m	19m	17.34m
Exp. wbh	20.16m	18.74m	17.54m

Table 35: Comparison of delivery heads for different operating points

The agreement between numerical and experimental results for both impeller configurations is very good, the maximum deviation is less than 2% which is within the measurement uncertainty. The characteristics from the head curve can be clearly seen, namely that the delivery head decreases for increasing flow rate and vice versa. This underlines that the numerical pump model adequately resolves the main flow characteristics. Furthermore, the efficiency reduction caused by the balancing holes is again clearly visible both from the experiments and the simulations. However, the relative differences between the delivery heads in cases with or without balancing holes obtained from CFD are somewhat higher than those from the experiments.
The complete sets of boundary values evaluated from the CFD results at the outer cavity radius are given in the next two tables.

		$Q/Q_{opt}=0.6$	$Q/Q_{opt}=1$	$Q/Q_{opt}=1.2$
bh	p_e [Pa]	270823	252737	241945
	β_e	0.458	0.42	0.456
	φ_G	0.001929	0.001896	0.001695
wbh	p_e [Pa]	271621	255263	243504
	β_e	0.547	0.566	0.47
	φ_G	0.001722	0.00155	0.0016856

Table 36: Boundary conditions for the shroud side chamber at different operating points

		$Q/Q_{opt}=0.6$	$Q/Q_{opt}=1$	$Q/Q_{opt}=1.2$
bh	p_e [Pa]	273317	252528	245315
	β_e	0.4052	0.395	0.376
	φ_G	0.0007366	0.0006425	0.0006367
wbh	p_e [Pa]	278673	262627	247051
	β_e	0.347	0.3975	0.401
	φ_G	-	-	-

Table 37: Boundary conditions for the hub side chamber at different operating points

At the outer radial location, the cavity flow is closely linked to the flow in the volute and the impeller outflow. First, the results for the shroud side chamber are discussed. As it is expected from a general head curve, the averaged pressure at the outer cavity radius increases for decreasing pump flow rate and vice versa. Furthermore, the pressure-build up is noticeably higher for the impeller without balancing holes. The core rotation at the cavity entrance of the front side chamber is significantly higher for all three operating points in absence of balancing holes which suggests that the net angular momentum flux increases. As mentioned before, this is a result of the shifting of the flow field towards the pump inlet when the impeller is not equipped with balancing holes. As can be seen from the flow fields presented later on, this statement applies for both off-design points as well.
The leakage flow rate in the cavities increases for smaller pump flow rates. This is not surprising because the overall pressure difference across the cavity, respectively the impeller, is higher. Compared to the impeller without balancing holes, the leakage flow rate in the shroud side chamber is higher in case of the impeller with balancing holes although the entrance pressure p_e is smaller. A possible explanation is that the entrance rotation of the fluid for impeller without balancing holes is significantly higher which leads to a sharper pressure drop across the radius caused by the incoming angular momentum flux. This reduces the effective pressure in front of the sealing gap and thus the leakage flow rate which can be generally calculated for the sealing gap from the following relation:

$$Q_{gap} = 2\pi\mu r_{gap} t \sqrt{\frac{2\Delta p_{gap}}{\rho}} \qquad \textbf{Eq. 166}$$

In this equation, μ denotes the through-flow coefficient that is composed of the friction factor and the pressure loss number analogous to the flow in pipes. These magnitudes are usually mainly determined from empirical correlations that have to be derived from experiments.

The equation clearly shows that a smaller pressure difference across the sealing reduces the resulting leakage flow across the gap.
In the hub side chamber, the flow rate shows the same tendency as in the shroud side chamber. Comparing the configurations with and without balancing holes, the pressure difference increases with respect to the shroud side chamber. This originates from the fact that a part of the fluid energy is not converted into kinetic energy to create a through-flow and therefore is maintained as pressure. Moreover, the entrance rotation of the fluid is consistently lower for closed balancing holes because the raised pressure deflects the impeller outflow towards the front side chamber.
The averaged circumferential velocity of the fluid at the outer cavity radius decreases for increasing flow rate of the pump in case of the impeller with balancing holes. This is a consequence of more low energy fluid (with a smaller circumferential velocity component) returning from the volute into the rearside chamber.
The leakage flow rate in case of balancing holes is significantly smaller than in the front side chamber resulting from the higher flow resistance of the sealing gap and the balancing holes. For the entrance core rotation in the case of a hub side chamber without leakage no general tendency can be seen and the flow is likely to be determined from the flow conditions in the volute.
Next, the pressure distributions in the side chambers are discussed. Generally, the pressure in the pump increases at part load and decreases at overload conditions. In the front side chamber, the flow structure remains principally the same as in the design point. For the impeller without balancing holes, the pressure drop is consistently higher due to the increased angular momentum flux entering the side chamber. The angular momentum fluxes entering the frontside and rearside cavity are given in the following two tables:

Shroud side chamber						
	Balancing holes			Without balancing holes		
Q/Q_{opt}	β_e	φ_G	Ang. Mom. Flux [Nm]	β_e	φ_G	Ang. Mom. Flux [Nm]
0.6	0.458	0.00193	2.376	0.547	0.00172	2.533
1	0.420	0.00190	2.142	0.566	0.00155	2.359
1.2	0.456	0.00170	2.079	0.470	0.00169	2.131

Table 38: Angular momentum fluxes entering the shroud side chamber

Hub side chamber						
	Balancing holes			Without balancing holes		
Q/Q_{opt}	β_e	φ_G	Ang. Mom. Flux [Nm]	β_e	φ_G	Ang. Mom. Flux [Nm]
0.6	0.405	0.00074	0.803	0.347	-	-
1	0.395	0.00064	0.683	0.398	-	-
1.2	0.376	0.00064	0.644	0.401	-	-

Table 39: Angular momentum fluxes entering the hub side chamber

The angular momentum fluxes in the front side chamber slightly decrease with increasing pump flow rate and are always higher in case of the impeller without balancing holes. The latter can also be seen from the pressure distribution because the stronger gradient of the pressure curve compared to the impeller with balancing holes. This originates from the increase in the core rotation caused by the higher angular momentum flux leading to a sharper radial pressure drop.
Concerning the hub side chamber, the decrease of the leakage flow rate with increasing pump flow rate is clearly visible in the resultant pressure drop across the sealing gap. The pressure difference across the gap is continuously reduced if the pump flow rate increases (Fig. 134, Fig. 136). As in the shroud side chamber, the entering angular momentum flux is also reduced in the rearside cavity for increasing pump flow rate due to the overall reduction of the leakage flow rate. Moreover, the entrance rotation decreases because the secondary flow field from the impeller becomes more aligned in radial

direction since the volute appears to be designed for higher flow rates. As a consequence, the side chamber is fed by more low energy fluid from the volute.

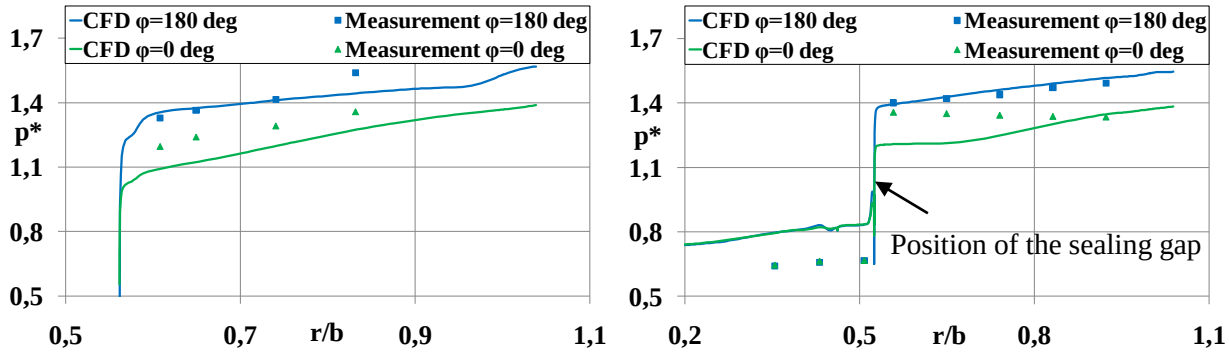

Fig. 134: Comparison between experimental and numerical results for the front side chamber (left) and rearside chamber (right)- impeller with balancing holes at part load (Q/Q_{opt}=0.6)

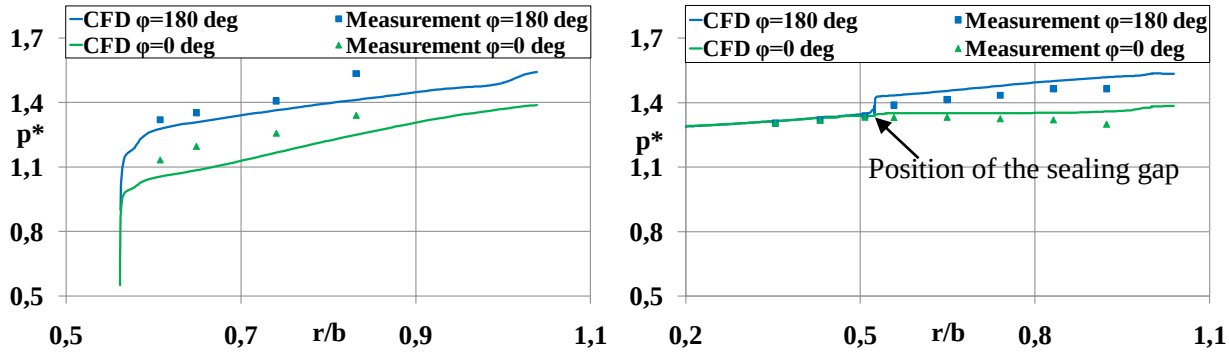

Fig. 135: Comparison between experimental and numerical results for the front side chamber (left) and rearside chamber (right) - impeller without balancing holes at part load ($Q/_{Qopt}$=0.6)

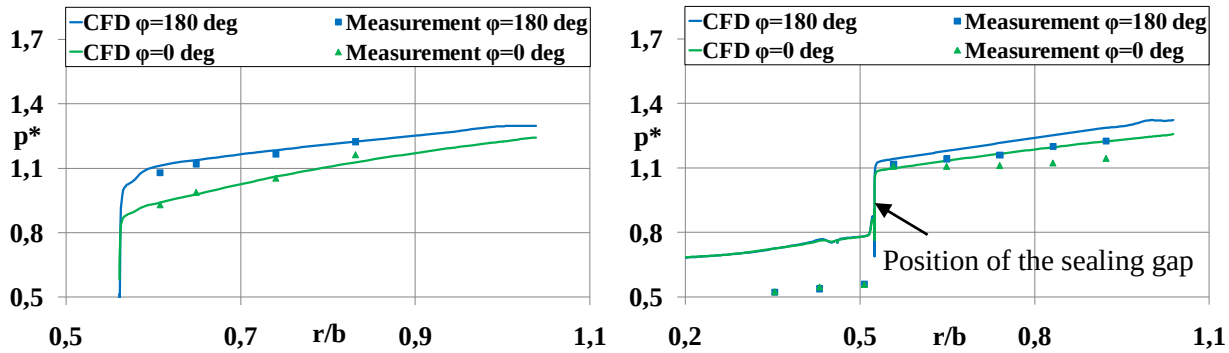

Fig. 136: Comparison between experimental and numerical results for the front side chamber (left) and rearside chamber (right) - impeller with balancing holes at overload (Q/Q_{opt}=1.2)

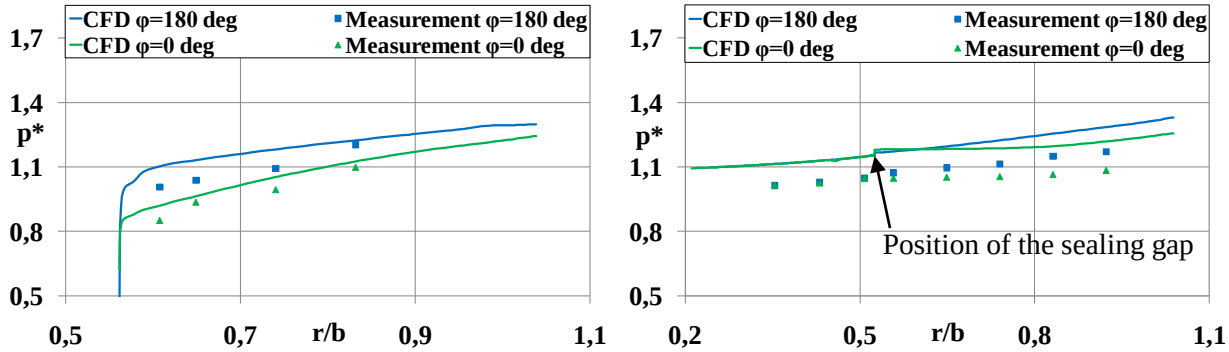

Fig. 137: Comparison between experimental and numerical results for the front side chamber (left) and rearside chamber (right) - impeller without balancing holes at overload (Q/Q_{opt}=1.2)

From the pressure diagrams for part and overload conditions it can be concluded that the basic relationships remain the same as in the design point, except that the overall pressure level varies according to the operating point of the pump. Looking at the diagrams in Fig. 136 and Fig. 137, an appreciable reduction of the pressure difference between the two tangential locations at φ=0 deg and φ=180 deg becomes clear. This indicates that the volute casing seems to be originally designed for a higher flow rate. Also the pressure distributions for the overload point in case of closed balancing holes indicate that the wake region caused by the pressure asymmetry became significantly smaller in size (Fig. 138, Fig. 139). The contrary prevails at the part load point where the size of the wake region increases. Furthermore, when the balancing holes are closed, the influence of viscosity can be clearly seen in the rearside chamber for smaller radial coordinates. The viscosity has a homogenizing effect on the pressure distributions and the curves overlap at lower radii.

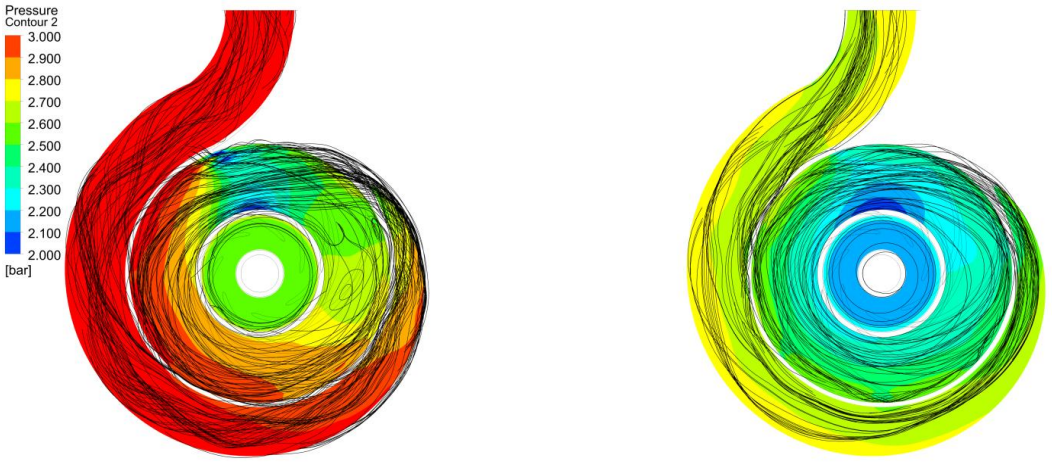

Q/Q_{opt}=0.6 Q/Q_{opt}=1.2

Fig. 138: 3D streamlines and pressure contours in the hub side chamber at z/s=0.917 (close to the stator)

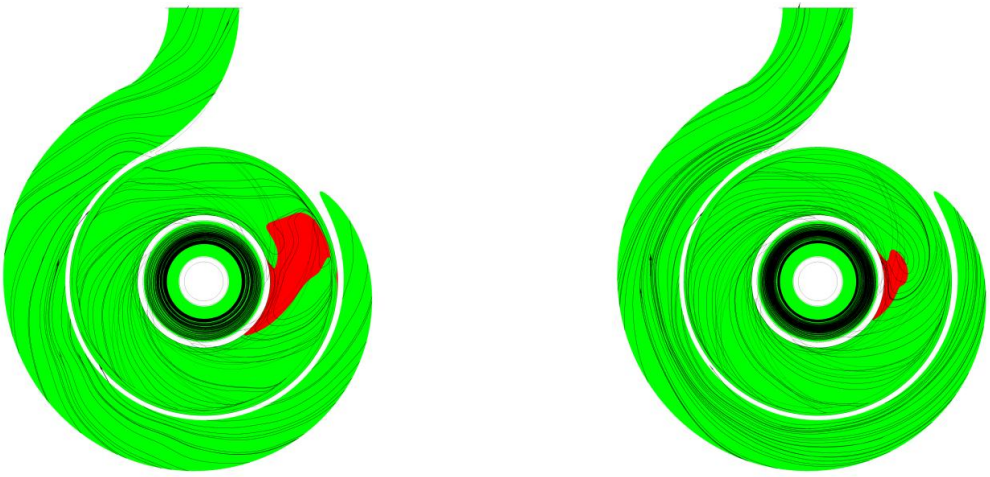

Q/Q_{opt}=0.6 Q/Q_{opt}=1.2

Fig. 139: 3D streamlines and direction of fluid rotation in the hub side chamber at z/s=0.917 (close to the stator)

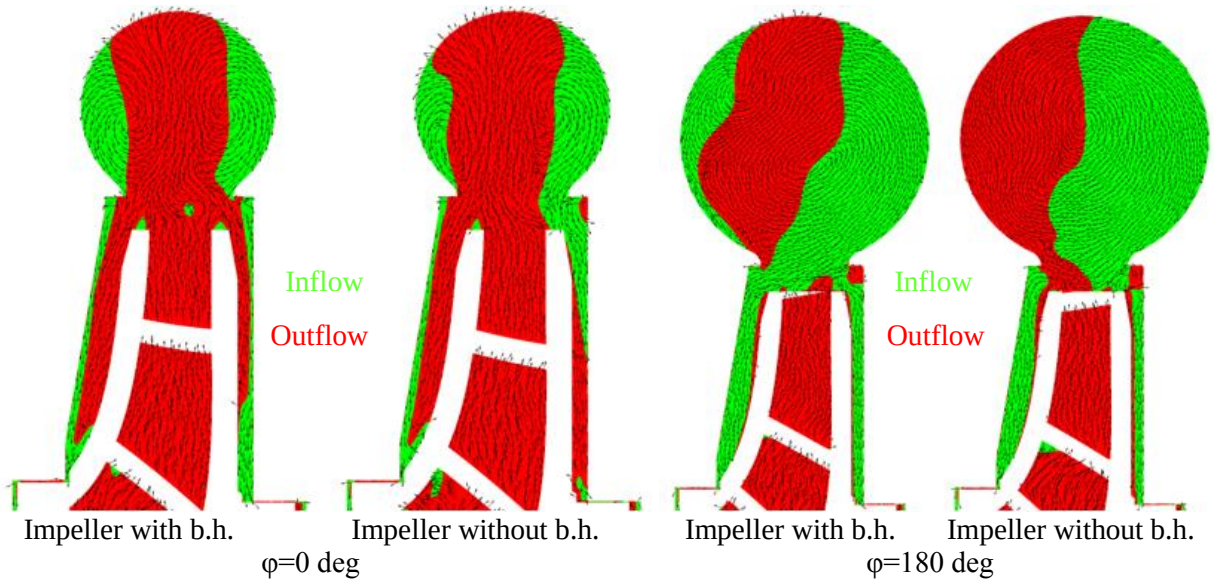

Fig. 140: Comparison of secondary flow patterns at part load (Q/Q_{opt}=0.6)

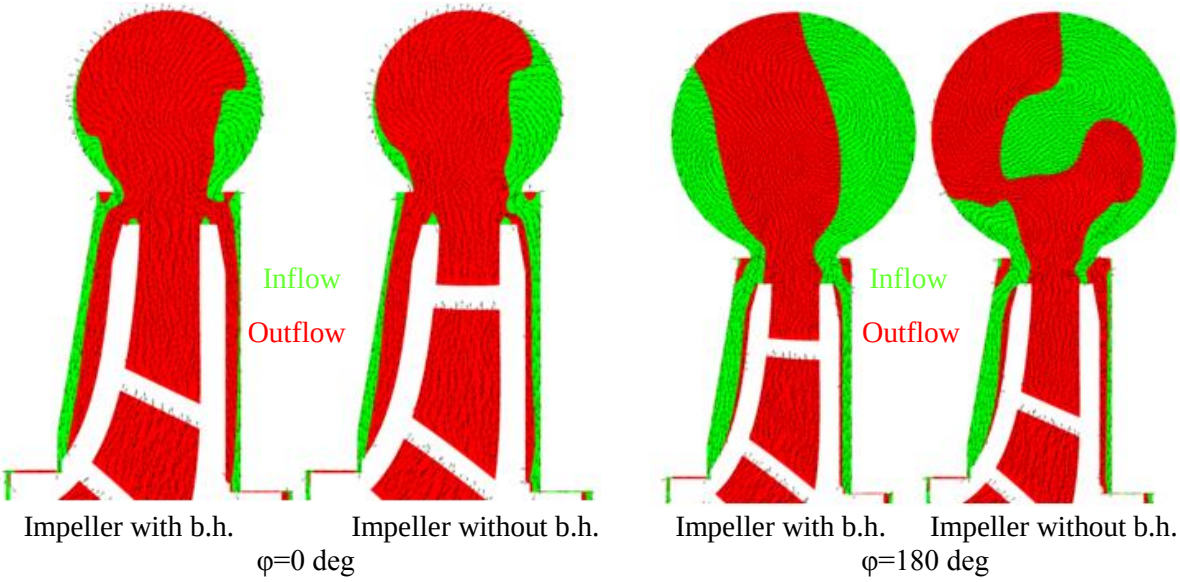

Fig. 141: Comparison of secondary flow patterns at overload (Q/Q_{opt}=1.2)

The secondary flow patterns confirm the presumption that the volute is designed for a higher flow rate because the secondary flow component is much better aligned in the radial direction at both control planes at overload conditions. Again, the same principal relations as for the design point apply. Closing the balancing holes deflects the flow field towards the suction side of the pump increasing the net angular momentum flux and thus the pressure drop in the front side chamber. The pressure distributions in the hub side chamber allow the conclusion that flow regime III persists for all operating points. In contrast, regime IV is present for all operating points in the front side chamber.
In Fig. 142 and Fig. 143 the diagrams for the analytical calculation at part load and overload are given. It can be generally stated that the determination of the pressure distribution in the side chambers using a 1D dimensional flow model is a challenging task. The particular pump used in this study clearly shows that even in the design point the pressure is a function of the tangential coordinate, both in the volute and in the side cavities. This emphasizes the strong coupling between these two components in centrifugal pumps with volute casing where the side cavities are relatively open. Consequently, a modeling approach based on the assumption of rotationally symmetric conditions can only yield an average estimate without taking into account the complex 3D circumstances. At best, the assumption of rotationally symmetric conditions applies in the design point provided that both the pump and the casing are designed for the same flow rate.

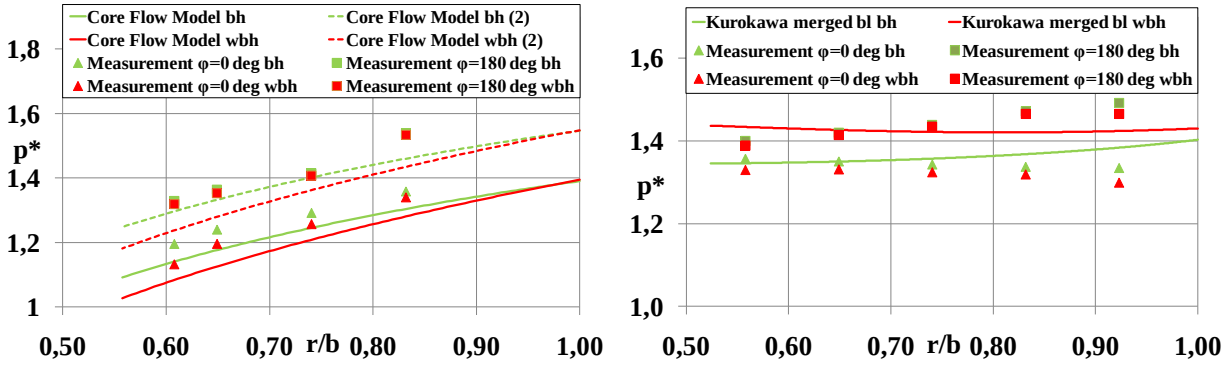

Fig. 142: Comparison between experiments and analytical calculation (left: front side chamber, right: rearside chamber) for part load $Q/Q_{opt}=0.6$

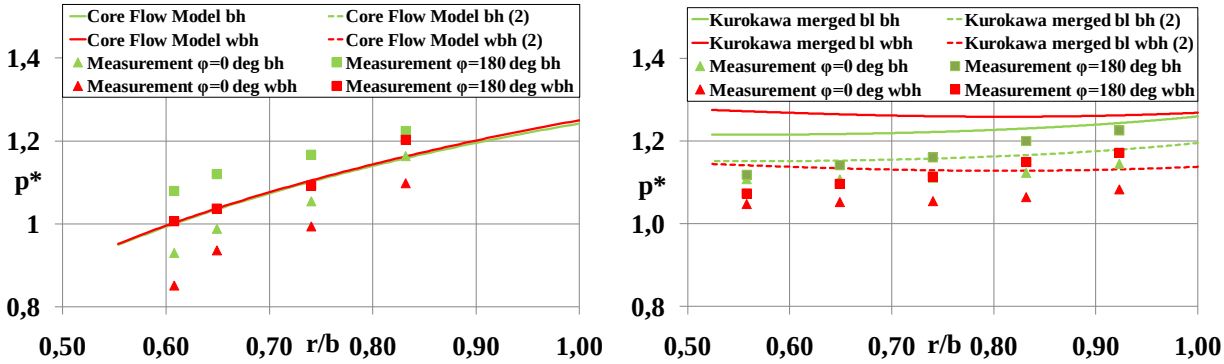

Fig. 143: Comparison between experiments and analytical calculation (left: front side chamber, right: rearside chamber) for part load $Q/Q_{opt}=1.2$

However, the applied methods give a good estimate of a mean pressure distribution if adequate boundary conditions for the pressure, the entrance rotation and the leakage flow rate are assigned. This consistently applies for the flow in the shroud side chamber at all three operating points. Nevertheless, the pressure boundary condition in the front side chamber evaluated from the numerical simulation at part load appears to be predicted somewhat too small. In this case, the use of an extrapolated value from the experiments (denoted by "(2)") clearly improves the calculation with respect to the experiment. In contrast to this, the boundary value in the hub side chamber at overload is somewhat overestimated.

According to the results, for all three operating points investigated, the flow in the front-side chamber corresponds to the Batchelor type of flow no matter if the impeller has balancing holes or not. In the hub side chamber, the flow conditions are inherently different due to the small axial gap width. This is clearly indicated by the radial evolution of the pressure with a much lower gradient and different shape. The reason for this behavior is that shear forces act along the whole gap width and are not limited to the vicinity of the rotating respectively stationary wall. This leads to smaller changes in the pressure distribution. Ordinary design procedures as outlined for example in **Gülich [34]** generally assume that Batchelor type of flow is present and can thus lead to erroneous results. However, many geometrical configurations can occur in industrial pumps. For example, **Bahm [6]** investigates the resulting axial force in a single stage pump with volute casing. This pump has a very large axial gap width in the hub side chamber as can be seen in Fig. 144. Besides, the previously proposed flow model is expected to give noticeably improved results in case of such a broad axial spacing.

If the balancing holes are closed, the angular momentum flux entering the shroud side chamber increases which can be seen from a slightly higher gradient in the pressure curves. This results from the shift in the flow field in the meridional plane towards the suction side of the pump. The major changes in the hub side chamber occur along the sealing gap. Due to the absence of an axial flow component, the pressure drop across the sealing gap vanishes and the pressure is mainly determined by the rotation of the fluid. Moreover, the pressure decreases only slightly in radial direction. From the diagrams it appears as if this case is better captured by the numerical simulation since the agreement with the experimental data improved in absence of balancing holes.

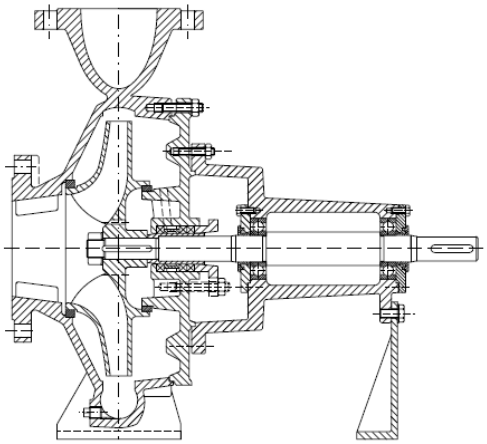

Fig. 144: Centrifugal pump with broad axial gap width in the hub side chamber used in the experimental investigation by Bahm [6]

The obtained results emphasize the interplay of the flow conditions in the volute and at the impeller outlet with the side cavities. Both the secondary flow in the volute and the main flow from the impeller determine the inflow conditions for the side chamber. Even a small intrusion, for example by closing the balancing holes, leads to remarkable changes in the whole system. The increase of the incoming angular momentum flux in the hub side chamber, despite reduced leakage, clearly demonstrates this. Moreover, the complexity of the whole flow system complicates any analytical pre-estimation procedures. The reliability of one dimensional flow models can certainly be improved by reducing the uncertainty in the determination of the boundary values. This is proven by the comparisons where the quality of the solution is improved by using extrapolated values from the experiment as boundary condition.

The flow in the side chambers is additionally strongly dependent on the operating point of the pump. In the front side and the rearside chamber, the leakage flow rate is consistently reduced when the flow rate of the pump is increased for the impeller with balancing holes. The reason is that the overall pressure difference across the cavity and hence across the sealing gap is lower for this case. However, when no balancing holes are present, the leakage flow rate in the hub side chamber is zero and in the shroud side chamber the leakage is higher for $Q/Q_{opt}=1.2$ than for $Q/Q_{opt}=1$. This is due to the resulting pressure drop in the side chamber. The increase in the core rotation towards the hub must be greater and thus the resulting effective pressure difference across the sealing gap is reduced which finally determines the leakage flow rate across the sealing gap.

Another important magnitude of the engineering interest is the resulting frictional resistance of the rotating surfaces. The resulting torque can be determined from the core rotation by summing up the differential torques resulting from the numerical integration method using **Eq. 87**. The results obtained for the pump are compared with the numerical values from the CFD simulation. In the rearside chamber, the friction torque is calculated by use of the following expression given in **Owen and Rogers [64]** for the moment coefficient in case of flow regime III subjected to a superposed through-flow:

$$c_M = 0.336 G^{-\frac{1}{4}} Re_\varphi^{-\frac{1}{4}} \int_{\frac{a}{b}}^{1} \bar{r}^{\frac{15}{4}} (1-\beta)^{\frac{7}{4}} d\,\bar{r} \qquad \textbf{Eq. 167}$$

Introducing the definition for the moment coefficient and rearranging yields an expression for the differential torque that has been implemented in the calculation procedure:

$$dM = 0.168 \frac{\bar{r}^{\frac{15}{4}} (1-\beta)^{\frac{7}{4}}}{G^{\frac{1}{4}} Re_\varphi^{\frac{1}{4}}} \rho \Omega^2 \mathrm{b}^5 \mathrm{d}\bar{\mathrm{r}} \qquad \textbf{Eq. 168}$$

The obtained results for the shroud side respectively hub side chamber are depicted in Table 40 and Table 41. In general, the torques obtained from the flow models and CFD show some quantitative differences but are of the same order of magnitude. However, the general tendencies using the flow models are more reasonable with respect to the aforementioned findings. In the shroud side chamber, the frictional resistance of the rotor decreases with decreasing net flow of the pump. The reason is that the angular momentum flux entering the side chamber increases as a result of an increased leakage. This applies for both cases with and without balancing holes. The same is valid for the hub side chamber (with leakage) although the relative changes with the operating point are smaller due to the different flow regime. If no through-flow is present in the rearside chamber, the resulting disk friction torque increases since no energy is brought into the system any more by an external leakage flow. Moreover, the torque changes only insignificantly in dependance on the operating point since the rotational velocity remains constant and no major parameter changes are present in absence of leakage.
An increase in the leakage flow rate through the side chambers leads to a deterioration of the volumetric efficiency. In contrast to this, the friction efficiency of the side chamber increases because of the reduced disk friction torque. Both effects are contrary to each other and determine the secondary efficiency that again influences the overall pump efficiency.

		$Q/Q_{opt}=0.6$	$Q/Q_{opt}=1$	$Q/Q_{opt}=1.2$
Flow model	bh	0.575	0.66	0.752
	wbh	0.398	0.375	0.7312
CFD	bh	0.61594	0.65386	0.56184
	wbh	0.486	0.4314	0.5381

Table 40: Comparison of the frictional torques [Nm] for the shroud side chamber

		$Q/Q_{opt}=0.6$	$Q/Q_{opt}=1$	$Q/Q_{opt}=1.2$
Flow model	bh	0.8464	0.8899	0.9074
	wbh	1.221	1.221	1.221
CFD	bh	0.78936	0.70836	0.75925
	wbh	1.08	0.945	0.9027

Table 41: Comparison of the frictional torques [Nm] for the hub side chamber

Although no experimental values are present, the results indicate the potential of 1D models to predict the torque of the rotating surfaces. Problems with the prediction of the frictional resistance of the disk can occur in CFD calculations. However, the general flow field can still be predicted sufficiently. A reason might be that the flow in this case is mainly determined by the characteristics of an external angular momentum flux rather than by the rotation of the disk. The overall flow field is then satisfactorily predicted by CFD although certain details of the flow, like the disk friction torque, may be poorly predicted. For this reason it is assumed that the use of wall functions for the determination of the disk torque must be treated with care. **Craft et al. [21]** use a modified analytical wall function in their numerical approach to take into account the skewing of the velocity vector in the near-wall sublayer of the rotating disk. The skewing of the velocity vector is usually not accounted for if standard log-law wall functions are employed. This indicates that the use of standard wall functions in commercial CFD codes can be problematic in the case of rotating flows.

7 Integration and Summary of Results

In the present study analytical, numerical and experimental investigations of the flow in rotor-stator cavities are accomplished. Outgoing from an idealized cavity model, a new one-dimensional flow model for the radial core rotation distribution is developed under the assumption of a flow regime with two boundary layers and an inviscid core region. This flow structure is expected to apply in the majority of applications especially with respect to increasing Reynolds numbers as they can be found in modern centrifugal compressors. The model takes into account the interaction of the entering fluid with a stationary radial shroud by means of an additional correction function. Furthermore, a different approach for the prescription of the wall shear stresses is embedded based on the pipe flow analogy. Most analytical models apply the strictly empirical Blasius relation (e.g. **Hamkins [36]**, **Daily and Nece [24]**) which is valid only within a certain Reynolds number range. The modified approach uses

the logarithmic law of the wall which is not bounded by this restriction. Since the logarithmic law represents an implicit expression for the friction coefficient, an iterative solution procedure is required. Either of the chosen friction laws requires information about the radial evolution of the boundary layer thickness. A formula for the radial rotor boundary layer thickness is proposed based on an approach originally suggested by **Poncet et al. [71]**. Comparisons with the experimental data obtained by **Lauer [50]** and two similar flow models underline the capability of the model to give an improved prediction of the radial core rotation distribution as the major flow parameter. Furthermore, the proposed flow model has proven a general validity since it is successfully applied for the prediction of the radial pressure distribution for both a radial compressor (thermal turbomachinery) and a centrifugal pump (hydraulic turbomachinery).

Numerical calculations are presented in the second part using the commercial CFD codes Ansys Fluent and Ansys CFX. The investigations focus on the prediction of the mean flow quantities in rotor-stator cavities. The results confirm the general flow structure in the case of a wide gap with two separate boundary layers and an inviscid core region. However, even for the geometrically simple model of an enclosed rotating disk, the core rotation can be a function of the radial coordinate as a result of transition from laminar to turbulent flow close to the rotating disk. For this case, the use of an advanced transition model proposed by **Langtry [49]** leads to a significant improvement although the model is not capable of resolving transition due to pure cross-flow instabilities which are considered as a major source of instability in rotating flows. The inability of the model to predict transition due to cross-flow instabilities is demonstrated for transitional flow along a free disk. Consequently, other transition phenomena are expected to occur alongside in the enclosed rotating disk case. 2D unsteady LES revealed that vortices role up due to the turning of the fluid at the outer radial casing. These vortices travel downstream on the stationary wall and are convected through the core towards the rotating disk. This process is suspected to additionally influence the stability of the boundary layer on the rotor.

Moreover, CFD calculations have been performed for rotor-stator configurations investigated in a large research project reported by **Radtke and Ziemann [78]**. The main focus is on the derivation of modeling guidelines that could be applied to the prediction of the flow in the centrifugal pump and the capability of common modeling strategies to predict the cavity flow for industrial applications. Since the investigation focuses on the prediction of mean flow quantities, the SST model proves to be a good choice in combination with the curvature correction function by **Menter and Smirnov [56]**. In terms of simulating the flow in a complete centrifugal pump, several restrictions arise with respect to the computational effort. Furthermore, problems with the solver are encountered when trying to reduce to y+ value below 2 in order to enable an explicit computation of the boundary layer flow. This may be attributed to the increased mesh quality demands for an explicit computation of the boundary layers. For this reason and with regard to the computational costs, all obtained results are based on the use of wall functions incorporating the automatic wall treatment in CFX.

Finally, investigations of the flow in the side chambers of a centrifugal pump with volute casing are accomplished. Numerical simulations of the complete pump including the side chambers are used to predict the flow fields for different operating points. Furthermore, two configurations of the impeller are examined, namely with and without balancing holes. Measurements of the radial static pressure distribution in both side chambers at two different tangential positions and the delivery head are additionally performed to support the numerical results. A close agreement for the delivery head is found in all configurations and operating points. In general, the pressure distribution in the shroud side chamber agrees well with the numerical results. Somewhat larger deviations occur in the hub side chamber. Due to the different gap widths, the flow structures in the side chambers of the present pump are inherently different. In the shroud side chamber, the axial distance between the rotating and the stationary wall is large enough so that two separate boundary layers can develop on the rotor and the stator. In the hub side chamber, merged boundary layers are present due to the small axial spacing. Consequently, the obtained pressure distributions are quite dissimilar. The influence of shear stresses across the whole axial extent leads to a significantly reduced pressure drop compared to the front side chamber. As a result, the axial forces on the walls do not balance.

The flow regimes are estimated a priori using the circumferential Reynolds number Re_φ and the dimensionless axial gap width G in a diagram based on the insights of **Daily and Nece [24]**. Since only a small leakage flow is present in the rearside cavity, the method seems to be quite useful in order to determine the required calculation method for design purposes according to the flow regime.

The flow in the side chambers is strongly coupled with the flow in the volute and the impeller outflow. In the standard configuration, the impeller is equipped with balancing holes. Closing these holes drastically changes the flow conditions in the rearside chamber. Even the pressure distribution in the front side chamber is altered due to a totally different secondary flow field in the volute. More precisely, the angular momentum flux increases because more high energy fluid is entrained directly from the impeller. The reason for this is an axial pressure gradient at the outer impeller radius that shifts the flow field towards the suction side of the pump.

For the centrifugal pump under consideration, the pressure in the side cavities is a function of the circumferential coordinate as a consequence of the interaction with the volute casing. Almost rotationally symmetric conditions can apply only, if at all, in the design point. In the present pump, even at design flow rate the pressure changes in the tangential direction in the volute and consequently in both side chambers, too. This leads to variable flow conditions in tangential direction and also to a radial force on the impeller which can cause an eccentric deflection. If the impeller is in an eccentric position, the sealing gap height is not constant anymore in the circumferential direction which directly influences the leakage flow.

For the impeller configuration without balancing holes, a recirculation pattern in the rearside chamber develops. In this region, the fluid rotates in the opposite direction than the impeller. This is a direct consequence of the inhomogeneous pressure pattern and demonstrates that the outer pressure field from the volute strongly dictates the flow conditions even in the narrow rearside chamber. Since no recirculation region is found if the impeller is equipped with balancing holes, the radial flow component is supposed to suppress the formation of the wake.

The proposed flow model yields reasonable results in the front side chamber since the gap width allows for the formation of two separated boundary layers on the rotating disk and the stationary casing. In the rearside chamber, a considerably smaller axial gap width prevents the formation of Batchelor flow and the flow is strongly viscosity affected. As a result, the radial pressure drop is reduced with a completely different characteristic compared to the front side chamber. Therefore, an approach proposed by **Kurokawa and Sakuma [47]** is used to calculate the radial pressure distribution that takes into account the axial gap width. The incorporated flow models emerge from the assumption of axis-symmetric flow conditions and can therefore only yield an average estimate of the actual complex flow structure. However, the theoretical results lie well between the measured data at the two circumferential positions as long as sufficiently accurate boundary conditions are applied.

Concluding, the flow structure in the side cavities of a real machine is very complex and inseparably influenced by the interaction with the flow in the adjacent components. The main flow features encountered in studies of the flow in rotor-stator configurations are found to occur also in practical applications but are superposed with additional flow effects from the adjacent components. Thus, analytical flow models can yield reasonable results if accurate boundary conditions are provided at the interfaces. Especially at off-design conditions this is a difficult task because large discrepancies in the boundary values can be present for both side chambers.

8 References

[1] Abdel Nour, F., Debuchy, R., Bois, G., Naji, H., 2010, On Numerical and Analytical Modelling of Flow in a Rotor-Stator System without Superposed Flow: Experimental Comparison, The 13th International Symposium on Transport Phenomena and Dynamics of Rotating Machinery (ISROMAC-13), ISROMAC13-TS46, Honolulu, Hawaii, USA.

[2] Altmann, D., 1972, Beitrag zur Berechnung der turbulenten Strömung im Axialspalt zwischen Laufrad und Gehäuse von Radialpumpen, Dissertation, TU Magdeburg.

[3] Altmann, D., 1984, Bestimmung der Radreibungsverluste bei radialen Kreiselpumpen mit offenen Rückenschaufeln, Technische Mechanik, Band 5, Nr. 4, Seite 53-61.

[4] Andersson, H.I., Lygren, M., 2001, Turbulent flow between a rotating and a stationary disk, Journal of Fluid Mechanics, Vol. 426, p. 297-326.

[5] Andersson, H.I., Lygren, M., 2006, LES of open rotor-stator flow, International Journal of Heat and Fluid Flow, Vol. 27, No. 4, p. 551-557.

[6] Bahm, F.U., 2000, Das Axialschubverhalten einstufiger Kreiselpumpen mit Spiralgehäuse, Dissertation, Universität Hannover.

[7] Baibikov, A.S., V.K. Karakhan'yan, 1973, Method of Calculating Axial Force in a Centrifugal Pump with Allowance for Leakage, Journal Thermal Engineering, Vol. 20, No. 9, p. 85-88.

[8] Baibikov, A.S., 1998, Method of Calculation of a Turbulent Flow in an Axial Gap with a Variable Radius between a Rotating Disk and an Axisymmetric Casing, Journal of Engineering Physics and Thermophysics, Vol. 71, No. 6, p. 1072-1081.

[9] Batchelor, G.K., 1951, Note on a class of solutions of the Navier-Stokes equations representing steady rotationally-symmetric flow, The Quarterly Journal of Mechanics and Applied Mathematics, Vol. 4, No. 1, p. 29-41.

[10] Bayley, F.J., Owen, J.M., 1969, Flow between a rotating and a stationary disc, Aeronautical Quarterly, Vol. 20, p. 333-354.

[11] Bennet, T.P., Worster, R.C., 1961; The Friction on Rotating Disc and Effect on Net Radial Flow and Externally Applied whirl, British Hydromechanics Research Association, Report RR691.

[12] Bödewald, U.T., 1940, Die Drehströmung über festem Grunde, Zeitschrift für angewandte Mathematik und Mechanik, Band 20, Nr. 5, Seite 241-253.

[13] Brady, J.F., Durlofsky, L., 1987, On rotating disk flow, Journal of Fluid Mechanics, Vol. 175, p. 363-394.

[14] Broecker, E., 1959, Theorie und Experiment zum Reibungswiderstand der glatten rotierenden Scheibe bei turbulenter Strömung, Zeitschrift für angewandte Mathematik und Mechanik, Band 39, Nr. 1/2, Seite 68-76.

[15] Bubelach, T., 2009, Untersuchung der Radseitenraumströmung in einer Einschaufelrad - Abwasserpumpe, Dissertation, TU Berlin.

[16] Cebeci, T., Abbott, D.E., 1975, Boundary Layers on a Rotating Disk, AIAA Journal, Vol. 13, No. 6, p. 829-832.

[17] Cheah, S.C., Iacovides, H., Jackson, D.C., Ji, H., Launder, B.E., 1994, Experimental Investigation of Enclosed Rotor-Stator Disk Flows, Experimental Thermal and Fluid Science, Vol. 9, No. 4, p. 445-455.

[18] Chew, J.W., Vaughan, C.M., 1988, Numerical Predictions for the Flow Induced by an Enclosed Rotating Disc, Gas Turbine and Aeroengine Congress and Exposition, Paper No. 89-GT-127, Amsterdam, Netherlands.

[19] Cochran, W.G., 1934, The flow due to a rotating disk, Proceedings of the Cambridge Philosophical Society., Vol. 30, p. 365-375.

[20] Cooper, P., Reshotko, E., 1975, Turbulent Flow Between a Rotating Disc and a Parallel Wall, AIAA Journal, Vol. 13, No. 5, p. 573-578.

[21] Craft, T., Iacovides, H., Launder, B., Athanasios, Z., 2008, Some Swirling-flow Challenges for Turbulent CFD, Flow, Turbulence and Combustion, Vol. 80, No. 4, p. 419-434.

[22] Czarny, O., Iacovides, H., Launder, B.E., 2002, Precessing vortex structures in turbulent flow within rotor-stator disc cavities, Flow Turbulence and Combustion, Vol. 69, No. 1, p. 51-61.

[23] Da Soghe, R., Facchini, B., Innocenti, L., Micio, M., 2010, Analysis of Gas Turbine Rotating Cavities by a One-Dimensional Model: Definition of New Disk Friction Coefficient Correlations Set, Journal of Turbomachinery, Vol. 133, No. 2, p. 021020-1 - 021020-8.

[24] Daily, J.W., Nece, R.E., 1960, Chamber dimension effects on induced flow and frictional resistance of enclosed rotating disks, Journal of Basic Engineering 82, p. 217-232.
[25] Daily, J.W., Ernst, W.D., Asbedian, V.V., 1964, Enclosed Rotating Discs with Superposed Through-Flow, Massachusetts Institute of Technology, Report No. 64.
[26] Debuchy, R., Poncet, S., Abdel Nour, F., Bois, G., 2009, Experimental and Numerical Investigation of Turbulent Air Flow Behavior in a Rotor-Stator Cavity, 8th European Turbomachinery Conference, Graz, Austria.
[27] Dijkstra, D., Van Heijst, G.J.F., 1983, The flow between two finite rotating discs enclosed by a cylinder, Journal of Fluid Mechanics, Vol. 128, p. 123-154.
[28] Dorfmann, L.A., 1958, Resistance of a rotating rough disc, Zh.tekh.Fiz., Vol. 28, p. 380-386.
[29] Dorfmann, L.A., 1963, Hydrodynamic resistance and the heat loss of rotating solids, Oliver and Boyd, Edinburgh.
[30] Elena, L., Schiestel, R., 1995, Turbulence Modeling of Confined Flow in Rotating Disk Systems, AIAA Journal, Vol. 33, No. 5, p. 812-821.
[31] Goldstein, S., 1935, On the resistance to the rotation of a disc immersed in a fluid, Proceedings Cambridge Philosophical Society, Vol. 31, p. 232-241.
[32] Gregory, N., Stuart, J.T., Walker, W.S., 1955, On the Stability of Three-Dimensional Boundary Layers with Application to the Flow Due to a Rotating Disk, Philosophical transactions of the Royal Society / Series A, Mathematical, physical and engineering sciences, Vol. 248, p. 155-199.
[33] Gülich, J.F., 2003, Disk friction losses of closed turbomachine impellers, Forschung im Ingenieurwesen, Band 60, Nr. 2, Seite 87-95.
[34] Gülich, J.F., 2010, Handbuch Kreiselpumpen, Springer-Verlag, Berlin, Germany.
[35] Haddadi, S., Poncet, S., 2008, Turbulence Modeling of Torsional Couette Flows, International Journal of Rotating Machinery, Volume 2008, Article ID 635138, 27 pages.
[36] Hamkins, C.P., 1999, The Surface Flow Angle in Rotating Flow: Application to the Centrifugal Pump Impeller Side Gap, Dissertation, TU Kaiserslautern.
[37] Iacovides, H., Theofanopoulos, I. P., 1991, Turbulence modeling of axisymmetric flow inside rotating cavities, International Journal of Heat and Fluid Flow, Vol. 12, No. 1, p. 2-11.
[38] Iacovides, H., Toumpanakis, 1993, Turbulence modelling of flow in axisymmetric rotor-stator systems, 5th International Symposium on Refined Flow Modelling and Turbulence Measurements, Paris, Int. Assoc. Hydr. Res., p. 835-842.
[39] Iino, T., Sato, H., Miyashiro, H., 1980, Hydraulic Axial Thrust in Multistage Centrifugal Pumps, ASME Journal Fluids Engineering, Vol. 102, No. 1, p. 64-69.
[40] Itoh, M., Yamada, Y., Imao, S. Gonda, M., 1992, Experiments on turbulent flow due to an enclosed rotating disk, Experimental Thermal and Fluid Science, Vol. 5, No. 3, p. 359-368.
[41] Itoh, M., 1995, Experiments on the turbulent flow in the narrow clearance between a rotating and a stationary disk, Turbulent Flows - Proceedings of the Forum, 1997 ASME/JSME Fluids Engineering and Laser Anenometry Conference and Exhibition, Aug. 13-18 1995, edited by B.F. Carroll, T. Kobayashi, and M. J. Morris, Vol. 208, p. 27-32.
[42] Kármán, Th. v., 1921, Über laminare und turbulente Reibung, Zeitschrift für angewandte Mathematik und Mechanik, Band 1, Nr. 4, Seite 233-252.
[43] Kreith, F., 1968, Convection heat transfer in rotating systems, Advances in Heat Transfer, Vol. 5, Academic Press, Inc, USA, p. 129-251.
[44] Kurokawa, J., Toyokura, T., 1972, Study on Axial Thrust of Radial Flow Turbomachinery, The second international JSME Symposium Fluid Machinery and Fluidics, Tokyo, p. 31-40.
[45] Kurokawa, J., Toyokura, 1976, Axial Thrust, Disc Friction Torque and Leakage Loss of Radial Flow Turbomachinery, International Conference on Pump and Turbine Design and Development, Vol. 1, Paper 5-2, Glasgow, England.
[46] Kurokawa, J., Toyokura, T., 1978, Roughness Effects on the Flow along an Enclosed Rotating Disc, Bulleting of the JSME, Vol. 21, No. 162, Paper No. 162-8, p.1725-1732.
[47] Kurokawa, J., Sakuma, M., 1988, Flow in a Narrow gap along an Enclosed Rotating Disk with Through-Flow, JSME International Journal, Series II, Vol. 31, No. 2, p. 243-251.
[48] Lance, G.N., Rogers, M.H., 1962, The Axially Symmetric Flow of Viscous Fluid between Two Infinite Rotating Discs, Proceedings of the Royal Society of London, Series A, Mathematical and Physical Sciences, Vol. 266, p. 109-121.

[49] Langtry, R.B., 2006, A Correlation-Based Transition Model using Local Variables for Unstructured Parallelized CFD Codes, Dissertation, University of Stuttgart.
[50] Lauer, J., 1999, Einfluss der Eintrittsbedingung und der Geometrie auf die Strömung in den Radseitenräumen von Kreiselpumpen, Dissertation, TU Darmstadt.
[51] Launder, B.E., Li, S.-P., 1994, On the elimination of wall-topography parameters from second-moment closure, Physics of Fluids, Vol. 6, No. 2, p. 999-1006.
[52] Launder, B., Poncet, S., Serre, E., 2010, Laminar, Transitional and Turbulent Flows in Rotor-Stator Cavities, Annual Review of Fluid Mechanics, Vol. 42, p. 229-248.
[53] Littell, H.S., Eaton, J. K., 1994, Turbulence characteristics of the boundary layer on a rotating disk, Journal of Fluid Mechanics, Vol. 266, p. 175-207.
[54] Lomakin, A.A., 1940, Axial Pressure in Centrifugal Pumps, Taking into Account the Influence of the Gap Size in the Packing Rings, Sovietskoe Kotloturbostroenie, Vol. 12, p. 431-437.
[55] Menter, F.R., Kuntz, M., Langtry, R., 2003, Ten Years of Industrial Experience with the SST Turbulence Model, Turbulence, Heat and Mass Transfer, Vol. 4, p. 625-632.
[56] Menter, F.R., Smirnov, P.E., 2009, Sensitization of the SST Turbulence Model to Rotation and Curvature by Applying the Spalart-Shur Correction Term, Journal of Turbomachinery, Vol. 131, No. 4, p. 041010-1 – 041010-8.
[57] Morse, A.P., 1988, Numerical prediction of turbulent flow in rotating cavities, Journal of Turbomachinery, Vol. 110, No. 2, p. 202-211.
[58] Morse, A.P., 1991, Assessment of Laminar-Turbulent Transition in Closed Disk Geometries, Journal of Turbomachinery, Vol. 113, p. 131-138.
[59] Möhring, U.K., 1976, Untersuchung des radialen Druckverlaufes und des übertragenen Drehmomentes im Radseitenraum von Kreiselpumpen bei glatter, ebener Radseitenwand und bei Anwendung von Rückenschaufeln, Dissertation, TU Braunschweig.
[60] Oberlack, M., 2001, A unified approach for symmetries in plane parallel turbulent shear flows, Journal of Fluid Mechanics, Vol. 427, p. 299-328.
[61] Owen, J.M., 1969, Flow between a Rotating and a Stationary Disk, Doctor of Philosophy Thesis, Sussex University.
[62] Owen, J.M., Pincombe, J.R., 1980, Velocity measurements inside a rotating cylindrical cavity with a radial outflow of fluid, Journal of Fluid Mechanics, Vol. 99, No. 1, p. 111-127.
[63] Owen, J.M., 1989, An Approximate Solution for the Flow Between a Rotating and a Stationary Disc, Journal of Turbomachinery, Vol. 111, No. 3, p. 323-332.
[64] Owen, J.M., Rogers, R.H., 1989, Flow and Heat Transfer in Rotating-Disc Systems, Volume 1: Rotor-Stator Systems, Research Study Press, Taunton, Somerset, UK.
[65] Owen, J.M., 2000, Flow and heat transfer in rotating disc systems: some recent developments, Turbulence, Heat and Mass Transfer, Vol. 3, p. 35-58.
[66] Pantell, K., 1950, Versuche über Scheibenreibung, Forschung auf dem Gebiete des Ingenieurwesens, Band 16, Nr. 4, Seite 97-108.
[67] Pastore, A., 2011, Numerische Simulation des hinteren Radseitenraums einer radialen Kreiselpumpe, Studienarbeit, Universität Duisburg-Essen, Duisburg, Germany.
[68] Pavesi, G., 2006, Impeller Volute and Diffuser Interaction, presented during the AVT-143 RTO AVT/VKI Lecture Series held at the von Karman Institute, Rhode St. Gense, Belgium.
[69] Pearson, C.E., 1965, Numerical Solutions for the Time-Dependent Viscous Flow between two Rotating Coaxial Discs, Journal Fluid Mechanics, Vol. 21, No. 4, p. 623-633.
[70] Petry, N., Benra, F.K., König, S., 2010, Experimental Study of Acoustic Resonances in the Side Cavities of a High-Pressure Centrifugal Compressor Excited by Rotor/Stator Interaction, Proceedings of ASME Turbo Expo 2010: Power for Land, Sea, Air, GT2010-22054, Glasgow, UK.
[71] Poncet, S., Chauve, M.P., Le Gal, P., 2005, Turbulent Rotating Disk Flow with Inward Through-Flow, Journal Fluid Mechanics, Vol. 522, p. 253-262.
[72] Poncet, S., Schiestel, R., Chauve, M.P., 2005, Turbulence Modelling and Measurements in a Rotor-Stator System with Throughflow, Engineering Turbulence Modelling and Experiments ETMM6, Elsevier (New-York), p. 761-770.
[73] Poncet, S., Schiestel, R., 2007, Numerical modeling of heat transfer and fluid flow in rotor-stator cavities with throughflow, International Journal Heat Mass Transfer, Vol. 50, p. 1528-1544.

[74] Poncet, S., Da Soghe, R., Facchini, B., 2010, RANS modeling of flow in rotating cavity system, V European Conference on Computational Fluid Dynamics ECCOMAS CFD 2010, Lisbon, Portugal.
[75] Pope, S.B., 2009, Turbulent Flows, Cambridge University Press, Cambridge, UK.
[76] Rabs, M., Benra, F.K., Dohmen, H.J., Schneider, O., 2009, Investigation of Flow Instabilities Near The Rim Cavity Of A 1.5 Stage Gas Turbine, Proceedings of ASME Turbo Expo 2009: Power for Land, Sea and Air, GT2009-59965, Orlando, Florida, USA.
[77] Rabs, M., 2010, Personal correspondence.
[78] Radtke, F., Ziemann, M., 1983, Experimentelle und theoretische Untersuchung des Reibungseinflusses an rotierenden Scheiben, FVV Forschungsberichte Nr. 331, Frankfurt.
[79] Randriamampianina, A., Elena, L., Schiestel, R., Fontaine, A.P., 1997, Numerical Prediction of Laminar, Transitional and Turbulent Flows in Shrouded Rotor-Stator systems, Physics of Fluids, Vol. 9, No. 6, p. 1696-1713.
[80] Schlichting, H., 1979, Boundary Layer Theory, McGraw-Hill, 7th edition.
[81] Schlichting, H., Gersten, K., 2006, Grenzschicht-Theorie, Springer-Verlag, Berlin, Germany.
[82] Schouveiller, L., Le Gal, P., Chauve, M.P., 2001, Instabilities of the flow between a rotating and a stationary disk, Journal of Fluid Mechanics, Vol. 443, p. 329-350.
[83] Schubert, F., 1988, Untersuchungen der Druck- und Geschwindigkeitsverteilung in Radseitenräumen radialer Strömungsmaschinen, Dissertation, TU Braunschweig.
[84] Schultz-Grunow, F., 1935, Der Reibungswiderstand rotierender Scheiben in Gehäusen, Zeitschrift für angewandte Mathematik und Mechanik, Band 15, Seite 191-204.
[85] Senoo, Y., Hayami, H., 1976, An Analysis on the Flow in a Casing Induced by a Rotating Disk Using a Four-Layer Flow Model, Transactions of the ASME, Journal of Fluids Engineering, Vol. 99, p. 192-198.
[86] Séverac, É., Poncet, S., Serre, É., 2007, Large Eddy Simulation and Measurements of Turbulent Enclosed Rotor-Stator Flow, Physics of Fluids, Vol. 19, No. 8.
[87] Sigloch, H., 2006, Strömungsmaschinen, Carl Hanser-Verlag, München, Germany.
[88] Soo, S.L., 1958, Laminar flow over an enclosed rotating disk, Journal of Basic Engineering, Vol. 80, No. 2, p. 287-296.
[89] Spalart, P.R., Shur, M.L., 1997, On the Sensitization of Turbulence Models to Rotation and Curvature, Aerospace Science and Technology, Vol. 1, No. 5, p. 297-302.
[90] Spurk, J.H., Strömungslehre, 1996, Springer-Verlag, Berlin, Germany.
[91] Stepanoff, A., 1932, Leakage Loss and Axial Thrust in Centrifugal Pumps, ASME Paper HYD-54-5, p. 65-103.
[92] Stuart, J.T., 1954, On the effects of uniform suction on the steady flow due to a rotating disc, Quaterly Journal of Mechanics and Applied Mathematics, Vol. 7, No. 4, p. 446-457.
[93] Stewartson, K., 1953, On the Flow between Two Coaxial Rotating Disks, Proceedings of the Cambridge Philosophical Society, Vol. 49, p. 333-341.
[94] Szeri, A.Z., Schneider, S.J., Labbe, F., Kaufmann, H.N., 1983, Flow between two rotating disks - part 1: basic flow, Journal of Fluid Mechanics, Vol. 134, p. 103-131.
[95] Tamm, A., 2002, Beitrag zur Bestimmung der Wirkungsgrade einer Kreiselpumpe durch theoretische, numerische und experimentelle Untersuchungen, Dissertation, TU Darmstadt.
[96] Theodorsen, T., Regier, A., 1944, Experiments on drag of revolving cylinders and streamline rods at high speeds, NACA Report, No. 793.
[97] Truckenbrodt, E., 1954, Die turbulente Strömung an einer angeblasenen rotierenden Scheibe, Zeitschrift für angewandte Mathematik und Mechanik, Band 34, Heft 4/5, Seite 150-162.
[98] Truckenbrodt, E., 1989, Fluidmechanik, Springer Verlag, Berlin, Germany.
[99] Vaughan, C.M., 1986, A numerical investigation into the effect of an external flow field on the sealing of a rotor-stator cavity, Dissertation, University of Sussex.
[100] Watanabe, K., Budiarso, Ogata, S., Uemura, K., 2007, Drag Reduction of an Enclosed Rotating Disk with Fine Spiral Grooves, Journal of Environment and Engineering, Vol. 2, No. 1, p.97-107.
[101] Wiederuh, E., Lingelbach, T., 1989, Die Axialschubberechnung radialer Turbomaschinen, VDI-Verlag, Düsseldorf, Germany.

[102] Will, B.C., Benra, F.K., 2008, The Rise of Complexity in Describing Fluid Flow in Rotating Cavities, Proceedings of FEDSM2008, ASME Fluids Engineering Conference, FEDSM2008-55341, Jacksonville, Florida, USA.
[103] Will, B.C., Benra, F.K., 2009, Investigation of the Fluid Flow in a Rotor-Stator Cavity with Inward Through-Flow, Proceedings of FEDSM2009, ASME Fluids Engineering Conference, FEDSM2009-78503, Vail, Colorado, USA.
[104] Will, B.C., Benra, F.K., Dohmen, H.J., 2010, Numerical and Experimental Investigation of the Flow in the Side Cavities of a Centrifugal Pump, The 12th International Symposium on Transport Phenomena and Dynamics of Rotating Machinery, ISROMAC13-2009-0002, Honolulu, Hawaii, USA.
[105] Will, B.C., Benra, F.K., Dohmen, H.J., 2011, Investigation of the Flow in the Side Chambers of a Centrifugal Pump with Volute Casing, 10th International Symposium on Experimental Computational Aerothermodynamics of Internal Flows, Brussels, Belgium
[106] Wu, X., Squires, K.D., 2000, Prediction and investigation of the turbulent flow over a rotating disk, Journal of Fluid Mechanics, Vol. 418, No. 1, p. 231-264.
[107] Zacharos, A., 2008, The use of unsteady RANS in the computation of 3-dimensional flows in rotating cavities, PhD Thesis, School of MACE, University of Manchester.
[108] Zandbergen, P.J., Dijkstra, D., 1987, Van Kármán swirling flows, Annual Review of Fluid Mechanics, Vol. 19, p. 465-491.
[109] Zilling, H., 1973, Untersuchung des Axialschubs und der Strömungsvorgänge in den Radseitenräumen einer einstufigen radialen Kreiselpumpe mit Leitrad, Dissertation, Universität Karlsruhe.

Curriculum Vitae

Der Lebenslauf ist in der Online-Version aus Gründen des Datenschutzes nicht enthalten.